Computational Models for the Simulation and Monitoring of Developing Crystalline Deposits Originating from Dripping Process Liquors.

Michael Christopher Harry Dawson

Submitted in accordance with the requirements for the degree of

Doctor of Philosophy

University of Leeds

School of Chemical and Process Engineering and

School of Civil Engineering.

September 2014

Jointly Authored Publications

The candidate confirms that the work submitted is his own, except where work which has formed part of jointly authored publications has been included. The contribution of the candidate and the other authors to this work has been explicitly indicated below. The candidate confirms that appropriate credit has been given within the thesis where reference has been made to the work of others.

The work in Chapter 3, 4 and 5 of the thesis has appeared in publication as follows:

- M. Dawson, D. Borman, R. B. Hammond, D. Lesnic and D. Rhodes. Modelling the morphology of crystalline deposits evolving from impinging droplets of salt solution. *South African Conference on Computational and Applied Mechanics, NH Lord Charles Hotel, Somerset West, South Africa*, 14th-16th January, 2014.

- M. Dawson, D. Borman, R. B. Hammond, D. Lesnic and D. Rhodes. Moving boundary models for the growth of crystalline deposits from undetected leakages of industrial process liquors.*Computers & Chemical Engineering*, 71:331-346, 2014.

I was responsible for the development and implementation of the models, execution of the numerical experiments and analysis of the results. The contributions of the other authors were in the advice of potential numerical simulations and the editing of the papers.

The work in Chapter 6 of the thesis has appeared in publication as follows:

- M. Dawson, D. Borman, R. B. Hammond, D. Lesnic and D. Rhodes. Meshless detection of an internal moving boundary. *Proceedings of the 8th UK Conference on Boundary Integral Methods, Leeds University Press*, Pages 17-24. 2011.

- M. Dawson, D. Borman, R. B. Hammond, D. Lesnic and D. Rhodes. Predicting a time evolving accumulating crystalline formation using a meshless boundary tracking approach. *Particulate System Analysis, Hilton Grosvenor Hotel, Edinburgh, UK. (CD-ROM).* 5th - 7th September, 2011.

- M. Dawson, D. Borman, R. B. Hammond, D. Lesnic and D. Rhodes. Detection of a two-dimensional moving cavity. *International Journal of Computer Mathematics*, 89(11):1569-1582, 2012.

- M. Dawson, D. Borman, R. B. Hammond, D. Lesnic and D. Rhodes. A meshless method for solving a two-dimensional transient inverse geometric problem. *International Journal of Numerical Methods for Heat & Fluid Flow*, 23(5):790-817, 2013.

I was responsible for the development and implementation of the models, execution of the numerical experiments and analysis of the results. The contributions of the other authors were in the advice of potential numerical simulations and the editing of the papers.

Acknowledgements

I would like to extend my most sincere gratitude to my supervisors, Dr. Duncan Borman, Prof. Daniel Lesnic and Dr. Robert Hammond. Their dedication and patience in mentoring me throughout the past four years is greatly appreciated. Their insightful suggestions and encouragement have helped motivate me and reach my potential during my time at Leeds.

I would like to give my thanks to the National Nuclear Laboratory and Sellafield Ltd, for their most generous funding and support, and the opportunity to work on such a unique problem. Particularly I would like to thank Dr. Dominic Rhodes and Andrew Milliken who throughout the years have been paramount in helping coordinate the project, bridging the gap between industry and academia.

Most importantly, I would like to thank my partner Laura, for her unconditional love, understanding and patience with me. Her help and support over the years has been of utmost importance to me throughout my research. I would also like to thank my parents for instilling in me a passion for learning, supporting me at every step and ultimately getting me where I am today.

Abstract

The work in this thesis focused on several problems relating to the growth and fouling of crystal mass in industrial environments, due to leakage of salt solutions or process liquor. The work has direct application to the nuclear industry, where the size and morphology of material deposits heavily impact on their associated criticality risk. An absence of clear methods and techniques to either predict or non-invasively monitor the growth of these crystalline deposits proves problematic for industrial specialists. Therefore the main part of the thesis focused on the development and implementation of models such that the growth behaviour of crystalline formations could be evaluated and quantified for varying physical parameters. This was accomplished through both the adaptation of previous geological models, and the development of a coupled multi-physics model such that fluid flow, heat transfer and crystallisation mechanisms could be considered.

The models were validated against an experimental dataset provided by the National Nuclear Laboratory, and results were shown to be in good agreement. Through parametric studies it was determined that the characteristic shape of the formation was heavily determined by the initial solution concentration, flow velocity, temperature and the rate of evaporation.

A method for the non-invasive monitoring of the deposits was also investigated through the solution of a geometric inverse problem governed by the transient two-dimensional heat equation. A meshless numerical method, namely the method of fundamental solutions was used as a direct solver in a complicated highly non-linear constrained minimisation. The model was shown to perform well when reconstructing simple shapes with highly contaminated input data. Additionally, complex shapes were also captured with a reasonable degree of accuracy and stability.

Contents

List of Figures

List of Tables

Nomenclature

A_f	Interfacial area (m^2)
A_l	Surface area of liquid inlet (m^2)
A_a	Surface area of gaseous inlet (m^2)
B	Width of film (m)
$B(0,1)$	Ball centered at the origin of radius 1
$\mathbf{B}$	Vector of body forces
c	Concentration ($mol\,m^{-3}$)
c^*	Saturation concentration ($mol\,m^{-3}$)
$\mathbf{c}$	MFS constants
c_p	Specific heat capacity ($J\ Kg^{-1}\ K^{-1}$)
D	Diffusivity ($m^2\,s^{-1}$)
D_ϕ	Helmholtz diffusivity ($m^2\,s^{-1}$)
E	Evaporative flux ($kg\,m^{-2}\,s^{-1}$)
$\tilde{E}$	Energy (J)
F	Rate of precipitation ($mol\,m^{-2}\,s^{-1}$)
$\tilde{F}$	Fundamental solution
$\mathbf{F_{damped}}$	Dampening force through mesh
$\tilde{f}$	Outer fixed boundary temperature
G	Growth rate ($m\,s^{-1}$)
$\mathbf{g}$	Acceleration due to gravity ($m\,s^{-2}$)
$\tilde{g}$	Outer fixed heat flux
$\tilde{g}^\eta$	Noisy heat flux
H	Heaviside function
h	Film height (m)
h_E	Enthalpy ($J\ Kg^{-1}$)
$\tilde{h}$	Defect boundary temperature or heat flux
$\mathbf{I}$	Identity matrix
J	Nucleation rate
K	Overall growth coefficient ($m\,s^{-1}$)
$\tilde{K}$	Initial condition collocation parameter
k_d	Constant of mass transfer ($m\,s^{-1}$)
k_r	Constant of surface integration ($m\,s^{-1}$)
k_{spring}	Spring constant factor
L	Surface length (m)
Δl	Length of linear element (m)
M	Temporal MFS parameter
M_s	Molar mass of substance in solid form ($kg\,mol^{-1}$)
m	Mass (kg)
N	Spatial MFS parameter
N_i^j	Number of nodes
N_ϕ	Helmholtz normalisation factor
$\mathbf{n}$	Unit normal vector
p	Pressure (Pa)
p_{atm}	Atmospheric pressure (Pa)

Q	Mass flow rate of liquid ($\mathrm{kg\,s^{-1}}$)
Q_a	Mass flow rate of air ($\mathrm{kg\,s^{-1}}$)
Q_v	Volumetric flow rate ($\mathrm{m^3\ s^{-1}}$)
Re	Reynolds number
$\mathbf{r}$	Defect boundary radial parameterisation
S	Objective function
ΔS	Nodal displacement vector
S_λ	Regularised objective function
T	Temperature (°C)
$\mathbb{T}$	Deviatoric stress tensor
T_{in}	Solution temperature prior to entry into domain (°C)
$\tilde{T}$	Full time of interest
t	Time (s)
Δt	Pseudo time-step (s)
U	Approximate MFS temperature
$\tilde{u}$	Temperature
$\mathbf{u}$	Fluid velocity ($\mathrm{m\,s^{-1}}$)
$\tilde{u_0}$	Initial temperature
V	Cell volume ($\mathrm{m^3}$)
$V_{molecule}$	Molecular volume ($\mathrm{m^3\ mol^{-1}}$)
$\mathbf{x_{dis}}$	Displacement (m)
α_q	Volume fraction with respect to phase 'q'
$\delta_{Nusselt}$	Nusselt solution (m)
ϵ	Overall order of the crystal growth system
$\epsilon_{i,j}$	Random noise variable
η	Order of the reaction
$\Gamma(t)$	Time dependent internal defect
$\partial\Gamma(t)$	Internal defect boundary
λ	Regularisation parameter
μ	Dynamic viscosity ($\mathrm{Pa\,s^{-1}}$)
ν	Kinematic viscosity ($\mathrm{m^{-2}\,s^{-1}}$)
Ω	Domain
ϕ	Modified evaporation rate ($\mathrm{kg\ s^{-1}}$)
ϕ_0	Evaporation rate ($\mathrm{kg\ s^{-1}}$)
ρ	Density of solution ($\mathrm{kg\,m^{-3}}$)
ρ_s	Solid density ($\mathrm{kg\,m^{-3}}$)
σ	Surface tension
τ	MFS solution time
θ	Angle of inclination from the horizontal
$\theta_{contact}$	Contact angle

Superscript

tr	Transpose of vector/matrix

Subscript

aq	Substance is in aqueous form
f	Cell face index
l	Substance is in liquid form
q	Phase q
s	Substance is in solid form

Chapter 1

Introduction and Background

The research presented in this thesis focuses on developing computational models which simulate the growth of crystalline deposits for the case of leakages of industrial process liquors. The work has direct applicability to the nuclear industry, where leakages of highly active liquors can precipitate out to form crystalline deposits of solid fissile material. These formations can potentially have harmful effects or pose a possible criticality risk. The severity of the effects are dependent on the size and shape of the formation and therefore these parameters are of key interest when modelling. Models developed in this research will allow the prediction of crystalline formations through time for varying process, environmental and material properties.

Whilst the aforementioned models will provide insight into potential formations for a range of given plant conditions, which may allow the development of efficient safety protocols and possible future plant design, the radiation output from crystalline formations prevents any standard monitoring equipment being placed in the plant. Due to this there are difficulties detecting leakages, and once detected it is not always possible to assess the severity of the incident. Therefore the second part of the research within this thesis will also attempt to assess and develop numerical models which may aid in the monitoring and assessment of formations from detected leakages, using non invasive measurable data.

The remainder of this chapter gives an overview of the current problems associated with crystal growth and deposition in industry. Additionally, problems specific to the nuclear industry are discussed in further detail, as they are to be the focus of the research here.

Finally, the key research questions that this thesis aims to address are stated along with a proposed methodology, which is summarised through several concise research objectives.

1.1 Overview

Development of models regarding crystal growth has received much focus from researchers in chemical process related industries over the past few centuries, as crystal growth is the primary mechanism in the manufacture of a wide range of industrial products. J. W. Mullin, a pioneer of crystallisation research through recent decades stated,

> "Today there are few sections of the chemical industry that do not, at some stage, utilize crystallization as a method of production, purification or recovery of solid material. Apart from being one of the best and cheapest methods available for the production of pure solids from impure solutions, crystallization has the additional advantage of giving an end product that has many desirable properties." *J.W. Mullin, Crystallization, 1961* [134].

As stated, crystal growth technology is present in a diverse range of industries, some of which include manufacture of food, electronic components, silicon production for semiconductors, and pharmaceutical products to name a few. In 1979 it was estimated that 5,000 tonnes of bulk crystal were produced worldwide [34]. As of 1999 this had increased to 20,000 tonnes, with silicon production accounting for 60% of the bulk crystals produced [165]. Due to emerging technology such as the ever increasing popularity of hand-held devices and smart phones, it is no surprise that the demand for silicon is constantly on the rise, and as of 2005 the worldwide production of silicon alone was 48,000 tonnes [19]. The annual turnover in 2005 for bulk crystal production in western Europe alone was nearly $1 Bn [19]. It is therefore no surprise that a large quantity of crystal growth research focuses on the the optimisation of the chemical processes and design of equipment such that the highest yield and finest quality of product is achieved.

Whilst much of the understanding behind the fundamental chemistry of crystallisation and its behaviour under varying conditions is derived from this research, not all crystallisation problems are related to the optimisation of crystal growth. Crystallisation often occurs as an undesirable by-product of a chemical process or unexpected event, such as

pipe or vessel leakage. Fouling in heat exchangers and heat transfer surfaces is a prime example of this, and whilst fiscal motivation to carry out research may not be as immediately obvious as research aimed at production and manufacture, the costs due to fouling are still substantial. Due to this, research focused on crystallisation fouling has received interest over the past 50 years. Whilst research has made some progress in the mitigation of the fouling process, the prevention of fouling of heat exchanger and heat transfer surfaces still remains a major unresolved problem in industry.

The research within this thesis focuses on the modelling of crystallisation of impinging droplets of process liquor from pipe or vessel leakages. Whilst not strictly identical to fouling on heat exchanger surfaces, there are significant similarities. Aqueous solution is subject to a change in thermal or atmospheric conditions and a crystallisation reaction occurs, leaving unwanted deposits. Unlike the majority of crystallisation fouling in industry, the problem here is unique as we consider leakages occurring within a nuclear process environment. Whilst fouling in heat exchangers can lead to loss of capital through process downtime or maintenance costs, deposition of heavy metal solids can hold safety implications, as materials are often toxic and can have radiological properties. Thus, additional considerations have to be made. The size, shape and location of the formations need to be known such that leakages can be safely intervened, minimising risk to the operator.

Despite the aforementioned importance of understanding crystallisation of heavy metal process liquors in events such as leakages, it currently poses a large gap in knowledge for nuclear engineers. Furthermore, research relating to the general case of crystal deposition or fouling from impinging droplets is scarce. Whilst the chemistry and criticality-shape relationship of fissile materials is generally well understood, their crystallisation behaviour and spatial deposition configuration when coupled to complex fluid flows is less understood. Therefore work here will develop several multi-physics approaches which will allow the coupling of both the fluid flow and the crystallisation kinetics.

In nuclear reprocessing environments when handling materials with hazardous, radioactive properties it is not always straight forward to monitor process infrastructure in its entirety using standard monitoring equipment. Whilst it is imperative that engineers have a strong understanding of the behaviour of crystalline growth for various process conditions, it is

also it is also vital that sufficient techniques are available in order to detect the leakage and subsequently remotely assess its severity. Most nuclear facilities are designed such that any potential leakage would be contained in large concrete cladded chambers. The ability to remotely inspect these chambers would therefore impact on clean up procedure, minimising risk to the operator. Therefore work here will attempt to develop models which hold potential for future use in the non-invasive monitoring and detection of crystalline formations.

1.2 Mass Deposition and Fouling in Industry

Fouling or 'undesired deposition of material on a surface' is currently a major problem across chemical related industries. It is anticipated that whilst this thesis pays particular attention to fouling in the nuclear industry, the techniques developed here will hold relevance to fouling and mass deposit problems throughout the chemical process industry.

1.2.1 Underlying Mechanisms for Fouling

Whilst fouling is still a major unresolved problem in heat transfer, past research has allowed an understanding behind the underlying mechanisms. Epstein [65] summarised this such that the possible mechanisms of fouling and it's physical processes could be depicted in a $5x5$ matrix. This work stated that the 5 possible underlying mechanisms for fouling were as follows:

- *Crystallisation Fouling* usually occurs on heat transfer surfaces. When aqueous process solutions are subject to a change in thermal conditions, and hence a change in solubility, crystallisation occurs in order to bring the solution back to equilibrium. Fouling of inverse soluble salts such as calcium carbonate, silica and calcium sulphate is common in the process industry, as these deposits generally form on heated surfaces. Conversely, normal soluble salts, such as sodium nitrate, will crystallise when a drop in temperature is experienced, e.g. on a cooled surface.

- *Particulate Fouling* occurs due to aggregation and flocculation of particles within the flow. Particles suspended in the flow then deposit on a surface. Suspended particles

can often be a by-product of an upstream crystallisation, chemical or corrosive reaction.

- *Biological Fouling* generally occurs in water streams, where micro-organisms such as algae, yeast or bacteria attach themselves to heat transfer surfaces. These micro oganisms usually form films, or 'biofilms'.

- *Corrosion Fouling* occurs when a chemical reaction takes place between the fluid and the heat transfer surface. Corrosion products can form layers on the heat transfer surface which resist heat transfer. Additionally, corrosion products can detach, forming particles which deposit downstream.

- *Chemical Reaction Fouling* is where various reactants within the solute undergo a chemical reaction in which a solid product is formed. These can then deposit on the heat transfer surface. Whilst the heat transfer surface is not a reactant in this type of fouling, it can often act as a catalyst in the reaction. These reactions are common in milk processing and industries containing hydrocarbons such as the petroleum industry.

As fouling can be caused by many potential mechanisms, and often a fouling problem will be due to a combination of several of these, it is often unknown how much of the total fouling can be attributed to each physical process. However, the work in this thesis mainly restricts the problem to that of crystallisation fouling.

1.2.2 Impact of Fouling in Industry

As previously mentioned, as there are many underlying mechanisms which cause fouling it is no surprise that problems are experienced throughout a diverse range of industries. Examples of which include the food engineering industry [52, 98], the oil processing industry [103, 21], biological fouling in the marine environment [108, 77] and a wide range of other process related industries which use heat transfer surfaces or heat exchangers [11, 197, 133]. Whilst the specific mechanism or cause of fouling is often different, the implications of problems due to fouling are often shared throughout industry. These implications are now categorised and discussed.

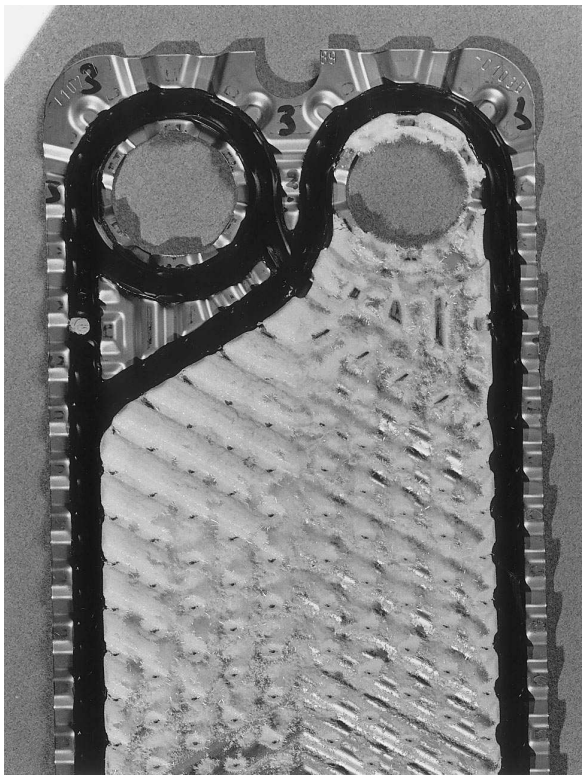

Figure 1.1: Fouling on a heat transfer plate [17].

1.2.2.1 Fouling Impact: Thermal Resistance

Solid deposits on heat transfer surfaces (Figure 1.1) increase the thermal resistance or lower the overall heat transfer coefficient. This means that more energy is required in order to maintain a specific outlet temperature. Due to this, additional fuel or energy costs are incurred such that the reduction in heat transfer is accounted for. This can also be potentially harmful in certain industries, such as the milk process industry, where failure of the fluid to reach a specific temperature allows bacteria to remain in the solution [98].

1.2.2.2 Fouling Impact: Increased Pressure Drop

In addition to the thermal implications of fouling, deposits in pipes or channels can also lead to a decrease in cross-sectional area and increase in surface roughness, hence leading to an increase in pressure drop. An example of this can be seen in Figure 1.2. Due to this, additional energy costs are incurred as a result of pumps requiring more energy. It is stated in [49] that more heat exchangers are taken out of service due to the increased pressure

Figure 1.2: Limescale deposition in a pipe [64].

drop than due to the increase in thermal resistance. These deposits, if not removed can also lead to a full blockage, which can halt the production process completely.

1.2.2.3 Fouling Impact: Increased Equipment Costs

Previous research has allowed manufacturers to quantify the expected level of fouling by the use of a 'fouling factor'. These factors are often predetermined or methods exist in order to obtain them. For shell and tube heat exchangers a popular list of predetermined factors for differing fluids is supplied by the Tubular Exchanger Manufacturers Association (TEMA). Using these factors heat exchangers are designed such that their surface area is enlarged or 'over-sized' relative to the 'fouling factor'. The increased surface area of the heat exchanger allows additional heat to pass into the fluid, therefore counteracting the thermal resistance due to fouling. It is estimated that heat exchangers and heat transfer surfaces are over-sized on average by 15-50% [11]. This incurs additional manufacture costs due to increased amount of materials required. Furthermore, process plants require more space due to the enlarged equipment. Whilst this method can be reasonably effective, there has been reports that an overestimate in fouling factor leads to decreased fluid velocities, which can actually increase the rate of fouling.

1.2.2.4 Fouling Impact: Maintenance and Cleaning

Finally, removal of the exchanger for cleaning purposes often requires plant to shut down. Therefore losses will be experienced in production incurred during these periods. Whilst most plants will factor in for this and have scheduled cleaning, such that the cleaning process can be optimised, unscheduled or emergency shut-downs do occur. The losses due to these unscheduled shut downs can be significant. Moreover, the cleaning chemicals can be costly and they can also have negative environmental impact if not disposed of correctly.

Clearly, fouling can negatively impact industry in a variety of ways. Despite this, it is understandable that research in this area may not immediately appear as important or as fiscally attractive as that relating to the research concerned with optimising the process for growth of manufactured crystals, however, studies have estimated the loss of capital due to fouling is approximately 0.25% of the national GDP (gross domestic product) [150], in 1999 this was estimated to be $2.5 billion in the UK alone. Clearly, the economic impact due to fouling across process industries is severe and it is therefore important that attention is given to these problems such that models are developed, allowing the mitigation or cessation of fouling.

1.3 Mass Deposition Problems Specific to the Nuclear Industry

The nuclear industry is no exception when considering fouling problems. Due to having several complex chemical processes, heat exchangers are generally used extensively in both the power generation and reprocessing industry. These are therefore susceptible to the same problems of heat exchanger and heat transfer fouling as experienced throughout all process industries.

Whilst the same economic impact applies to the nuclear industry, additional considerations also have to be made. Particular care has to be taken with mitigation of fouling, and cleaning processes have to be optimised, as any manual intervention required by a plant worker leads to a possible radiation dose, therefore reducing human intervention is critical.

The systems in place are designed with precision such that scheduled clean up protocols are implemented in order to minimise worker contact. However nuclear engineers, particularly within the reprocessing sector at Sellafield (Figure 1.3), are interested in the fouling behaviour of process liquors which are removed out of the standard process cycle. Whilst heat exchangers and heat transfer surfaces are designed with mitigation of fouling effects in mind, such that safety and clean up protocols can be designed with the informed knowledge of the surfaces expected behaviour, it is more difficult to predict and make informed assessments regarding the behaviour of process liquors if removed from the standard process equipment, such as fouling on the surrounding infrastructure due to leakages of process liquors.

In order to fully understand the problem, knowledge of the reprocessing industry is needed. The following sections will give an overview of the nuclear reprocessing industry, along with details of previously experienced problems, such that key areas for research can be targeted.

1.3.1 Nuclear Reprocessing and THORP

Nuclear reprocessing is the chemical extraction of reusable nuclear materials from spent nuclear fuel. Reprocessing was originally developed in order to extract nuclear material for weapons purposes, however later it was used for commercial power generation [7]. Fuels are generally dissolved in aqueous solution and various chemical processes are undertaken to remove and purify the uranium and plutonium from the solution.

One site in the UK which carries out nuclear reprocessing on spent fuels is the Thermal Oxide Reprocessing Plant (THORP) at Sellafield, UK (Figure 1.4). Nuclear engineers at THORP have particular interest in models regarding the crystallisation of solid fissile material from aqueous solutions. In order to understand the justification and need for such models the remainder of this section will give background information into the THORP facility and previous problems experienced.

The THORP facility at Sellafield is a $4 Billion plant owned by the Nuclear Decommissioning Authority (NDA) and operated by Sellafield Ltd, first operational in 1994 [38].

Figure 1.3: Sellafield Nuclear Power Plant, UK, [166].

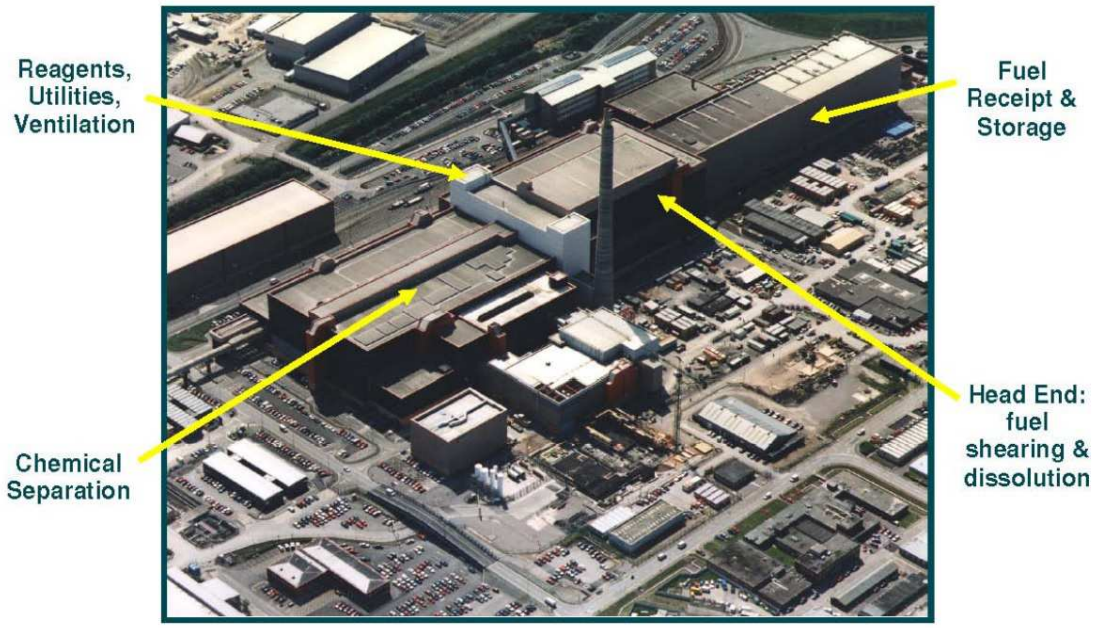

Figure 1.4: Thermal Oxide Reprocessing Plant, Sellafield. [38].

THORP takes spent nuclear fuel and extracts reusable fissile products using the PUREX chemical cycle. Initially spent fuel is delivered from both domestic and international sources via a rail network connected to Sellafield. The spent rods are then stored in large ponds (Figure 1.5) until ready for reprocessing. At the start of the cycle, the fuel is removed from the pond and is sheared into 5cm lengths [38], the fissile materials are then dissolved in nitric acid to form highly active (HA) liquor. At this stage the liquor is transferred to a series of large suspended vessels (accountancy tanks), such that the quantity of liquor can be remotely observed and recorded.

This nitric acid solution is then treated with various organic solutions in order to separate the plutonium and uranium, the remaining highly active waste is then transported away to be vitrified and stored. Once separated the plutonium and uranium are reintroduced into a nitric acid solution. Through various precipitation and calcination processes, solid plutonium and uranium materials are then extracted from the nitric acid solutions. Approximately 97% of the spent fuel is recycled to produce reusable uranium (96%) and plutonium (1%) solids, and 3% of the fuel is high level nuclear waste. An overview of the PUREX cycle from [38] can be seen in Figure 1.6.

Figure 1.5: Nuclear fuel storage tanks prior to the reprocessing process, courtesy of Sellafield Ltd.

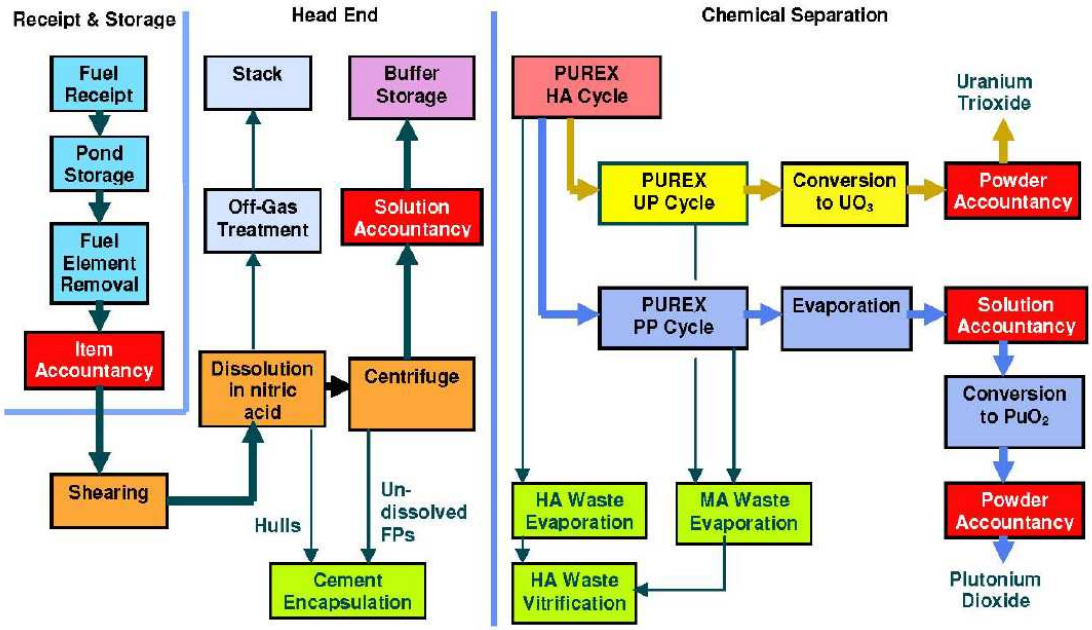

Figure 1.6: Flow map of THORP PUREX process, [38].

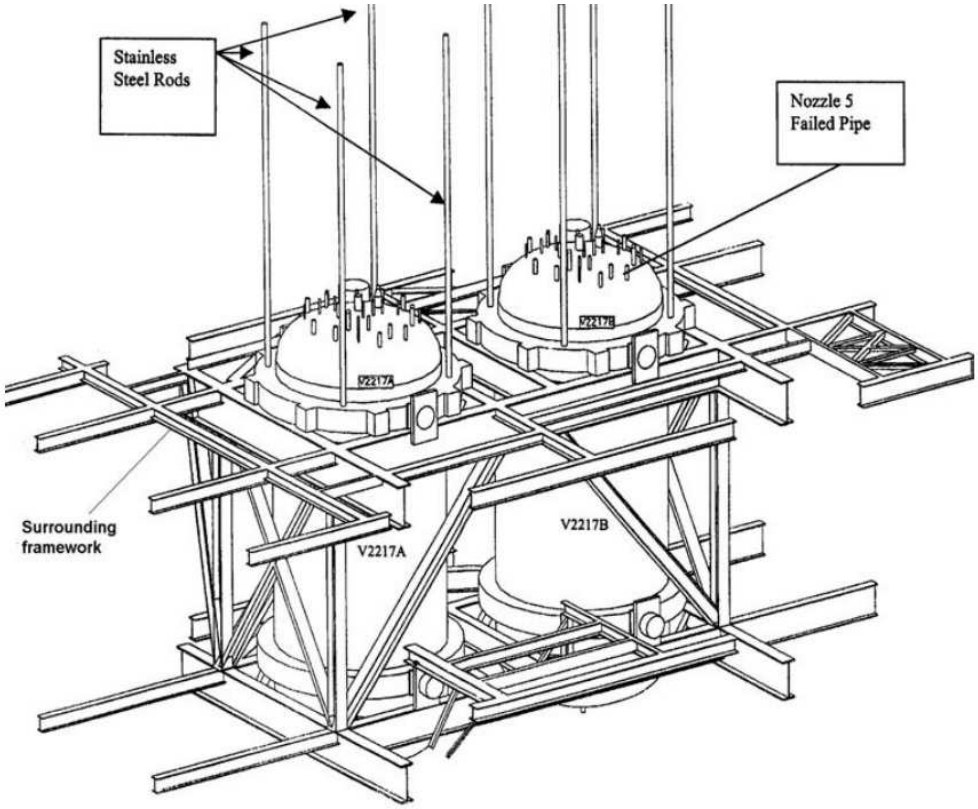

Figure 1.7: Accountancy tank from THORP leakage 2005, [85].

The need for models which describe the growth of solid deposits from leakages of these solutions was brought about by a problem in 2005 which caused the temporary shut down of the THORP plant.

1.3.2 Process Liquor Leakage Incident at THORP, 2005

In 2005 it was discovered that 83,000 litres of HA solution had leaked undetected over a period of approximately 7 months [85]. It was found that the leakage of liquor had occurred due to breakage of one of the pipes connecting to the accountancy tanks at the final stage of the head end process in Figure 1.6. A diagrammatical representation of the tank can be seen in Figure 1.7. It is thought that the breakage was due to pipe fatigue brought about due to the oscillatory motion of the suspended tanks.

The tanks in question were contained within a concrete cladded cell, which was designed

such that there would be no need for routine entry during the lifetime of the process plant. Safety measures which allowed the non-invasive monitoring of the cell were put in place. The floors of the cell were inclined such that any leakage within the cell would flow down to a sump. Sumps were partially filled with nitric acid and equipment was in place to monitor the fluid level. In addition to this, hatches were built into the cell such that cameras or remote maintenance equipment could be placed inside the cell if needed. Due to the high levels of radiation no cameras could be permanently placed within the cell.

It was later discovered that the leak went undetected due a failure in the fluid level equipment in the sump. Under normal conditions the monitoring equipment could display 5 different levels, low-low, low, normal, high, high-high. These levels would relate to the current height of fluid in the sump. Plant operators should be alerted if levels reach 'high' or a rapid change in readings occur. The 'high' level alarm should have triggered at a solution volume of 15 litres however, the equipment was faulty and continued to display 'low' even though 83,000 litres had leaked from the tank. Plant operators were eventually alerted to the problem when it was noted that the accountancy tank measurements for the quantity of liquor was not agreeing with records for the delivered quantities [85].

It was later established that the cell was successful in containing all the process liquor. Following this, the cell was cleaned and investigations were carried out regarding the cause of the incident and it's potential threat. Results from this investigation would impact on the feasibility of THORP resuming processing. Whilst containment was proven successful the nuclear criticality implications of the incident had to be assessed.

1.3.3 Nuclear Criticality Safety

> "A criticality accident occurs when a nuclear chain reaction unintentionally occurs in fissile material, such as enriched uranium or plutonium. This releases neutron radiation, which poses a great hazard to personnel and equipment. The purpose of nuclear criticality safety is to prevent a nuclear chain reaction in operations with fissile material outside a nuclear reactor." *Health and Safety Executive* [85].

There have been 22 reported occurrences of criticality incidents outside of the reactor

since the beginning of nuclear power generation. Of these incidents, 21 occurred with fissile materials dissolved in a solution or slurry and 1 of the incidents involved solid material. Out of these 22 incidents there has been reported 9 fatalities due to radiation poisoning. There has been no record of any explosions or damage to equipment, however this does not imply that it is not possible. It is therefore clear that every measure should be taken such that criticality incidents do not occur.

The risk of criticality is measured by a 'effective neutron multiplication factor', k_{eff}. When $k_{eff} = 1$ criticality is reached and a chain reaction is sustained such that each fission reaction causes a following fission reaction. Supercriticality is defined as $k_{eff} > 1$, such that the number of fission reactions increases exponentially. For $k_{eff} < 1$, or a subcritical reaction, a chain reaction cannot be sustained.

The 'critical mass' of an object is the minimum mass for which $k_{eff} = 1$. It is known that the critical mass of a fissile material is dependent on several key factors [121], which are now discussed.

1.3.3.1 Criticality Factor: Geometry

A perfectly spherical shape will give the smallest critical mass for a material. Departure from this shape allows a greater surface area through which the neutrons can escape, which implies that a larger mass is needed for the material to become critical. Generally speaking, criticality is an undesirable trait outside of the reactor, therefore fissile materials are generally stored in shapes that decrease the chance of criticality. These tend to be either slabs (cuboid of narrow thickness) or a cylinder with small radius. Critical masses have long been established for these shapes [53, 141]. For more complex shapes, modern numerical Monte Carlo codes, such as MONK [131], MCNP and KENO [35] can calculate the value of k_{eff}.

1.3.3.2 Criticality Factor: Temperature

The higher the temperature, the faster the velocity of the neutrons. As the neutron's velocity increases, the chance of a successful fission reaction decreases. Therefore for a critical material where $k_{eff} = 1$ at room temperature, when exposed to a increase

in temperature the material would become subcritical, $k_{eff} < 1$. Also, an increase in temperature decreases the density of the shape due to thermal expansion.

1.3.3.3 Criticality Factor: Density

The higher the density of material, the lower the critical mass. Therefore, a given mass in a subcritical state could become critical if the density is increased through either a change in pressure or temperature.

1.3.3.4 Criticality Factor: Reflectors and absorbers

The critical mass of fissile material can be altered by surrounding or submerging it in another substance. Certain substances reflect the escaped neutrons back into the fissile material, such as water and steel. This is an important consideration in the storage and transport of nuclear materials. For example, the critical mass of a spherical, solid metal piece of Pu_{209} (plutonium) is 10kg. When surrounded by water the critical mass is reduced to 5.45kg and when encased in steel it is 4.49kg [113]. Therefore close attention to the surroundings have to be paid when carrying out a criticality assessment. Moreover, certain materials such as cadmium, boron, or gadolinium can absorb neutrons, hence increasing the critical mass.

1.3.3.5 Criticality Factor: Interaction

Care has to be taken when considering multiple fissile materials in close proximity. Two subcritical masses could become critical due to neutron interaction between them.

1.4 Experiments Regarding Impinging Droplets of a Surrogate Liquor

Whilst no criticality incidents occurred during the THORP leakage of 2005, in order for THORP to resume operation a valid safety case had to be made such that under varying conditions, critical masses would not be reached. The National Nuclear Laboratory (NNL, previously Nexia Solutions) hypothesised that:

> "Liquor from a sufficiently slow leak might experience evaporation of much of its solvent thereby delaying or preventing it reaching the leak detection

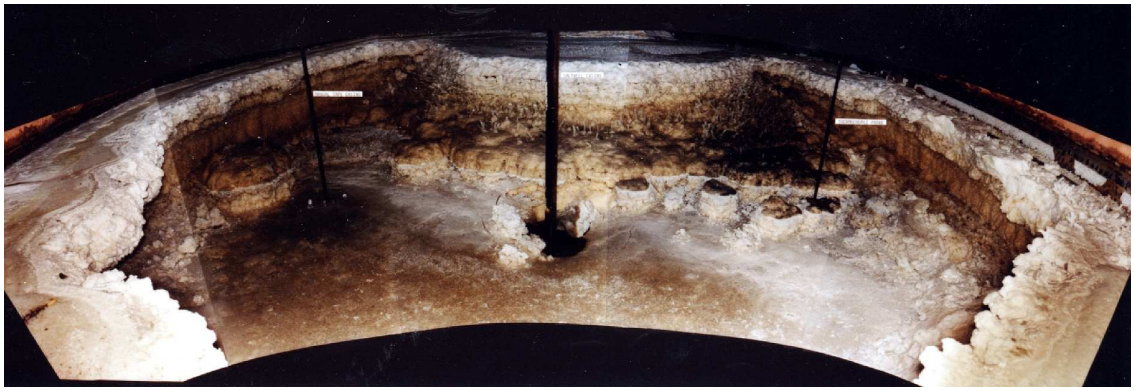

Figure 1.8: Precipitate formations fouling the cell surfaces, found in drained storage tanks in Hanford, USA. Copyright of Washington State Department of Ecology.

> system. In such a case liquor solutes would be expected to crystallise as solid deposits, mostly on the cell floor. Accumulation of some types of material could in time, possibly achieve a critical mass." *THORP Simulated Crystal Accumulation Trials, Nexia Solutions, 2007* [175].

Similar occurrences have been observed where heavy metal solutions have precipitated out. An example of this is at the nuclear waste storage facilities in Hanford, USA [59]. The majority of stored waste was previously removed from these tanks due to detected leakages. Upon inspection it was found that the residual solutions had precipitated out leaving white crystalline deposits on the surfaces of the cell, these can be observed in Figure 1.8. These deposits proved difficult to remove, with many resources being allocated to assess safe methodologies in order to remove and dispose of the deposits [170, 154]. In addition to this, research has been carried out into the criticality and contamination risk that these formations pose [61, 184]. Clearly an understanding of the deposition behaviour of solutions could have aided in the prevented or clean up of this occurence. As part of the safety investigation, regarding the THORP leakage, an experimental trial was carried out by the NNL, such that surrogate salt solutions were dripped onto inclined plates for varying parameters, in order to test the aforementioned hypothesis.

1.4.1 Experimental Setup

Plates of $1m^2$ were used such that they replicated those found in the THORP containment cells. These were gradiented with a 1:125 incline towards a low corner, beneath which a

sump was placed to collect the fluid. Plates were constructed out of polished steel with 1mm rivets places around the edge in order to mimic the weld joint in the THORP cells. These surfaces were then placed in a temperature controlled chamber and surrounded with a plastic sheet curtain, in order to minimise air flow and contain any solution splash (Figure 1.9). A surrogate solution of sodium nitrate was used as it was thought to display similar chemical and physical properties to that of the heavy metal solutions found in the THORP plant. Solutions were dripped onto the centre of the plate through the use of a suspended dripper unit, which had a temperature controlled thermostat such that the solution could be kept to a constant 30°C. This system allowed the easy modification of both the drip height and flow rate. The growth of deposits was monitored qualitatively through the use of regular photography, and quantitatively through measurements of key features, such as the width and height, for periods of up to 70 days. The suspended dripper and a typical deposition build up can be observed in Figure 1.10. Additional information such as air velocity, temperature and humidity was also monitored. Dynamic evaporation rates were obtained in a separate experiment where the net loss of pure water was calculated when dripped onto the plate over a continual period.

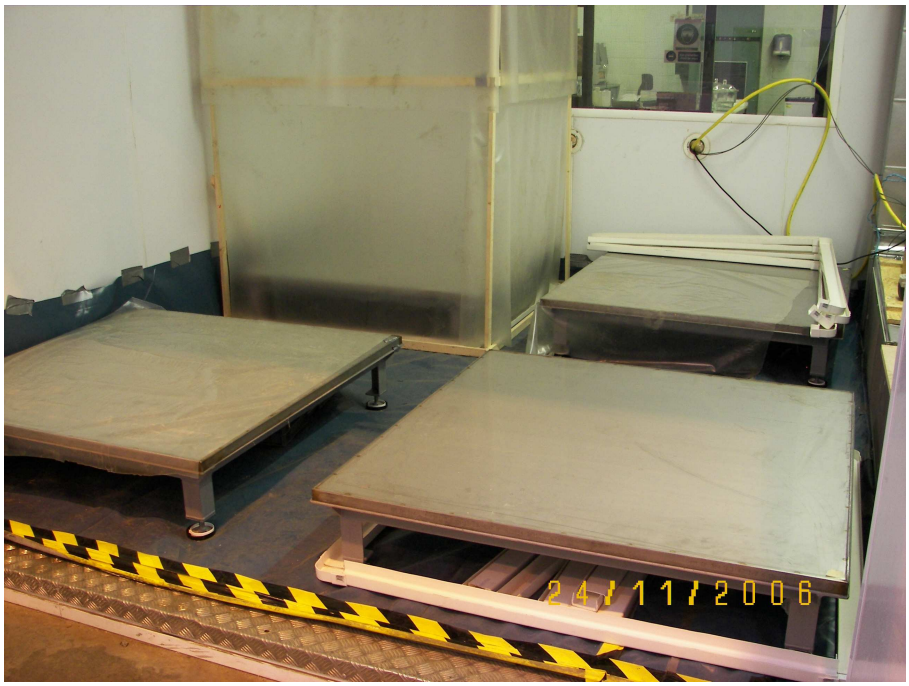

Figure 1.9: Steel plates used in dripper experiments.

Figure 1.10: Suspended dripper with crystalline deposition across an inclined plate.

1.4.2 Results

The following section discusses the key observations for the drip trial experiments. Results in this section will focus on the qualitative behaviour of the crystallising solutions for varying conditions.

1.4.2.1 Initial Concentration: 1 Molar solution

Trials with 1 Molar sodium nitrate solution were dripped from a height of 2m at a rate of 5 litre/day. After 1 day the solution precipitated to form the deposit observed in Figure 1.11. Deposition was sparse, with a large clear region. The clear region was roughly elliptic with radii of approximately 1m, centred on the point of solution impact. The radius parallel to the path to the sump was slightly elongated.

The deposits were observed to decrease in depth close to the clear region, quickly build to a maximum height and then slowly decrease as distance from the point of impact increased.

From analysing concentrations of the solution at the run off, it was clear to see that significant evaporation had taken place, with a 2% increase in concentration (mass of salt

Figure 1.11: 1 Molar sodium nitrate precipitation after 1 day.

/ mass of water) occurring. It was noted that some solution was found to precipitate on the curtains surrounding the plate due to the initial droplet splash, this was in the region of 3.2-4.5% of the total crystalline solids recovered.

1.4.2.2 Initial Concentration: 5 Molar solution

The 5 Molar solution was thought to be of a concentration typical to the majority of liquors found in the THORP plant. In this trial, the drip rate was decreased to 2.5 litre/day such that run off to the sump was reduced. An initial drip height of 2m was used.

It was found that the 5 Molar case formed annular deposits similar to the previous 1 Molar case. However, the clear area below the dripper was now much smaller, as observed in Figure 1.12 (approximately 0.3m) and the annular deposition was much more pronounced. Initially a clear region ran directly down the plate, allowing the solution to reach the sump. However, as the formations grew through time, the solids blocked the path to the sump, restricting solution exit and eventually completely preventing solution run-off, as observed in Figure 1.13. Red dyes were introduced to the solutions in order

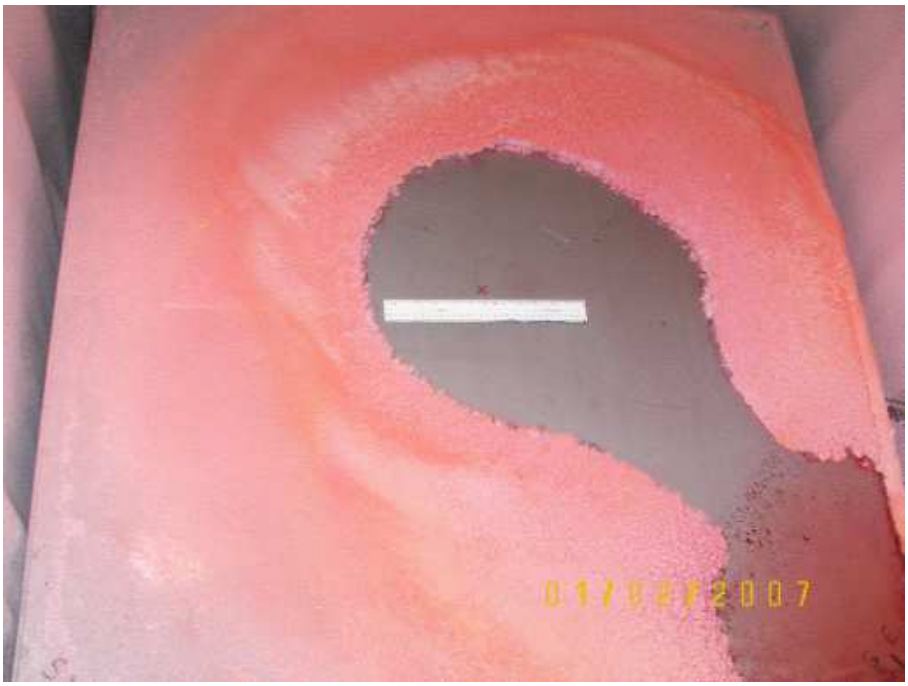

Figure 1.12: 5 Molar sodium nitrate precipitation after 14 day.

to observe the flow's interaction with previous crystalline formations. It was observed that the solutions continued traversing across the plates through the porous crystalline material. It was also noted that in addition to travelling across the plate, solution was also wicked vertically through the structures, causing localised increases in deposition height across the plate.

After extensive growth it was found that the solution was blocked, or partially blocked, from the sump, reducing run off. When this occured, the solution began to pool extensively under the drip site. In this region it was found that continuous crystal growth and dissolution was occurring, such that the clear central region was constantly contracting and dilating.

In addition to this initial trial, experiments were undertaken to assess the effects of varying the drip height. Firstly, the drip was lowered to a height of 1m. From these trials it was observed that the clear area below the drip was roughly the same size, but the overall size of the crystalline annulus was now smaller. The outer edge of the bed was also observed to be more sharply defined. Splatter effects on the outside curtain were

Figure 1.13: 5 Molar sodium nitrate precipitation after 36 day.

now seen to be less. It was noted that the continual growth and dissolution behaviour was now less well defined.

Next, the experiment was trialled at a lower height of 0.5m. At this height there was virtually no splashing, and the central clear region was now even smaller. Lateral development of the surrounding crystal beds was much slower. Again, the oscillatory crystallisation and dissolution behaviours in the clear region were less apparent.

1.4.2.3 Initial Concentration: 8 Molar solution

The 8 Molar trials were undertaken in order to represent the upper level of concentrations of process liquor and in order to gauge the effects of the 'worse case scenario'. In these trials it was hypothesised that under high concentrations, formations may begin to form under the drip. In order to reduce the structural disurbance from the trial, only low drip heights of 0.5m and 1m were tested. It was found that droplets began to quickly crystallise around the impact point, forming a widening crystalline bed. Solution continued to run off at the sump, however unlike the previous trials, no clear path was observed. For this case, the kinetic energy of the drip kept a small pit at the point of impact, how-

ever this was subsequently filled by crystalline deposits. Over time a small conic pillar of crystalline solid began to form directly under the drip point, as observed in Figure 1.14. It was observed that this central formation reduced splashing of the solution. The remainder of the crystalline bed was relatively flat, however continued to grow in height. It was noted that the outer edge of the formation was clearly defined, much like the 1 m, 5 Molar case. Crystallisation favoured the downhill direction, and after 14 days there was cessation of the solution flow to the sump. It was found that the central tower formation continued to grow in height for approximately 37 days. The growth after 32 days can be observed in Figure 1.15. At this point the tower collapsed under its own weight, after which a new tower began to grow in place of the old one, as observed in Figure 1.16.

The 8 Molar trial was run again with a reduced drip height of 0.5m. Due to the reduced kinetic energy, a pit under the drip point was not observed. With reduced drip height the formation radius appeared to be smaller, however the bed depth grew at an increased rate. Cessation of solution flow to the sump due to blockage occurred at 32 days.

Samples of the crystalline material showed that the crystalline bed varied in porosity, however the centralised tower formation was almost completely solid.

1.4.3 Discussion of Results

The results from the drip trials were not what the engineers at the NNL initially hypothesised. Initial intuitions suggested that all the solids deposited from the solution would be contained in piles of crystals under the drip site. Behaviour similar to this was only experienced in the 8 Molar case, however, crystalline solids were also deposited in a circular pattern around this central pile. This behaviour was generally unreproducible for solutions of lower concentration, where at 1 Molar the solution produced almost no deposition, with the majority of solid material being recovered from the sump. Additionally, the 5 Molar solution produced large annular crystalline formations. During the 5 Molar experiments liquid films were observed to pool under the drip and close to the sump, initially, no solid deposits were seen in these regions, however deposits eventually formed in the film close to the sump, and solution was subsequently prevented from leaving the plate. Despite this, solids never grew directly under the drip site for the 5 Molar case.

Figure 1.14: 8 Molar sodium nitrate precipitation after 3 day.

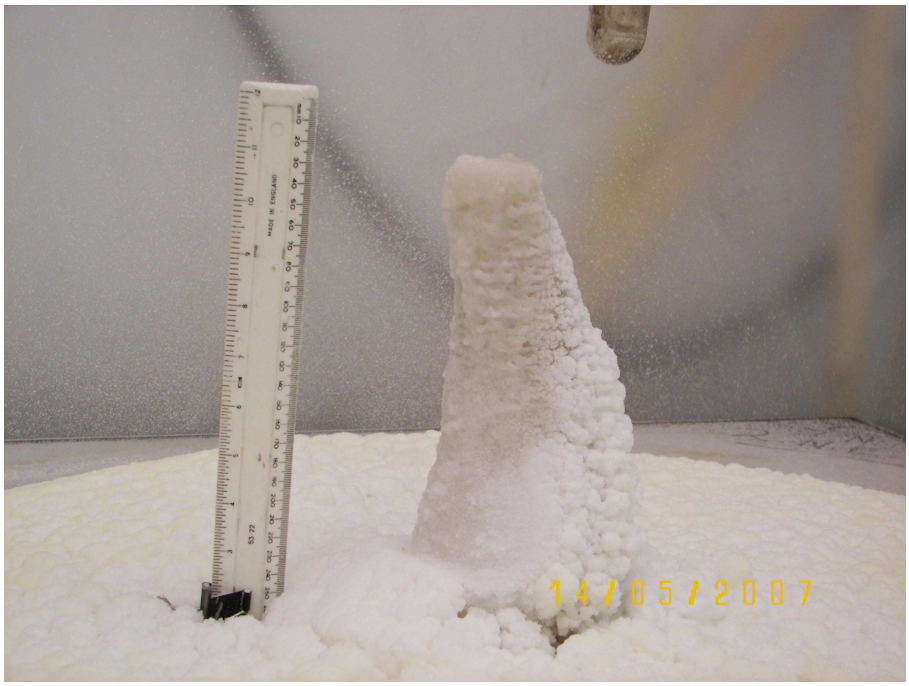

Figure 1.15: 8 Molar sodium nitrate precipitation after 32 day.

Figure 1.16: 8 Molar sodium nitrate precipitation after 70 day. New tower growth is observed next to the previously collapsed formation

Whilst these results were different from the expected behaviour, it was not necessarily a negative point with regards to criticality. The annular formations were most comparable with the standard 'slab' geometry, whilst the towers were most comparable to a cylindrical geometry. As the criticality risk of slab is generally less than that of a cylinder, with a slab usually having a higher critical mass, the annular formations are favourable over towers. However, for the 8 Molar case it was found that the central tower formation was surrounded by a circular crystalline bed, the criticality implications of these composite shapes are unknown and therefore further investigation would be needed. Behaviour of solutions with concentrations less than 8 Molar but greater than 5 Molar also need to be determined, as it is expected there will be a limiting value such that no tower formations are experienced, with concentrations higher than this value producing growth under the drip. Moreover, the impact of these parameters on the size and shape of the formations could hold important implications, for example if the characteristic shape of the tower formations changed from roughly cylindrical to a more hemispherical shape.

Whilst the range of possible morphologies and geometries the crystalline material demon-

strated in the experiments was larger than hypothesised, it was also found that the majority of solids produced were of a porous nature, leading to a variety of unexpected behaviour and subsequent implications. An example of this being that the height of the solid material generally decreased away from the drip point, however due to the aforementioned porous solids, wicking or capillary flow in the crystalline bed caused localised increases in material height across the plate, leading to a 'cobbled' field effect. Additionally, oscillatory crystallisation and dissolution occurred at the centre of the annulus for the 5 Molar experiments, which caused the size of the clear region under the drip to vary in size, through time. It was also found that for the case where multiple plates are joined, such as in a cell environment, crystalline material can form a porous bridge over the weld edges therefore allowing the spreading of leakage across multiple plates. In addition to the unexpected behaviour of the crystalline growth due to the porous wicking effects, the variable density and porosity of these materials would need to be considered in criticality calculations, particularly the implications of a porous solid being filled with a heavy metal solution.

It was found that scenarios exist for sufficiently slow leaks, such that an inadequate level of liquid may reach the sump and hence fail to trigger the safety alarms. This was usually due to either; the majority of fluids evaporating across the plate before reaching the sump, the fluids being contained within previous porous solids across the plate, or full blockage of the access to the sump. A fuller understanding of this behaviour would be needed in order to ensure that safety measures within the cells were sufficient.

1.4.3.1 Identification of the Occurring Physics

In order to fully understand the behaviour of impinging droplets of crystallising salt solution, it is important that all the individual physics are well understood. Once this is achieved an understanding into the implications of these behaviours when coupled together can be gained. Summarising, it is important that the following physical process are understood:

- *Droplets, Free Fall, Impact and Splashing.* Solutions initially form into droplets which free fall through the air. Droplets then impact onto the solid surface, or

previously deposited liquid. Following impact droplets either splash across the surface or deposit to form thin liquid films under the drip. An understanding of the velocity of the falling liquid and how long it remains in free fall would be needed. Velocity information is likely to have an effect on the splashing behaviour, allowing the calculation of the quantity and location of splashed liquid. In addition to this the length of free fall is likely to affect mechanisms such as heat transfer and evaporation, these will influence the chemical behaviour post impact.

- *Gravity Driven Film flow.* A proportion of the droplets do not splash, but rather coalesce to form thin liquid films under the drip site. Due to the incline of the surface, gravity drives the film down to the sump. The velocity and thickness of this film is likely to impact on the rate of crystalline deposition. Gravity driven films often become unstable and rivulets are formed, the non-uniform nature of the fluid flow could also lead to irregularities in the mass deposition.

- *Crystallisation.* Any solution has a given solubility limit. This is the saturation point, such that no more solids can be dissolved into the solution. This solubility limit is dependent on the temperature and quantity of liquid such that if a saturated liquid undergoes a temperature change or volumetric change, the solubility limit can drop. If this occurs the solution becomes supersaturated. Crystallisation is the integration of solute molecules into a lattice formations, which occurs in order to bring the solution back to an equilibrium state. Crystallisation is a complex process, where the size, shape and rate at which the crystals are formed are all heavily influenced by varying physical factors. An understanding of how these factors couple together is required.

- *Heat Transfer.* As mentioned, the temperature of the solution directly impacts upon its solubility. Not only this, it impacts on the rate of the crystallisation reaction. In addition to this, the temperature of the fluid impacts on its rheological behaviour, and hence how it acts during the droplet and film phase.

- *Evaporation.* The volume of liquid affects the solubility of solution. Evaporation decreases the volume, therefore increasing the concentration. This can lead to a state of supersaturation, such that crystallisation occurs. Evaporation is dependent on the temperatures of the liquid and gaseous phase, air humidity and the air

velocity field.

- *Dissolution.* Due to the dynamic nature of the temperature conditions, a change in temperature can in fact increase the solubility limits of the solution. When this occurs previously crystallised material can dissolve back into the solution. A strong understanding of the localised temperature and concentration of solution is therefore required.

- *Flow through porous media.* The crystalline material formed is of varying density and porosity. Subsequent liquid interacts with this solid material such that it flows around it, dissolves it or flows through it. Capillary effects due to surface tension can have a strong effect on the solution flow, such as the solution wicking up against gravity, through the crystalline material.

1.5 Research Aims, Objectives and Methodology

The primary aim of this work is to develop numerical models which describe the size and shape of crystalline deposits from salt solutions for varying process, environmental and material properties. These models will allow insight into the criticality and safety implications that a leakage of nuclear process liquor could pose. Furthermore, the work aims to investigate and develop methods for the non-invasive monitoring and detection of formation growth through time. The research attempts to meet these aims through the achievement of several key objectives, each of which is approached through a concise research methodology, as follows;

1. Identify the physics occurring within the NNL's sodium nitrate drip experiments and highlight current numerical approaches for modelling these physics.

    - Analyse reports from NNL experiments.
    - Carry out a literature review on methods for crystallisation.
    - Carry out a literature review on methods for other identified physics.

2. Target and demonstrate appropriate methods for coupling the previously identified physics such that crystalline growth and deposition from solution can be described.

- Carry out a literature review on the methods for coupling the previous models such that a multi-physics model for crystal growth can be developed.
- Adapt previous models for the purpose of modelling the growth of deposits from a typical salt solution.
- Identify the strengths and limitations with the adapted model.
- From this work, propose a new model which captures the most critical physics and addresses the previously targeted limitations.

3. Develop a robust two-dimensional CFD moving boundary framework for generalised mass deposit problems.

   - Develop user defined functions for a moving boundary CFD problem.
   - Advance to multiphase, capturing a liquid film.
   - Optimise user defined functions, solver settings and initial meshing for robustness and accuracy.

4. Develop a multi-physics CFD model using the previous moving boundary framework such that it includes the targeted physics in order to demonstrate the growth of crystalline formations from salt solutions. Validate this model with data from NNL sodium nitrate drip trial experiments.

   - Advance the previous framework to a pseudo three dimensional case.
   - Add additional physics, i.e. evaporation and heat transfer.
   - Collate and assess relevant data from the NNL drip trials.
   - Obtain a set of input parameters for the model which relates to the experimental drip trials.
   - Compare key results and features from the model for different input conditions, through time, against the experimental data.

5. Determine the model's sensitivity to process, material and environmental parameters.

   - Run the previously validated model for varying environmental parameters, such as: ambient air temperature, air humidity, air velocity, wall temperature.

- Run the model for varying material parameters, such as: solution and solid density, viscosity, kinetic crystallisation parameters,
- Run the model for varying process parameters such as: solution flow rate, solution temperature.

6. Investigate and develop methods for the non-invasive monitoring and detection of formation growth through time.
   - Carry out a literature review for current non-invasive models.
   - Develop a model for solving geometric inverse problems, using thermal data.
   - Carry out an optimisation of the model.
   - Test the robustness of the model for a variety of potential formation shapes.
   - Assess the applicability and necessary considerations required when applying the model to an industrial setting.

1.6 Thesis Outline

This section outlines the chapter layout of the thesis.

Chapter 1: Introduction and Background. A background into the problems associated with fouling and mass deposition in industry is given in this chapter. Problems specific to the nuclear industry are also discussed, with particular attention paid to the additional considerations required due to the radioactive nature of materials. The research in this thesis was motivated by a previous incident that occurred in 2005 at the THORP nuclear reprocessing facility. Background information regarding this problem is given along with experimental work carried out by the NNL. The key aims and objectives of the research are given, along with the research methodology.

Chapter 2: Current Numerical Models and Techniques for Application in Crystal Growth and Mass Deposition Problems. This chapter reviews the literature regarding numerical models currently used for capturing crystal growth in a manufacture setting or fouling related problems.

Chapter 3: Adaptation and Implementation of Geological Models for Industrial Crystallisation Problems. This chapter recreates a model previously used for modelling geological stalagmite formations, often found in underground caves. The model is then adapted for the time and length scales of the problems found in this thesis. A short parametric study is completed. Advantages and limitations of the model are discussed.

Chapter 4: Development of a Coupled CFD and Moving Boundary Framework. Here a framework is developed which couples computational fluid dynamics (CFD) with moving boundary techniques, such that the moving boundaries allow the capture of mass deposition. This chapter focuses on the implementation of the framework, such that user defined codes are developed and solvers are optimised. Meshes are optimised for accurate and robust solutions.

Chapter 5: Simulating the Crystalline Formation Growth from a Thin Film of Surrogate Liquor. In this chapter, a moving boundary axisymmetric CFD model is extended from the previous two-dimensional one. Furthermore, additional physics is incorporated. The model is then validated against the NNL drip trials. Once successfully validated parametric studies are carried out to see how the solution changes with varying process, environmental and material parameters.

Chapter 6: A Meshless Moving Boundary Model for the Non-Invasive Capture of Growing Crystalline Structures. In this chapter, a non-invasive numerical method is developed, such that a two-dimensional inverse geometric problem is solved using the method of fundamental solutions for the time-dependent heat equation. The model is then numerically tested for a variety of different geometries and boundary conditions.

Chapter 7: Conclusions, Implications of the Research and Further Work. Here the main findings of the research will be concluded. Additionally, the implications of the research will be highlighted and potential areas for further work will be addressed.

Chapter 2

Current Numerical Models and Techniques for Application in Crystal Growth and Mass Deposition Problems

2.1 Overview

This chapter attempts to address the current theories regarding crystal growth. In addition to this, previous studies are reviewed, in which models are developed and utilised such that crystal growth or mass transfer processes can be described. Fouling on industrial equipment due to crystallisation or other mass transfer process is a major problem in many industries. Moreover, crystal growth occurs in many different natural environments, such as the deposition of calcite in caves which leads to large formations such as stalagmite and stalactites.

This chapter will discuss the various techniques and approaches used throughout crystal growth research and assess their appropriateness for the problem addressed in this thesis.

The problems investigated in this thesis involve several fluid flow phenomena. As the fluid flow acts as a transport mechanism for the dissolved solute, such that this later

crystallises, it is important that the fluid flow is captured accurately. Therefore in addition to research regarding crystal growth, various models for capturing the types of fluid flow will be discussed.

2.2 Crystallisation Theory

Crystallisation from solution consists of two stages; nucleation and growth. The initial nucleation stage consists of the clustering or grouping of atoms or molecules in solution. Once these formations reach a stable size, crystal growth can occur. The rate at which these processes occur is determined by the current environmental conditions, material properties and the mass of solute dissolved within the solvent. In order to model complex crystal growth systems it is vital that these concepts are considered, therefore the remainder of this section will address these concepts in order to have the fundamental understanding of supersaturation, nucleation and crystal growth kinetics required.

2.2.1 The Driving Force for Crystal Growth Mechanisms: Solubility and Supersaturation

For a given volume of solvent, a specific mass of solute can be dissolved, this is know as the solubility of solution and is measured in units of concentration (molarity), or mass. The solubility level of a solution is dependent on the temperature, pressure, mass of solvent, or pH. For the majority of materials the solubility rises with increasing temperature, however there are some exceptions, such as calcium and barium sulphate. These are known as inverse soluble salts. In addition to this, the solubility's dependence on temperature is often complex, non-linear relationships are not uncommon and often the behaviour can differ for varying temperature intervals (such as a change from an inverse to a non-inverse solubility relation).

It is typical that the solubility of a solution is displayed in the form of a solubility curve, such that the solution concentration at the solubility limit is plotted against the temperature. An example of which can be observed in Figure 2.1. From this figure it is clear to see that calcium sulfate behaves as a non-inverse soluble salt for solutions at temperatures $0 - 40°$C. Once the solution exceeds these temperatures it then behaves as an inverse soluble salt, with the solubility decreasing with increasing temperature.

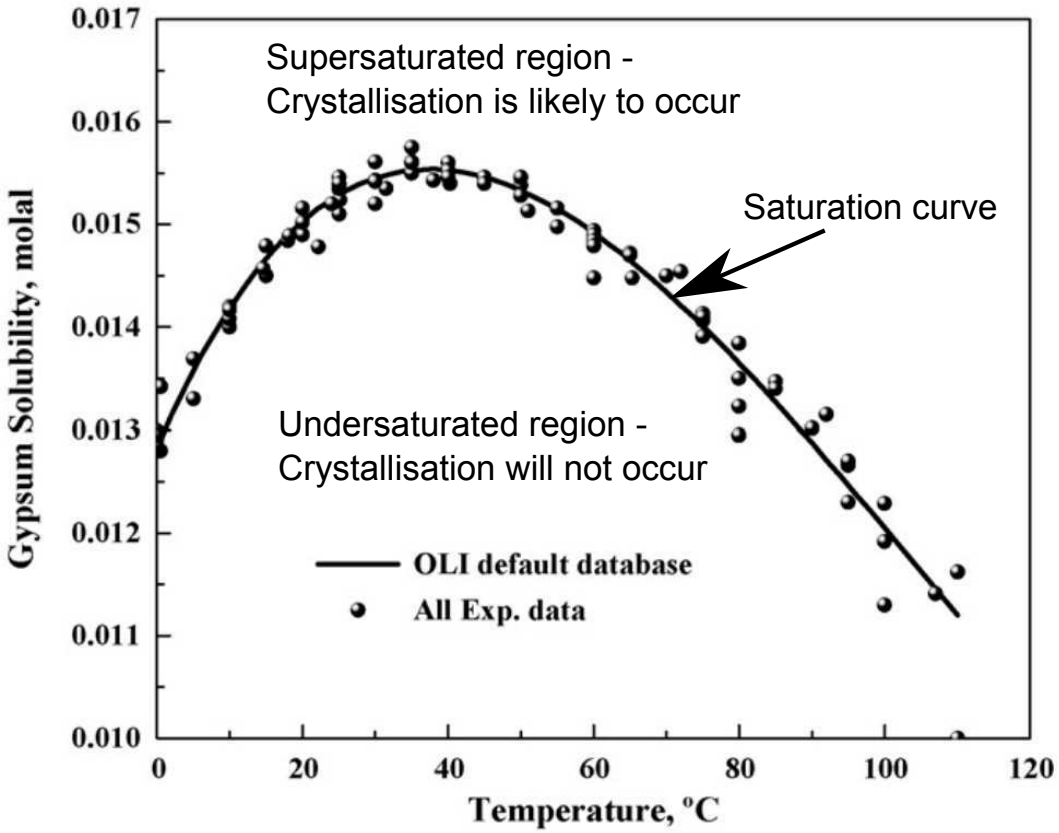

Figure 2.1: The solubility - temperature relationship for gypsum (calcium sulfate dihydrate) adapted from [12].

Generally speaking, the rate of crystal growth is proportional to the level of supersaturation, the reader should however be aware that this concept is only appropriate when considering crystallisation from solution. Crystallisation can also occur in pure materials during the transition from a liquid to a solid when the temperature drops below the melting point (also known as undercooling). Examples of which include the freezing of water to ice and the solidification of molten metals. Whilst the techniques used to model these processes will be assessed, they are not the main focus of the work here.

Whilst it is generally accepted that a solution has to be in supersaturated state for crystallisation to occur, this does not guarantee that crystals will begin to form. As previously mentioned, before crystallisation can begin a nucleation process has to occur.

It is not uncommon that low levels of supersaturation do not provide a strong enough driving force for stable nuclei to form and therefore no crystal growth is experienced. This is known as the metastable region. The following subsection will further discuss the nucleation process and its fundamental kinetic theories.

2.2.2 Nucleation

Nucleation is the process by which ions or molecules within solution aggregate or cluster to form a solid body known as a nucleus or seed. There are a number of different mechanisms by which this can occur, these can be classified into two main categories, namely, primary nucleation and secondary nucleation.

2.2.2.1 Primary Nucleation

Primary nucleation occurs in systems where crystalline matter does not currently exist, it is often considered the 'classical' form of nucleation and typically requires high levels of supersaturation to occur [95]. The primary nucleation mechanism can occur both homogeneously and heterogeneously, such that a homogeneous reaction is where spontaneous nucleation occurs in the bulk of a clear fluid, whilst a heterogeneous reaction is where the nucleation occurs on a foreign particle or surface.

Nucleation can be can be thought of as the formation of a new phase from an existing phase, whereby an interface at the boundary of a new phase is formed. During this process a change in free energy occurs. Gibbs first considered this change in free energy such that,

$$\Delta G = \Delta G_s + \Delta G_v, \tag{2.1}$$

where ΔG is the total free energy change, $\Delta G_s > 0$ is the free energy cost to create a interface at the boundary of the new phase, and $\Delta G_v < 0$ is the energy gain due to a new volume being created.

When considering the classical case of a spherical nucleus being formed from a homogeneous reaction, it was found that the rate of nucleation could be given by [134] ,

$$J = A_{hom} \exp -\frac{16\pi\gamma^3 V_{molecule}^2}{3K^3T^3(\ln S)^2}, \tag{2.2}$$

where A_{hom} is the coefficient of homogeneous integration, S is the supersaturation, γ is the interfacial tension, T is the temperature, K is the Boltzmann constant (1.3805×10^{-23} J K^{-1}) and $V_{molecule}$ is the molecular volume.

Heterogeneous nucleation is when the process occurs either on a surface or foreign material. This particular nucleation mechanism becomes significant at lower supersaturations as the overall free energy required is less than that for homogeneous nucleation. This is because the surface area is less than the classical spherical case of homogeneous nucleation, and therefore less energy is required to form the interface. Shnel and Garside [147] determined that the rate of heterogeneous nucleation could be described by,

$$J = A_{het} \exp -\frac{16\pi\gamma^3 V_{molecule}^2 f(\theta_{contact})}{3KT^3(\ln S)^2}, \tag{2.3}$$

where A_{het} is the coefficient of heterogeneous nucleation and $f(\theta_{contact}) < 1$ is the scaling factor, which is dependent on the contact angle. The contact angle is determined by the surface tensions between the phases.

Whilst kinetic theories for nucleation have been established, both are dependent on nucleation coefficients. It is widely accepted that there are currently no methods for determining these parameters by theoretical means [95], and as such they have to be obtained empirically. This can often lead to difficulties as parameters can change when considering different systems. Despite this, the kinetic models described do offer insight into the impact of physical factors on the rate of nucleation, and also present a suitable means with which to correlate experimental data.

2.2.2.2 Secondary Nucleation

Secondary nucleation is a process that occurs due to the presence of existing crystals in the solution and the interactions between themselves or local environment. An example of a secondary nucleation mechanism is fluid shearing. The shear stresses across the crystal face due to the fluid can sweep weakly bonded molecules away from the crystal, these molecules then go on to form nuclei of their own. Various other mechanisms for secondary nucleation have been identified and details of each mechanism can be found in [72]. Summarising, the main mechanisms are:

- contact
- shear
- fracture
- attrition
- needle

Secondary nucleation is a complicated process. These complex systems can often have several of the aforementioned processes occurring at any given time and therefore it is typically difficult to determine which of the mechanisms are dominant on nucleation rates. This can lead to difficulties when attempting to model or correlate experimental data in systems where secondary nucleation is significant [27].

As mentioned, once the nuclei reach a critical radius, crystal growth can occur. This section has discussed classical theories for nucleation, which are summarised in Figure 2.2. However, once stable nuclei are formed, mechanisms unrelated to these govern the proceeding crystal growth process. The following subsection will discuss the kinetic theories for crystal growth.

2.2.3 Crystallisation Kinetic Models

Unlike the previous kinetic theories for nucleation, throughout the years there have been many different theories on the underlying mechanisms for crystal growth. The earliest theories considered the surface energy of a growing crystal [75]. These suggested that crystals grew in a way such that their surface free energy was minimised. In liquids, where molecules can move freely, the state with minimum free surface energy and hence minimum surface area, is spherical. Clearly, as the crystal is solid, growth has to follow the characteristic shapes of the faces. It was later proposed that crystal faces with a high lattice density (quantity of molecules in that particular lattice plane) are generally more stable and therefore have a low surface energy, and that these these faces would have the minimum growth velocity [33].

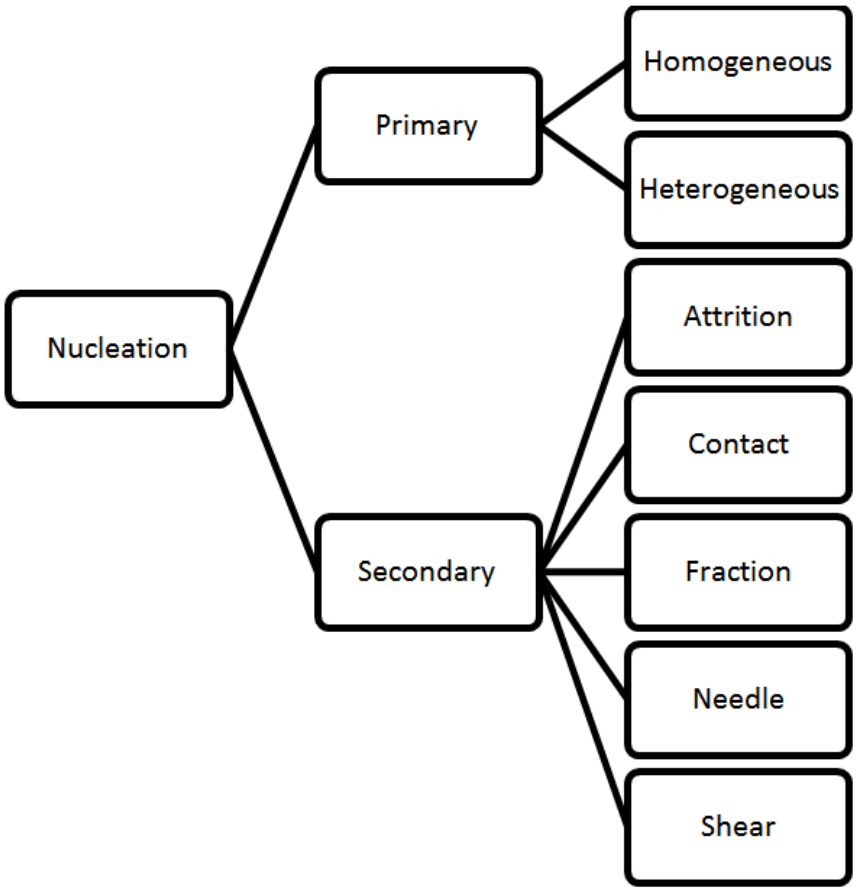

Figure 2.2: Schematic of the nucleation process.

Whilst these theories are attractive from a thermodynamic perspective there is little quantitative evidence to support them. It is generally accepted and easily observable that the crystal growth rate depends on both the supersaturation and solution properties, and these theories include neither of these. Authors have also disputed the validity of these theories [33], showing that experimental behaviour can differ greatly from the theoretical results [97]. Therefore in order to correlate growth rate to these variables, alternative theories have to be considered.

The first crystallisation models which attempted to correlate the rates of crystallisation with the level of supersaturation suggested that crystal growth was purely a diffusional process [139]. This theory suggested that during crystallisation, the depletion of solute

close to the crystal face would cause a localised drop in solution concentration, also known as a mass transfer boundary layer. It was then assumed that due to the concentration gradient, solute would diffuse from the bulk of the solution to the crystal face. It was stated that the crystal growth rate was dependent both on the size of the boundary layer and the rate of diffusion, such that,

$$\frac{1}{A}\frac{dm}{dt} = \frac{D}{\delta}M_s(c - c^*), \tag{2.4}$$

where m is the mass of crystal deposited, M_s is the molecular mass, A is the area of the growth surface, D is the diffusivity, δ is the mass transfer boundary layer thickness, c is the concentration and $c^* = c^*(T)$ is the saturation concentration, where T is the temperature.

Much like the boundary layer theory for heat transfer, it is known that when increasing the flow velocity parallel to the crystal face the size of the mass boundary layer also decreases [24]. This would suggest that in highly agitated systems the diffusion pathway could potentially decrease to nearly zero, and would imply an almost infinite rate of crystallisation. As this is intuitively not physically possible, this diffusion theory for crystallisation does not hold. Furthermore, if crystal growth was purely a diffusional process, the rate of dissolution would be the same as the rate of crystallisation. Experiments have shown that this is not the case, as can be seen in [135].

Clearly, as crystallisation is not purely diffusional, then some addition process must occur. This process is often referred to as the surface integration step and describes the process in which diffused solute molecules are integrated into the crystalline lattice. There are a number of classical theories behind the mechanisms governing the integration of solute into the crystalline lattice. The majority of these theories can be generally categorised as adsorption layer theories.

The first theory of surface adsorption was proposed by Kossel in 1934. This theory stated that crystals are adsorbed into a layer of size 1nm to 10nm adjacent to the crystal surface. In this layer molecules are free to diffuse across the surface of the crystal where they can then attach to one of 3 types of sites. These sites are named the terrace, step or kink and a visual representation of them can be seen in Figure 2.3. Kossel postulated that the

most energetically favourable site for the molecule to integrate, would be the kink site, due to it having the most bonds with the existing lattice. Due to this, the crystal face would eventually fill until a flat surface is formed.

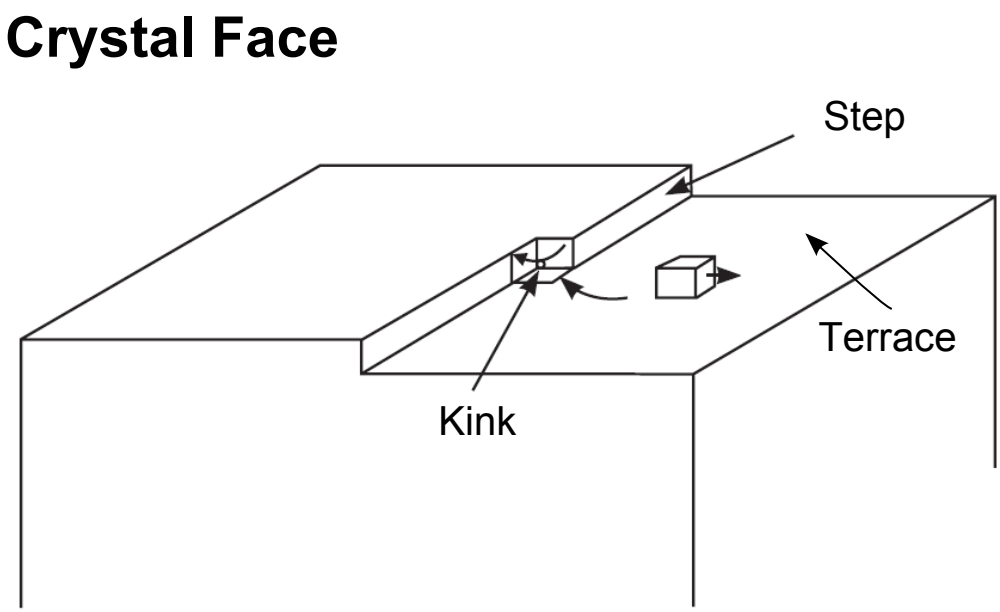

Figure 2.3: Model of the crystal face, adapted from [95].

Once a surface is complete, a mechanism for beginning a new layer must occur. Initial theories suggested that this new layer was formed by nucleation on top of the previous layer, known as 2D Nucleation. Equations which describe 2D nucleation rates can be derived much like the rate equation for 3D spherical nucleation, however these suggest that growth should not occur at low supersaturations. Experimental work [180] has shown that crystals do in fact grow at low supersaturation, much lower than those needed to induce nucleation [116]. This disagrees with the previous theory and would suggest that crystal growth does not occur by the 2D nucleation mechanism for low supersaturated solutions. Whilst this is observed to be the case at low supersaturation, theories have been developed such as the birth and spread model [142], which assumes that the main mechanism for layer growth at high supersaturations is two-dimensional nucleation.

For solutions at low supersaturations, Burton-Cabrera-Frank (BCF) [39] suggested that, instead of 2D nucleation, layers are grown through a spiral dislocation. An example of a

spiral dislocation on a crystal face can be seen in Figure 2.4.

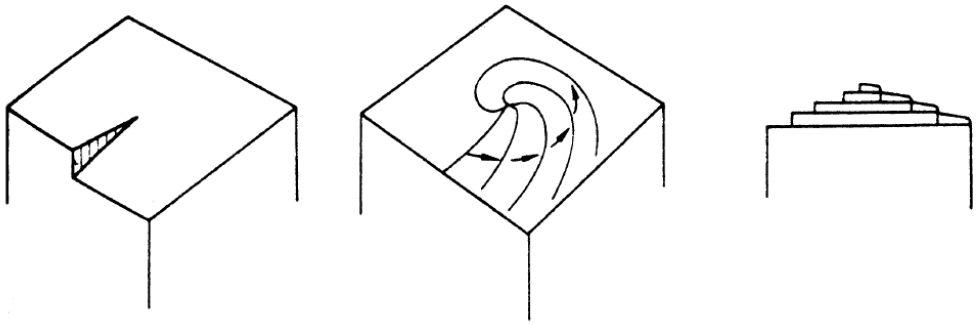

Figure 2.4: Example of a crystal face growing from a spiral dislocation, [134].

Due to the continuous nature of the spiral formation, the need to start a new layer is removed as in two-dimensional nucleation. The BCF model states that the growth rate of the crystal face is given by,

$$A\left(\frac{c-c^*}{c^*}\right)^2 \tanh\left(\frac{Bc^*}{c-c^*}\right), \tag{2.5}$$

where A and B are empirical coefficients, which are specific to the system. These constants are often complicated and can depend on the temperature and crystal morphology. Due to this, A and B can be difficult to determine experimentally [134]. Despite this, the model does offer some insight into crystallisation behaviour, with growth rates following a parabolic relationship with supersaturation at low supersaturation, but a linear relationship at higher level supersaturation. These different behaviours can be attributed to the change in mechanism for the particular solution supersaturation, such that at low supersaturation, spiral growth is the dominant process. At higher saturations 2D nucleation mechanisms take place, and at very high saturations molecules attract to the lattice in a sporadic fashion, leading to spherulitic, fractal, and dendritic patterns [56]. The mechanisms for growth and behaviour predicted by the BCF model can be observed in Figure 2.5.

The BCF model was derived for crystal growth from vapours, whoever, the diffusion of the solution through the liquid medium can have a strong influence on the crystal growth behaviour [50]. Thus, additional models have to be considered which can take into account

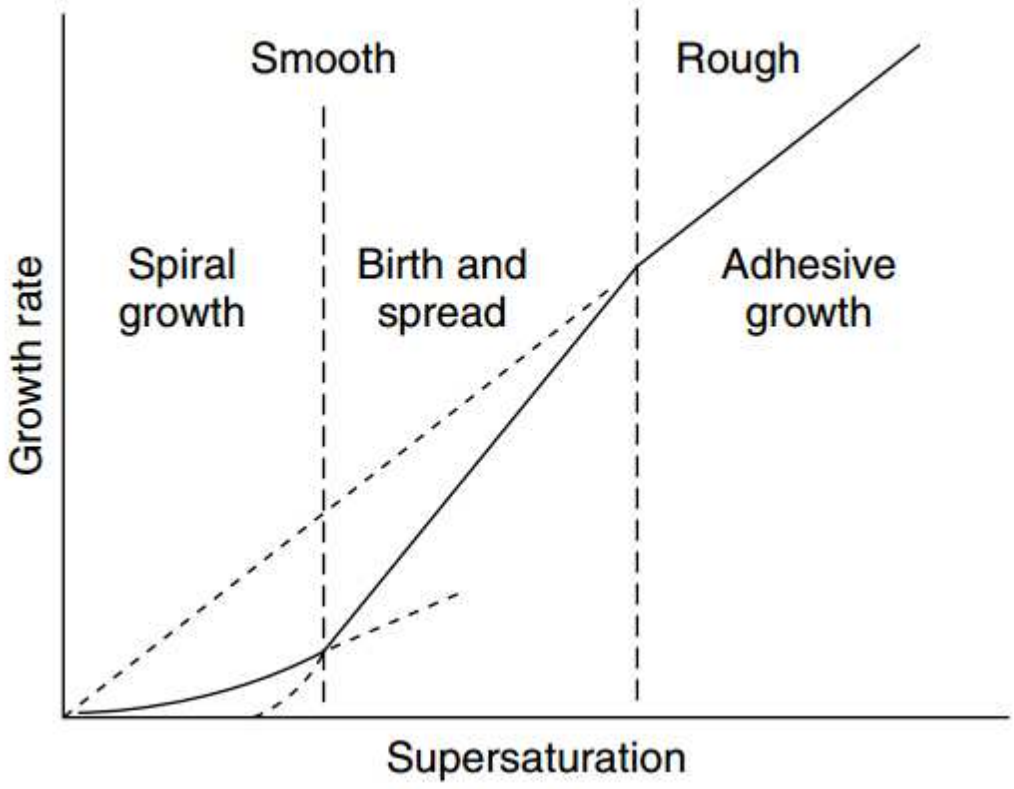

Figure 2.5: The Burton-Cabrera-Frank (BCF) and the mechanisms for crystal growth, [56].

the effects of the solution flow. Gilmer et al. [76] derived a model which incorporates the BCF with bulk volume diffusion, however it requires multiple coefficients which are difficult to determine experimentally. Alternative models for incorporating bulk diffusion with crystal growth have also been developed [51]. However, whilst these new models can offer some insight into crystallisation behaviour, their complexity makes them challenging for industrial application.

Due to the aforementioned problems with implementing the previous models for industrial purposes, a simple model which focuses on coupling the diffusion of solute through the liquid volume and the integration of solute into the crystalline lattice is often used. This model is commonly referred to as the reaction-diffusion or two-step mass transfer model (TSM).

The reaction-diffusion model assumes that as solute attaches to the lattice, it is depleted from the solution local to the crystal face. This results in a region of lower concentration solution close to the crystal. Due to this, solute diffuses from the bulk of the solution to the crystal face. As previously mentioned, models have been developed which assume crystallisation is a purely diffusional occurrence. These theories were however easily proved incorrect by experimental evidence. The model now expands on these previous purely diffusional models by adding an additional relationship such that the surface integration step is considered. Therefore the reaction diffusion model is described by,

$$\frac{1}{A}\frac{dm}{dt} = k_d M_s (c_{bulk} - c_{interface}), \tag{2.6}$$

where $k_d = \frac{D}{\delta}$ is the coefficient of mass transfer, m is the mass of crystal deposited, c_{bulk} is the concentration in the bulk of the solution and $c_{interface}$ is the concentration at the crystal surface. The growth rate with regards to the surface integration can be described by

$$\frac{1}{A}\frac{dm}{dt} = k_r M_s (c_{interface} - c^*)^\eta, \tag{2.7}$$

where k_r is the coefficient of surface integration, c^* is the concentration at saturation and η is the order of the reaction [134].

The coefficients k_d and k_r are often dependent on the conditions of the system, such as the temperature and fluid velocity, however for a particular system they are often considered constant. The behaviour of the system is heavily determined by the relative dominance of the diffusion or integration step, and can often give insight into the impact of varying the system parameters. Garside attempted to quantify this by an 'effectiveness factor' [71] which determines the relative importance of diffusion or surface integration on the system (an effectiveness factor of 0 signifies a purely diffusional process).

There is currently no known method to determine the parameters k_d and k_r analytically and therefore they have to be determined experimentally. However, due to the difficulties measuring the concentration at the interface ($c_{interface}$), experimentalists tend to correlate crystal growth data to,

$$\frac{1}{A}\frac{dm}{dt} = KM_s(c_{bulk} - c^*)^{\epsilon}, \tag{2.8}$$

where K is the coefficient of crystal growth, and ϵ is the overall order of the crystal growth system. Generally speaking, it is difficult to separate the values of k_d and k_r from the measured value of K. Some studies attempted to estimate a value for k_d through measuring crystal dissolution rates, which is classically thought to be a diffusional process. However it is thought that, for certain materials, crystal dissolution contains an additional disintegration step and therefore these methods may not be valid [28]. Additionally, researchers attempted to estimate k_d through empirical mass transfer correlations such as the Frossling equation [134, 171], however this method is often reliant on approximations of the system properties. Despite these aforementioned complications researchers have made efforts to develop alternative methods such that these parameters can be isolated from growth data without the use of mass transfer correlations [110]. However it is noted that these methods are invalid for $\eta = 1$.

Clearly, the reaction-diffusion model does have limitations and in some circumstances complications can be experienced when attempting to determine coefficients for the models. Although due to its simplicity it cannot explain complex behaviours such as the layer growth of crystals or the faceting of crystal faces, this model continues to be the most common approach for industrial chemical engineers (both when correlating experimental data and modelling crystal growth phenomena).

2.2.3.1 Summary

This section has discussed the development of crystal kinetic theories throughout the past century, including the current prevailing models used today. Whilst significant progress has been made regarding these theories, there are often difficulties and limitations when implementing these models to describe crystal growth. Current theories for crystallisation kinetics advanced the previous methods of crystal growth, such that the solute diffusion effects are considered, however, in complex systems other physics which are not considered can impact greatly on the rate of crystal growth. Examples of which include; industrial crystallisation reactors, where non-homogeneous distributions of varying sized crystals

can be found, or systems which consider complex fluid regimes, such as the problem considered in this research work. Hence, additional techniques which further couple fluid flow or other physics to the previously discussed crystallisation kinetics models will be considered.

2.3 Fluid Flow and Computational Fluid Dynamics

In this section various methods and models which describe the fluid dynamics are evaluated. At this stage the coupling of the crystallisation kinetics is not considered as this section will focus on the fluid dynamics exclusively.

The majority of models assessed in this section when discussing fluid flow phenomena will be some application or variation of numerical solutions to the Navier Stokes (NVS) equations. The NVS equations describe the transportation of momentum throughout a fluid system and are the fundamental basis for most computational fluid flow problems. This equation can be written as,

$$\frac{\partial}{\partial t}(\rho \mathbf{u}) + \nabla \cdot (\rho \mathbf{u}\mathbf{u}) = -\nabla p + \nabla \cdot \mathbb{T} + \mathbf{B}, \tag{2.9}$$

where p is the pressure, $\mathbf{u} = (u_1, u_2, u_3)$ is the fluid velocity, ρ is the density, $\mathbb{T} = \mu\Big(\nabla \mathbf{u} + (\nabla \mathbf{u})^{tr} - \frac{2}{3}(\nabla \cdot \mathbf{u})\mathbf{I}\Big)$ is the deviatoric stress tensor, $\mathbf{I}$ is the identity matrix, $\mathbf{uu}$ and $\nabla \mathbf{u}$ are second rank tensors, μ is the dynamic viscosity and $\mathbf{B}$ is the body force (i.e. when considering the gravitational force $\mathbf{B} = \rho \mathbf{g}$, where $\mathbf{g}$ is the acceleration due to gravity).

For most practical applications, the NVS equations are highly non-linear, and therefore solutions cannot be obtained through analytical means, except for very specific circumstances. Due to this, highly evolved numerical methods are used to solve them. These techniques as a collective are usually referred to as computational fluid dynamics, or CFD. This involves the mapping of a numerical grid over the geometry of interest, such that the equations can be discretised and solved over the grid using numerical methods, such as the finite volume method (FVM) or the finite element method (FEM) [66, 115, 155]. It is very common in fluid flow problems that an incompressibility condition can be given such that $\nabla \cdot \mathbf{u} = 0$ [6], assuming constant viscosity (2.9) then simplifies to,

$$\rho\Big(\frac{\partial \mathbf{u}}{\partial t} + (\mathbf{u}\cdot\nabla)\mathbf{u}\Big) = -\nabla p + \mu\nabla^2\mathbf{u} + \mathbf{B}, \tag{2.10}$$

The FVM allows (3.5) to be discretised such that the following set of equations are obtained,

$$\rho\frac{\partial u_i}{\partial t}V + \sum_{f}^{N_{faces}} (\rho u_i u_j n_j A)_f = -\sum_{f}^{N_{faces}} (p n_i A)_f + \sum_{f}^{N_{faces}} (\mu\frac{\partial u_i}{\partial x_j} n_j A)_f + B_i V. \tag{2.11}$$

These equations are then solved over every cell in the computational grid, such that N_{faces} denotes the number of faces in a cell, subscript f denotes the index of the cell face, A is the area of the face, $\mathbf{x} = (x_1, x_2, x_3)$ is the directional vector, $\mathbf{u} = (u_1, u_2, u_3)$ is the velocity vector, B_i is the body force in the ith direction, V is the cell volume and the face normal vector is given by $\mathbf{n} = (n_1, n_2, n_3)$. Where summations are enclosed by subscript f the values inside are taken at the cell face, f.

Clearly the discretised NVS equations are much more approachable than their continuous counterpart. However, the precise approach in which the discretised NVS equations can be solved is often complex and involves the use of sophisticated techniques in order to successfully couple the fluid momentum to the pressure. Furthermore, flow variables are stored at the cell centre, therefore numerical techniques are required such that the face values can be interpreted from the cell centres. There are a number of different numerical methods in which the face values can be calculated, each having its own strengths and weaknesses. A variety of solution methods also exist in order to step the solution through time. A summary of the various solution methods for CFD can be found in [6].

Whilst the aforementioned methods outline the most common CFD techniques, there are other methods which are less commonly used in CFD, some of which include the use of 'meshless' numerical methods such that a numerical grid need not be implemented. Other methods solve the Boltzmann equation instead of the NVS [47]. The following subsections will discuss how CFD techniques can be implemented in order to describe the main fluid dynamics features experienced in the crystallisation of impinging droplets, namely, droplet impact and thin film flow. The aforementioned systems are physically complex and often the governing physics are not well understood. In addition to this, solutions of the full

NVS equations are often computationally expensive and therefore simpler, alternative methods can be attractive. Due to these difficulties, a broad range of research will be considered here, including; experimental work, analytical techniques, models based on simplifications of the NVS equations, and also the previously discussed CFD methods. This will allow the reader to gain an informed appreciation of the governing physics, the challenges when modelling them, and the currently available techniques for doing so.

2.3.1 Droplet Impact

The problem of interest (before flowing down the surface and crystallising) consists of falling droplets of liquid impacting on a inclined surface. This section will focus on previous works which have attempted to capture this behaviour. Problems of this nature are often challenging to solve, as they involve multiple fluids, are transient in nature and can exhibit various different behaviours depending on the system properties. Also multiple physics such as surface tension effects, the geometry and properties of the surface, and any existing liquid on the surface can all play an important role.

Research on droplet impact is usually separated into studies regarding impact onto liquid films and studies regarding the impact onto solid surfaces. This is because the governing physics, and hence modelling considerations, between the two are markedly different. Generally speaking, the impact of droplets onto an existing liquid film, where the film thickness is a lot greater in magnitude than the surface roughness, is well understood. Impact phenomena are usually separated into either splashing or spreading, where a splash is defined as an event where liquid is ejected from the crater formed by impact, either from the crown or centre (see Figure 2.6). Ejection from the centre, also know as a Worthington jet, is less common and [193] states these only occur when the film height is greater than the droplet diameter. The behaviour of the droplet impact is a result of the competing forces of inertia and surface tension. Whilst gravity will affect the acceleration of the droplet as it free falls, its effect is considered negligible during the impact. Also, the viscosity is considered to have minimal effect on the impact behaviour. Inertia forces attempt to drive the impacted droplet upwards whilst the surface tension attempts to arrest this motion. The relative magnitude of the forces determines whether the droplet splashes or spreads.

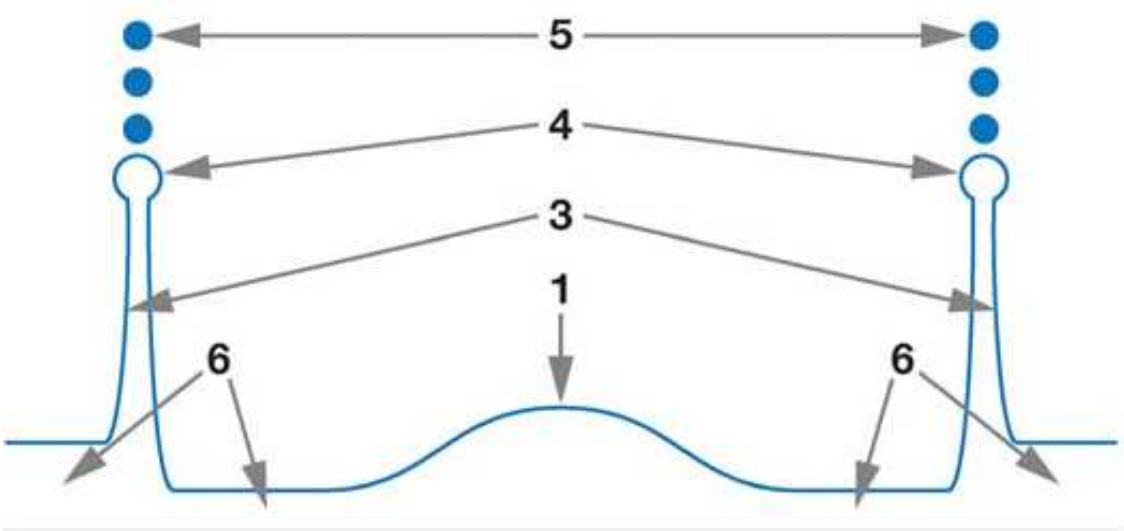

Figure 2.6: Diagram of the characteristic behaviour of a droplet splash on an existing liquid film, taken from [193]. Where 1 is the residual top of impacting the drop, 2 is the wall, 3 is a section of crown-like sheet propagating outward, 4 is a cross-section of the free rim, 5 are secondary droplets formed from cusps of the free rim and 6 is a liquid layer on the wall.

The splashing of droplets on liquid films is considered a complex process and usually advanced numerical methods would be required to describe the process in full. However, several semi empirical correlations have been developed which can offer some basic insight into the behaviour of an impacting droplet. One of the main results of this nature was posed in [194], where it was determined experimentally that the minimum velocity for a splash from a continuous drip to occur was,

$$V_0 \geq 18(\frac{\sigma}{\rho}^{\frac{1}{4}} \upsilon^{\frac{1}{8}} f^{\frac{3}{8}}) \tag{2.12}$$

where V_0 is the impact velocity, σ is the surface tension, ρ is the fluid density, υ is the dynamic viscosity and f is the impact frequency. This threshold has also been shown to hold true in CFD studies such as [158]. The authors in [158] use a multiphase CFD model, namely the volume of fluid (VOF), which through the advection of a scalar property, the volume fraction (denoting the fraction of a given fluid phase within a cell) captures the interface between both the liquid and gaseous phases. Details regarding the mathematics and computational implementation of the VOF will be omitted at this stage, as they will be discussed in detail in Chapter 4. The splashing criteria in (2.12) was also shown to

be appropriate for droplets impacting obliquely [161] and for droplets impacting on an inclined surface [174]. However, in these cases V_0 is replaced by the the velocity normal to the surface when considering inclined surfaces.

Other studies have been carried out which implement the VOF model for modelling droplet dynamics, [79] uses the VOF combined with the level-set method to model the droplet impact behaviour on liquid films. The VOF model is classified as a diffusive interface method, such that due to the numerical implementation of the model, the boundary between phases is not defined by a sharp interface, but rather by a graduated transition from one phase to the next. This behaviour can often lead to problems when considering additional physics that occur at the interface. A classic example of this is the implementation of a surface tension model where the surface force generated due to surface tension is dependent on the curvature of the interface. As the interface is not sharply defined, it is often difficult to accurately calculate the surface curvature and this can lead to non-physical results being produced by the model. Unlike the VOF, the level-set method is a sharp interface model [146] and therefore does not suffer from the same limitations when calculating the curvature of the interface. However, the model in [146] performs poorly when preserving volume conservation, making it unsuitable to accurately model fluid flows. Due to this, the study in [79] couples the VOF with the level-set method, such that the VOF model describes the transport of the volume fraction, whilst the level-set method is used for geometric calculations where surface normals and curvatures are required. This method was shown to greatly reduce complications when using the continuum surface force (CSF) surface tension model [30]. The study reports that the complete droplet impact behaviour can be captured over a time frame of 5×10^{-3}s. Results are also in agreement the with the splashing criteria.

For situations where the velocity was shown to be below this threshold, spreading was seen to occur. The droplet impact propagates waves through the film, where expressions for the wave frequency and magnitude were also determined in [158]. This may also be an important point for consideration as studies have shown that unsteady waves may have a impact on mass deposition rates [187].

Whilst the impact of droplets on liquid films is well understood, the impact of droplets

on solid surfaces is less so. In these situations, the properties of the solid surface play a major role in the behaviour proceeding impact. Researchers have made some progress modelling this phenomenon computationally, however problems are seen to occur when attempting to implement physically correct boundary conditions at the moving contact line. The moving contact line defines the contact between the solid surface, liquid droplet and gaseous phase, as shown in Figure 2.7.

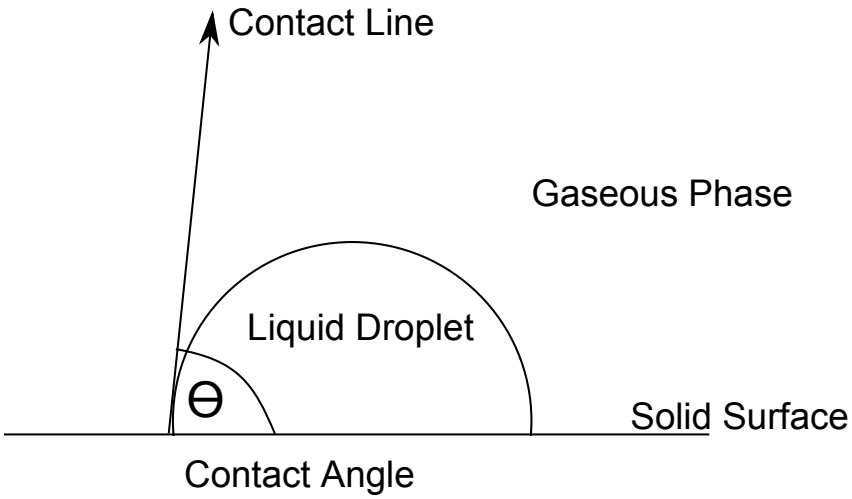

Figure 2.7: Diagrammatical representation for the moving contact line when considering a droplet on a solid surface.

Often CFD simulations impose no-slip boundary conditions for the wall surface. This implies that that at this point, the velocity component parallel to the boundary is stationary. This however can often lead to complications when modelling impacting droplets, as this method tends to lead to a singularity at the contact line [167]. Researchers have experimented with different boundary conditions, however it is usual for either experimentally obtained results to be superimposed or a fixed angle to be specified at the contact line.

An example of a numerical implementation which attempts to address these problems through the imposition of varying contact angles can be found in [109]. Here authors use the VOF model to model the impact of non Newtonian droplets onto a dry surface. The authors initially impose an empirically calculated, constant contact angle on the droplet at the point of impact. Once the droplet impacts and advances along the surface, it even-

tually reaches a point of rest. After this point the droplet begins to recede and a different contact angle is imposed for this motion. As the impact behaviour is heavily determined by the surface tension effects, much like the previous study, the authors implement the CSF surface tension model [30]. Results from this study suggest that the variable contact angle technique performs well, with computational results being in good agreement with experimental data.

Surface tension effects are important when considering the impact of droplets and therefore it is often critical that these effects are captured accurately. The previously discussed CSF model is known to suffer from several limitations, such as the dependence on the surface curvature, however as the majority of commercial CFD packages have utilised this for a considerable period of time, it remains to be the most popular surface tension model. Despite this, there are a number of alternative models in which the surface tension can be captured, a critical assessment of several current surface tension models can be found in [16].

In addition to these aforementioned studies which attempt to address droplet impact from a fundamental perspective, many researchers have carried out studies for droplet impact in industrial scenarios. Droplet impact and spreading (typically with no splash) has been studied in [13], where experimental work was carried out on molten metal droplets for impact velocities of 1.0 to 4.0 ms^{-1} and substrate temperatures from 25 to 240°C. The authors determined from the experiments that the spread radius of droplets could be described by,

$$D_{max} = D_0 \sqrt{\frac{We + 12}{3(1 - \cos\theta_{contact}) + 4(\frac{We}{\sqrt{Re}})}}, \tag{2.13}$$

where D_{max} is the maximum droplet spreading distance, D_0 was the initial droplet diameter, We is the Weber number, given by $We = \frac{\rho D_0 V_0^2}{\sigma}$, $\theta_{contact}$ is the liquid-solid contact angle, and $Re = \frac{\rho D_0 V_0}{\mu}$ is the Reynolds number.

It was found that this expression was less accurate for situations where the droplet solidified on impact. An analytical study on this was carried out in [22] where similar expressions were formulated.

2.3.1.1 Summary

Much research has been carried out in order to understand the impact dynamics of falling droplets. Both analytical and experimental studies have been carried out in order to establish the threshold for splashing and spreading of droplets. In addition to this modern studies are using advanced numerical techniques to capture the splash of a droplet. Despite the large amount of research in this area, there are still difficulties with the implementation of correct boundary conditions in many approaches. Furthermore, the impact of droplets on dry surfaces is still not well understood. The problem assessed in this thesis takes place over periods of up to 30 days, whilst research has shown that CFD simulations capture impact dynamics over a period of 5ms. It is therefore likely that a full CFD simulation of droplet dynamics over this full time-frame would be challenging. It is envisioned that due to this the semi empirical correlations will be more useful. Additionally, as the problem considered is observed to show that leakages occur over long time-scales, the short term behaviour is likely not to have a major impact on the overall problem. Experimental data from the NNL has suggested that after relatively short periods of time, liquid films begin to form across the impact surface, therefore in addition to the droplet behaviour it is also critical that the of the behaviour of liquid films is well understood. The next section will assess previous experimental and computational studies regarding the modelling of fluid films.

2.3.2 Liquid Films

Due to their common occurrence in industry, the ability to explain and model the behaviour of liquid films has been a popular subject of investigation for researchers over the past century. In 1916 Nusselt developed analytical solutions to describe the height of smooth, laminar, gravity driven films [140]. This theory was developed in conjunction with heat transfer theories in falling thin films. This work determined that the film thickness, h, could be given by the expression,

$$h = \delta_{Nusselt} = \sqrt[3]{\frac{3\mu\ Q}{\rho^2 g B \sin\theta}}, \tag{2.14}$$

where μ is the dynamic viscosity, $\delta_{Nusselt}$ is the Nusselt solution, B is the width of the film, θ is the angle of the plane and Q is the mass flow rate of liquid.

This theory however only held for smooth laminar flows, and even though remaining laminar, films were found to oscillate and become 'wavy' at relatively low Reynolds numbers. Experimental results have shown that the minimum Reynolds number for a film to remain sufficiently smooth is approximately $Re = 30$ [24].

In order to account for the wavy nature of the films, [99] reported that the average film height would in fact be lower than that predicted from the Nusselt solution (2.14). Through analytical methods, the authors determined that the film height could be described by $h = 0.92\delta_{Nusselt}$. Despite this, experimental work has not always agreed with this theory, and has shown the average film height to fall both above and below the Nusselt solution [132, 198, 4].

Whilst the Nusselt solution has shown to be inaccurate when considering the transient, wavy nature of film flows, and is only valid under specific conditions, this approach is still used extensively in computational models today. Often it is unnecessary to capture a high resolution solution describing the exact motion of a film, and therefore models which require a simple description of the fluid flow implement the Nusselt solution in order to establish a basic geometric approximation. Once the flow properties have been calculated, this solution can then act as a platform in which additional physics can be solved. Examples of models where this methodology has been used can be found in [117, 162, 129].

Whilst simplified theories are still used extensively and can offer insight into the behaviour of the film, for a more accurate description (including waves or films over complex geometries) more complex numerical models are required. For example, [181] studied the flow of a thin film flowing down an inclined plane. The authors in this work carried out both experimental work, in order to gain an appreciation for the physics of the problem, and then later carried out transient two-dimensional CFD calculations in CFX-4, a commercial software package, using the homogeneous multiphase model [199] (CFX's equivalent of the VOF model). In some cases surface tension effects are also known to be important when considering the motion of liquid films and therefore, the CSF surface tension model is employed. Furthermore, for transient calculations the same complications are experienced at the film leading edge, or contact line, much like the models concerned with

capturing droplet impact considered in Section 2.3.1.

Three-dimensional studies have also been carried out on the flow of liquid films down inclined planes, e.g. shear flow down a duct was studied in [111]. Whilst the driving force for the film motion is different to that of gravity driven films, the techniques used here to capture the film are still applicable. In [111], the VOF model, together with the CSF surface tension model was used. The authors employed a simple model at the contact line, such that a constant angle was imposed. Unlike the previous studies, a steady state fluid solver was used, and the transient terms in the governing equations are no longer considered. Results from this study were shown to be in good agreement with experimental data and surface tension effects were shown to have a strong impact on the width of the film, however they had relatively little impact on the height of the film. A review of surface tension models when coupled to the VOF for the modelling of liquid films can be found in [16, 2].

In [1], the authors studied wavy falling films using a combination of a transient in-house DNS (Direct Numerical Simulation) CFD code [157] and the VOF model. The CSF model was implemented to capture the effects of the surface tension. Additionally, the heat transport and species transport equation were solved. The latter equation allows description of matter which is transported by both the advective motion of the fluid, and the diffusion of solute through the film, therefore allowing the calculation of the species concentration, spatially and temporally, throughout the film. Results from this study showed that the inner structure of the film, particularly the downward velocities due to its wavy nature had a large influence on both the species transport and heat transfer throughout the film. In a laminar, smooth film species can only travel adjacent to the flow via the diffusive mechanism, however these waves cause the advective motion of the species both towards the liquid - solid interface and away from the liquid-gas interface. Furthermore, wavy films possess a larger surface area on the liquid-gas interface than an equivalent flat interface and therefore a larger heat transfer coefficient is observed.

Whilst several of the computational studies observing liquid films have been discussed, it should be noted that these numerical techniques allow for the addition of complex physical effects, which otherwise would not possible through analytic approximations such as

the Nusselt solution. Additional physics were included into the VOF model for thin films down inclined planes in [80], where authors used OpenFOAM [144], an open source CFD package, to solve the three-dimensional transient NVS equations coupled with the VOF model for non-Newtonian fluids. The authors also implement the CSF model to account for surface tension effects. This study was shown to be in good agreement with experimental data. Similar studies have been carried out using OpenFOAM for thin films, such as in [55]. The authors in [55] used a similar implementation of the VOF model with the CSF surface tension model, however they implemented an adaptive meshing routine. This alleviates some of the aforementioned problems with the diffusive interface, such that the mesh at the interface is refined and the diffusion across the interface is minimised. This study also assesses the stability limits of the film, as the experimental data had also shown that under certain circumstances fingering patterns or rivulets can occur. Figure 2.8 demonstrates a typical unstable film where rivulets are present.

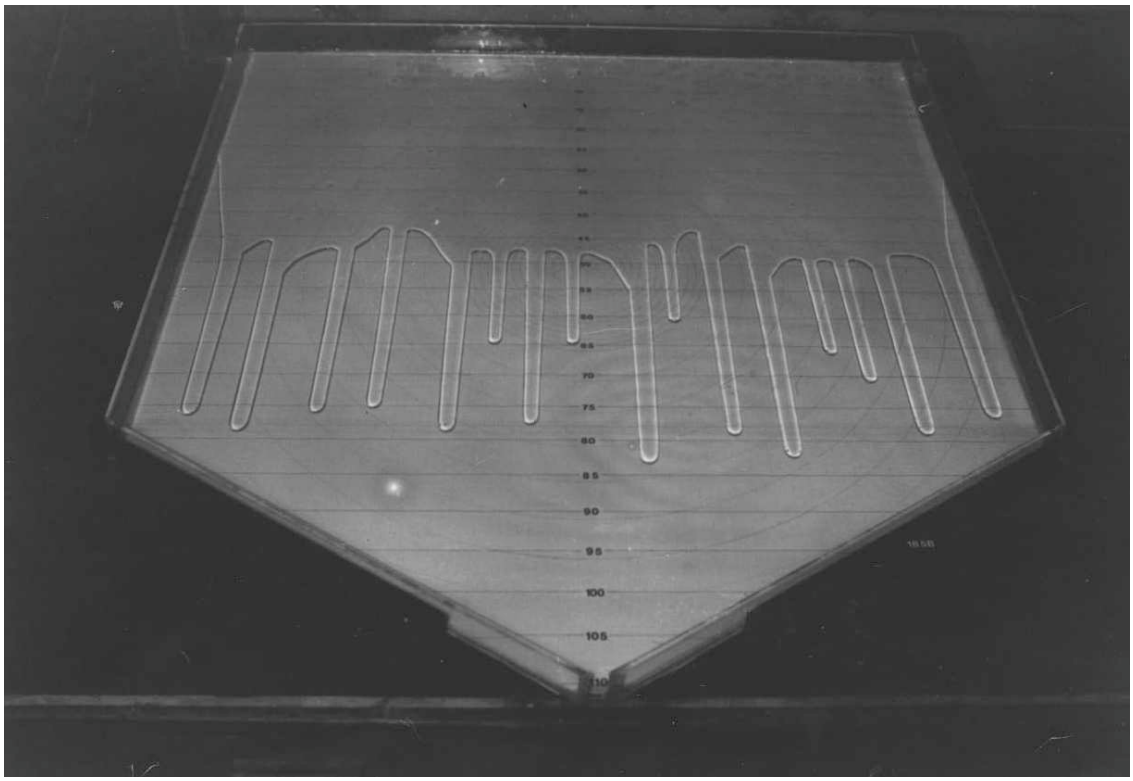

Figure 2.8: Example of an unstable film, where rivulets are formed [145].

Clearly, the VOF model is used extensively in a range of applications which require the

capture of interfaces between multiple immiscible fluids, and can reveal a number of physical phenomena. A summary of these different applications can be found in [93]. Whilst solution of the full NVS equations with the VOF can capture a range of physical effects, it is not without its drawbacks, e.g. it can be extremely computationally demanding. For an accurate transient solution, very small time-steps have to be used. This implies that phenomena over large time-scales are generally infeasible to solve transiently. Moreover, the VOF is a diffusive interface method, and whilst this can offer some advantages, such as making the system less numerically stiff, it can also offer some major drawbacks. A primary complication when using the VOF model is that the mesh in the region of the interface has to be highly refined in order to minimise numerical diffusion, which can often be difficult to implement if the interfacial position is not known *a priori*. Furthermore, these highly refined meshes, when coupled with the need for small timesteps, can be extremely computationally demanding and therefore place limitations on the time and length-scales which can feasibly be considered. The diffusive nature of the interface can also cause problems when implementing interfacial physics, such as surface tension, evaporation and heat transfer due to latent heats. Due to these drawbacks, authors have attempted to simplify the problem of thin films down inclined planes. Under various situations, such as when the flow is either very slow, or the characteristic stream-wise length is a lot greater than the film thickness, inertia effects can be ignored, an example of this being the Nusselt theory. Using these assumptions the full, transient NVS equations can to be simplified, such that an equation which governs the evolution of the film height can be formulated. This method is also know as the lubrication approximation [145]. The advantages of such a method is that the problem loses one degree of freedom, for example a two-dimensional problem for flow velocity $\mathbf{u}(x, y)$ reduces to a one-dimensional problem for film height $h(x)$. An extensive study which assesses the applicability of this method for modelling thin films down inclined planes can be found in [74]. The authors in [74] show derivations of the lubrication approximation for thin films over surfaces which contain small topological changes such as bumps and troughs. In addition to the mathematical derivations, the authors present numerical finite difference and finite volume formulations for the problem. The system is still complex to solve due to the need for a segregated pressure-film height solver (much like the pressure-momentum coupling in traditional CFD). Results from this study are shown to be in excellent agreement with the experimental results in [58]. Whilst this type of modelling reduces the complexity of

the NVS equations, additional physics can still be coupled to the lubrication equations. For example the same authors as in [74] later develop their model to include evaporative effects, which can be found in [73]. Authors in [145] also include additional physics into the lubrication approximation, such as evaporation, heat transfer and films over complex geometries. Additionally, [89, 3] use the lubrication approximation to assess the effects of surface tension in liquid films of both Newtonian and non-Newtonian fluids.

As the evolution equations for the lubrication approximation are simpler than the NVS, this allows additional mathematical analysis to be carried out on the equations, which otherwise would not have been possible. The authors in [62] carry out analysis on the lubrication approximations to determine the stability limits of the film. Once the film becomes unstable, it splits into a fingering pattern.

2.3.2.1 Summary

The ability to model and understand the behaviour of liquid films has been a key subject of interest for researchers over the past century. Early research saw the development of analytical approximations for film flow, which are still used today. These models are often implemented into modern studies where a simple approximation of the fluid flow is sufficient. In comparison to numerical CFD methods, such as the FVM and FEM, these analytic approximations are relatively easy to implement and additionally the computational cost for calculations is low. In situations where a more complex description of the fluid flow is required, such as when a transient solution, or when additional physics or complex geometries need to be considered, research has shown that multiphase CFD models, such as the VOF model, can provide accurate solutions. Whilst these models are robust, due to their computational costs they do have limitations when considering the length and time-scales of a problem. This chapter has also discussed an intermediate step between the analytic approximations and full NVS equations, in the form of the lubrication approximation. This modelling approach allows the simplification of the NVS equations. These methods reduce the number of variables considered in the problem, hence reducing computational cost. Also due to their simplicity, relative to the NVS equations, mathematical analysis can be carried out on the equations, such that information about the system can be obtained e.g. stability limits. However, these models

have limitations, such as they can only be applied under specific conditions and numerical methods are still needed to solve the problem.

2.4 Computational Crystal Growth Models

This section will assess computational methods for implementing the previously discussed crystallisation kinetic models. The previous kinetic models describe the rate of crystallisation with respect to the levels of supersaturation in the solution, whilst these model hold true, the level of supersaturation at the crystal face in a real system can often be attributed to a number of physical factors, such as heat transfer, evaporation and the dynamics of the fluid flow. Due to this, kinetic models have to be coupled to computational models which can describe the individual phenomena, and their interaction between each other.

Due to the large occurrence of crystallisation in a multitude of processes, it is no surprise that a large amount of research has been carried out for a variety of applications. This section will separate the various applications into the following subsections and assess work from each in order to gain a broad appreciation for the various possible approaches:

- **Fundamental crystal growth studies**
  Research here relates to growth of a crystal from a single seed or nucleus. It tends to focus on the techniques used to model crystallisation, often implementing non-physical, non-dimensional parameters, rather than using parameters relating to real life crystallisation problems.

- **Crystal growth optimisation in industry**
  Studies in this section focus on modelling the optimisation of industrial crystal growth processes. One major application in this field is crystal growth in large scale reactors. In addition, studies which focus on the growth of single, large crystals are considered.

- **Crystallisation and precipitation fouling in industrial equipment and infrastructure**
  As discussed in Chapter 1, fouling in industry is a major problem. Due to the major cost implications associated with industrial fouling, there is a large volume

of research carried out in order to understand and minimise this problem. This subsection will discuss pertinent aspects of this research.

- **Models for describing geological formations**
  Models describing the growth of crystalline formations that occur in nature are considered such as stalagmite and stalactite growth, icicle formations and the deposition of calcite in rivers and streams.

2.4.1 Fundamental Crystal Growth Studies

Fundamental crystal growth studies tend to focus on framing crystal growth problems as a moving boundary problem, where the moving boundary describes the crystal interface as it grows through time. The vast majority of studies tend to focus more on assessing the applicability and accuracy of numerical methods, than describing growth for practical industrial usage.

The moving boundary methods for crystal growth can be separated into two classes; sharp interface models and diffusive interface models. Sharp interface models generally model the solid-liquid interface explicitly, such that there is an exact divide between the phases. In the majority of commercial CFD software this is accomplished via moving mesh techniques. Whilst this method offers clarity between the interfaces, it is often considered difficult as moving the mesh in a robust manner is often challenging to implement. Furthermore, singularities can often occur due to the sharp interface, and the system of equations can be considered 'stiff' and therefore difficult to solve. Classically, moving boundary methods were posed as sharp interface models, with the mathematical formulation classed as a 'Stefan problem' [128]. Stefan problems have been a major subject of interest over the past century, and are not limited to crystallisation problems. They can generally be used to describe most problems involving a moving interface, such that a kinetic expression can be imposed upon it.

The most popular methods for solving a moving boundary problem using CFD techniques, are diffusive interface models. These models are often referred to as 'fixed grid' methods, such that the separation of the phases can be described without alterations to the mesh. This offers many advantages as it alleviates the difficulties experienced when implement-

ing sharp interface models. As mentioned, the governing system of equations for sharp interface models are stiff, and therefore it can often be difficult for numerical solvers to obtain accurate or even correct solutions. Fixed grid diffusive methods contain numerical diffusion across the interface, meaning that there is a graduated transition from one phase to the next, as seen in Figure 2.9. This approach can often make it easier for numerical solvers to obtain a solution to the moving boundary problem. Despite this, these methods can pose their own problems due to the diffusive nature of the interface, particularly when applying physics which occur on the phase boundaries. The most common methods for fixed grid, moving boundary methods include; phase field, volume of fluid and level set methods. This section will assess studies carried out using these methods.

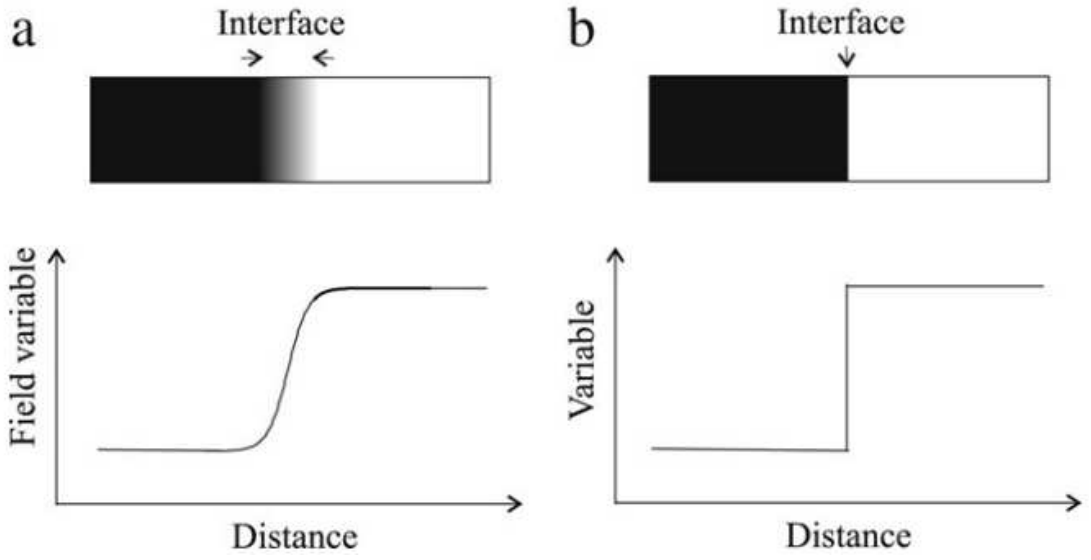

Figure 2.9: Diagrammatical representation of a (a) diffusive interface solution and (b) sharp interface solution, for a one-dimensional problem [130].

2.4.1.1 Phase Field Methods

The phase-field method is a diffusive interface method, where a phase parameter, ϕ is introduced which describes different phases of a system, i.e. for a liquid-gas system, in the liquid region $\phi = -1$ and in the gaseous phase $\phi = 1$, these phases are then separated by a diffuse interface of a certain thickness, where the phase field parameter transitions from -1 to 1. The exact mathematics of phase field method can change depending on the application, however generally speaking differential equations which describe the evolution

of the phase variable, ϕ are solved. The phase field equation takes the general form [163],

$$\frac{\partial \phi}{\partial t} = M\nabla^2 f(\phi) + g(\phi) \tag{2.15}$$

where ϕ is the phase field variable, M denotes the interface width, f and g are functions of the phase field, however their exact form depends on the physical application being considered. For example when using the phase field method to model the advected interface between two fluids, $g = -\mathbf{u} \cdot \nabla\phi$ and $f(\phi)$ is a function relating to the chemical potential of the system [70]. The ability to control the interface width, offers great advantages when using numerical methods to solve the phase field equation (2.15), as it can both decrease the stiffness of the system of equations and increase solver stability. Whilst this is the case, the phase field method does have limitations, such as the governing equations are a phenomenological description of the system and only take on a physical meaning at the sharp interface limit [130].

As the studies in this section tend to focus on the application of the method, systems are often simplified such that either heat transfer or the solute concentration is captured. Often the liquid is considered stationary, such that the NVS does not require solving. The authors in [45] derive the phase field equations for both the solidification and crystallisation where the driving force for phase change are the temperature and solution concentration, respectively. Systems are formulated in one-dimension such that numerical calculations are kept simple. Results from the phase field system are compared to the solution of the sharp interface model which is solved analytically. Results were shown to be in reasonable agreement. Similar work was carried out in [163] where phase field equations were developed in two-dimensions for both temperature dependent solidification and solution dependant phase change. No advective effects due to a fluid phase were considered, however a new adaptive mesh method was developed such to increase the numerical stability and accuracy of the system. The adaptive meshing functioned such that regions across the interface were refined.

Whilst the aforementioned studies do not include fluid flow, the phase field method is more than capable of describing not only fluid systems but also a number of systems with moving phase boundaries. Examples of phase field formulations for capturing the

interface between multiphase fluid flows can be found in [14, 5], however, no phase change is experienced in these systems.

Phase field methods for phase change problems have also been carried out where fluid flow effects are considered. The authors in [192] formulated the phase field equations in order to model dendritic formations, grown from a single crystal seed. The equations are formulated both in two dimensions and three dimensions, and solved alongside the energy equation and the NVS equation. The authors in this study implemented similar adaptive meshing techniques to those of [163]. Results from the two-dimensional study agreed well with classical results, however it was found that the system was highly three-dimensional in nature and therefore, only three-dimensional calculations agreed with the experimental data.

The phase field method is used extensively in phase change problems, however it is not without its downsides. Namely, the phase field equations only make physical sense at the sharp interface limits. There is need for adaptive meshing at the phase separation interface, such that an accurate, stable solution can be found. Additionally, no studies have been found which implement a liquid-solid phase change when considering a system with multiple fluids.

2.4.1.2 Other Diffusive Interface Methods

Another fixed grid method of interest is the VOF method. Whilst this was discussed previously for the modelling of multiple fluid phase problems, such as droplet impact and thin film modelling (Section 2.3), it also has applications in phase change and crystallisation problems. The previously discussed VOF models considered the advection of a volume fraction throughout the system, this volume fraction allowed the distinction between the multiple fluid phases and the interface between them. These equations can now be modified such that, instead of a volume fraction denoting the volume of fluid in a given cell, the volume fraction can represent the volume of solid. Moreover, instead of the volume fraction being advected relative to the fluid motion, this can now be advected due to a kinetic term representing a solidification or crystallisation process.

A recent study [112] solved the VOF equation in order to describe the growth of dendritic

formations from a single seed. The phase change was a temperature driven reaction from a melt, and therefore the energy equation was also solved. In this study the convective effects of the fluid were not considered.

The VOF model has also been used to solve crystal growth from solution. The authors in [112] solved the VOF equation in order to describe the growth of crystals from organic solutions. The authors solved the NVS equations for a single phase fluid, and a sink term dependent on the volume fraction was imposed such that the fluid did not flow in the crystalline regions. Furthermore, the solute transport equations were solved such that solution concentration in the fluid could be obtained. The surface integration step from (2.7) was imposed on the crystal interface, such that the growth was proportional to the local supersaturation.

2.4.1.3 Sharp Interface Model

Li et al. posed the growth of a single crystal as a Stefan-type problem solving a scalar diffusion equation for the solution concentration [118]. Crystal kinetics were applied on the crystal surface, such that the growth was proportional to the solution's supersaturation at the surface. This work allowed the modelling of dendritic formations suspended within a stagnant fluid through a front tracking technique.

Clearly, fixed grid methods do offer many advantages and therefore, are used extensively in crystallisation and phase change problems. They are not without their draw backs and therefore deforming grid methods or sharp interface models do offer some advantages.

2.4.2 Crystal Growth Optimisation in Industry

2.4.2.1 Growth of Crystal Populations in Large Scale Reactors

Problems of this type are often complex as not only do they consider the crystallisation kinetics, they also consider the temperature, solution concentration and flow field. Whilst these properties are also considered in the studies discussed in Section 2.4.1.1, the problems here also need to consider the size distribution of the solid crystals in the reactor. Crystals for industrial purposes generally have to be grown to a specific size, therefore models can help determine the optimal conditions for a particular process. One com-

mon method for modelling systems of multiple crystals is the population balance model [86, 67, 48, 23]. The population balance allows the modelling of crystal growth over multiple crystals and the consideration of nucleation and birth of new crystals within the reactor is also possible. The authors in [48] use population balance modelling for capturing the growth of barium sulphate in a stirred tank reactor, as seen in Figure 2.10. The model assumes that crystal birth due to secondary nucleation is negligible, however they do consider both primary homogeneous and heterogeneous nucleation and crystal growth. Nucleation is given by the kinetic rates given in Section 2.2.2, and the integration step equation in (2.7) is used for the crystal growth. Momentum, heat and solute transport are also solved. The local population of crystals is assumed not to influence the fluid flow. The final crystal size distribution was shown to be in good agreement with experimental results.

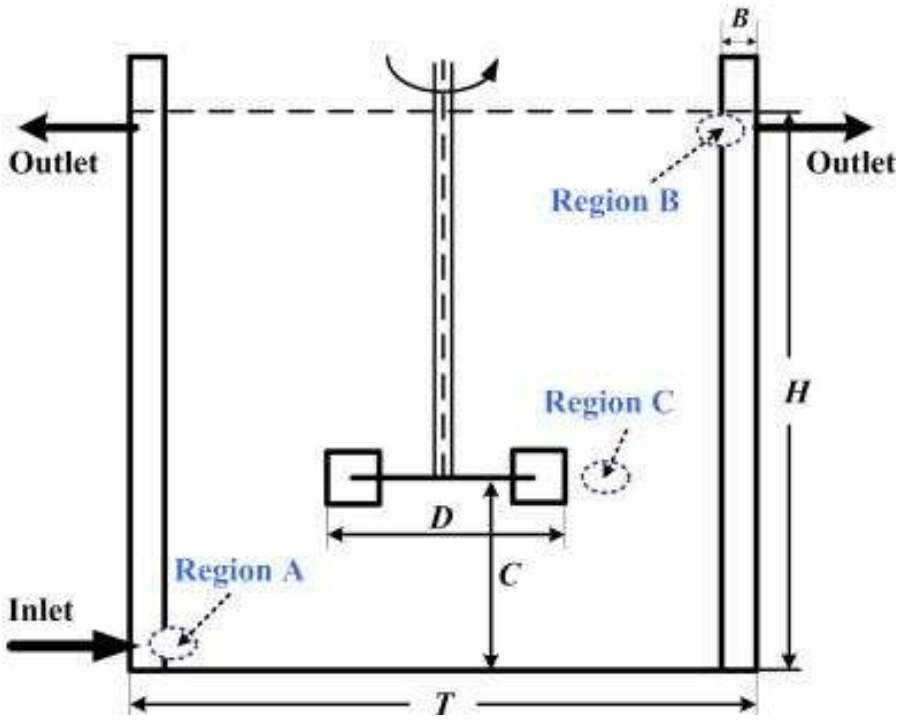

Figure 2.10: Geometry of a stirred tank crystallisation reactor from [48].

The authors in [23] considered a two-dimensional model for the growth of needle shaped crystals and specifically consider secondary nucleation. Results from the study demonstrated how the final crystal size distribution can change with varying conditions. Addi-

tionally, it can be observed that as the conditions change, the dominant mechanism for growth varies between secondary nucleation, where many small crystals can be seen, and crystal growth, where a fewer number of crystals can be seen but of a larger size.

The growth of ice crystals in large scrapped exchangers, can be considered as crystal growth from a melt, and has also been modelled in [9]. Numerous studies have also been used to capture this phenomena in the food industry, relating to the mass production of sorbet. Whilst an unusual application, the ice crystals within the product have to fall within a specific size range. In addition to the population balance equations, these studies solved for both nucleation and growth kinetics. Like the other studies, the crystals were assumed to have no impact on the fluid flow.

Further studies that use population balance models coupled the crystal kinetic models to crystal growth in non-stirred reactors [86, 67, 48]. Also, the population balance has been applied to other types of growth equipment, such as the mixed jet pipe [188].

These models not only play an important role in crystal growth reactors, but are also used in other applications such as the growth of biological agents in stirred tank reactors [123, 63]. The main disadvantage with these models is that they very rarely have an impact back on the flow, and the crystals are generally considered freely suspended within a fluid. Whilst these crystal populations are advected by the fluid, they are not considered as particles and therefore, no deposition behaviour is observed.

2.4.2.2 Growth of Large Singular Crystals

In addition to large scale reactors in which populations of crystals are grown, a large portion of crystal growth technology relates to the growth of large single crystals, such as synthetically manufactured sapphire crystals which are used in various different applications, such as the manufacture of shatter or scratch resistant glass, electronics and optics. Another crystal of interest is KDP, which has multiple uses in the optics industry. Crystals for these applications generally have to be grown to specific size and shapes and therefore modelling these processes are often challenging as temperature, solution concentration and fluid flow all have a major impact, and the growth conditions at each crystalline face can vary dramatically. Due to the size of the crystal, these flow variables

can change significantly through time as the crystal grows in size and shape.

The authors in [160] modelled the growth of a large single crystal of KDP in an 800 litre tank. The authors solved the NVS equations to describe the motion of the fluid. Due to the high Reynolds numbers experienced in the tank, the authors applied the $k-\epsilon$ turbulence model [96] to capture any turbulent phenomena close to the crystal. Additionally, surface stresses generated by the fluid flow were also measured on the crystal face, as these are known to influence to quality of the grown crystal on a microscopic scale. For the short time interval that this assessment was carried out, it was assumed that relatively little crystal growth occurred and the crystal was considered as a stationary object, with no slip boundary conditions at the face. The same authors then advanced the model in [159] where in addition to the NVS, species transport equations were solved in order to determine the concentration distribution close to the crystal, and how varying the flow parameters alters this distribution. Additional physics was included into the model such that the rheological properties of the fluid, e.g. density and viscosity, were dependent on the local concentration. Observing the concentrations is particularly important as it has been shown to vary greatly depending on the face, if the crystal is to be grown to specific shape then these concentrations need to be closely controlled.

The authors in [119] also carry out CFD calculations in order to describe the conditions inside a tank for KDP crystal growth. Again, for the timeframe under investigation the crystal is assumed to be stationary. In the study the authors make extensive use of the reaction-diffusion model (as described in Section 2.2.3) in order to correlate experimental data. k_d is then estimated using mass transfer correlations, i.e. the Sherwood number [24]. Using non linear optimisation techniques, the value of k_r and the order of reaction is obtained. These values are then applied to the CFD model in the form of the crystal kinetic reaction term in (2.7). Applying the reaction term as a boundary condition then allows the authors to model the concentration boundary layer close to the crystal. The authors in [186, 185] also use the reaction terms determined in this study to assess the conditions in other equipment for the growth of KDP crystals. Particular attention to how the concentration field changes with varying stirrer speeds was given in [185] .

As mentioned, similar techniques are often used for models which optimise artificial sap-

phire crystals. One such study was conducted in [46] where authors model the development of crystals from a melt. Instead of solving for the solution concentration, the energy equation is solved. Again, these authors assume that, over the time frame that the system is being assessed, no motion occurs of the crystal frame, so these techniques are purely to assess the temperature and flow close to the crystal face.

2.4.2.3 Summary

Crystal growth in industry usually relates to either the growth of multiple crystals in large tanks, or the growth of large singular crystals. The brief review in this section has covered the two main methods used when attempting to model these widely different scenarios. As discussed, the population balance model allows the capture of varying crystal sizes in a non-homogeneous reactor, moreover, the model can consider: the birth of crystals (due to either primary or secondary nucleation), the breakage of crystals (under certain flow conditions) and the aggregation of multiple crystals. The models, however, are not without limitations, the population balance does not model each individual crystal but rather an average crystal size in compartmentalised regions across the computational grid. Furthermore, this model has been shown only where a single fluid phase is considered. Also, the model has limitations for two way coupling with the fluid flow, meaning that whilst the flow impacts directly on the crystal size distribution, it is considered to have relatively little impact on the flow. There has been mention in previous studies that the solution density can relate to the CSD and crystal density, however there has been no application where crystals can deposit and act as solid boundaries or particles within the flow.

The modelling techniques presented for the growth of single crystals allow the investigation into how parameters such as flow speed, temperature and concentration may affect the growth of crystals. The models show how crystal kinetic models maybe applied to CFD through the use of the solute transport equation and boundary conditions on the crystal face. In these models diffusion is usually modelled explicitly through the transport equations, therefore only the surface integration step in the reaction-diffusion equations discussed in Section 2.2.3 is applied. Additionally, the studies identified only consider crystal growth from single fluid phase. A thorough summary of research carried out over the past decade on the growth of large singular crystals can be found in [60, 195].

2.4.3 Crystallisation and Precipitation Fouling in Industrial Equipment and Infrastructure

A significant portion of this research relates to capturing fouling phenomena within industrial equipment [152, 98]. In these situations mass transfer occurs and deposits are formed in pipes or on equipment walls. These deposits can affect both the local fluid properties, such as the pressure and velocity, and the heat transfer to and from the equipment walls, as shown by [126] when investigating deposition in pipe flows.

A single fluid phase CFD model with heat transfer effects was developed in [98]. The model was used to capture rates of deposition across a heated plate when considering the pasteurisation of diary products. However, as it was assumed that over the time of interest the deposition would have no impact on the fluid flow, only the instantaneous rates of mass transfer were calculated. As such there was no physical depiction of the deposited mass considered.

A single continuum fluid phase moving boundary model with discrete particles transported in the bulk of the fluid was developed [122]. Particles settle and deposit on a surface, the boundary then moves such that the displacement accounts for the the volume of mass deposited. This technique ensured that deposited mass would change the fluid flow. Here, this model was developed for the purpose of describing ash deposition, however it would be applicable in flows where crystal growth from homogeneous nucleation in the bulk of the fluid was a dominant physics.

A model was developed in [32] for computationally simulating the deposition of an inverse soluble salt on heat transfer surfaces, such that crystals deposit when the solution is heated, as shown in Figure 2.11. This approach uses a modified reaction-diffusion which accounts for both crystal deposition on the walls and the removal of crystal mass due to shear stresses from the flow. The removal term in this model is dependent on the local geometry (deposition height), fluid velocity, temperature stresses and an empirical parameter relating to the crystal adhesion. A temperature dependent Arrhenius reaction term for k_r is given and a velocity dependent relationship for k_d is obtained from a mass

transfer correlation using a previously calculated Sherwood number. It is unknown why the authors do not model diffusion through solution of the transport equations. This model does not account for the change in flow due to build ups of solid by changing the computational geometry, but rather makes a crude adjustment to the inlet velocity (i.e. as the fluid volume in the domain decreases the velocity increases relative to this due to conservation of mass). It is thought that this method may be sufficient for a uniform surface / deposition pattern, however localised changes in geometry may not be accounted for. The results for the mass deposition are displayed in terms of an overall fouling resistance, which is the average deposited mass height divided by the thermal conductivity, this term can be thought of as the increase of resistance to the flow of heat (mK/W). The fouling resistance is also the reciprocal of the heat transfer coefficient, which can be obtained experimentally from measurement of the heat fluxes and temperatures. As the fouling layer is not passed to the computational domain, the heat flux into the fluid is calculated using a simple model based on the average height of the fouling layer where in this case fluid is being heated. The study uses a non-homogeneous density profile for the solid, such that the density of the fouling layer is dependent on both the deposition height and the local position in the film.

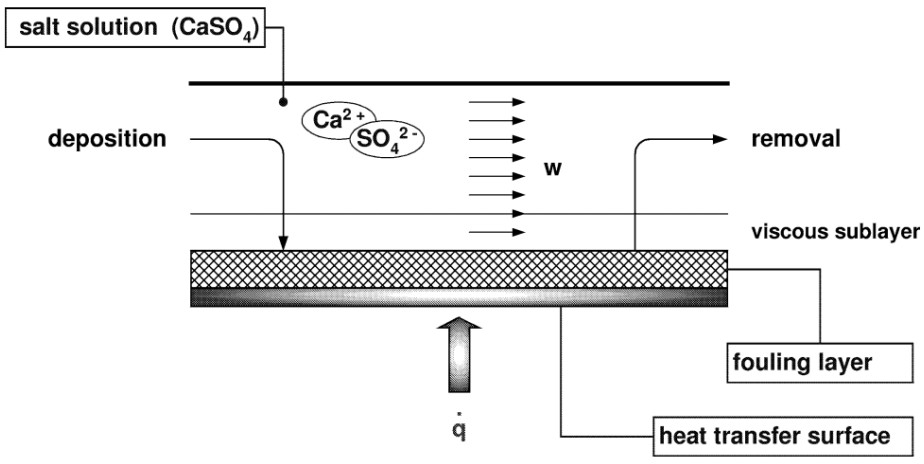

Figure 2.11: Diagrammatical representation of the fouling process, [32].

The authors of [148] applied the same numerical model over a variety of different shaped heat transfer surfaces, which are later validated with experimental data. The concept being that structured heat transfer surfaces will reduce fouling in certain areas, and therefore

improve the level of heat transfer. Initial results from the paper observe that that changing the surface shape does have significant effects on the level of fouling.

Whilst the aforementioned studies focus on the computational simulation of crystallisation fouling phenomena, the majority of other related studies appear to be experimental. The reaction-diffusion model was used in [14] to correlate different deposit removal terms to experimental data and hence calculate the empirical constants within the models. However, the parameters were not used in any further modelling simulation.

A study was carried out in [31] on the deposition of $CaCO_3$, also an inverse soluble salt, on a heat transfer surface. The study calculates fouling resistances experimentally. The main purpose of this study was to use the obtained data to estimate parameters for the value of k_r (in (2.7)) for $CaCO_3$. However, diffusion and removal terms were ignored when considering experimental results. This paper was purely for parametric estimation, and no computational experiments were carried out.

It was observed in [125] how varying heat exchanger designs also impact on the rate of fouling, specifically in micro heat exchangers. The study focuses on experimental results and uses a bulk heat balance (heat in / heat out) to calculate the reduction in the rate of heat transferred to the solution due to fouling. The larger the rate of fouling, the slower the rate of heat transfer. This study calculates an overall value for the fouling resistance across the whole heat exchanger surface, but neglects information regarding localised deposition values. It was found that increasing the number of channels in a micro exchanger reduces the level of fouling.

Fouling during the milk pasteurisation process was observed in [29], particularly the effects of when pulsed flow conditions are used. Again, the study was purely experimental, however it was shown that pulsating the flow leads to improved removal of the solute. A similar study was carried out by [68] when considering $CaSO_4$. These studies also concluded that using pulsed flow conditions can reduce the overall amount of fouling. Again these studies were experimental and only measured the overall fouling resistance. Therefore no localised information regarding the deposition positions was given.

The authors in [54] develop a two-dimensional moving boundary model to describe the fouling of crude oil on a shell and tube heat exchanger. For the purposes here, this can be considered as flow through a pipe where the fouling occurs only on one side (the heated side). The authors state that the majority of models relating to fouling do not take into account the local variation in fouling height, and consider a constant heat transfer coefficient across the heat transfer surface and fluid, therefore they can be inaccurate when considering large heat exchangers. In order to rectify this, authors present a moving boundary model such that a sharp interface separates the fouling layer from the fluid flow. Simplified fluid models are used, such that the velocity is assumed constant in the direction perpendicular to the transfer surface, and is calculated by the mass flow rate and available cross sectional area. Heat transfer is solved throughout the system by solving the energy equation, where differing heat transfer coefficients are considered in the heat transfer surface, fouling layer and fluid. The heat transfer equations are solved using the commercial modelling package, gPROMS, which harnesses the FVM.

Clearly much research has been carried out in the area of fouling, particularly on heat transfer surfaces. The majority of authors employ a bulk calculation such that they can calculate the overall heat transfer coefficient or pressure drop due to fouling. They do not however take into account the local fouling and flow conditions. Some authors have tried to consider the problem further by developing models which can predict the local deposition of the fouling phenomena. Despite this, flow conditions are approximated and therefore the effects on the fluid due to the small-scale variations in fouling structure may not be captured. Much like the previously discussed crystal growth models in Section 2.4.2.2, studies regarding fouling generally only consider a single fluid phase.

2.4.4 Models for Describing Geological Formations

The observations in the experimental work carried out by the NNL have suggested that the crystalline formations were found to have similarities to geological formations, particularly stalagmite formations, which can be observed in Figure 2.12 and 2.13 [162, 15, 168, 169, 104, 105]. Many formations and structures found within nature are often the result of mass being deposited from a liquid, these processes usually occur over long periods of time, and often lead to large formations. Therefore, models have to account for the unusually large length and time scales, and thus alternative modelling approaches to

those previously discussed for crystal growth have to be considered. Whilst the length and time scales considered in the problem here are smaller than those in a geological setting, they are still considerably larger than those observed in the majority of crystallisation problems. Due to this, studies regarding the deposition of solid matter or phase change in nature are reviewed in this section. It should be noted that as the fiscal impact of crystallisation modelling is much greater when considering models for the purpose of minimisation of fouling or the optimisation of industrial crystal growth, there is considerably more research relating to these topics than those regarding geological phenomena.

The authors in [82] study the behaviour of a 2D channel flow, as calcite from the solution is deposited on the channel bottom. This work was carried out in order to further understand the deposition behaviour in rivers and streams. The authors solve the NVS equations using NaSt2D code [137] in order to obtain the flow within a 2D channel. The solution is then coupled to a growth kinetic model which is determined by the local supersaturation. In these systems the level of supersaturation is not only dependent on the temperature of the solution, but also the level of carbon dioxide present. Multiple solute transport equations are solved in order to calculate the level of supersaturation based on the local CO_2 levels. The study also demonstrates how obstructions in the flow can in fact enhance the rate of calcite growth. Much like previous crystallisation studies, the work here only assesses the instantaneous crystal growth rates through solution of the solute transport equations and does not include any mass deposition in the model.

Another area of particular focus is stalagmite growth, authors in [162] develop a coupled fluid flow, crystallisation model in order to model the growth of stalagmites through time. The model assumes that the stalagmite is axisymmetric, and that it can be described by a series of linear segments. As the rate of crystallisation is assumed slow relative to the fluid flow for a given point in time a steady solution to the fluid flow can be assumed. As this is the case, the steady state Nusselt solution (2.14) is taken over each of the linear segments in order to approximate the fluid flow over the entire formation. The reaction-diffusion equation is then coupled to the fluid flow in order to calculate the deposition rate. Following this, the boundary describing the flow is moved through time, for a discrete timestep, to describe the growth. After this, a new steady state solution to the fluid flow is calculated over the moved geometry. This process continues iteratively

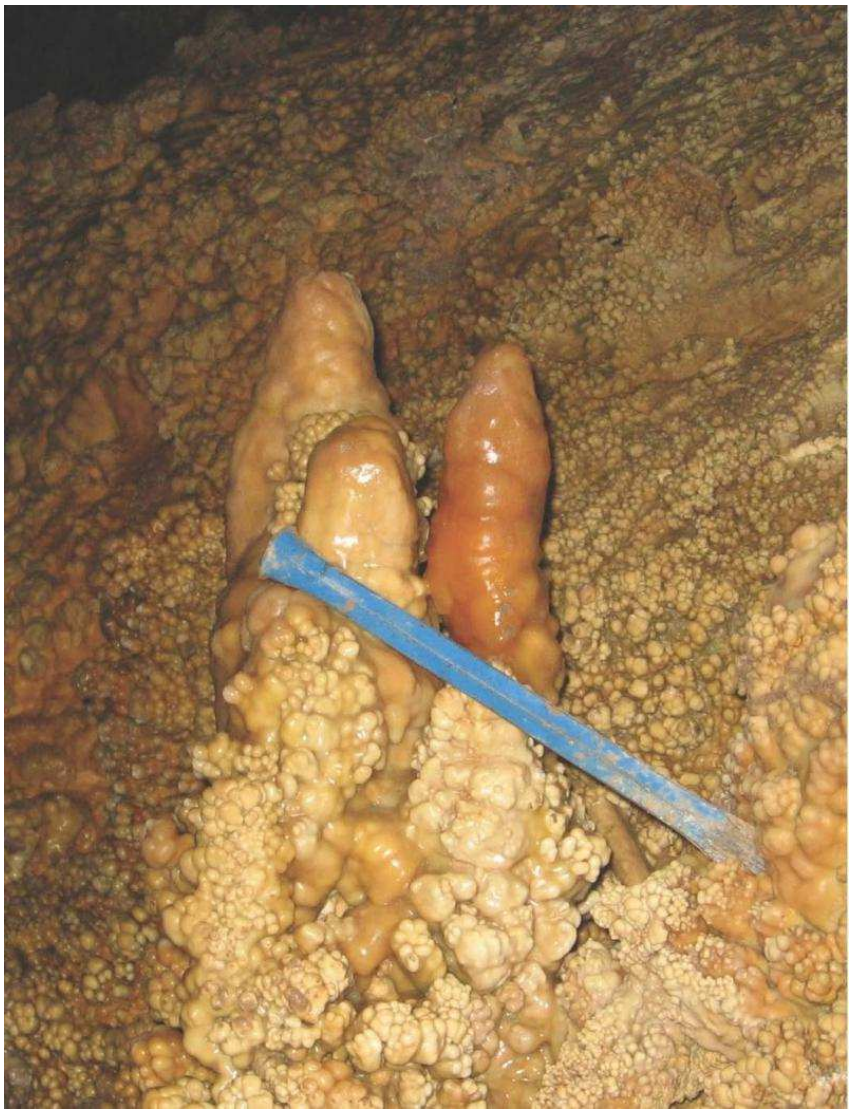

Figure 2.12: Example of stalagmite growths in underground caves at an early stage of growth. Courtesy of UMass Amherst.

through time until a desired solution time is reached. Coefficients from this study were obtained from previous experimental results [37]. Results from this model agree well with previous models and geological data, as seen in Figure 2.14. As mentioned, one of the main difficulties with geological modelling is the timescales in which the problems occur over, this pseudo-steady state approach is then particularly useful, as the solution can progress through time with relatively large timesteps (1 year). Time steps of this magnitude would be infeasible for a fully transient CFD simulation. It should be noted that other models have been developed for stalagmite growth, however these models do not

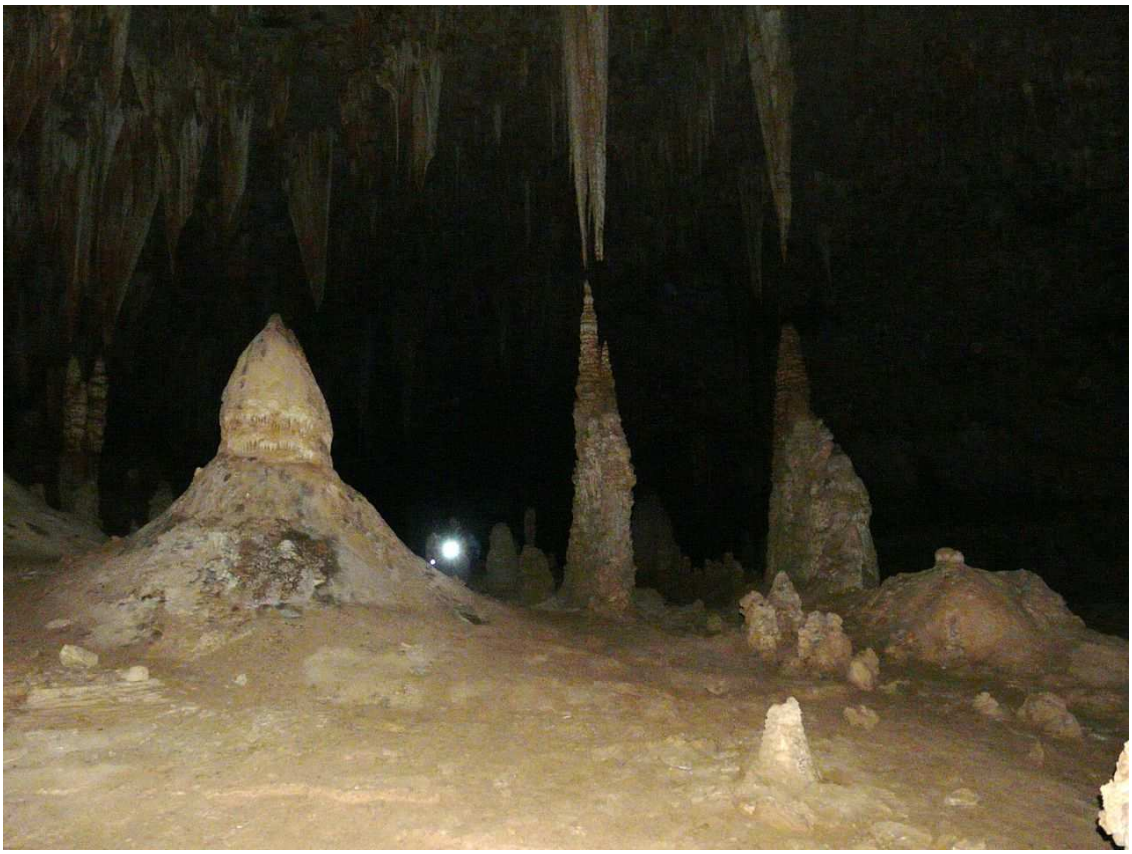

Figure 2.13: Example of developed stalagmite growths in underground caves [189].

consider the fluid flow and simply impose that the stalagmite's growth is relative to a given exponential or Gaussian function [104, 105].

A thorough review of other geological studies can be found in [127].

2.5 Summary of the Published Research

The fluid dynamics observed in the problem under consideration is relatively well-understood, and much research being carried out on droplet impact and thin film flow. However, these different phenomena occur over largely differing timescales, e.g. the behaviour of droplet impact is described over a 5ms timeframe, whilst the problem of interest occurs within periods up to 30 days. The film flows become roughly steady state after several hours. Due to the relatively slow rate of crystal growth these flows can be considered at steady state over given periods of time. Therefore, when considering the full timeframe of the

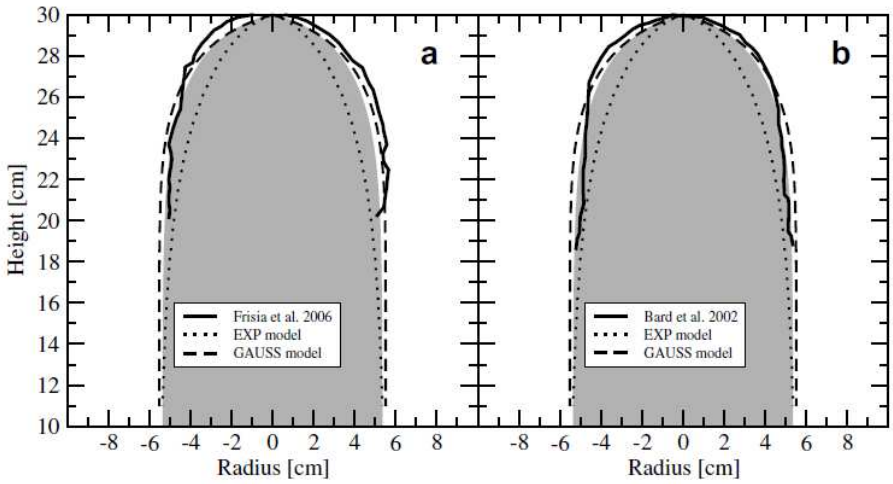

Figure 2.14: Predicted stalagmite formations from [162] when compared to geological data measured in [69] and [18]. The results from the model in [162] are given by the grey shaded area.

problem it is unlikely that a full transient CFD simulation is feasible. However, there are many semi-empirical calculations which may be of use.

When describing multiple system of crystals, such that crystals are grown in large reactors, much research has been carried out on the population balance models. However, whilst these models are useful for describing large heterogeneous populations of crystals suspended in a flow, the models do not allow the crystals to influence the flow behaviour. Moreover, no studies have been found which allow for the deposition of these crystals onto a solid surface.

Crystal growth and deposition is common in the fouling of industrial process equipment. The majority of research in this field implements bulk crystal growth models, such that the overall effects of fouling can be quantified. These models however do not predict the localised effects due to fouling or give a geometric interpretation of the fouling layer. Some research has been carried out on describing the localised deposition patterns, however these models tend to implement simple approximations to the fluid flow. As this is the case, phenomena due to the fluids interaction with the localised fouling layer micro structure can often be neglected.

Models describing the growth of crystalline deposits that occur naturally in geology have also being examined. These models are particularly attractive, as the problems encountered generally occur over large length and timescales. Due to this, methods appropriate for describing coupled fluid and crystal growth phenomena have been developed. Furthermore, models consider problems involving multiple fluid phases. From assessing studies in other areas of crystal growth research, it has been noted that this is particularly uncommon. Despite the advantages of these models, they are not without their limitations. Studies in this field have been shown to use simple approximations to describe the individual physics, e.g. fluid flow, diffusion and crystal growth. Additionally, due to the specific nature of the environment in which these geological formations are developed, physical effects such as heat transfer and evaporation are not experienced. These effects are therefore not included in the models presented in the geological studies.

Clearly, there is a large volume of research focused on crystal growth. As the problem being studied here is particularly unique, no one study has been seen to be completely appropriate for modelling the growth of industrial salt formations from impinging droplets. However, this review has highlighted several approaches and techniques which may be developed and coupled for the problem under investigation.

Chapter 3

Adaptation and Implementation of Geological Models for Industrial Crystallisation Problems

3.1 Introduction

This chapter reports the development of a moving boundary method for describing the growth of crystalline formations from impinging droplets of salt solution through time. The model uses previous techniques describing the growth of stalagmites presented in [162]. As discussed in Chapter 2, crystallisation research and modelling techniques are often concerned with growth over small lengths (relative to those considered in the NNL drip trials). In addition to this, the timescales in which these crystallisation problems are considered are often relatively short. Whilst these studies do offer insight into the possible behaviour of systems involving crystallisation, it is difficult to make a direct mapping between these studies and the problem here. Though this is the case for the majority of crystallisation studies, geological formations form over hundreds, if not thousands of years and therefore models which consider this phenomena do not suffer from the same time and length scale restrictions as the aforementioned studies. Due to the slow growth of the crystal formations relative to the fluid flow, it is assumed that a separation of time-scales can be imposed, such that over a given time-frame a steady state solution for the fluid flow can be considered. These pseudo-transient methods which are common in geological modelling [162, 169] will allow the description of formations over timescales that would

not have been possible with the more traditional crystal growth methods. In addition to this, from observing experimental results carried out by the NNL, the characteristic shape of the growths from saturated solutions is similar to that of geological stalagmites (as seen in Figure 3.1). This study will therefore evaluated these models further in order to test their appropriateness when considering the problem here.

Despite the previously mentioned similarities, there are some differences between the systems, such as the chemistry and driving force for crystallisation. In the geological model CO_2 is absorbed from the atmosphere and surrounding soil. The dissolved CO_2 changes the pH of the solution, and consequently increases the solubility of the water. This in turn allows the water to dissolve calcium carbonate, obtained from predominantly limestone within the soil, forming calcium bicarbonate, namely the forward reaction:

$$\mathrm{CaCO_{3(s)}} + \mathrm{H_2O_{(l)}} + \mathrm{CO_{2(aq)}} \Leftrightarrow \mathrm{Ca(HCO_3)_{2(aq)}}, \tag{3.1}$$

where s, l and aq represent the molecules in their solid, liquid and aqueous forms, respectively. The calcium carbonate solution then flows down into underground caves, where the CO_2 concentrations are much lower. The change in concentration causes CO_2 to leave the solution, which in turn makes the solubility decrease within the solute and crystallisation able to occur (backward reaction in (3.1)). This process is known as CO_2 degassing, and it is the driving mechanism for crystallisation in the case of stalagmite and various other speleothem formations.

When considering the problem addressed within the NNL experiments, sodium nitrate is dissolved within a solvent (water), as shown by the forward reaction:

$$\mathrm{NaNO_{3(s)}} \Leftrightarrow \mathrm{Na^{+}_{(aq)}} + \mathrm{NO^{-3}_{(aq)}}. \tag{3.2}$$

Due to a change in environmental conditions, the solution experiences a drop in temperature, and a loss of volume due to evaporation. These processes cause the solution to become supersaturated, allowing a crystallisation mechanism to occur. While these differences are present, they should not affect the models applicability when modelling salt solutions.

(a)

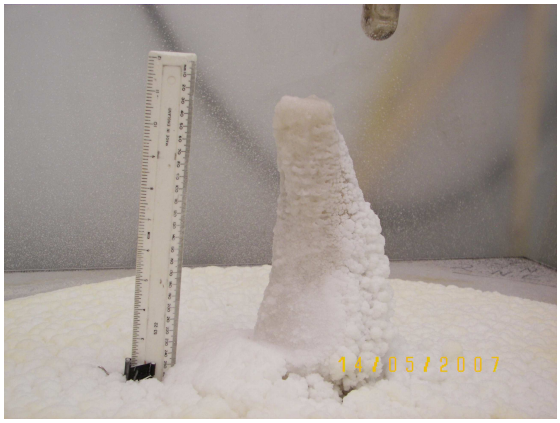

(b)

Figure 3.1: (a) The 'Witch's Finger' stalagmite in the Carlsbad Caverns, New Mexico (Courtesy of the American National Park Service) and (b) 8 Molar sodium nitrate precipitation after 32 day from the NNL drip trials.

This chapter will discuss how the different parameters affect the final formations, and in turn make assessments as to how this could potentially affect criticality in a possible nuclear reprocessing environment. Specifically, this section will focus on the second objective of the thesis, such that an appropriate method for coupling fluid flow and crystal growth is developed and evaluated fully (see Section 1.5).

3.2 Methodology

The section will outline the mathematics employed by the model, namely the formulation for the fluid flow, crystal growth and the coupling between the two. In addition to this, the computational implementation is discussed, along with a mesh independency study.

3.2.1 Governing Equations

3.2.1.1 Fluid Flow

The model here (which is similar to that described in [162]) assumes that the crystal growth formation can be described by a series of moving linear elements. The simplification to the geometry allows both the fluid flow and crystallisation to be considered over each individual element. A diagrammatical representation of an element is provided in Figure 3.2. This section describes the fluid dynamics when considering a slow, thin fluid film, flowing across an element.

Assuming that the liquid film, is a laminar, incompressible fluid and that the timescales for the fluid flow are much shorter than those of the crystal growth, we can assume that for a given interval of time, Δt, the temporal changes within the fluid flow are negligible. The liquid film can then be described by the steady state, two-dimensional, incompressible Navier-Stokes equations,

$$\frac{1}{\rho}\nabla p + (\mathbf{u}\cdot\nabla)\mathbf{u} = \nu\nabla^2\mathbf{u} + \mathbf{g}, \tag{3.3}$$

$$\nabla\cdot\mathbf{u} = 0, \tag{3.4}$$

where p is the pressure, $\mathbf{u} = (u, v)$ is the fluid velocity, ρ is the density, ν is the kinematic viscosity, $\mathbf{g}$ is the acceleration due to gravity, $\mathbf{x} = (x, y)$, and θ is the angle of the surface incline, see Figure 3.2.

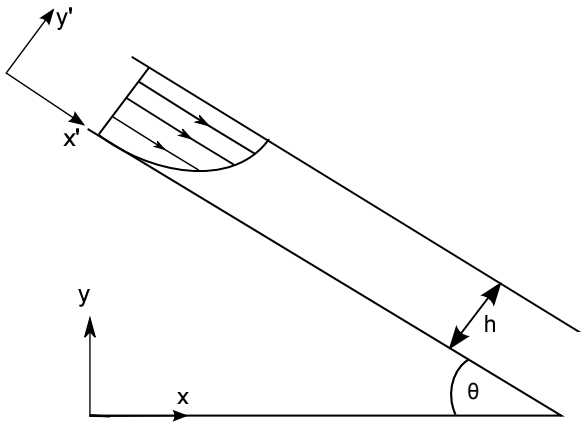

Figure 3.2: Flow down an inclined plane.

If the flow is sufficiently thin or sufficiently slow (dimensional analysis gives the requirement that the Reynolds number $Re = \frac{U_0 h}{\nu} << \frac{L^2}{h^2}$, where U_0 is the characteristic speed, L and h are the length in the stream-wise direction and the film thickness, respectively [173]) the inertia term, $(\mathbf{u} \cdot \nabla)\mathbf{u}$, can be neglected and then (3.3) can be simplified to,

$$\nabla p = \mu \nabla^2 \mathbf{u} + \rho \mathbf{g}, \tag{3.5}$$

where $\mu = \rho\nu$ is the dynamic viscosity.

For mathematical simplicity in this derivation we now redefine the coordinate system such that x' is the distance down the plane and y' is the height above the plane. The velocity vector is redefined such that u' is the streamwise velocity down the plane and v' is the velocity perpendicular to the plane. As the flow can be considered unidirectional as fluid only flows parallel to the plate, the x' and y' components of (3.5), can be simplified to,

$$\frac{\partial p}{\partial x'} = \mu \frac{\partial^2 u'}{\partial y'^2} + \rho g \sin\theta, \quad \frac{\partial p}{\partial y'} = -\rho g \cos\theta, \tag{3.6}$$

From the y'-component of ∇p in (3.6), imposing the constraint that the pressure is con-

stant along the free-surface, $p = p_{atm}$, it can be seen that,

$$p(y') = p_{atm} + \rho g(h - y')\cos\theta,$$

and therefore $\frac{\partial p}{\partial x'} = 0$. Imposing the no-slip boundary condition, $u' = 0$ on $y' = 0$ and no shear at the free surface, $\frac{\partial u'}{\partial x'} = 0$ on $y' = h$, an expression for the streamwise velocity is given by,

$$u(y') = \frac{\rho g \sin\theta}{\mu}\Big(hy' - \frac{1}{2}y'^2\Big). \tag{3.7}$$

Considering a plate of width B, with no cross-stream variation (direction perpendicular to the $x - y$ plane) in the flow, the mass flow rate, Q, can be written as,

$$Q = \int_0^B \int_0^h \rho u \, dy' \, dz' = \frac{\rho^2 g B h^3 \sin\theta}{3\mu}. \tag{3.8}$$

This can then be rearranged to give the Nusselt film height [24],

$$h = \sqrt[3]{\frac{3\mu \, Q}{\rho^2 g B \sin\theta}}. \tag{3.9}$$

For a given mass flow rate Q, the average velocity across a perpendicular cross-section of the flow is given by,

$$u = \frac{Q}{\rho h} = \sqrt[3]{\frac{gBQ^2 sin\theta}{3\mu\rho}}. \tag{3.10}$$

It should be noted that even though this is shown to be mathematically true from dimensional analysis, experiments have suggested that the flow can become wavy for $Re \approx 30$ [24]. In these cases the flows are inherently transient in nature and therefore this flow model may not be appropriate.

3.2.1.2 Crystal Growth

Now that a model has been given to describe the fluid flow, a model that accounts for the transportation of solute within the flow and the following crystallisation mechanism needs to be considered. The crystallisation model being used within this work is based on the reaction diffusion model, as discussed in Section 2.2. Here crystal growth is separated into two key processes, namely, diffusional transport and surface integration, a pictorial representation of which can be found within Figure 3.3. As previously discussed

in Section 2.2, this theory assumes that close to the crystal surface, there is a localised depletion of solute due to the ongoing crystallisation process that generates a mass transfer boundary layer (Region B in Figure 3.3). Immediately above the crystal interface, also known as the surface integration layer (Region C in Figure 3.3), complex molecular interactions take place such that the free ions within solution are integrated into the crystal lattice. The basic formulation for the reaction-diffusion model was given in Section 2.2

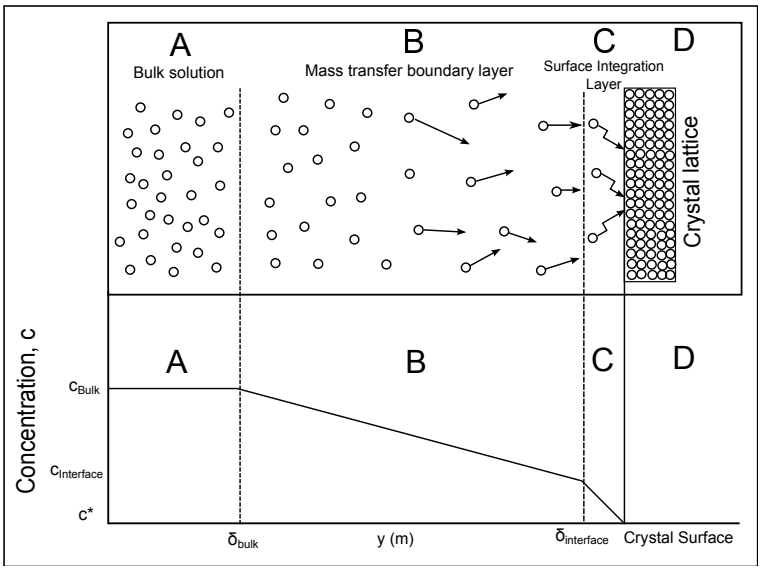

Figure 3.3: Two-step crystallisation model.

in terms of rate of mass deposition. The reaction-diffusion model will now be re-framed for use when considering a geometric growth rate, with parameters and a coordinate system appropriate to the physical problem considered in the NNL sodium nitrate drip trials.

As it is assumed that solute ions do not cluster close to the crystal surface (no local increase in concentration), the volume diffusion and surface integration step occur at equal rates. Where the growth rate, G ($\mathrm{m\,s^{-1}}$), can be described by the rate of diffusion of solute through the film,

$$G(\mathbf{x},t) = k_d \frac{M_s}{\rho_s}(c(\mathbf{x}+\delta_{bulk}\mathbf{n},t) - c(\mathbf{x}+\delta_{interface}\mathbf{n},t)). \tag{3.11}$$

Here, k_d is the coefficient of mass transfer, c is the concentration of solution [$\mathrm{mol\,m^{-3}}$], $\mathbf{x} = (x, y)$ is the position on the crystal surface. The normal to the crystal surface is given by $\mathbf{n} = \mathbf{n}(\mathbf{x})$. The normal distance between the crystal surface and the termination

of the surface integration layer is denoted by, $\delta_{interface}$. Also, δ_{bulk} is the normal distance between the crystal surface and the bulk of the fluid (see Figure 3.3). The molecular mass of the solid crystal material in question is denoted by M_s and the density is denoted by ρ_s. The growth rate can also be expressed in terms of the surface reaction step by,

$$G(\mathbf{x}, t) = k_r \frac{M_s}{\rho_s}(c(\mathbf{x} + \delta_{interface}\mathbf{n}, t) - c^*)^\eta, \tag{3.12}$$

where k_r is a coefficient of surface integration, $c^* = c^*(T)$ is the concentration at solution saturation for temperature, T, and η is the order of the reaction. The surface reaction step is not assumed to be linear, and generally takes the order $0 < \eta \leq 2$.

Whilst most literature refers to k_d and k_r as constants, this can often be incorrect. The coefficient of surface integration is generally dependent on the temperature of the solution, i.e. $k_r = k_r(T)$, and is often framed as an Arrhenius type expression [183]. The coefficient of mass transfer by diffusion is determined by both the width of the mass transfer boundary layer, δ_{bulk}, which is dependent on the solution velocity, $\mathbf{u}$ and the solute diffusivity, $D = D(T)$, i.e. $k_d = (\mathbf{u}, T)$. For a particular problem these are often considered to be constant, however they may change significantly with varying conditions.

The author currently knows of no way to mechanistically determine the individual values of k_r and k_d. Some authors have been successful in determining empirical correlations for common industrial materials [119]. Despite this, it is often difficult to use crystal growth data to inversely determine the parameters k_r and k_d. This is due to the inability to accurately measure the concentration of solute in the surface integration layer, $\delta_{interface}$. Consequently, experimental crystal growth data are generally correlated to,

$$G_e(\mathbf{x}, t) = K \frac{M_s}{\rho_s}(c(\mathbf{x} + \delta_{bulk}\mathbf{n}, t) - c^*)^\epsilon, \tag{3.13}$$

where K is the overall growth coefficient, ϵ is the overall order of growth and G_e is the observed crystal growth rate. This expression allows observed growth rates to be correlated to easily observable parameters such as the concentration in the bulk of the solution. It should be noted that only for specific values of η can an analytical expression for K in terms of k_r and k_d be derived such that $G = G_e$. For example, the growth rates of sodium nitrate and calcium carbonate are known to be linearly dependent on the

concentration gradient at the surface integration interface, $\eta = 1$ and therefore, for this linear order system it can be shown that,

$$K = \frac{k_r k_d}{k_r + k_d}, \tag{3.14}$$

and $\epsilon = 1$. In a similar way analytical expressions can be obtained for the non-linear example with $\epsilon = 2$. For more complex system, additional techniques such as regression analysis or non-linear optimisation are often required [110, 119].

As the model here employs a steady state approximation for the fluid system (assumed to remain valid over time frames of Δt), the continuous growth model described above must be discretised and coupled to the simplified fluid flow given in (3.10).

3.2.1.3 Coupled System: Fluid Fluid with Crystal Growth

The profile of the formation is approximated by a series of linear elements. Initially the surface of length L is divided into $N-1$ elements and a general linear element bounded by nodes $\mathbf{x}_i^j$ and $\mathbf{x}_{i+1}^j$, where $\mathbf{x}_i^j = \mathbf{x}(x_i^j, y_i^j, t_j)$ is considered. The initial inclined surface is discretised by,

$$\mathbf{x}_i^0 = \left(\frac{L}{N-1}(i-1)\cos\theta, L\sin\theta\left(1 - \frac{i-1}{N-1}\right), 0\right), \qquad i = 1, ..., N. \tag{3.15}$$

The time taken for a parcel of fluid to travel from $\mathbf{x}_i^j$ to $\mathbf{x}_{i+1}^j$ is denoted by τ. Due to the conservation of mass, the amount of solute precipitated into this local area during time τ must equal the amount of solute lost from the volume of solution. Therefore, for a plate of uniform width B (direction perpendicular to the (x, y) plane) the following mass balance equation is obtained,

$$B||\mathbf{x}_{i+1}^j - \mathbf{x}_i^j||F_i^j\tau = Bh_i^j||\mathbf{x}_{i+1}^j - \mathbf{x}_i^j||(c_i^j - c_{i+1}^j), \tag{3.16}$$

where $h_i^j = h(\mathbf{x}_{i+1}^j)$ (m), $c_i^j = c(\mathbf{x}_i^j)$ (mol m^{-3}) is the concentration of solute within the solution, and $F_i^j = F(c_i^j)$ (mol m^{-2}s^{-1}) is the local deposition rate. A diagrammatical representation of this can be seen in Figure 3.4.

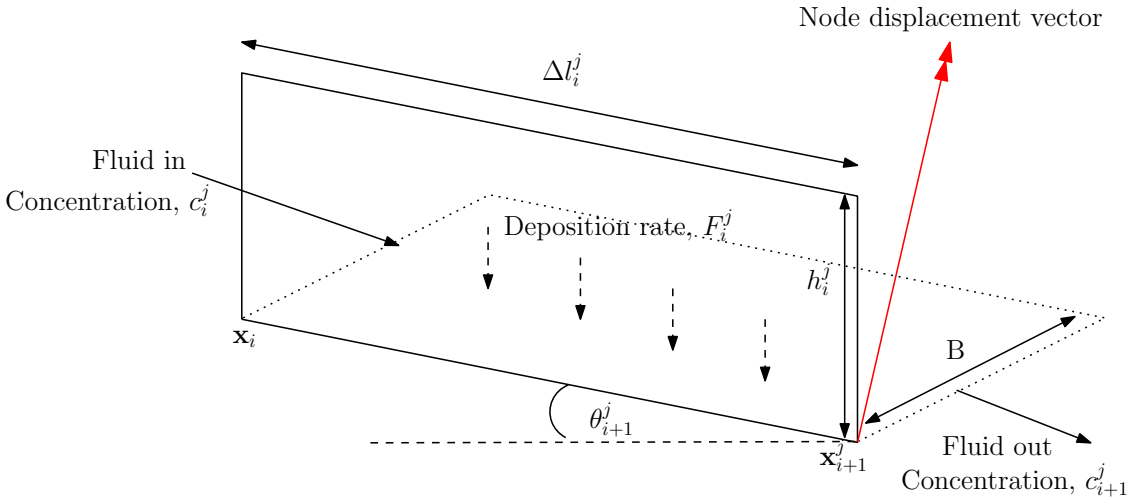

Figure 3.4: Crystal growth and mass conservation over a linear element.

Given that the deposition rate F_i^j can be written as,

$$F_i^j = G_i^j \frac{\rho_s}{M_s}, \tag{3.17}$$

where G_i^j is the growth rate at $\mathbf{x}_i^j$, if $\epsilon = 1$ and $\eta = 1$, equation (3.13) implies

$$F_i^j = K(c_i^j - c^*). \tag{3.18}$$

Then, from the mass balance equation (3.16), we can obtain the relation,

$$F_{i+1}^j = F_i^j \Big(1 - \frac{K\tau}{h_i^j}\Big). \tag{3.19}$$

However, as we want an expression which omits the local film height h_i^j, we use the fact that $\rho h_i^j v_i^j = \frac{Q}{B}$ and $v_i^j = \frac{\Delta l_i^j}{\tau}$, where v_i^j is the average velocity across the element bounded by $\mathbf{x}_i^j$ and $\mathbf{x}_{i+1}^j$, and Δl_i^j is the length of this element, to obtain the final recurrence relation,

$$F_{i+1}^j = F_i^j \Big(1 - \frac{\rho K B \Delta l_i^j}{Q}\Big), \qquad i = 1, ..., N-1 \tag{3.20}$$

and $F_1^j = K(c_1^j - c^*)$.

The nodes are then moved to describe the crystalline growth after a period of Δt by,

$$\mathbf{x}_i^{j+1} = \mathbf{x}(x_i^j + G_i^j \Delta t \cos\theta_i^j, y_i^j + G_i^j \Delta t \sin\theta_i^j, t_j + \Delta t), \qquad i = 1, ..., N, \quad j = 0, ..., M, \tag{3.21}$$

where $M\Delta t$ is the final simulated crystal growth time, G_i^j is determined at each time, t_j, by equations (3.17) and (3.20), $\theta_{i+1}^j = \tan^{-1}\left(\frac{y_i^j - y_{i+1}^j}{x_{i+1}^j - x_i^j}\right)$ and $\theta_1^j = \frac{\pi}{2}$.

3.2.2 Computational Implementation

The model described by (3.20) and (3.21) was implemented using MATLAB [124] such that the width of the surface is defined as $B_i(x_i) = 2\pi R_i$, where $R_i := R(x_i)$ denotes the local distance perpendicular to the axis of rotational symmetry. This is because the work assumes the crystalline formation forms an axisymmetric configuration in which the fluid flows down, as shown in Figure 3.5. The computational domain was discretised such that a one-dimensional grid was placed along the initial surface, with constant initial spacing Δl_i^0. In addition to this, a timestep Δt was imposed, the size of these parameters are determined in the following section.

3.2.2.1 Preliminary Mesh and Timestep Independence Study

A suitable initial mesh spacing and timestep has to be selected for the model to be robust such that it remains valid for any possible perturbation of the boundary and that the solution is not dependant on the discretisation. The presentation of the model given in [162] does not include a discussion of the mesh size, and the timestep used in this work is $\Delta t = 1$ year. Clearly this is not suitable for the work here, as the formations are generated over an approximate timeframe of 30 days. When choosing a timestep parameter, it is important that the timestep is large enough that the computational expense of the model is kept to a minimum, while being small enough that the solution remains accurate.

With these considerations in mind, the first set of numerical experiments assessed the spatial discretisation of the model. A timestep $\Delta t = 1$ minute was used, as it was assumed that, whilst this is computationally demanding, this parameter is small enough that the temporal discretisation will not influence the solution obtained, therefore allowing an independent assessment of the spatial resolution.

It can be observed that the deposition rate at the apex, F_0 is dependent on K, c and c^*, therefore for a constant solution concentration and solution temperature, the overall height of the formation is solely determined by the crystal growth coefficient. Due to this, a value of K is selected such that a maximum height exceeds those observed in the NNL experimental data, this should ensure that the meshing is robust for any likely outcome. In addition to the parameters specified in Table 3.1, the test material used here has a crystal growth coefficient of $K = 6 \times 10^{-6}$ m s^{-1}. It is known from (3.21) that the solution is dependent on the flow rate. For the purposes of testing the robustness of the mesh, the flow rate, Q, was varied such that a range of mesh displacements could be observed. It should be noted that at this stage, the parameters selected are not related to any particular physical phenomena or specific material properties. The initial geometry is defined as a 0.5m plate at an angle of $\theta_i^0 = 8 \times 10^{-3}$rad, with rotational symmetry assumed, as shown in Figure 3.5. The discretisation parameters that were tested are $\Delta l_i^0 = 5 \times 10^{-3}$m, 5×10^{-4}m and 5×10^{-5}m ($N = 101, 1001, 10001$).

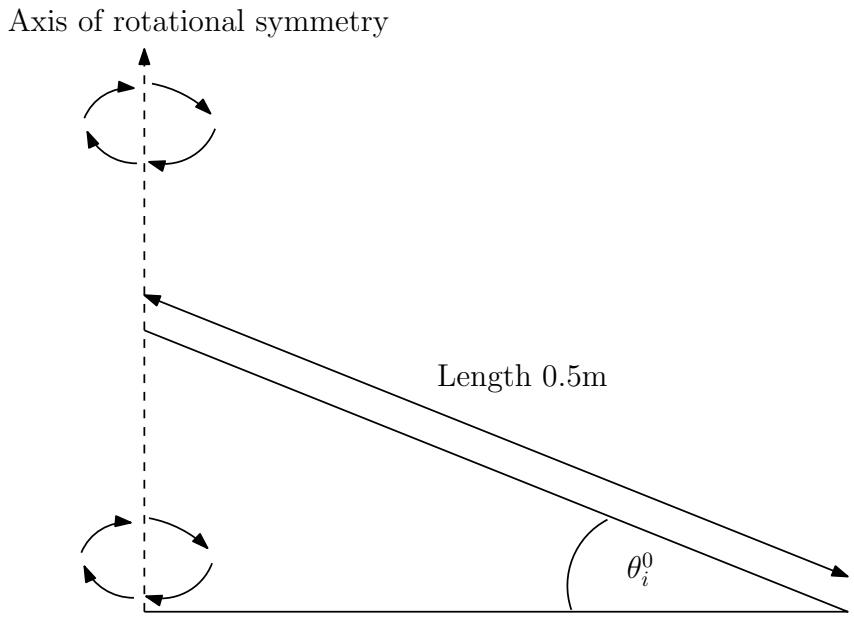

Figure 3.5: The initial geometry used in the mesh independency study for the adapted stalagmite model, with rotational symmetry about the axis.

The first computational experiment considered $Q = 1 \times 10^{-3}$kg s^{-1}, for various mesh sizes, after a simulated time of 30 days. Results are presented in Figure 3.6. From this figure it can be seen that for large deformations across the plate, all mesh sizes capture the

Crystal growth coefficient, K (m s^{-1})	6×10^{-6}
Mass flow rate, Q (kg s^{-1})	1×10^{-4} 5×10^{-4}, 1×10^{-3}
Initial node spacing, Δl_i^0 (m)	5×10^{-3}, 5×10^{-4}, 5×10^{-5}
Node Count, N	101, 1001, 10001
Initial concentration, c_1^j (mol m^{-3})	8000
Saturation concentration, c^* (mol m^{-3})	7500
Initial angle, θ_i^0 (rad)	8×10^{-3}
Solid Density, ρ_s (kg m^{-3})	2000
Solution Density, ρ (kg m^{-3})	1000
Molecular Mass, M_s (kg mol^{-1})	0.01
Timestep, Δt (s)	60
Total Timesteps, M	43200

Table 3.1: Parameters for the computational simulations for the mesh independency tests.

Node count, N	Computational time (s)
101	1.3
1001	11.1
10001	112.5

Table 3.2: Computational times for the adapted stalagmite model, for parameters in Table 3.1, when $Q = 1 \times 10^{-3}$ kg s^{-1}, for crystalline growth after 30 days.

formation, however there is a noticeable difference between the $N = 101$ and $N = 1001$ result. The difference between the $N = 1001$ and $N = 10001$ results however is negligible. The model was run on a stand-alone machine with a Intel Quad Core i7-4770k and 16gb ram, and whilst CPU intensive, it was not memory intensive. The computational times from the model are presented in Table 3.2, and it can be seen that the cost increases linearly with the discretisation size.

The mass flow rate was then decreased and Figure 3.7 shows the mesh displacement for $Q = 5 \times 10^{-4}$kg s^{-1}, for various mesh sizes, after a simulated time of 30 days. From this figure it can be seen that the width of the formation is now reduced. It is thought that as the width of the formation reduces, less nodal points are available in order to describe the growth, and therefore these formations are more difficult to capture. It can be seen that the result that for $N = 101$ is significantly different to the results for $N = 1001$ and $N = 10001$, while the results for $N = 1001$ and $N = 10001$ are relatively similar.

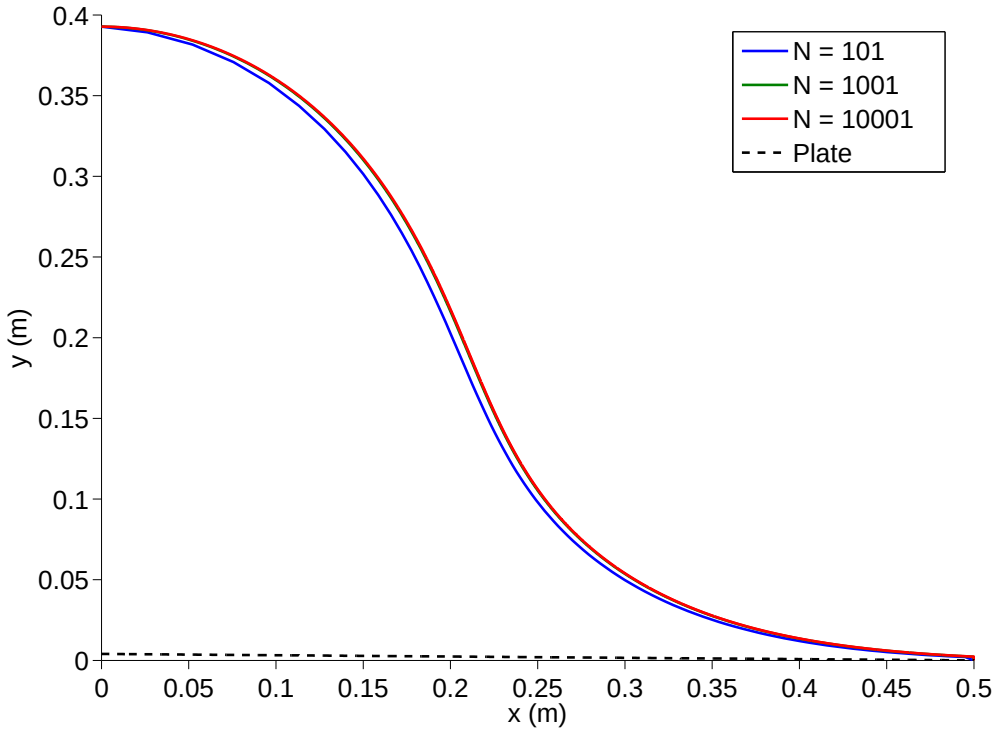

Figure 3.6: Plot of the growth when using the adapted stalagmite model, for parameters in Table 3.1, when $Q = 1 \times 10^{-3}$ kg s^{-1}, for crystalline growth after 30 days.

The discrepancies between the $N = 101$ and $N = 10001$ results appear to be larger than in the previous case. In addition to this, for the case of $N = 101$, the profile no longer appears to transition in a smooth fashion, suggesting that the number of nodal points in this region is too low.

To test this hypothesis further, a smaller mass flow rate was trialled. Figure 3.8 shows the mesh displacement for $Q = 1 \times 10^{-4}$ kg s^{-1}, for various mesh sizes, after a simulated time of 30 days. From observing the results in this figure, it can be clearly seen that the model now fails for the cases of $N = 101$ and $N = 1001$, with the formation appearing to spike rapidly up to the x-axis. The case for $N = 10001$ does not show this behaviour, however, much like the previous run for $Q = 5 \times 10^{-4}$ kg s^{-1}, the result near the apex is no longer smooth.

The work in [162] generally focused on results when implementing the model, rather than

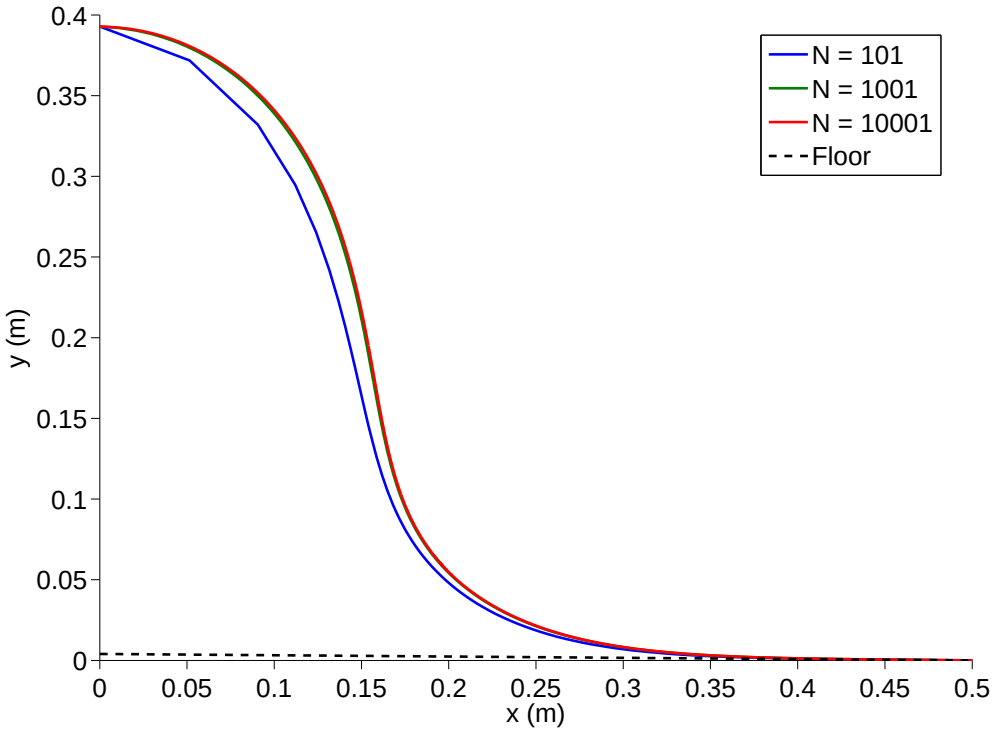

Figure 3.7: Plot of the growth when using the adapted stalagmite model, for parameters in Table 3.1, when $Q = 5 \times 10^{-4}$ kg s^{-1}, for crystalline growth after 30 days.

discussing the discretisation and computational implementation of the model. Therefore it is not known if the authors also experienced similar problems. Having identified these issues a thorough investigation into the models behaviour in these particular cases was undertaken.

The preliminary investigation regarding mesh independency for the spatial discretisation, highlighted some key issues. This study imposed a timestep such that it could be reasonably assumed that the solution was not influenced by the temporal discretisation. Before further studies were investigated further, the effects of the temporal discretisation were considered, such that the validity of this initial assumption could be evaluated.

In order to test the temporal discretisation, the timestep Δt will be gradually increased. The formations produced when using these parameters will be directly compared to the previous case for $Q = 1 \times 10^{-3}$ kg s^{-1} and $N = 10001$, as results for this parameter set

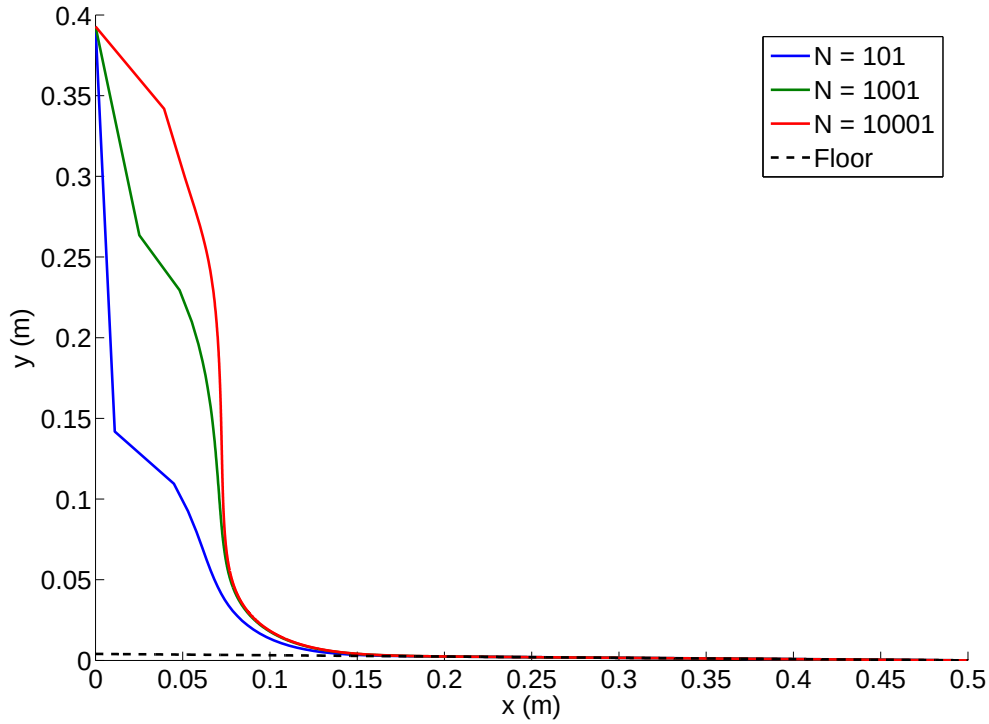

Figure 3.8: Plot of the growth when using the adapted stalagmite model, for parameters in Table 3.1, when $Q = 1 \times 10^{-4}$ kg s^{-1}, for crystalline growth after 30 days.

are assumed to be accurate.

From the results in Figure 3.9, it can be seen that the differences when changing the timestep, Δt, are relatively minor. The effects of varying the timestep are dominant in regions close to the apex. It should be noted that this is the case under constant model conditions, and for varying conditions a suitable timestep should be selected such that these changes are captured accurately.

3.2.2.2 Adaptive Meshing

The previous mesh independency study highlighted some key weaknesses with the current implementation of the model. Whilst the model may function under specific circumstances, as no *a priori* information regarding the growth of the formation should be known, it is essential that the model remains stable for a wide range of parameters. In order to address this problem, this section will assess the behaviour of spatial discretisa-

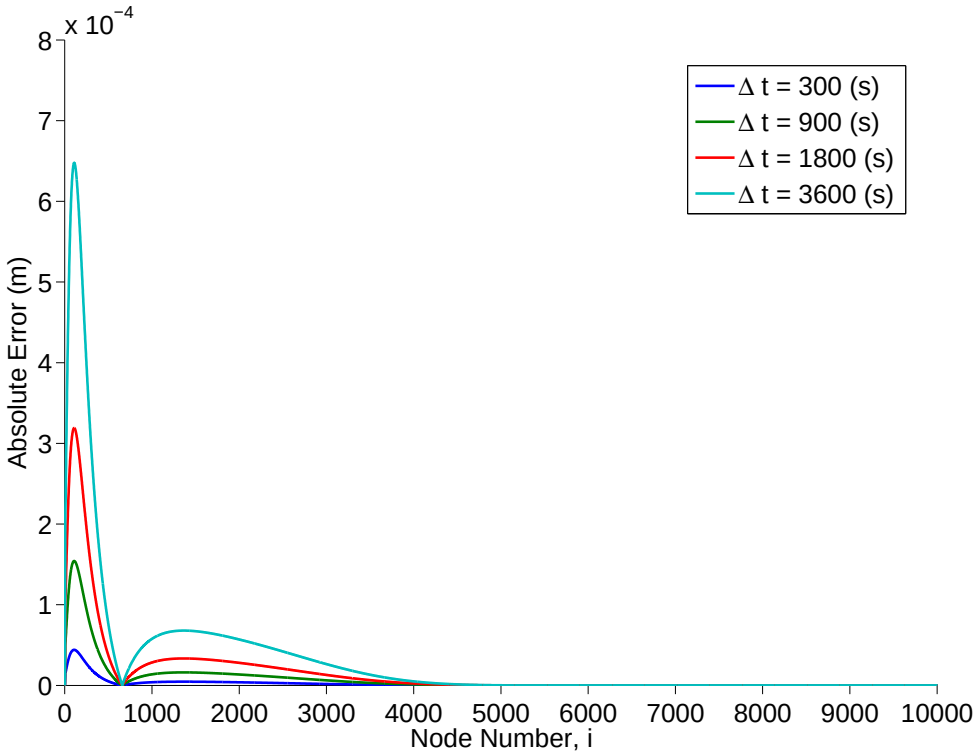

Figure 3.9: Plot of the absolute error, when comparing the formation for varying timestep Δt with the formation for $\Delta t = 1$ minute, for 30 days growth. Parameters correspond to those in Table 3.1, additionally $N = 10001$ and $Q = 1 \times 10^{-3}$ kg s^{-1}.

tion as the mesh deforms through time.

From Figure 3.8 it can be seen that when the number of nodal point is low, the model fails. With higher numbers of elements, the linear elements of the model can be clearly observed, suggesting a lack of nodal points in this region. As a preliminary assessment of this behaviour, the result for $N = 10001$ in Figure 3.8 is assessed again, however now the positions of the nodes are marked and further detail regarding the models transient behaviour is provided. These results can be seen in Figure 3.10. From this figure, it can be observed that the nodes close to the apex quickly diverge as the solution is stepped through time. In addition to this, after 60 days growth, the model exhibits the same behaviour as the previous results when using a lower quantity of nodal points. On comparing the results at 30 days and at 60 days it would appear that whilst the node at the apex continues to grow vertically, the subsequent node experiences a negative growth.

Clearly for a supersaturated solution this is not physically correct and from observing (3.20) it can be seen that if the element length, $\Delta l_i^j > \frac{Q}{\rho K B}$, F_{i+1}^j, becomes negative and the model breaks down.

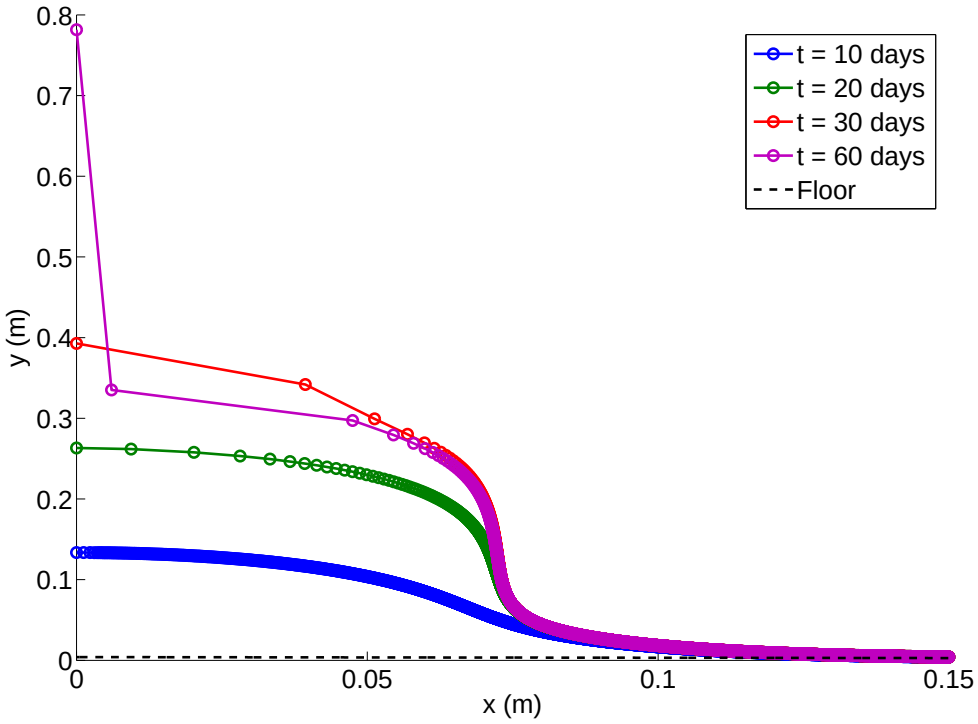

Figure 3.10: Plot of the nodal points when using the adapted stalagmite model, for parameters in Table 3.1, when $Q = 1 \times 10^{-4}$ kg s^{-1} and $N = 10001$, for crystalline growth through time.

In order to quantify this behaviour further, the element lengths for the result in Figure 3.10 after 30 days growth are shown in Figure 3.11. From this figure it can be seen that the element length increases rapidly for the first 900 nodes. A small contraction in element length is observed immediately after this, which is assumed to be at the base of the tower formation. Nearly 75% of the total element length remains unchanged, suggesting no growth occurs in these regions. This behaviour is further confirmed in Figure 3.12 where a cumulative count of the nodes relative to the model solution is provided. From this figure it can be observed that a very low portion of the initial nodes are contained within the main deformation. The node count increases super-linearly in the concave region at

the base of the growth, and afterwards increases in a linear fashion. This is less than desirable for multiple reasons. Firstly, in regions where large deformations or growth occurs, it would be advantageous to have more nodes in these regions such that these regions of interest can be captured with clarity. In addition to this, the majority of the nodes here do not undergo any deformation and therefore the additional computational cost is unnecessary.

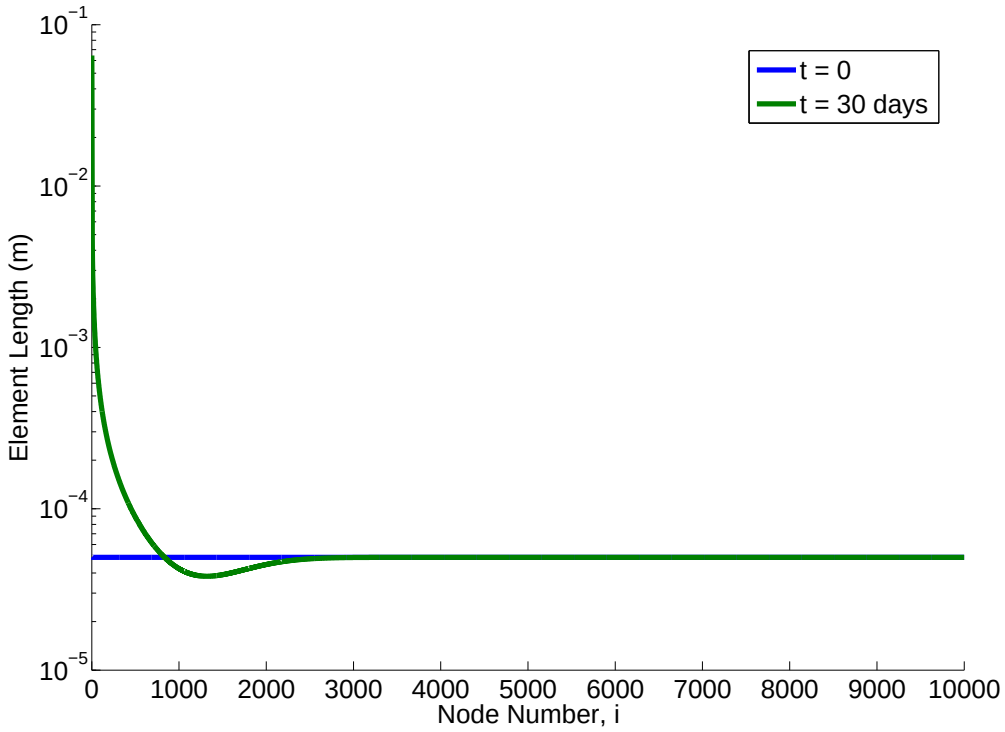

Figure 3.11: Plot of the element length when using the adapted stalagmite model, for parameters in Table 3.1, when $Q = 1 \times 10^{-4}$ kg s^{-1} and $N = 10001$, for crystalline growth of 30 days.

Given these observations it was decided to improve the previous implementation in the work of Romanov et al. [162], by developing and implementing an adaptive meshing routine. This routine imposed that after every time-step and hence displacement of the mesh, if $\Delta l_i^j > 2\Delta l_1^0$ then a new node was placed at the bisection of the element, $\frac{\mathbf{x}_i^j + \mathbf{x}_{(i+1)}^j}{2}$. This check is carried out across the mesh and the nodes are reordered appropriately. Due to this the total node count N becomes a dynamic variable, and is now specified by N^j,

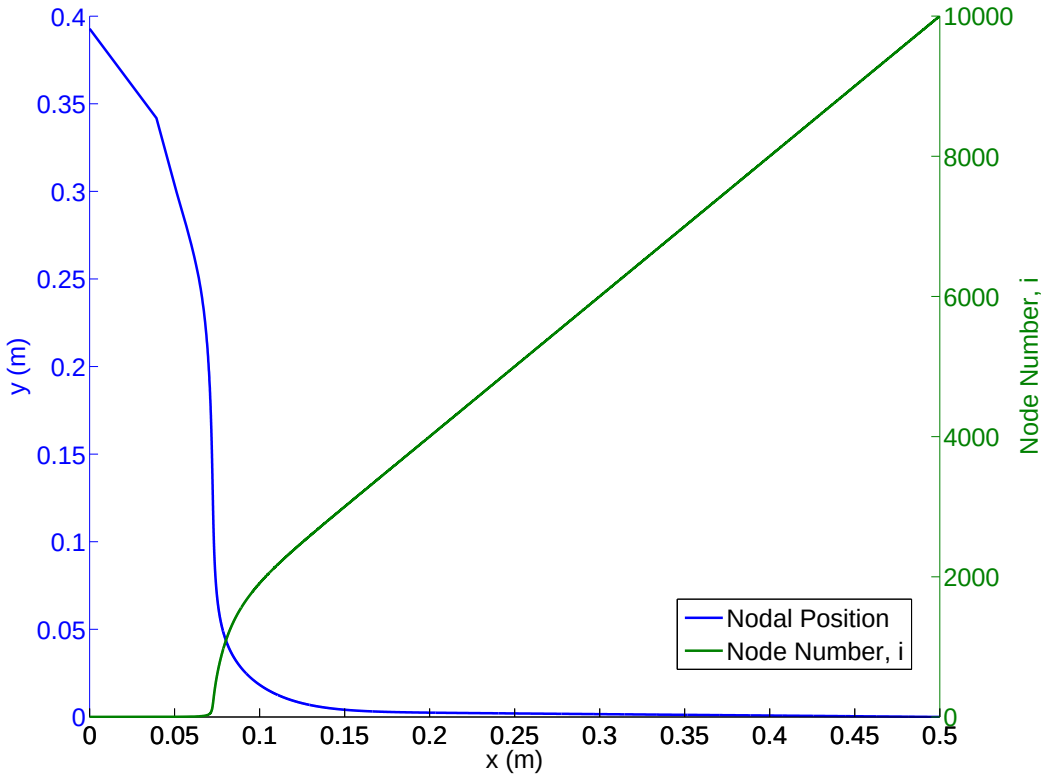

Figure 3.12: Plot of nodal distribution when using the adapted stalagmite model, for parameters in Table 3.1, when $Q = 1 \times 10^{-4}$ kg s^{-1} and $N = 10001$, for crystalline growth of 30 days.

which is the node count after the mesh has been displaced and the mesh adaptation has occurred.

Initial tests with the updated model showed that computational costs of the model almost doubled compared using the equivalent initial mesh size with no adaptation. When assessing the behaviour of the original model, it was clear that due to the node at the apex moving vertically and the following node being displaced at an angle, divergence of the nodes at this point occurred more rapidly than other nodes in the domain. This can be observed from the change in element lengths through time close to the apex, as seen in Figure 3.13. Therefore, in an effort to reduce computational cost, mesh adaption routines, excluding the initial element, are carried out after every 200 timesteps. The initial element connected to the apex is checked every time step. The full solver routine

is summarised in Figure 3.14.

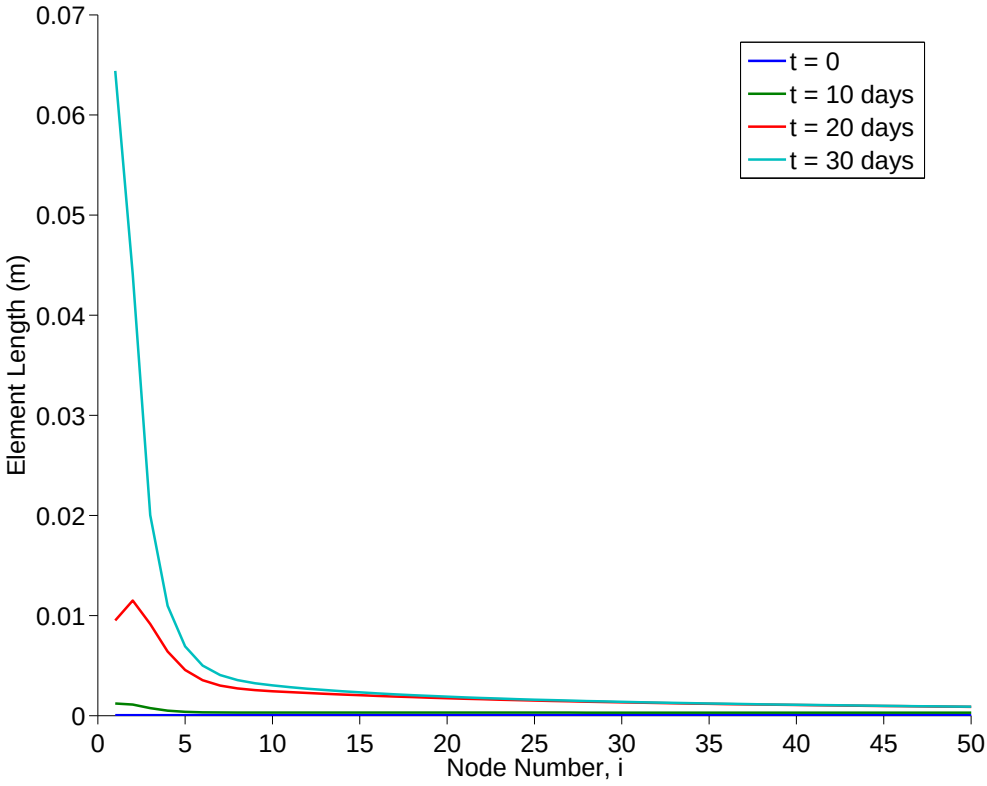

Figure 3.13: Plot of the element lengths, close to the apex of the formation, as they change through time. For $Q = 1 \times 10^{-4}$ kg s^{-1}, $N = 10001$ and parameters found in Table 3.1.

Tests with the new routine presented in Figure 3.14 were promising. An example case, corresponding to the case presented in Figure 3.8, using the parameters from Table 3.1 where $Q = 1 \times 10^{-4}$ kg s^{-1} and $N = 100$, is shown in Figure 3.15. Observing this figure, it can be seen that even though the same parameters were used, the inclusion of the mesh adaption routine alleviates the previous problems experienced. In addition to this the mesh size was reduced to $N^0 = 101$, therefore the reduction in computational time was highly significant.

To check that the mesh adaption was working correctly, the aforementioned case was run again, but this time using a mesh size of $N^0 = 10001$. Whilst this has been shown to be

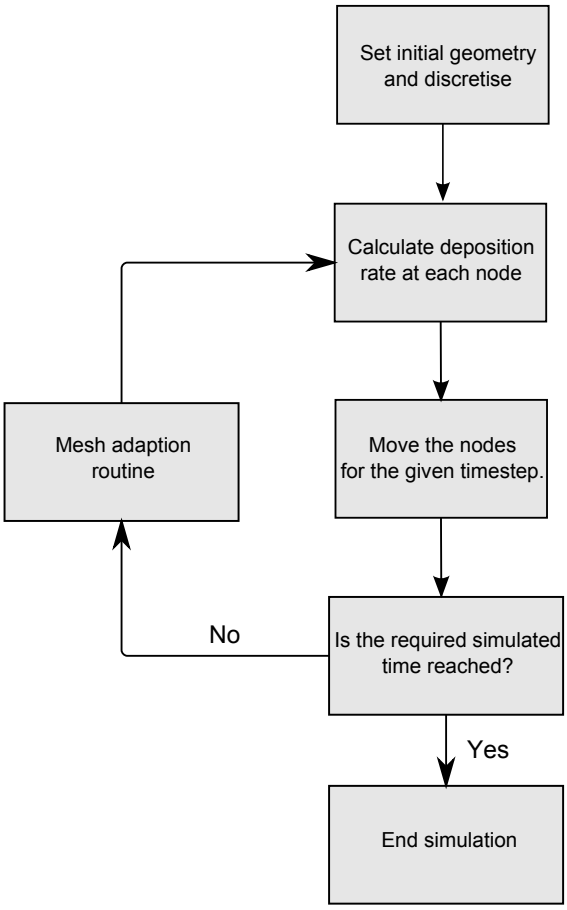

Figure 3.14: Flow chart for the solver procedure when considering the mesh adaption routine.

computationally unnecessary, this parameter was selected to be identical to the case presented in Figure 3.12 and therefore, a direct comparison could be made. The cumulative distribution of the nodal points is shown against the formation in Figure 3.16, such that the distribution of the nodes can be described.

Comparing Figure 3.16 with Figure 3.12, it can be seen that a larger number of nodes are contained within the regions of high deformation when using the mesh adaption routine. In addition to this, the element lengths were also calculated and can be seen in Figure 3.17. On comparing Figure 3.17 and Figure 3.11, it is clear that the adaption routine is functioning correctly. In the cases without adaption, the element size increased rapidly as you approached the apex. Clearly this behaviour is eliminated in the model that uses mesh adaption, with all element lengths remaining of a similar order of magnitude.

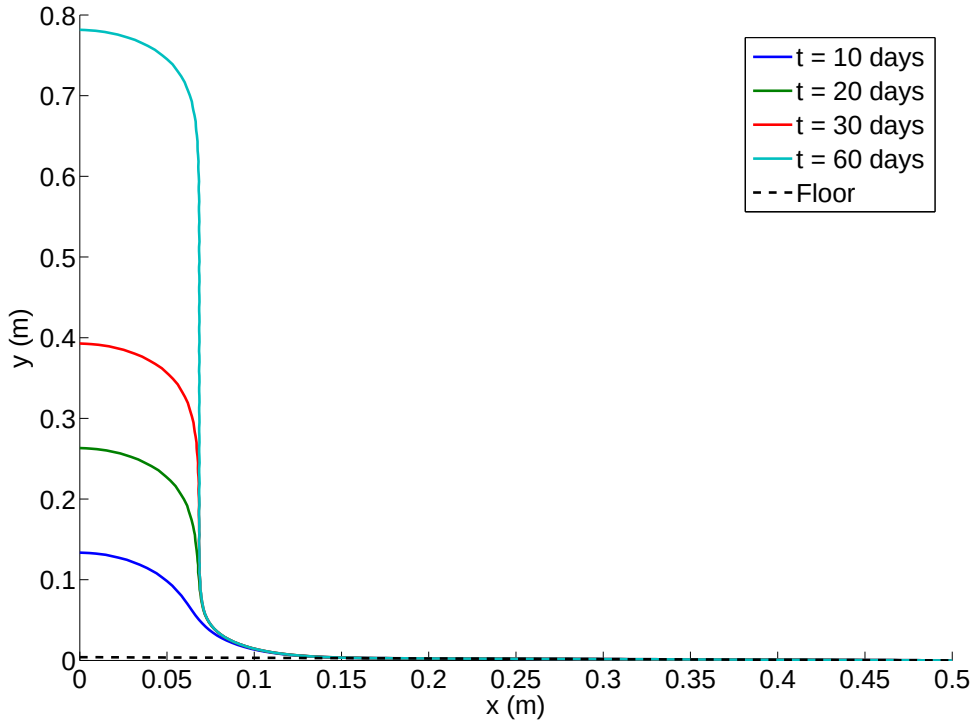

Figure 3.15: An example case for the adapted stalagmite model when using the adaptive meshing routine. For $Q = 1 \times 10^{-4}$ kg s^{-1}, $N = 101$ and parameters found in Table 3.1.

3.2.2.3 Mesh Independence with Adaptive Mesh Subroutines

Having established that the mesh adaption routine was functioning correctly, a new mesh independency study was carried out. The study used parameters presented in Table 3.3 and simulated the solution after 30 days. Results from this mesh independency test are presented in Figure 3.18. From this figure it can be seen that none of the results when using various mesh sizes suffered from the previous complications, which resulted in a low number of nodal points close to the apex. Whilst functioning, the case for $N = 101$ differs from the rest of the results. In previous computational experiments it was found that the majority of issues, due to a low node count, were found close to the apex, therefore Figure 3.19 shows a close up of the results in this region. In addition to this, the values for N^0 and N^{43200} can be found in Table 3.4. From Figure 3.19, the previous conclusion that $N^0 = 101$ differs significantly from the other mesh sizes is confirmed. In addition to this, there appears to be convergence of the solution, as N^0 is increased. This can be concluded, as there is no significant change in the solution when increasing the mesh

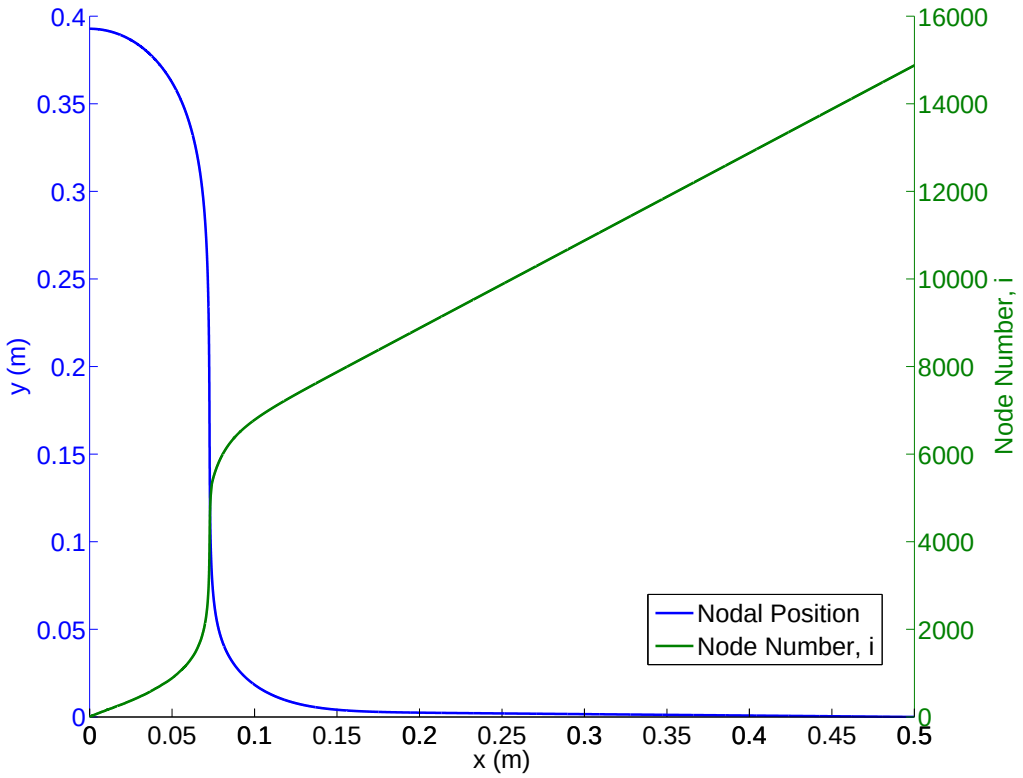

Figure 3.16: Plot of nodal distribution when using the adapted stalagmite model, for parameters in Table 3.1, when $Q = 1 \times 10^{-4}$ kg s^{-1} and $N^0 = 10001$, for crystalline growth of 30 days, with mesh adaption.

size from $N^0 = 1001$ to $N^0 = 10001$. Due to this, an initial mesh size of $N^0 = 1001$ was employed for all subsequent calculations. Additionally, a timestep of $\Delta t = 60$s was used.

Summarising, the adaptive meshing presented here solves the previously encountered difficulties with the model. The model is now robust and can describe a variety of formations with varying degrees of mesh deformation, with no *a priori* knowledge of the final formation shape. Additionally, the adaptive meshing routine allows the optimisation of nodal placement such that smaller mesh sizes can be used. This greatly reduces the computational costs of the model. The computational time for these numerical experiments can be found in Table 3.5.

Crystal growth coefficient, K (m s^{-1})	6×10^{-6}
Mass flow rate, Q (kg s^{-1})	1×10^{-4}
Initial node spacing, Δl_i^0 (m)	5×10^{-3}, 1×10^{-3}, 5×10^{-4}, 5×10^{-5}
Initial Node Count, N^0	101, 501, 1001, 10001
Initial concentration, c_1^j (mol m^{-3})	8000 (8 Molar)
Saturation concentration, c^* (mol m^{-3})	7500 (7.5 Molar)
Initial angle, θ_i^0 (rad)	8×10^{-3}
Solid Density, ρ_s (kg m^{-3})	2000
Solution Density, ρ (kg m^{-3})	1000
Molecular Mass, M_s (kg mol^{-1})	0.01
Timestep, Δt (s)	60
Total Timesteps, M	43200

Table 3.3: Parameters for the computational simulations for the mesh independency tests, when using adaptive meshing routines.

Initial Node count, N^0	Final Node Count N^{43200}	Percentage increase (%)
101	152	50.5
501	746	48.9
1001	1496	49.5
10001	14876	48.7

Table 3.4: Initial and final mesh sizes for the computational results presented in Figure 3.18.

Initial Node count, N^0	Computational time (s)
101	3.3
501	10.8
1001	23.0
10001	213.0

Table 3.5: Computational time for results presented in Figure 3.18

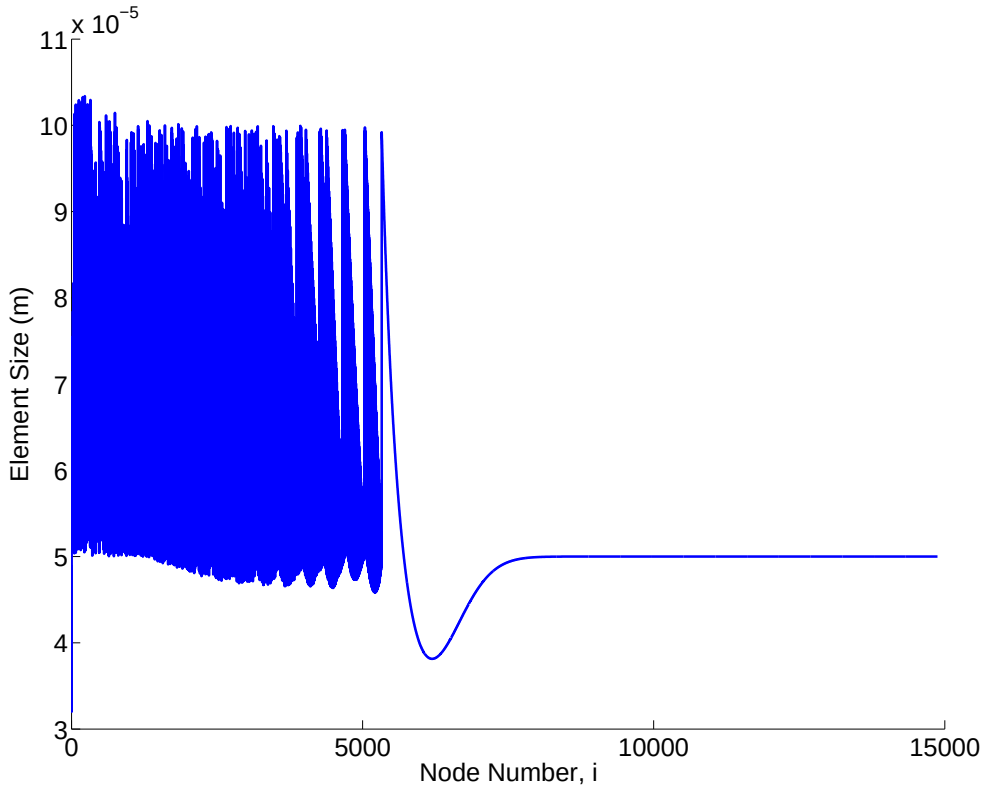

Figure 3.17: Plot of the element length when using the adapted stalagmite model, for parameters in Table 3.1, when $Q = 1 \times 10^{-4}$ kg s^{-1} and $N = 10001$, for crystalline growth of 30 days, with adaption.

3.3 Results and Discussion

This section focuses on the model when considering environmental and industrial crystal growth systems where model parameters are imposed that relate to published values for the specific materials in question. Initially, results from the geological case are reconstructed and compared with published results such that the model is confirmed to be working correctly. The model parameters are adapted such that the crystal growth of sodium nitrate under the conditions experienced in the NNL drip trials are considered. The model parameters are varied such that the impact of the various parameters on the growth behaviour, and hence the final growth formation are determined.

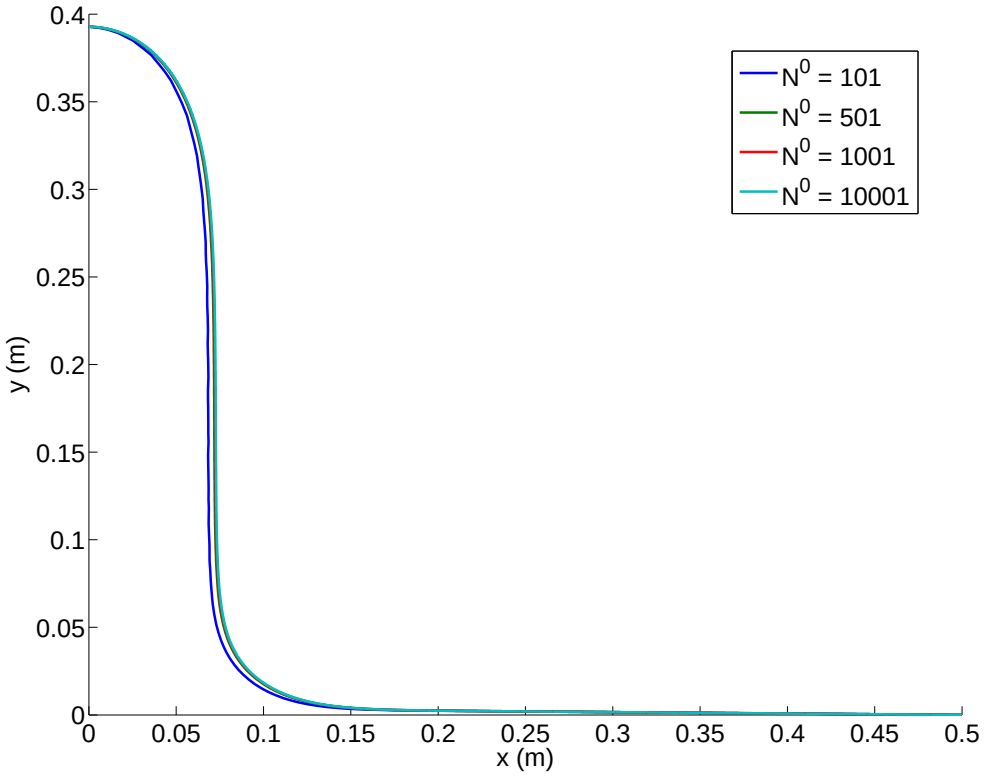

Figure 3.18: Plot of the growth when using the adapted stalagmite model for growth of 30 days when using adaptive meshing routines, for varying initial mesh size N^0. Parameters are given in Table 3.3.

3.3.1 Case 1: Reconstruction of the Geological Model

To check that the model had been correctly implemented, results were generated for the case of calcium carbonate to match those reported by Romanov et al. [162]. The parameters for this case can be found in Table 3.6. For ease of comparison with work presented in [162], flow rates in this section are given in terms of the volumetric flow rate, $Q_v = \frac{Q}{\rho}$.

Plots showing the time evolution of the boundary of the stalagmite formation from the model are provided in Figure 3.20. The profiles shown in Figure 3.20 are axisymmetric about $x = 0$. From this figure it can be seen that the geological model is functioning correctly, with the results from the MATLAB implementation of the model being virtually identical to the results presented in Romanov et al. Data from [162] was obtained through digitisation of the graphs using GetData Graph Digitizer V2.26. It is assumed that the

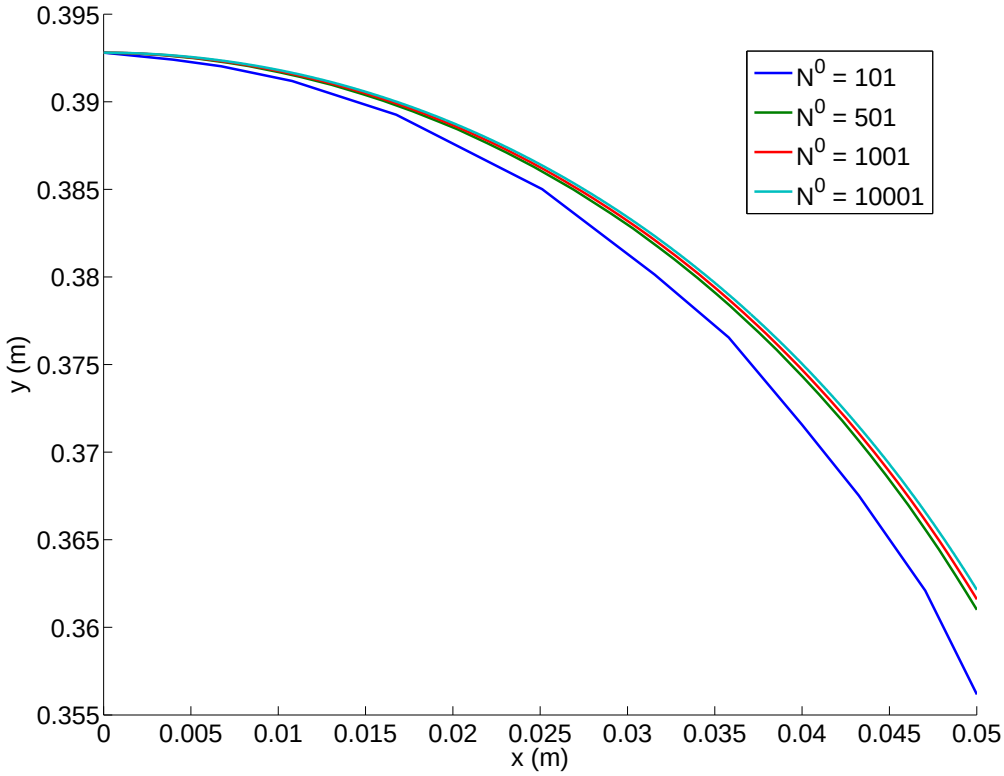

Figure 3.19: Plot of the growth close to the apex, when using the adapted stalagmite model for growth of 30 days when using adaptive meshing routines, for varying initial mesh size N^0. Parameters are given in Table 3.3.

slight discrepancies between the results are due to the difficulties involved in digitising the data.

3.3.2 Case 2: Modelling the Growth of Sodium Nitrate under Conditions Experienced in the NNL Drip Trial

Once the model was verified as described in Section 3.3.1, the parameters in the model were adapted such that the model could be used to obtain results for the case of impinging droplets of sodium nitrate salt solution. Parameters for the modified Sodium Nitrate case are given in Table 3.7.

The solubility, c^* [mol m^{-3}], for this material can be expressed as,

Crystal growth coefficient, K (m s^{-1})	1.3×10^{-7}
Volumetric flow rate, Q_v (m^3 s^{-1})	5×10^{-8}
Initial node spacing, Δl_i^0 (m)	5×10^{-4}
Initial node Count, N^0	1001
Initial angle, θ_i^0 (rad)	1×10^{-5}
Solid Density, ρ_s (kg m^{-3})	2700
Solution Density, ρ (kg m^{-3})	1000
Molecular Mass, M_s (kg mol^{-1})	0.01
Timestep, Δt year	1
Total Timesteps, M	5000

Table 3.6: Parameters for the adapted stalagmite model for calcium carbonate, as found in [162].

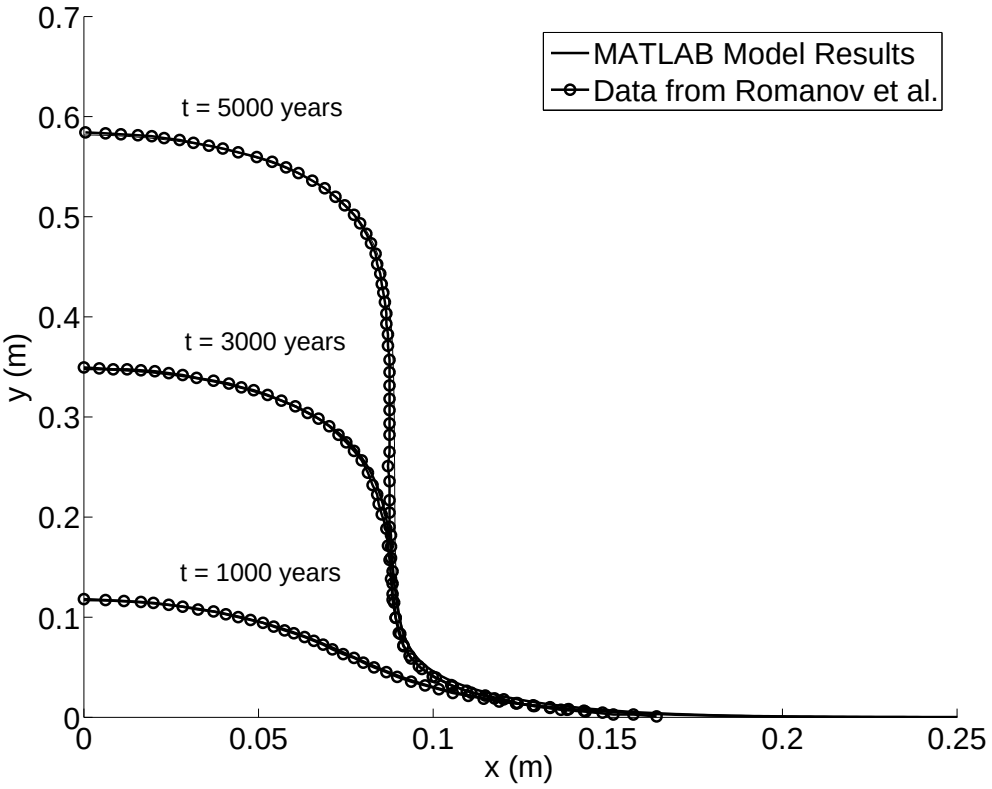

Figure 3.20: Axisymmetric plots of the stalagmite through time. Comparison of the MATLAB implementation of the model against results presented in Romanov et al., [162].

Crystal growth coefficient, K (m s^{-1})	8×10^{-6}
Initial node spacing, Δl_i^0 (m)	5×10^{-4}
Initial Node Count, N^0	1001
Initial concentration, c_1^j (mol m^{-3})	8000
Saturation concentration, c^* (mol m^{-3})	7500
Initial angle, θ_i^0 (rad)	8×10^{-3}
Solid Density, ρ_s (kg m^{-3})	2260
Solution Density, ρ (kg m^{-3})	1000
Molecular Mass, M_s (kg mol^{-1})	0.084
Timestep, Δt (s)	60

Table 3.7: Parameters for the adapted geological stalagmite model for sodium nitrate solution.

$$c^*(T) = 5055.95 + 98.452T, \tag{3.22}$$

where T is the solution temperature ($^\circ C$). It should be noted that the equations in this work assume that concentration is given in mol m^{-3}, however for ease of comparison with both the literature and NNL experimental data these will often be given in term of molarity (Molar). Also in this work we assume that the temperature of the liquid film is equal to the ambient room temperature, and remains constant throughout. Prior to entry into the system the solid matter is dissolved in a solvent at a higher temperature than this ambient room temperature. Upon entry into the domain the liquid solution experiences a drop in temperature. In order to simplify the model, we assume that this temperature drop is instantaneous, and therefore at any given point in time, an isothermal system can be considered.

As mentioned in Section 2.2.3, the rate of crystal growth depends partially on, K, the growth constant. Although this quantity depends on the temperature and velocity of the liquid, it is usually assumed constant when looking at a specific crystal growth scenario. Various values for K are reported in the literature [78, 143, 190]. The value of K when considering sodium nitrate was generated using an average value of K taken from these papers.

Now that the relevant physical and computational parameters have been prescribed, the model was run in order to calculate profiles of an axisymmetric growth. In Figure 3.21 the growth of these sodium nitrate solutions for an initial concentration, c_{in}, of 8 Molar can be seen through time. From this figure it can be seen that the tower formations are now much thinner and grow at a much faster rate to that of the calcium carbonate shown in Figure 3.20. Results found in the NNL sodium nitrate drip trials, reached an approximate height of 0.27m after 30 days, and widths of approximately 0.09m, therefore the results here appear to be of the same order of those experienced within the sodium nitrate drip trials. It should be noted that the results here are later validated against a later model, in Chapter 5. A more thorough quantitative analysis of the results when compared to experimental data is given here. The remainder of this section will generally give a more qualitative appreciation of the models behaviour for varying parameters. As previously mentioned, the results presented in Figures 3.20 and 3.21 are axisymmetric approximations of the crystalline structures as they growth through time. Figure 3.22 shows the three-dimensional representation of the results in Figure 3.21.

3.3.3 Case 3: Sodium Nitrate and the Impact of the Kinetic Growth Coefficients

The crystal growth coefficient used in Section 3.3.2 was an average value taken from [78, 143, 190]. As there is currently limited industrial interest concerning the optimisation of sodium nitrate crystals, information regarding its crystallisation kinetics is scarce and as such no empirical expressions relating the kinetic parameters to either the flow velocity or the temperature are present in the literature. In response to this, numerical experiments have been carried out, taking both the minimum and maximum kinetic values calculated from sodium nitrate crystal growth data and the average value previously used in order to assess the effects of K on the final formation growth, and give an approximate range of possible solutions.

Results for the crystal growth after 30 days, when implementing the various values of K can be observed in Figure 3.23. From this figure it can be seen that the crystal growth coefficient has a large impact on the size and shape of the final formation. Larger values of K lead to tall, narrow formations, isolated within a small region. For smaller values of K, the vertical growth of the formation is greatly reduced, however wider formations are

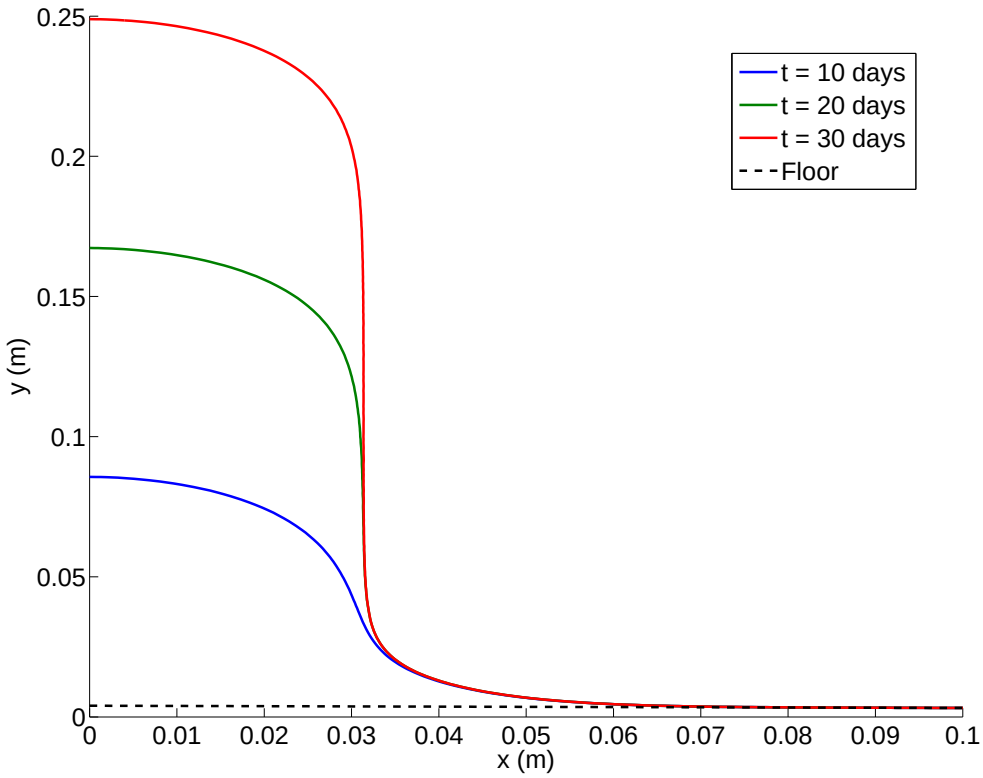

Figure 3.21: Axisymmetric plots of the Sodium Nitrate formation through time, when $Q = 2.89 \times 10^{-5}$ kg s^{-1}, $K = 8 \times 10^{-6}$ m s^{-1}, $c_{in} = 8$ Molar, $T = 27$°C. Additional parameters are given in Table 3.7.

now produced. These factors will therefore need to be carefully considered when making deductions about the parameters impact on the criticality of the formations, as changes in the characteristic shape can have a large effect.

3.3.4 Case 4: Sodium Nitrate with Parameters and the Impact of Environmental and Process Parameters

Following consideration of the impact of the coefficient of crystal growth, the impact of varying the process conditions, such as the flow rates, i.e. the rate or severity of a leakage, or the environmental conditions, such as the ambient temperature, were assessed.

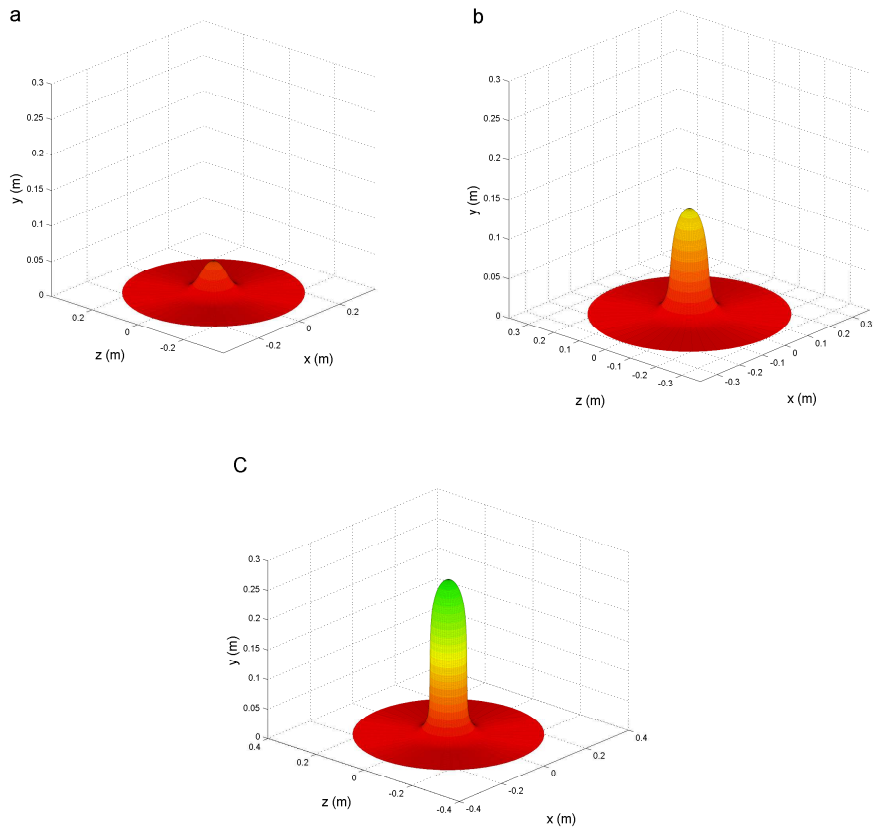

Figure 3.22: Three-dimensional plots of the stalagmite through time, after (a) $t = 10$ days, (b) $t = 20$ days, and (c) $t = 30$ days , when $Q = 2.89 \times 10^{-5}$ kg s^{-1}, $K = 8 \times 10^{-6}$ m s^{-1}, $c_{in} = 8$ Molar, $T = 27$°C. Additional parameters are given in Table 3.7.

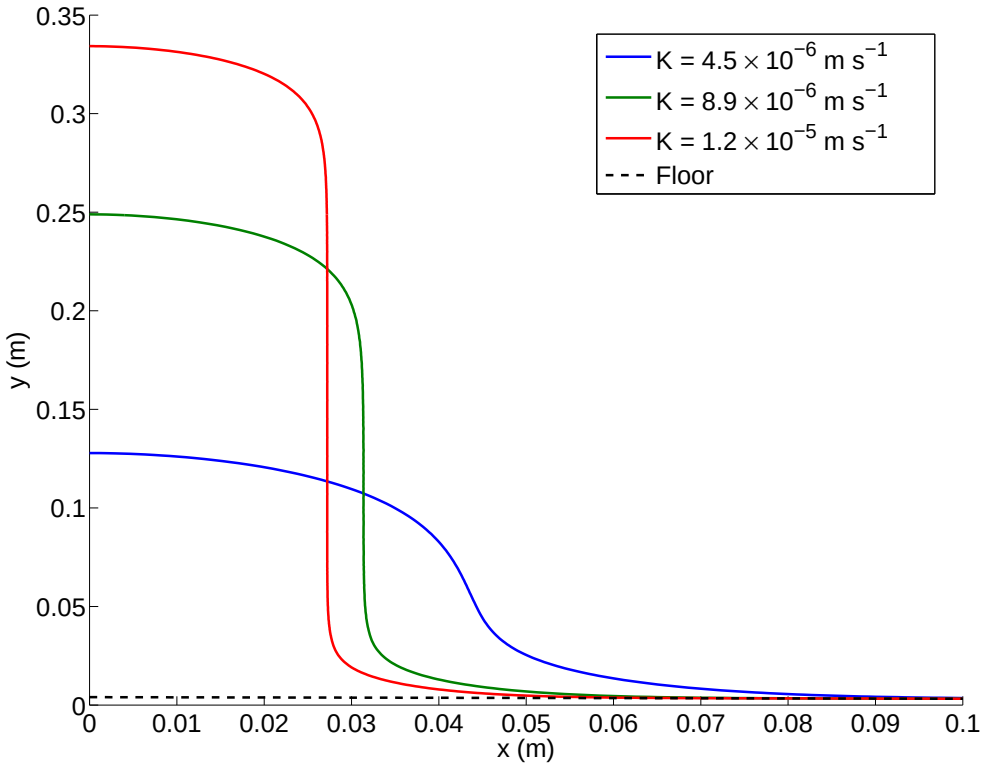

Figure 3.23: Axisymmetric plots of the Sodium Nitrate formation after 30 days growth, for varying crystal growth coefficient K, when $Q = 2.89 \times 10^{-5}$ kg s^{-1}, $c_{in} = 8$ Molar, $T = 27$°C. Additional parameters are given in Table 3.7.

3.3.4.1 Impact of temperature variation through time

The dataset of temperature data from the NNL experimental trials was small, with only 30 readings taken at irregular time intervals over a 30 day period. It was found that the experiment readings had a mean temperature of 27°C with a standard deviation of 2.3°C. As the readings were taken irregularly and infrequently it was unknown if this was a true representative measure of the conditions within the system environment. In order to assess the potential impact of the temperature, the model here was used to calculate the growth after 30 days when considering the mean temperature, and for the cases when temperature is one standard deviation variation from the mean. The results from these simulations can be seen in Figure 3.24. From this figure it is clear the model here predicts that the overall width of the formation does not change with variations in temperature, however the overall height can change significantly. It should be noted that these results

are based on the fact that the temperature remains at these extreme constant values for the duration of the 30 day period.

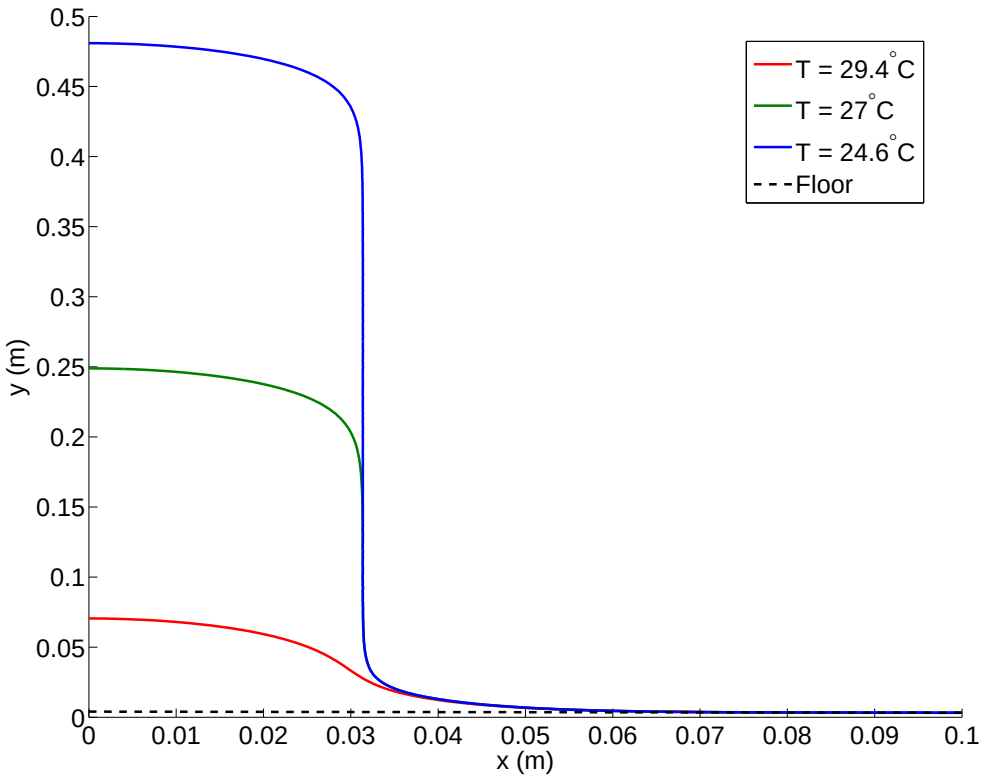

Figure 3.24: Axisymmetric plots of the Sodium Nitrate formation through time for varying temperature T, when $Q = 2.89 \times 10^{-5}$ kg s^{-1}, $K = 8 \times 10^{-6}$ m s^{-1}, $c_{in} = 8$ Molar. Additional parameters are given in Table 3.7.

Given these assumptions the model was run again, under the assumption that the temperature can vary on a day by day basis, such that the saturation value is given by,

$$c^* = 5055.95 + 98.452(normrnd(\mu, \sigma)), \tag{3.23}$$

where $normrnd(\mu, \sigma)$ generates a random number from a normal distribution with a mean μ and standard deviation σ. In this case $\mu = 27$ and $\sigma = 2.3$ were considered. The value of c^* was then updated when $j \bmod 1440 \equiv 1$. This study was carried out in order to provide a more realistic understanding of the behaviour under time varying environmental conditions.

The model was run, allowing the ambient temperature to vary temporally (still isothermal when considering the spatial variation), such that the temperature was calculated by $normrnd(27, 2.3)$ for each new day. The model was run 50 times in order to give an approximate range of feasible outcomes under this assumption. Results for this can be found in Figure 3.25. From this figure it can be seen that the range of heights at the apex is now much smaller than the range predicted when assuming a constant temperature at the previous temperature values. In addition to this, the observed apex height measured in the NNL experiments after approximately 30 days is marked on the figure, clearly this value falls within the feasible range predicted by the model.

As previously mentioned the value of K is dependent on the temperature. Therefore, it is expected from the results in Figure 3.23 and 3.24 that due to the variations in the temperature, the width of the formation and rate of vertical growth would also vary through time. As no empirical relations are available in the literature for the growth kinetics dependence on temperature, it is not possible to quantify this behaviour in the study here.

Now that the effects of the temperature on the growth of the formations have been considered, the effects of the mass flow rates will also be discussed. The NNL stated in their report of the experimental work that typical leakages experienced vary between $Q = 1.17 \times 10^{-5}$kg s^{-1} and $Q = 5.78 \times 10^{-5}$kg s^{-1} (assuming $\rho = 1000$ kg m^{-3}). Due to this, the effects of varying the mass flow was considered. In these computational experiments the other parameters were assumed constant and are given in Table 3.7. Results for this numerical experiment can be seen in Figure 3.26.

From Figure 3.26, it can be seen that as the mass flow rate increases, the formation width also increases. This parameter therefore needs careful consideration when predicting the potential criticality of heavy metal formations, as at low mass flow rates an almost cylindrical characteristic shape is observed, whilst at higher rates, the characteristic shape tends towards a hemi-spherical shape.

Romanov et al. used their implementation of the model for predicting the formations of stalagmite growth when considering variable mass flow rates, as seen in Figure 3.27.

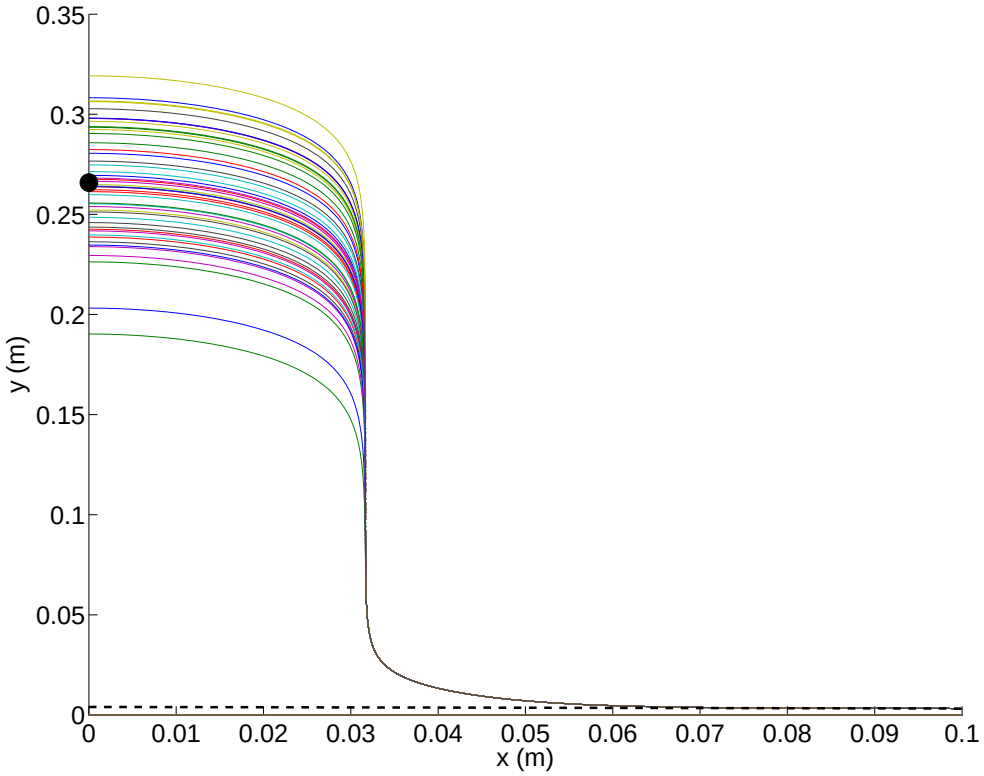

Figure 3.25: Axisymmetric plots of the Sodium Nitrate formation through time when considering random changes in temperature, using a the saturation value, c^*, given by (3.23) and $Q = 2.89 \times 10^{-5}$ kg s^{-1}, $K = 8 \times 10^{-6}$ m s^{-1}, $c_{in} = 8$ Molar. The coloured lines indicate a single computational experiment for 30 days growth. The (•) marker indicates the experimental apex height after 30 days. Additional parameters are given in Table 3.7.

The model predicts, and agrees with known facts about stalagmites, that the growth behaviour at the top of the formation is purely dependent on the current model parameters. The behaviour of the growth as you travel down the formation is determined by past conditions, and the base of the stalagmite is determined by the initial growth conditions. It is questionable as to whether the model would remain physically valid in regions where gravity acts away from the wall, as the the fluid remaining attached to the surface would depend on capillary forces. However, due to the growth of the formation away from the apex of the formation remaining stagnant, there is an argument that the model's behaviour in these regions is irrelevant. Due to these points the study here assumes that the model remains valid for these cases and will be used to describe the growth of the

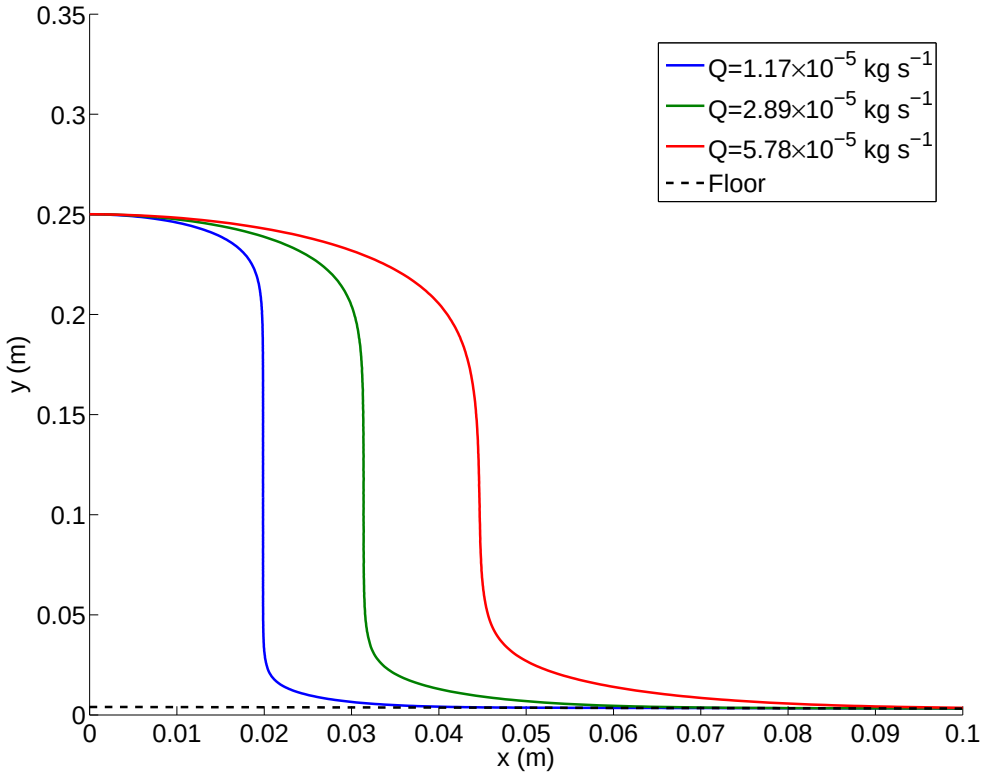

Figure 3.26: Plot of the growth after 30 days when varying the mass flow rate, Q, when $K = 8 \times 10^{-6}$ m s^{-1}, $c_{in} = 8$ Molar, $T = 27°$C. Additional parameters are given in Table 3.7.

formations when considering a variable mass flow rate.

The following computational experiment assumes that the process conditions experienced within the plant undergo a cyclic rotation, such that if a pipe or vessel leakage occurred, the flow rate would vary depending on the current fluid pressure within the pipe or vessel. As the NNL stated that leakages usually vary between $Q = 1.17 \times 10^{-5}$kg s^{-1} and $Q = 5.78 \times 10^{-5}$kg s^{-1}, the experiment here will assume that due to a fortnightly rotation of plant conditions, the leakage can be described by the variable mass flow rate,

$$Q^j = Q(t^j) = 2.89 \times 10^5 + 1.732 \times 10^{-5} \sin\left(\frac{2\pi t^j}{20160}\right), \quad \text{for } j = 0, ..., M. \tag{3.24}$$

The results for this experiment can be observed in Figure 3.28. From this figure it can

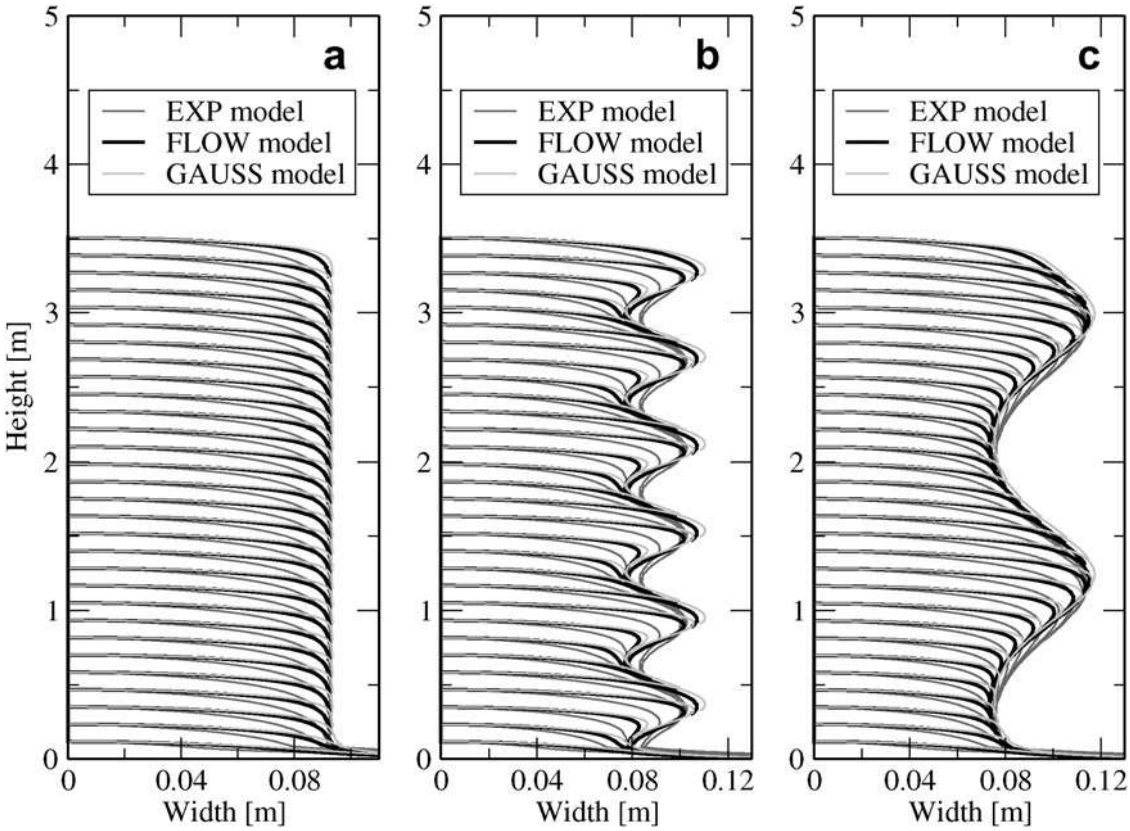

Figure 3.27: Plots of stalagmite growth given by the 'FLOW model' developed by Romanov et al. for mass flow rate $Q = \frac{V}{\tau}$, where V is the droplet volume and τ is the drip interval, given by $\tau = 30 + 13\sin(\frac{2\pi}{P}t)$ for (a) $P = 500$ years, (b) $P = 5000$ years, and (c) $P = 15000$ years, [162].

be seen that when imposing a cyclic mass flow rate, the formation takes a wavy profile. It should be noted that due to the formation taking a small portion of the domain, each axis has a different scale, therefore changes in the profile may appear to be slightly exaggerated.

In addition to cyclic conditions, if leakage occurs from a storage vessel, which is filled or emptied over given periods of time, it is likely that a constant decrease or increase of mass flow rates will be experienced. Therefore, Figure 3.29 shows the results for the linear increase from $Q = 1.17 \times 10^{-5}$kg s^{-1} to $Q = 5.78 \times 10^{-5}$kg s^{-1} and the reverse of this, such that the mass flow $Q = 5.78 \times 10^{-5}$kg s^{-1} decreases to $Q = 1.17 \times 10^{-5}$kg s^{-1} over a 30 day period. From this figure it can be seen that for an increase in mass flow rate, the width gradually increases as you move up the formations, conversely for a decrease

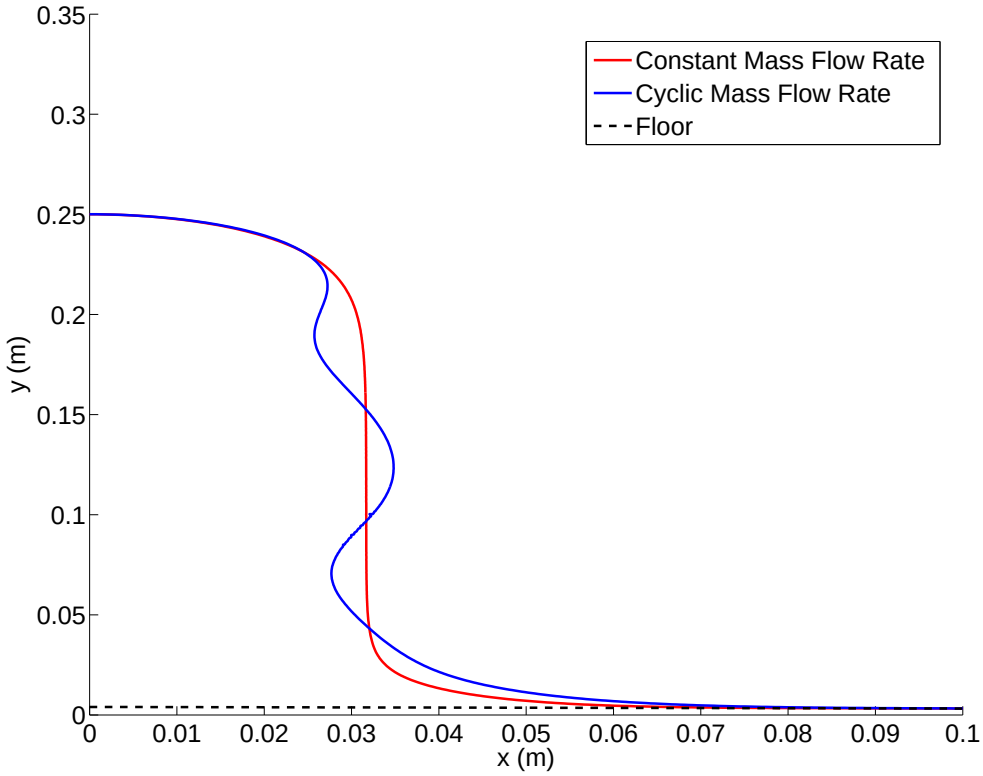

Figure 3.28: Plot of the growth after 30 days for a variable mass flow rate, given by (3.24) compared with $Q = 2.78 \times 10^{-5}$ kg s^{-1}. Here $K = 8 \times 10^{-6}$ m s^{-1}, $c_{in} = 8$ Molar, $T = 27°$C. Additional parameters are given in Table 3.7.

in mass flow rate the formation decreases with increasing height. From these numerical experiments it can be deduced that the growth behaviour at the top of the formation is governed by the current model conditions. As you move down the formation the growth behaviour catalogues the previous conditions through time. This agrees with the geological work, as researchers in this field consider the inverse problem such that atmospheric conditions can be deduced travelling back in time as you move down the stalagmite formations.

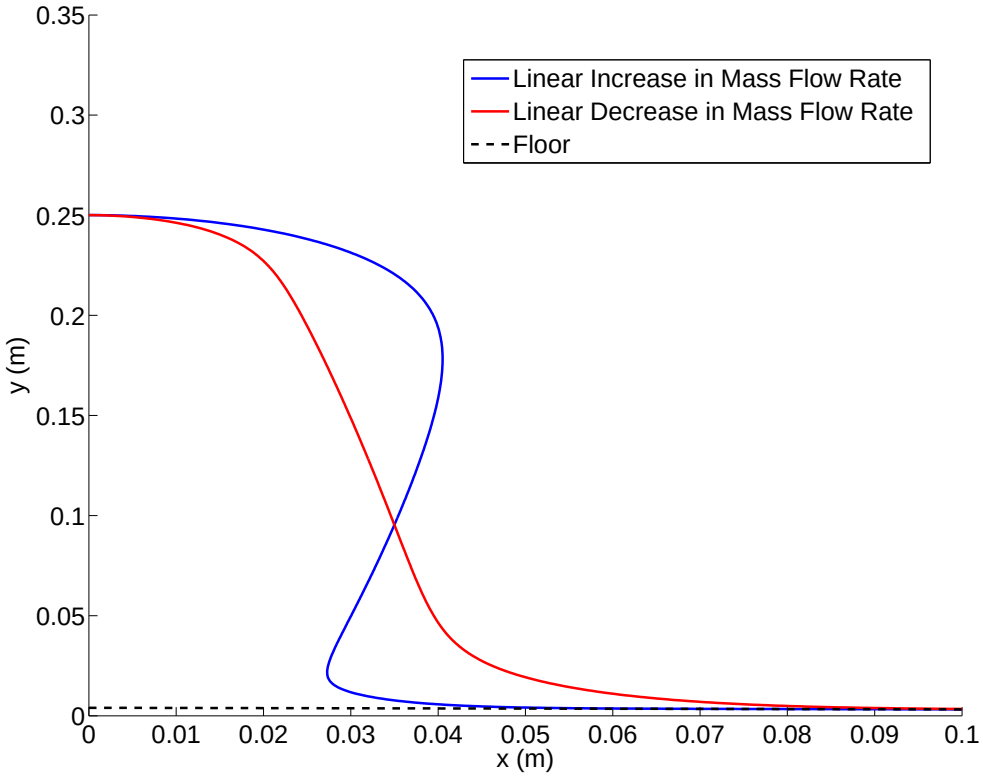

Figure 3.29: Plots of the growth after 30 days for both linearly increasing and linearly decreasing mass flow rates, when $K = 8 \times 10^{-6}$ m s^{-1}, $c_{in} = 8$ Molar, $T = 27°$C. Additional parameters are given in Table 3.7.

3.4 Summary and Conclusions

In this chapter a geological model taken from the literature for describing the growth of stalagmites has been adapted such that the crystalline growth of industrial salt solutions can be considered. Initial tests highlighted some weaknesses with the model's numerical discretisation when considering parameters similar to industrial salts. Due to this, additional adaptive meshing routines have been developed and an extensive study has shown that these alleviate the previously experienced problems.

Once mesh independency studies were carried out the adapted model was validated against the previously published results in [162]. Following this, the model was used to consider the growth of sodium nitrate over the time-scales considered in the NNL drip trials. Results were promising and formations were of a similar size and shape to the experimental trials.

Parametric trials investigated the effects of temperature on the system. It was observed that the formation height was shown to be particularly sensitive to variation in temperature. Due to the lack of experimental data regarding the variations in temperature through time, randomly generated, time variable, data which was designed to consider possible temperature fluctuations (based on the limited experimental data) was used. Through this a range of possible formations were obtained. From comparing the experimental data to these results, it was clear that the model was capable of predicting the formations obtained in the experiments. However, due to the sensitivity to changes in temperature, the model highlighted the need for regular, accurate, input temperature data, if uncertainty is to be reduced and an accurate solution obtained.

The effects of the crystal growth coefficient, K, were also investigated. The results suggest that the width and height of the final formation is highly dependent on this empirically calculated, material specific parameter. As mentioned in Chapter 2, this coefficient is a function of two simultaneous processes, namely the diffusion, and the surface integration or reaction step. Clearly the model has limitations as both these processes are dependent on the fluid flow properties and temperature. Due to this, and the models sensitivity to K, it is questionable whether a constant value for this is appropriate and results suggest

that for $K = K(T)$ the width would also change with varying temperature. However, as parameters relating to the quantification of these processes are limited in the literature (particularly for sodium nitrate), the approach here serves as a useful approximation.

Additionally, the effects of the mass flow rates were considered. Here it was shown that the width of the formation was sensitive to changes in the mass flow rate. In order to address the likely problem of a non constant mass flow rate, studies were carried out which imposed a time variable mass flow rate. These studies show that the formation reaches an equilibrium width for the conditions at a given point in time, as the formations grow taller the width of the deposited mass in this time-frame changes depending on current mass flow conditions. This agrees with the results in the geological literature, as a key area of interest is the formulation of inverse problems which consider the shape of stalagmite formations. These models suggest that the stalagmite shape at various heights can give information regarding the climate conditions at different points in time (i.e. the top most point gives information regarding the most recent conditions, and the base of the formation relates to the initial growth conditions).

Summarising, the work in this chapter has addressed the second objective of the research, posed in Chapter 1. Results from the model have offered insight into how the temperature, mass flow rate and crystal growth coefficient can affect the overall size and shape of the formation. Results have been shown to be highly sensitive to input parameters and therefore careful consideration needs to be taken with these if accurate solutions are to be obtained.

Chapter 4

Development of a Coupled CFD and Moving Boundary Framework for Crystallisation Problems

4.1 Introduction

The chapter reports the development of a computational framework which has the potential to describe crystalline growths from salt solutions as they form through time. The underlying principles of the model here are similar in nature to those of the adapted stalagmite model developed in Chapter 3. The previously described model assumes that the growth of crystalline mass can be described by a moving boundary, which is coupled to several other physical models which provide simple approximations to the fluid and solute transport. A similar approach is developed in this chapter with methods implemented to overcome some of the previous models limitations. The model in Chapter 3 uses analytic expressions to approximate the flow field of a thin liquid film. These models are only appropriate for a limited parameter set, i.e. slow or thin fluid films. In addition to this, diffusion of the solute through the film is accounted for by a constant parameter in the reaction-diffusion crystallisation model. As the effects due to diffusion are not modelled explicitly, its effect on the crystal growth does not vary with changing flow conditions. This is known not to be true, as the size of the mass transfer boundary layer (see Section 2.2.3), and hence relative impact of the diffusion changes depending on the flow velocity. In addition to the fluid flow and the diffusivity, the model neglects other physical

processes, e.g. the evaporation of solvent, the material's rheological dependence on environmental and flow parameters, and temperature effects. In some situations this can have a significant impact on the model predictions.

From Chapter 3, it can be seen that the previous model provides insight into the formation of crystalline deposits. Results when focusing on the central tower formation generally appear to be of similar sizes and shapes to those of the experimental work. However as mentioned, there are important physical processes that the model does not consider. The effects of neglecting these processes are clearly apparent when comparing experimental data to the model results, as some key features of the formations are not captured (e.g. growth away from the central tower formation). Therefore, in order to carry out a thorough study into the effects of parameters and their relative impact on the system, this chapter develops and evaluates an initial finite volume framework for coupling fluid flow with crystallisation. This framework then forms the fundamental basis for a model, which is developed in Chapter 5, allowing the modelling of crystalline formations and the relative impact of additional physics to be investigated.

This initial framework will focus on the three most fundamental processes observed in the problem, namely, fluid flow, solute transport and the deposition of solid mass. Each section within the chapter will specifically focus on and assess the modelling and implementation of techniques, such that each individual process is captured in an accurate and robust manner. A final section will focus on the coupling of these models, hence completing the framework for describing problems that involve mass deposition from a liquid solution.

The work in this chapter therefore directly addresses the 3rd objective of this research, as discussed in Section 1.5, by developing and assessing potential techniques for describing problems involving the crystallisation from liquid solution. It will provide a finite volume implementation specifically for the coupling of systems involving fluid flow when considering a moving boundary such that additional physics can be conveniently included at a later stage. It is expected that the inclusion additional physics will allow an improved model to be created, based on this initial framework such that the formations observed in the NNL drip trials can be considered.

4.2 Fluid Flow

Similarly to the model in Chapter 3, here we assume that the droplets impact on the surface of an inclined plate. After impact, droplets flow down the incline of the plate, forming a thin liquid film. Droplet splashing is neglected within this work as it is assumed the majority of the liquid lands close to the point of impact. As such, only the resultant liquid film will be considered. The mass flow rate of the droplets is averaged through time and it is assumed that entry of liquid into the system can be described by a constant flow rate perpendicular to the plate.

4.2.1 Introduction to the Numerical Methods

Here the Navier Stokes equation is solved in order to describe the transport of momentum. Unlike Chapter 3 which considered an incompressible flow, with constant density and viscosity, the work here will impose no such assumption. Due to this the conservation of momentum is given by,

$$\frac{\partial}{\partial t}(\rho \mathbf{u}) + \nabla \cdot (\rho \mathbf{u}\mathbf{u}) = -\nabla p + \nabla \cdot \left(\mu(\nabla \mathbf{u} + (\nabla \mathbf{u})^{tr})\right) + \rho \mathbf{g} \tag{4.1}$$

Alongside this the conservation of mass is given by,

$$\frac{\partial \rho}{\partial t} + \nabla \cdot (\rho \mathbf{u}) = S_m, \tag{4.2}$$

where S_m are the mass source/sink terms.

As the model is considered to be at a steady state, the time dependent terms in these equations can be ignored. Similarly to the approach presented in Section 2.3, these equations can then be discretised and solved over a numerical grid, which is mapped over the geometry of interest. In order to demonstrate how this is implemented the initial numerical discretisation presented in Section 2.3 is progressed. For continuity with the previous workings, the remainder of this section will further consider the discretisation of the incompressible equations in (3.3), however it should be noted that similar methods are used when considering (4.1).

A typical computational cell, along with its surrounding cells, can be seen in Figure 4.1. As in this work a cell-centred finite volume method is considered, variables stored within the finite volume solver relate to the value at the cell centre, however from observing the previously discretised form of (3.3), in (2.11), it can be seen that the discretised equations require the values at the cell face (see Figure 4.1). In addition to this, gradient values at the cell face are also required to be calculated. The equations in (2.11) can now be reformulated in terms of the steady state problem and the example finite volume grid in Figure 4.1. For simplicity the horizontal component, $u(x, y)$, of the velocity $\mathbf{u}(x, y)$ is considered by,

$$\sum_{(x,y)\in F} (\rho u A\mathbf{u} \cdot \mathbf{n}) = -\sum_{(x,y)\in F} pA(\mathbf{n} \cdot \hat{\mathbf{i}}) + \sum_{(x,y)\in F} (\mu A \nabla u \cdot \mathbf{n}), \tag{4.3}$$

where $(x, y) \in F = \{i - \frac{1}{2}, i + \frac{1}{2}\} \times \{j - \frac{1}{2}, j + \frac{1}{2}\}$ is the discrete set of coordinates for the cell face centre, $\mathbf{n} = \mathbf{n}(x, y)$ is the outward normal to the cell face, $\hat{\mathbf{i}}$ is the unit vector in the x-direction, $A = A(x, y)$ is the area of the cell face, μ is the dynamic viscosity and $p = p(x, y)$ is the pressure. It should be noted that when considering the vertical components of the velocity, the corresponding body forces due to gravity have to be considered.

As a cell-centred finite volume method is used here, the face values are unknown and therefore (4.3) needs to be reformulated in terms of the cell centre values. This can be accomplished through a variety of different finite difference methods, all of which have their own individual strengths and weaknesses. As the steady state case is considered in this work, only the methods for spatial discretisation are discussed. In addition to this, there are various numerical methods for calculating the gradient vector. Both of these considerations will be discussed in Section 4.2.1.1.

Once the face values are calculated using an appropriate discretisation scheme, a linear system can be obtained. For example, when considering the horizontal component of the velocity, $u(x, y) = u_{x,y}$, at point (i, j), the following equation can be obtained,

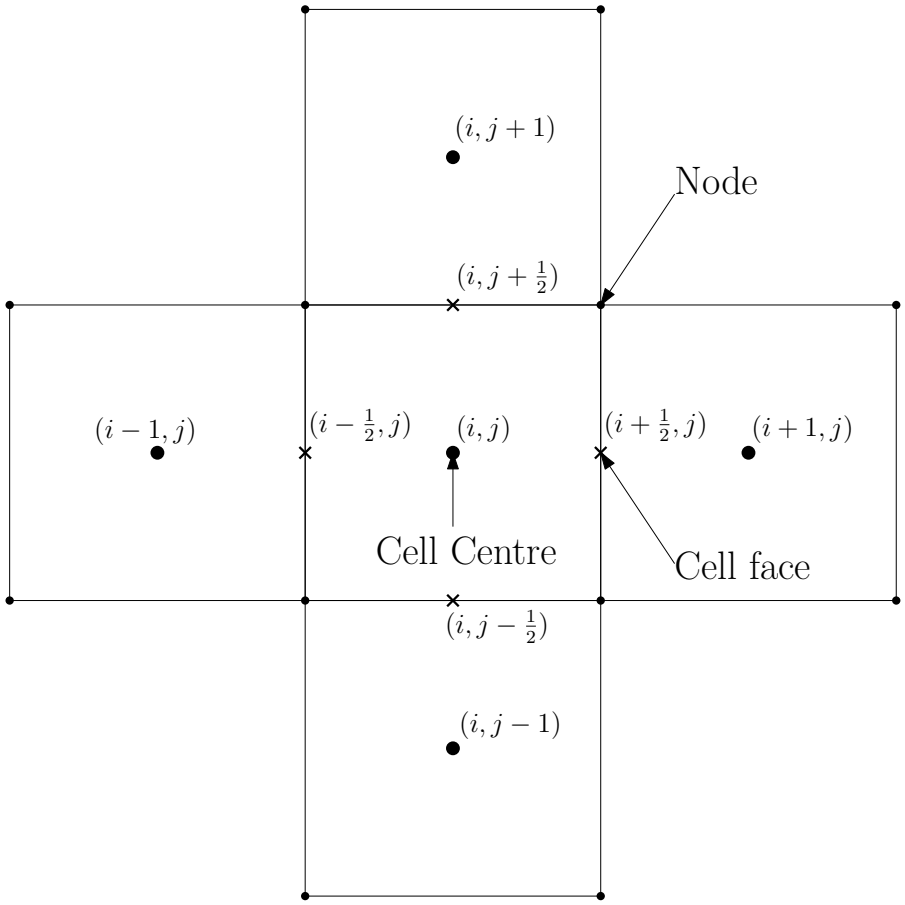

Figure 4.1: Plot of a simplified numerical grid when considering the finite volume method.

$$a_{i,j}u_{i,j} = \sum_{(x,y)\in C} a_{x,y}u_{x,y} + \sum_{(x,y)\in F} pA(\mathbf{n}\cdot\hat{\mathbf{i}}) \tag{4.4}$$

where $C = \{i-1, i+1\} \times \{j-1, j+1\}$ is the discrete set of coordinates for the neighbouring cell centres, $F = \{i-\frac{1}{2}, i+\frac{1}{2}\} \times \{j-\frac{1}{2}, j+\frac{1}{2}\}$ is the discrete set of coordinates for the cell face centres on (i, j). The linearised momentum coefficients are given by $a_{x,y}$, these are dependent on the choice of discretisation scheme used.

Due to complex coupling between pressure and velocity, there are a variety of approaches in which to solve the above linear system of equations. These can be generally classified into either segregated or coupled methods. Segregated methods take an iterative solution approach, such that an initial pressure field is assumed. Using this pressure field corresponding velocities can be calculated from (4.4). Following this, face mass flux values are calculated in each cell, such that, based on the continuity equation (3.4) (conservation of mass), the sum of the mass fluxes across a cell must be equal to zero. As the initial pressure field is approximated, this initial solution will not satisfy the continuity equation. A pressure correction term is then calculated such that the flow field satisfies mass conservation. Using this pressure correction term, the pressure field can then be updated. It should be noted that the pressure is corrected in an iterative fashion, such that only a fraction of the pressure correction term is applied at each iteration. This is for stability reasons, and is known as under-relaxation. This process is carried out iteratively until a suitable level of convergence is obtained.

There are a number of different methods for segregated velocity-pressure coupling, whose differences usually relate to the calculation and implementation of the pressure correction term. The primary available segregated solvers are, SIMPLE [149], SIMPLEC [178] and PISO [92].

As an alternative to segregated methods, the pressure-velocity equations can be solved in a coupled manner. Here the conservation of mass is directly enforced through modification of the linear system in (4.4) such that the pressure can be written in terms of the momentum coefficients. This overall system of equations is then solved to obtain both velocity and pressure fields. Generally speaking, the coupled solver takes fewer iterations

to converge, however more memory is required due to the larger number of unknowns in the governing system of equations [8]. The choice of method should be based on the specific problem being considered.

It should be noted that the linear systems being solved in both the segregated and coupled solvers here are often challenging, and therefore a variety of methods exist in order to solve them. Here the Gauss-Seidal method is used [81], along with the algebraic multigrid method (AMG) [90], which is used to increase the rate of convergence.

4.2.1.1 Spatial Discretisation

As discussed in Section 4.2.1, before the linear systems can be solved values for the flow variables and their respective gradients have to be calculated on the cell faces. The remainder of this section will focus on the discretisation of the velocity, such that face values and gradients can be obtained. The face values for the pressure are often calculated using complicated expressions. Details of a the most commonly used pressure interpolation schemes can be found in [156].

The most simple method for calculating the velocity values at the cell face, namely the first order upwind scheme, simply assumes that for a given face, the velocity at this point is equal to the cell centred velocity in the upwind cell, therefore for the x component of $\mathbf{u}$,

$$u_{i+\frac{1}{2},j} = \begin{cases} u_{i,j} & \text{when } \dot{m}_e > 0 \\ \\ u_{i+1,j} & \text{when } \dot{m}_e < 0, \end{cases} \tag{4.5}$$

where $\dot{m}_e$ is the mass flow rate from cell (i, j) to cell $(i + 1, j)$ (a negative value signifies fluid is flowing from $(i + 1, j)$ to (i, j)).

As the title suggests, this scheme is first-order accurate and therefore, is often not as accurate as higher-order schemes. In addition to this, this scheme has a tendency to introduce numerical diffusion into the solution. However, due to its simplicity is often

used for challenging problems, where obtaining a converged solution through use of higher order scheme may not be possible.

A second-order scheme [20] can also be used such that,

$$u_{i+\frac{1}{2},j} = \begin{cases} u_{i,j} + \nabla u_{i,j} \cdot \tilde{\mathbf{r}} & \text{when } \dot{m}_e > 0, \\ \\ u_{i+1,j} + \nabla u_{i+1,j} \cdot \tilde{\mathbf{r}} & \text{when } \dot{m}_e < 0, \end{cases} \tag{4.6}$$

where $\tilde{\mathbf{r}}$ is the displacement vector from the upwind cell centre to the connecting face of cell (i, j). Despite the increased accuracy this method is often known to produce oscillations in the solution, particularly when describing flows with variations in density or pressure.

Higher order methods are also available such as the Quadratic Upstream Interpolation for Convective Kinematics scheme (QUICK) [114], these methods increase the accuracy by taking additional values from further upwind computational cells. Again, these methods are known to suffer from instabilities. Often a blending between the low-order schemes and the high order schemes is employed, such that a high level of accuracy can be obtained, whilst still remaining stable.

In addition to the face values, the gradients also need to be calculated. There are several methods in which this can be achieved. The "Green-Gauss Cell-Based Gradient Evaluation" is one available method used [8]. Again, when considering the horizontal component of velocity, this model states that the gradient at the cell centre can be calculated via

$$\nabla u_{i,j} = \frac{1}{V_{i,j}} \sum_{(x,y) \in F} u_{x,y} A_{x,y} \mathbf{n}, \tag{4.7}$$

where $u_{x,y}$ is calculated from (4.6), $V_{i,j}$ is the volume of cell (i, j) and $A_{x,y} = A(x, y)$ is the face area. Gradient values at the face can then be calculated from (4.6), by using $\nabla u_{i,j}$ in place of $u_{i,j}$.

Alternatively a 'least-squares approximation' can be used. This method assumes that the

gradient can be calculated from the average values between adjacent cell centres. The relative weighting of each average (four for quadrilateral meshes) is varied when calculating the gradient. Details of this method can be found in [8].

An overview of the underlying numerical methods for the fluid flow equations have been provided. These for the basis of the models development in this work. The following section will discuss the implementation of a model which allows the consideration of multiple fluids within a system, such that thin liquid films can be described.

4.2.2 Volume of Fluid Method

There are currently many numerical models designed for capturing the flow of multiple fluids. In this work the volume of fluid (VOF) method which is specifically designed for the modelling of immiscible fluids and capturing the interface between them is used. An initial review of the literature has shown that the VOF model has been used extensively in the modelling of thin film flows [57, 84, 87]. These studies suggest that the model is appropriate for the work here. The following sections will discuss the mathematics of the VOF model, along with a number of studies that are undertaken to assess the effects of varying the numerical and computational implementation. This is necessary to establish an appropriate implementation for the model.

4.2.2.1 Mathematical Model

In addition to the solution of the equations outlined in (4.1) and (4.2), an equation which models the advection of a "volume fraction" is solved. This volume fraction equation is given by,

$$\frac{\partial}{\partial t}(\alpha_q \rho_q) + \nabla \cdot (\alpha_q \rho_q \mathbf{u}) = S_{\alpha_q}, \quad 0 \leq \alpha_q \leq 1, \quad \text{for } q = 2, ..., n, \tag{4.8}$$

where α_q, denotes the fraction of fluid within a computational cell with respect to the qth phase, ρ_q is the density of the qth phase, S_{α_q} is a the source/sink term relating to the qth phase and n represents the number of phases. Equation (4.8) is not solved for $q = 1$ and is calculated by,

$$\sum_{q=1}^{n} \alpha_q = 1, \tag{4.9}$$

in each computational cell. The velocity **u** satisfies equations (4.1) and (4.2). This shared field approach is dependent on the volume fractions of the phases through the properties of ρ and μ, where,

$$\rho = \sum_{q=1}^{n} \alpha_q \rho_q, \tag{4.10}$$

and,

$$\mu = \sum_{q=1}^{n} \alpha_q \mu_q, \tag{4.11}$$

where μ_q is the viscosity with respect to the qth phase.

Equation (4.8) is then discretised using the methods similar to those outlined in Section 4.2.1. The solution of these allows the transport of a scalar denoting the volume fraction. While this is the case, a scalar value located at the cell centre does not provide enough information in order to determine the position and orientation of the interface within that particular cell. The following section will discuss the various methods available such that these interface values can be determined.

4.2.2.2 Interface Reconstruction

The computational cells in which $0 < \alpha_2 < 1$ denote the region in which the interface between the fluid phases lie. Through techniques presented in this section, the position and orientation of the interface can be constructed (see Figure 4.2).

The original methods which solved the VOF attempted to develop the orientation of the interface using information provided by the finite volume scheme. Equation (4.8) was solved using a first order upwind scheme, and it was shown in [30] that the normal to the interface between the phases is described by,

$$\mathbf{n}_{interface} = \frac{\nabla \alpha_2}{|\nabla \alpha_2|}. \tag{4.12}$$

Much like when calculating the advection of a single fluid, these methods were shown to be highly diffusive, with the interface often being smeared across several cells [151]. As these diffusive phenomena are often alleviated by using higher-order schemes, when considering the Navier Stokes equations, it might seem intuitive that increasing the order

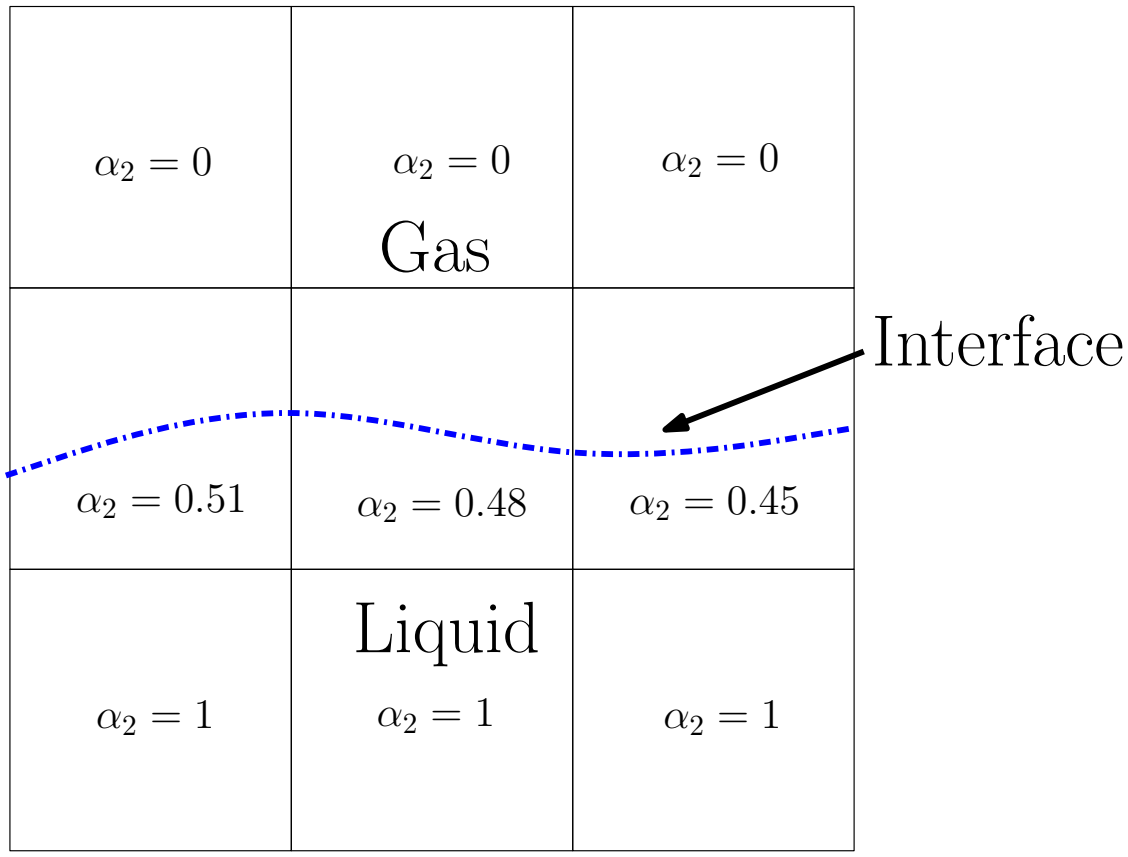

Figure 4.2: An example of a numerical grid showing the transport of the volume fraction along with the reconstructed interface between an immiscible gas and liquid.

would also reduce the smearing of the interface. Unfortunately, studies which considered solution of the VOF equation when implementing these schemes were also shown to be highly diffusive at the interface.

Due to such problems, researchers developed new methods in which the orientation and position of the interface could be described by a single linear element in each computational cell. This being the case, the interface is no longer diffusive and is able to be sharply defined. Studies regarding these methods, namely geometric reconstructive methods, can be found in [120, 138]. While these methods are shown to give highly accurate solutions to the VOF equation, they are not without their limitations. Geometric reconstruction of the interface is seen to be highly computationally demanding, and moreover, the method can only be implemented when considering the fully transient VOF model. These limitations suggest that the method is not appropriate for a range of situations, such as when the system is particularly complex and the computational demands are already high, or when a steady state solver is to be used. Due to this, researchers have developed other advanced finite volume discretisation schemes specifically for use with the VOF model, such that unwanted numerical diffusion is kept to a minimum.

Examples of these methods include the High Resolution Interface Capture (HRIC) method [136] and, the Compressive Interface Capturing Scheme for Arbitrary Meshes (CICSAM) [177]. As mentioned, upwind discretisation schemes often lead to numerical diffusion at the interface. It was found that downwind schemes (similar to upwind schemes in Section 4.2.1, but with face values that are calculated from the adjoining downwind cell) lead to a sharp interface, however the results produced are often non-physical [176]. Therefore, these schemes use a blending between both upwind and downwind discretisation in order to reduce numerical diffusion. Furthermore, a correction term is considered in the discretisation scheme, such that the initial calculated orientation of the interface influences the relative weighting of the upwind and downwind schemes. Studies regarding both the HRIC and CICSAM schemes, along with comparisons between the two, can be found in [93, 136, 176, 182]. It should be noted that whilst the CICSAM scheme is less computationally demanding than the interface geometric reconstruction methods, it still requires that a transient solver to be used. Therefore in situations where a steady state solver is used, the HRIC method should be implemented.

4.2.3 Mesh Implementation

While the numerical discretisation scheme is important in terms of the accuracy and resolution of the final results, the size, quality and type of numerical grid is also equally important. For practical applications of numerical methods where the geometry and domains in question are often highly complex, numerical grids can consist of a variety of different shapes. In three dimensions these mesh shapes include tetrahedrons, pyramids, hexahedrons and wedges. However in two dimensions, shapes are limited to quadrilateral or triangular elements. As the work here focuses on the implementation of a two-dimensional model, only the latter mesh types are considered.

In order to visualise numerical grids of either triangular or quadrilateral elements, a simple quadrilateral domain is meshed as observed in Figures 4.3(a) and 4.3(b). Generally speaking, quadrilateral meshes offer better accuracy and convergence in comparison to triangular meshes of the same number of elements, and therefore can have a significant impact on the computational solution times. However, triangular elements offer more flexibility when meshing complex geometries. The meshes shown in Figures 4.3(a) and 4.3(b) have a low number of elements, this is for visualisation purposes such that each element type can be clearly seen. In order to assess the effects of both meshes when using the VOF method, the meshes in Figures 4.3(a) and 4.3(b) were upscaled such that each contained 10,000 elements, uniformly across the domain (approximately 5 times the number of elements as those presented in Figures 4.3(a) and 4.3(b)) . The VOF model was then run for the domain in Figure 4.4 when using both triangular and quadrilateral meshes. Boundary conditions were specified such that a mass flow boundary condition is placed on the inlet, given by,

$$\mathbf{u} \cdot \mathbf{n} = \frac{Q}{\rho A}, \quad \text{on } \Omega_{inlet} \tag{4.13}$$

where $\mathbf{u}$ is the fluid velocity, $\mathbf{n}$ is the inward normal to the surface, Q is the mass flow rate of liquid, Ω_{inlet} is the boundary defining the fluid inlet and A is the area of the inlet.

The floor boundary, Ω_{floor}, has a no-slip boundary condition implemented, where $\mathbf{u} = \mathbf{0}$.

The outlet and top of the domain, Ω_{outlet} and Ω_{top}, are classed as a pressure outlets where

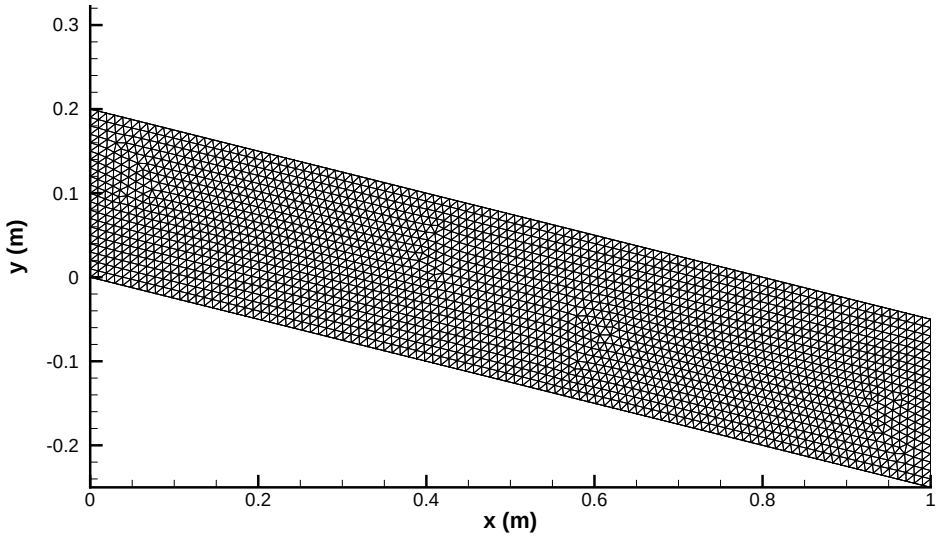

(a)

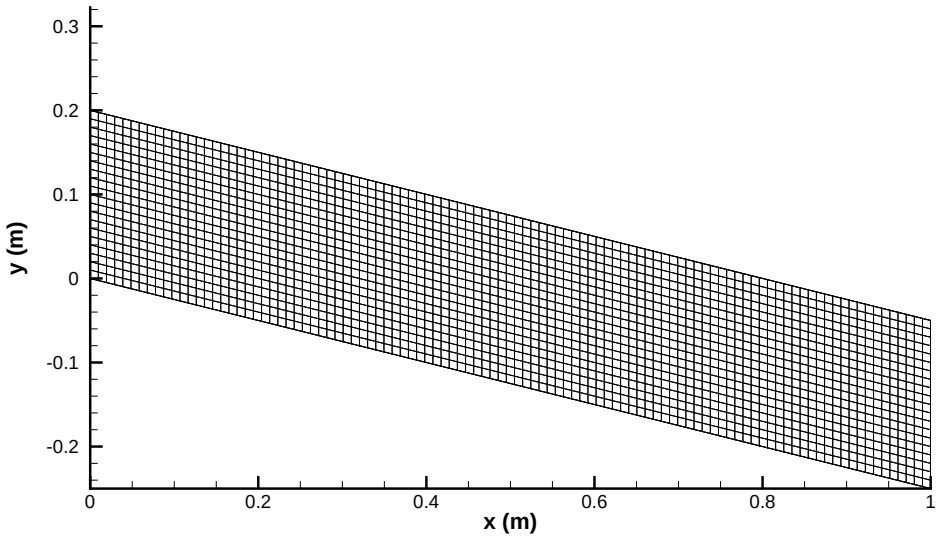

(b)

Figure 4.3: Example of (a) a simple triangular mesh and (b) a simple quadrilateral mesh.

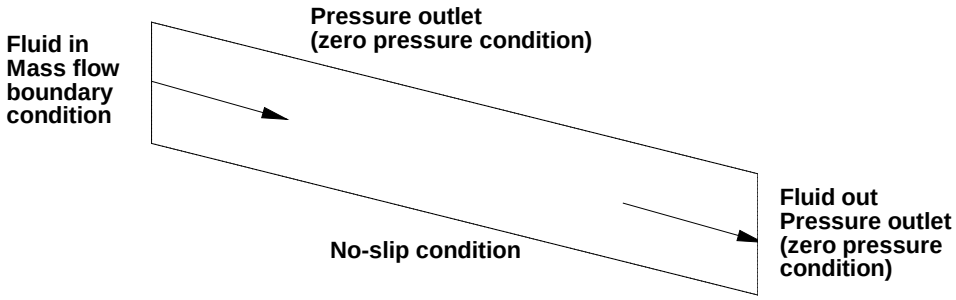

Figure 4.4: Schematic of the domain used in the VOF mesh trial, along with the specified boundary conditions.

a gauge pressure, $p' = p - p_{atm} = 0$ is specified, where p is the absolute pressure and p_{atm} is the atmospheric pressure. As this study was to test the effects of the meshing, the exact solver and flow parameters at this stage are arbitrary. The results from this simulation are presented in Figure 4.5. From this figure it can be clearly seen that when using the quadrilateral mesh, the model produces a much sharper interface. For the triangular mesh, the diffusion at the interface is severe, with the interface being smeared throughout the majority of the fluid film.

If some *a priori* estimate of the film height can be made, such that there is confidence that the film height will never exceed this value, a non-uniform mesh can be mapped onto the domain. Then the mesh in the region in which the interface is expected will contain a highly refined region of cells. An example of which can be seen in Figure 4.6. In order to clearly see the individual elements, only a portion of the domain has been shown.

4.2.3.1 Considerations for the Choice of Numerical Discretisation

Now that the basic principles for meshing of the VOF method have been discussed, trials of the various schemes are considered, such that the optimal discretisation scheme when solving the VOF can be chosen. This optimisation will allow a clear interface to be de-

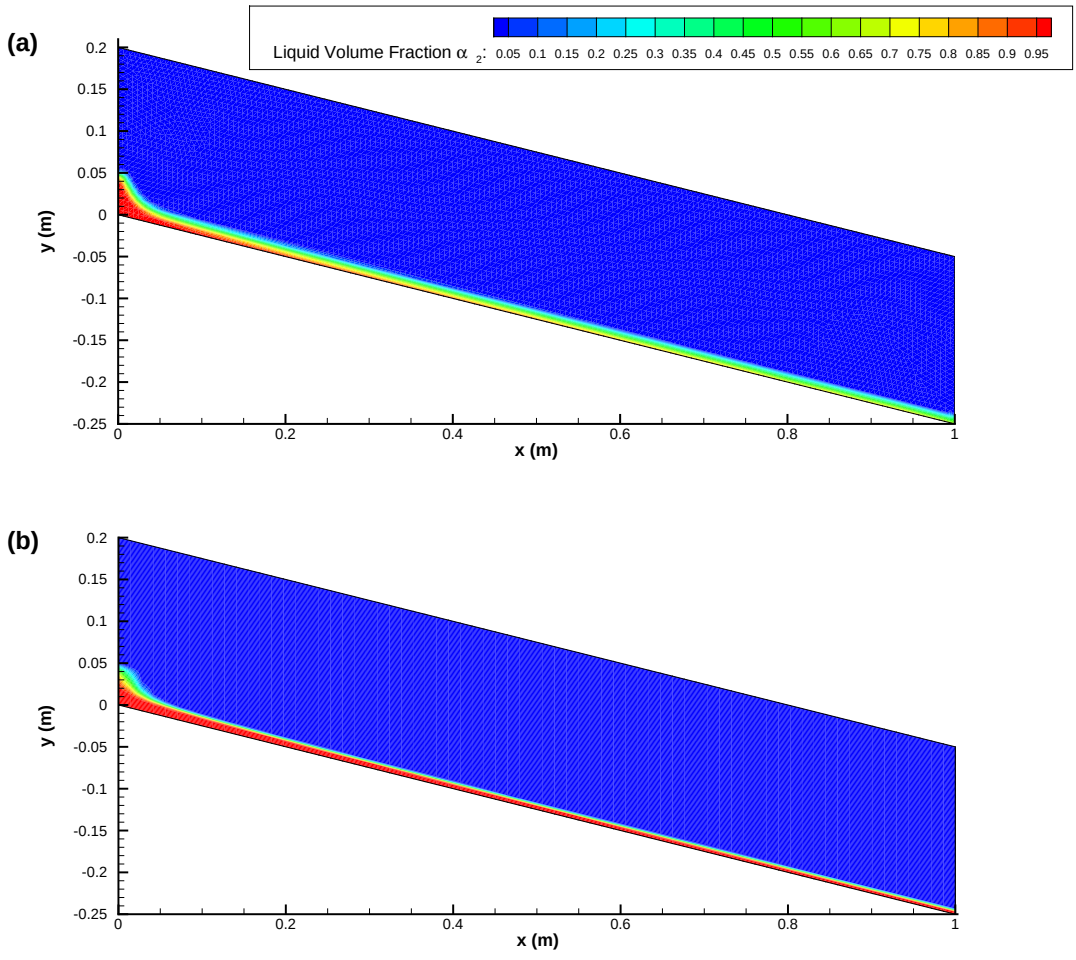

Figure 4.5: Results from the VOF, when using both (a) triangular and (b) quadrilateral meshes.

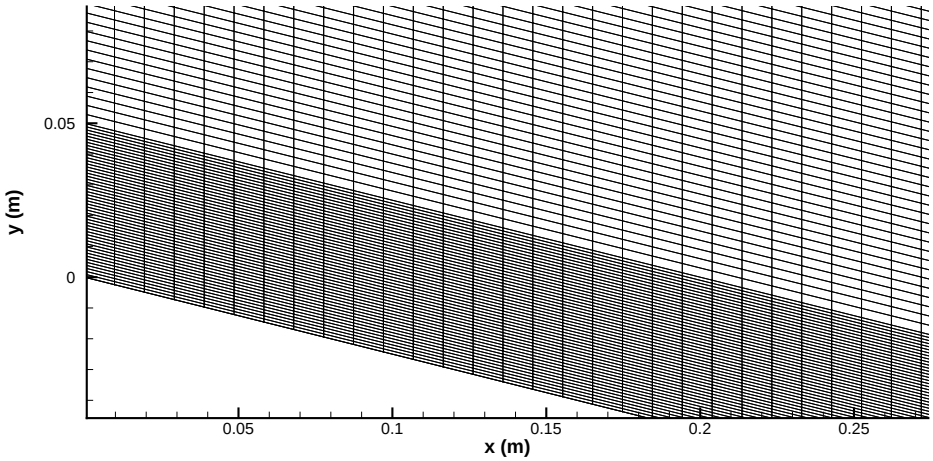

Figure 4.6: Plot of a section of the domain when using a non-uniform mesh.

fined, such that the mesh size can be kept to a minimum.

The VOF model was run using the boundary conditions used in Figure 4.4 and a non-uniform mesh of 10,000 elements, such as in Figure 4.6. As initial results confirmed that a quadrilateral mesh type was optimal for the VOF model, these studies also implement this mesh type. Results from this trial can be found in Figure 4.7. From this figure it can be seen that increasing the order to the discretisation scheme increases the clarity of the interface. These results also confirm that the HRIC scheme is the optimal scheme when using a steady state VOF solver.

4.2.4 Results

The initial investigations suggest that the VOF model is appropriate when modelling thin liquid films, however in order to give further confidence in the solution, the results here will be compared against the Nusselt solution, as shown in (2.14). Also, the size of the mesh used will also be varied, such that the solutions dependence on the mesh can be considered. The models will be run using a domain and boundary conditions similar to those presented in Figure 4.4. As the model in Chapter 3 is only appropriate for films that are either very thin or very slow, the dimensions and flow rates considered here will now be reduced. Parameters for the models are presented in Table 4.1 and the results for this computational trial can be seen in Figures 4.8(a) and 4.8(b). From these figures it can

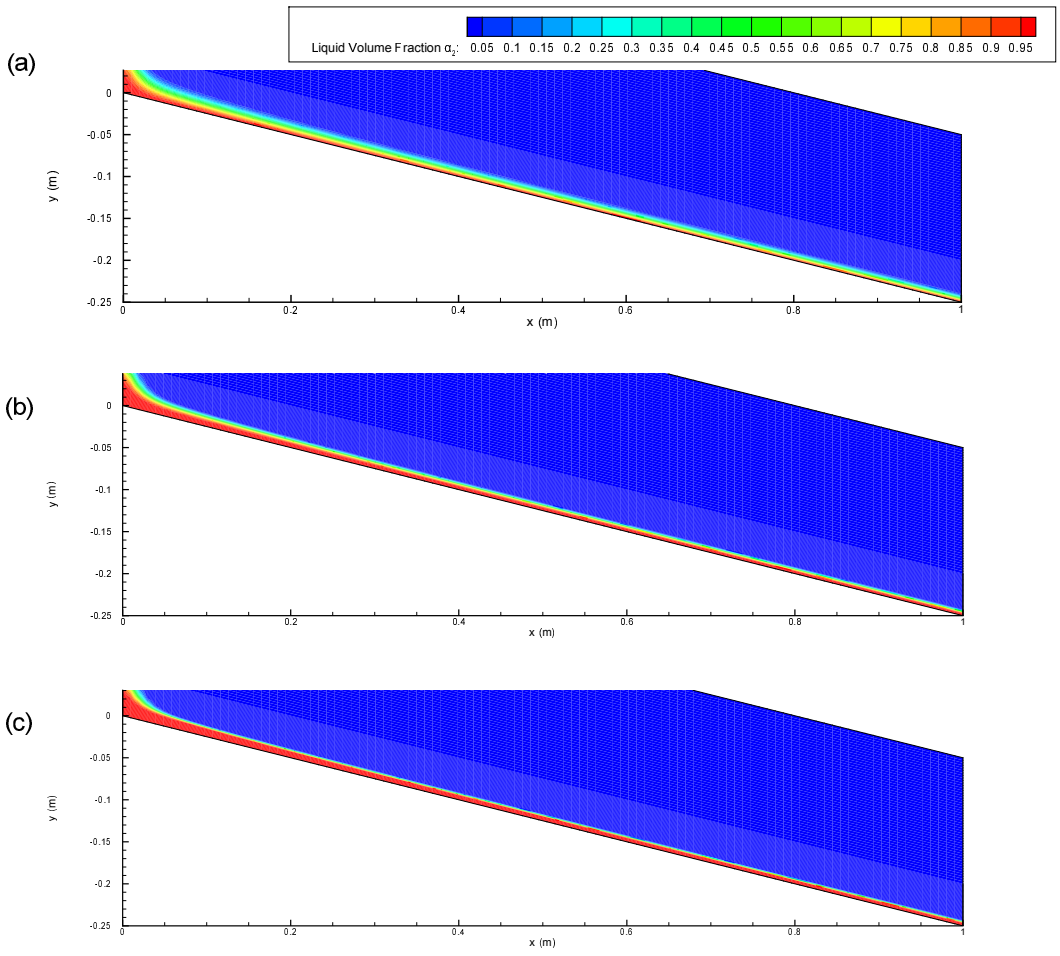

Figure 4.7: Results from the VOF, when using the (a) first-order upwind, (b) second-order upwind, and (c) HRIC discretisation scheme.

Mass flow rate, Q (kg s^{-1})	5×10^{-5}
Angle, θ (rad)	8×10^{-3}
Solution Density, ρ (kg m^{-3})	1000
Solution Viscosity, μ (Pa s^{-1})	0.001
Width, B (m)	1

Table 4.1: Parameters for the computational simulations when comparing the VOF model to the Nusselt solution (2.14).

be seen that as the mesh size increases the interface predicted by the model convergences to a steady solution. Furthermore, the VOF model appears to produce results similar to these of the Nusselt solution. When comparing these results it can be observed that the Nusselt solution gives a slightly thinner interface to that of the VOF model, however as discussed in Chapter 2, the Nusselt solution is often known to underpredict the height of the free surface. As this is the case the results obtained in this study offer reasonable confidence that the VOF is implemented and functioning correctly.

4.2.5 Summary

This section has assessed the various discretisation schemes that can be implemented when solving the VOF model. Several problems have been highlighted with numerical diffusion at the interface between the fluids when using the standard discretisation schemes typically used for solving the Navier Stokes equations. Results demonstrated that the interface accuracy and resolution greatly increases when using the HRIC scheme. This section has also highlighted the need for a high quality (preferably quadrilateral) mesh in the region of the interface. The position and orientation of the interface is shown to converge to a steady solution, as the mesh size is increased. Results were compared against the analytical Nusselt solution for thin liquid flows and are shown to be in good agreement. This trial therefore provides a reasonable level of confidence that the VOF method is both accurate and appropriate when considering the flow of liquid films similar to those observed in the NNL studies.

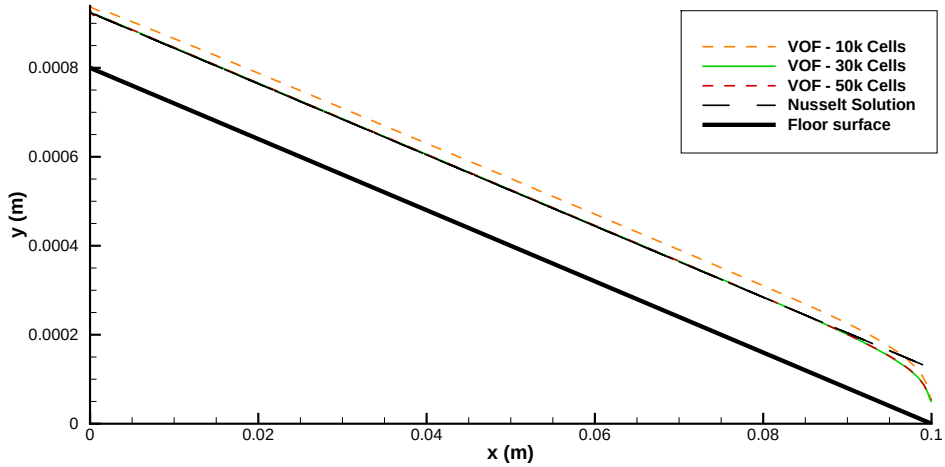

(a)

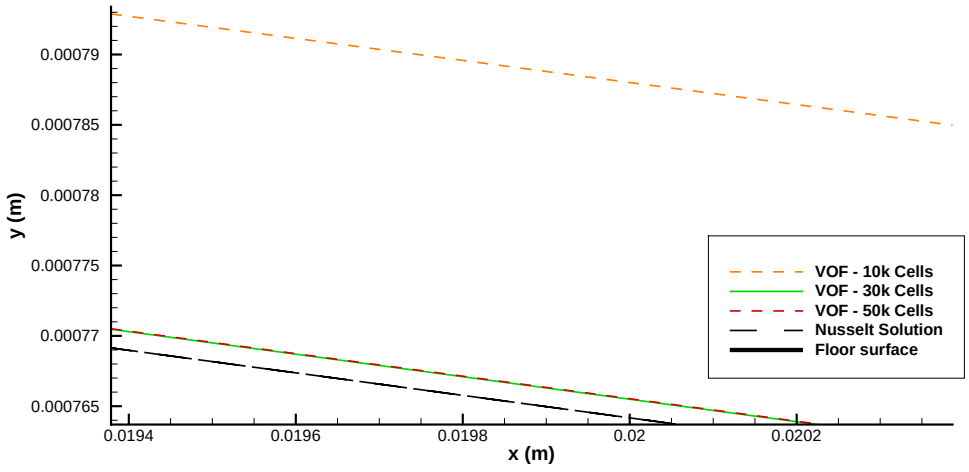

(b)

Figure 4.8: Plots of the interface, for (a) the full domain and (b) a small section of the film, obtained by the VOF model for varying mesh size when compared to the Nusselt solution, using the parameters given in Table 4.1.

4.3 Solute Transport

4.3.1 Governing Equations

Transportation of solute within a solution has been described by solving a scalar advection-diffusion equation in several studies (as discussed in Chapter 2.4). Examples of which can be seen in [118, 191, 183, 197]. This equation, namely the solute transport equation is given by,

$$\frac{\partial c}{\partial t} + \mathbf{u} \cdot \nabla c = \nabla \cdot (D \nabla c), \tag{4.14}$$

where c is the concentration of solute in solution and D is the diffusion coefficient or diffusivity of solute within the solution.

When coupled to the fluid flow, (4.1) and (4.2) are initially solved in order to obtain the momentum field. Once complete, the solute transport equation can then be discretised using the standard methods outlined in Section 4.2.1.

4.3.2 Domain and Boundary Conditions

In Chapter 2 it is stated that when a crystallisation process occurs, a low concentration region is observed close to the crystal face. This is because solute is absorbed from the solution into the crystal lattice. Solute from the bulk of the fluid then travels towards the crystal face due to the concentration gradient via diffusion. This effect was not observed in the model presented in Chapter 3, as it did not model the diffusion of solute explicitly. As the solute transfer equation now accounts for diffusive effects explicitly via a Fickien law, we can modify the previous reaction diffusion equation such that only the reaction, or surface integration step, is imposed. In order to test this the geometry in Figure 4.9 is considered. Boundary conditions for the fluid flow outlined in Section 4.2.3 are again used, however the additional boundary condition,

$$c(\mathbf{x}, t) = c_{in} \quad \text{for } \mathbf{x} \in \Omega_{inlet}, \tag{4.15}$$

is imposed, where the parameter c_{in} is the solution concentration upon entry into the domain.

On the crystal face $\Omega_{crystal}$ the conditions described in (3.12) are considered. As the surface integration layer is of the order 1-10nm above the crystal face, here it is assumed that the crystal face and surface integration layer are both identical and therefore the following flux condition can be imposed,

$$-D\frac{\partial c}{\partial n} = k_r(c(\mathbf{x},t) - c^*)^\eta, \quad \text{for } \mathbf{x} \in \Omega_{crystal} \tag{4.16}$$

where $\Omega_{crystal}$ is the boundary denoting the crystal surface, k_r is a coefficient of surface integration, $c^* = c^*(T)$ is the concentration at solution saturation for temperature, T, and η is the order of the reaction.

It should be noted that the energy equation can also be solved such that spatial and temporal variations in the temperature can be considered, and hence different saturation values obtained. Due to the uncertainty in the experimental temperature data highlighted in Chapter 3, the CFD studies in this work assume that the system is isothermal in both space and time. Therefore the work in this chapter will not solve the energy equation at this stage. Details of the energy equation and how it is implemented can be found in Chapter 5.

4.3.3 Results

An example of the results for the model with an arbitrary parameter set can be found in Figure 4.10. From this figure the low concentration region close to the crystal face can be seen.

Previous theory discussed in Chapter 2 stated that the width of the mass transfer boundary layer, and hence the effects of diffusion on the crystal growth, are dependent on the diffusivity and the flow velocity. In order to test this theory when using the solute transport equation, a short study was carried out such that the velocity and diffusivity were varied independently, and the height of the mass transfer boundary was observed. The parameters for these runs are given in Table 4.2.

Figure 4.11 shows the heights of the mass transfer boundary layer along the floor surface

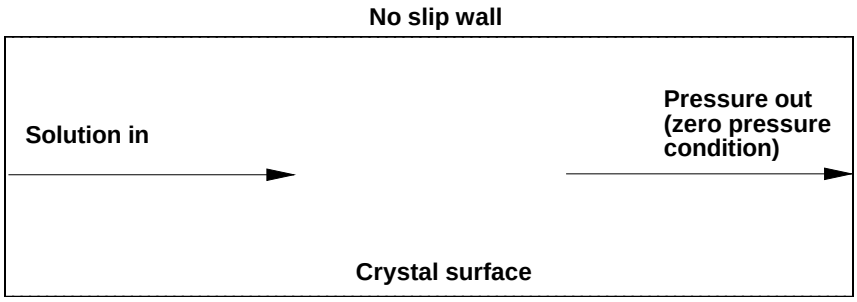

Figure 4.9: The domain and boundary conditions used when testing the solute transport model.

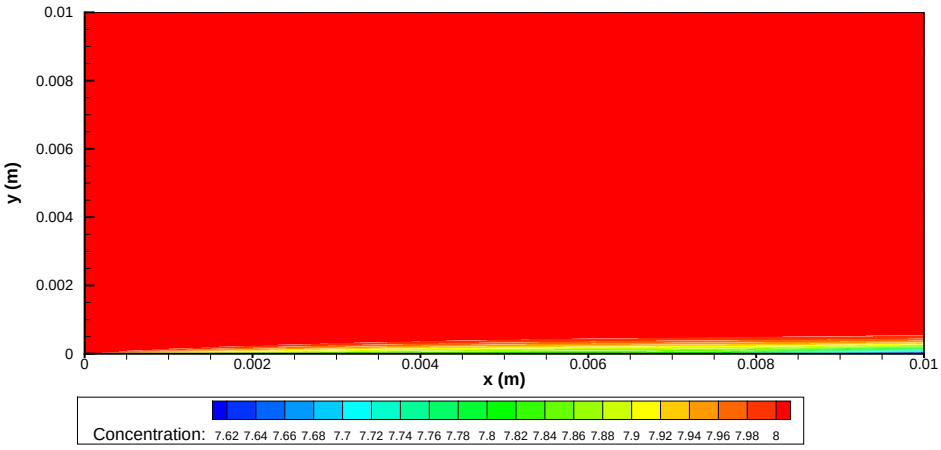

Figure 4.10: Plot of the solute concentration throughout the domain.

Coefficient of surface integration, k_r (m s^{-1})	8.9×10^{-6}
Initial concentration, c_{in} (Molar)	8
Solution density, ρ (kg m^{-3})	1000
Solution viscosity, μ (Pa s^{-1})	0.001

Table 4.2: Parameters for the computational simulations when testing the solute transport model.

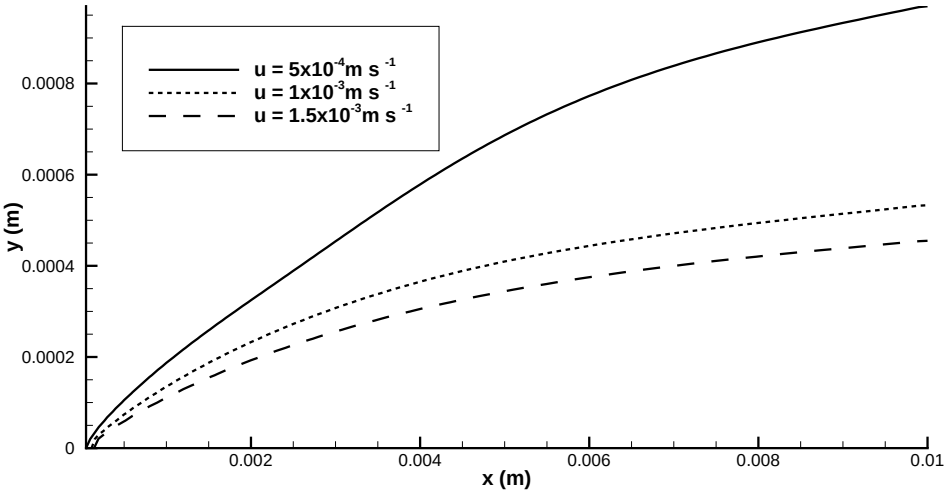

Figure 4.11: Plot of the mass transfer boundary layer for varying fluid velocity. The horizontal fluid velocity at the inlet is given by u.

when varying the flow velocity. The mass boundary layer is assumed to end when the concentration gradient perpendicular to the crystal face reaches zero. From observing the results in Figure 4.11 it can be clearly seen that as the velocity increases, the size of the mass transfer boundary layer decreases. It should also be noted that the concentration on the crystal face increases with the decreasing boundary layer width. These results agree with the theory presented in the original reaction-diffusion model, as discussed in Section 2.2.3.

Having considered the effects of the velocity on the mass transfer boundary layer. Computational experiments were carried out such that the effects of varying the diffusivity of solute within the solution can be considered. The mass transfer boundary layer thickness obtained from these computational runs are presented in Figure 4.12. From this figure, it can be observed that increasing the diffusivity consequently increases the thickness of the mass transfer boundary layer. Conversely, for low diffusivities a small region of very low concentration is found close to the crystal surface, this then sharply transitions to the bulk concentration value, which is reflected as a decrease in boundary layer height. The decrease in boundary layer height is due to the solutes inability to diffuse from the bulk of the solution and therefore lower concentrations are experienced on the crystal surface.

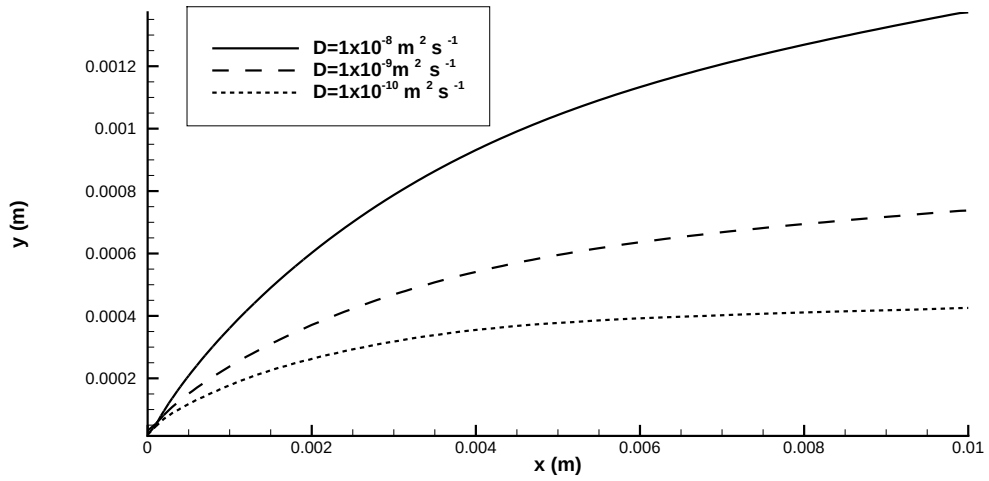

Figure 4.12: Plot of the mass transfer boundary layer for varying solute diffusivity, D.

4.3.4 Summary

The solution of the solute transport model is relatively simple to solve in comparison to the NVS equations or the VOF model. The aforementioned equations are challenging due to the pressure-velocity coupling and the unwanted inclusion of numerical diffusion at the interface. As neither of these have to be considered in the solute transport model, solution of the model is straight forward. Initial tests on the model suggested that the solution to the solute transport model has little variation when changing the numerical scheme, and accurate solutions were obtained when using computational grids with a relatively low number of elements (in comparison to the VOF model).

Studies in this section have confirmed that modelling the diffusion explicitly through the solution of the solute transport equations does in fact produce mass transfer boundary layers as discussed in the theory. Moreover, the results are consistent with previous experimental observations regarding the boundary layer thickness in relation to the flow velocity and solute diffusivity. As expected, this approach is an advancement on the previous reaction-diffusion model as the effects of the flow now alter the relative impact of the diffusion process.

4.4 Moving Boundary Methods

4.4.1 Introduction and Modelling Methodology

The description of mass deposition in CFD calculations can often be considered through a number of different numerical approaches. An overview of these different methods can be found in Section 2.4. These methods are generally separated into sharp and diffusive, moving boundary methods. A review of the literature in Chapter 2 highlighted that diffusive methods were used extensively when describing the crystal interface and its evolution through time. Whilst this is the case, there appear to be no studies which use diffusive methods when considering a multiphase fluid system (such as film flow). It is assumed that due to the thickness of the film and the impact of the gravitational forces on the behaviour, the fluid film is highly sensitive to the local geometry of the crystal surface. Therefore, it is expected that any numerical diffusion present at the crystal surface could therefore have a large impact on the accuracy and stability of the solution to the VOF equations. It is thus anticipated that these diffusive boundary tracking techniques are not appropriate when using the VOF model. As it is the intention to later couple the VOF model with a crystal growth model, a sharp interface model will be considered, such that the deposited solid is described by a non-diffusive moving boundary. As the system is assumed to be isothermal, there is no requirement to model heat transfer or any other physical effects within the crystalline solid itself (assuming a non-porous material), therefore no numerical grid is required for this region. As this is the case, the numerical domain used will be deformed such that the boundary describing the crystal-liquid interface (or floor surface at $t = 0$) will be moved. The displacement of this boundary will describe the volume of solid matter deposited.

For the type of sharp interface model discussed, once the boundary is displaced the computational grid representing the domain needs to deform such that it fits the domain at each new boundary position. The movement of the mesh can be described by a number of different approaches. In this case, for a given displacement of a boundary, the movement of the mesh is considered as a displacement force, the faces of the mesh elements are then assumed to be a network of springs, such that any force imposed by the displaced boundary is damped, this is described by Hooke's law,

$$\mathbf{F_{damped}} = -k_{spring}\mathbf{x}_{dis} \tag{4.17}$$

where $\mathbf{F_{damped}}$ is the force, k_{spring} is the spring constant factor and $\mathbf{x}_{dis}$ is the displacement.

In the system imposed here, the spring constant factor is normalised, such that when $k_{spring} = 0$ the connections between the nodes are rigid, and therefore no damping is enforced. In this case, the displacement is propagated throughout the entire system. For $k_{spring} = 1$ the damping is severe and therefore the displacement is contained to regions close to the boundary.

4.4.2 Effects of the Moving Mesh Parameters

In order to test a simple moving boundary case, such that the relevant importance of the spring constant factor can be observed, a simple rectangular geometry is considered, where a triangular mesh is mapped onto the domain. Figure 4.13(a) shows a small region of this domain such that the individual mesh elements can be seen.

A small displacement is then applied to the bottom boundary surface, and the mesh is moved to fit this new domain. Results from this can be seen in Figure 4.13(b) for when $k_{spring} = 1$. It should be noted that the remaining boundaries in the domain can move freely (in this study), therefore any propagation carried throughout the system can also affect these boundary nodes. From observing the results in Figure 4.13(b) it can be seen that whilst the mesh has been displaced to fit the new geometry, the quality of the mesh close to the deformation has deteriorated. As the spring constant is set to unity, the force due to the boundary motion is heavily damped, and therefore only the nodes close to the boundary are affected. This therefore leads to a reduction in volume of the cells close to the boundary and consequently they become skewed.

An additional run is then carried out for $k_{spring} = 0$ and the results are shown in Figure 4.13(c). From this figure it can now be seen that as the boundary displacement is propagated throughout the entire mesh, the cell volume and quality remains constant

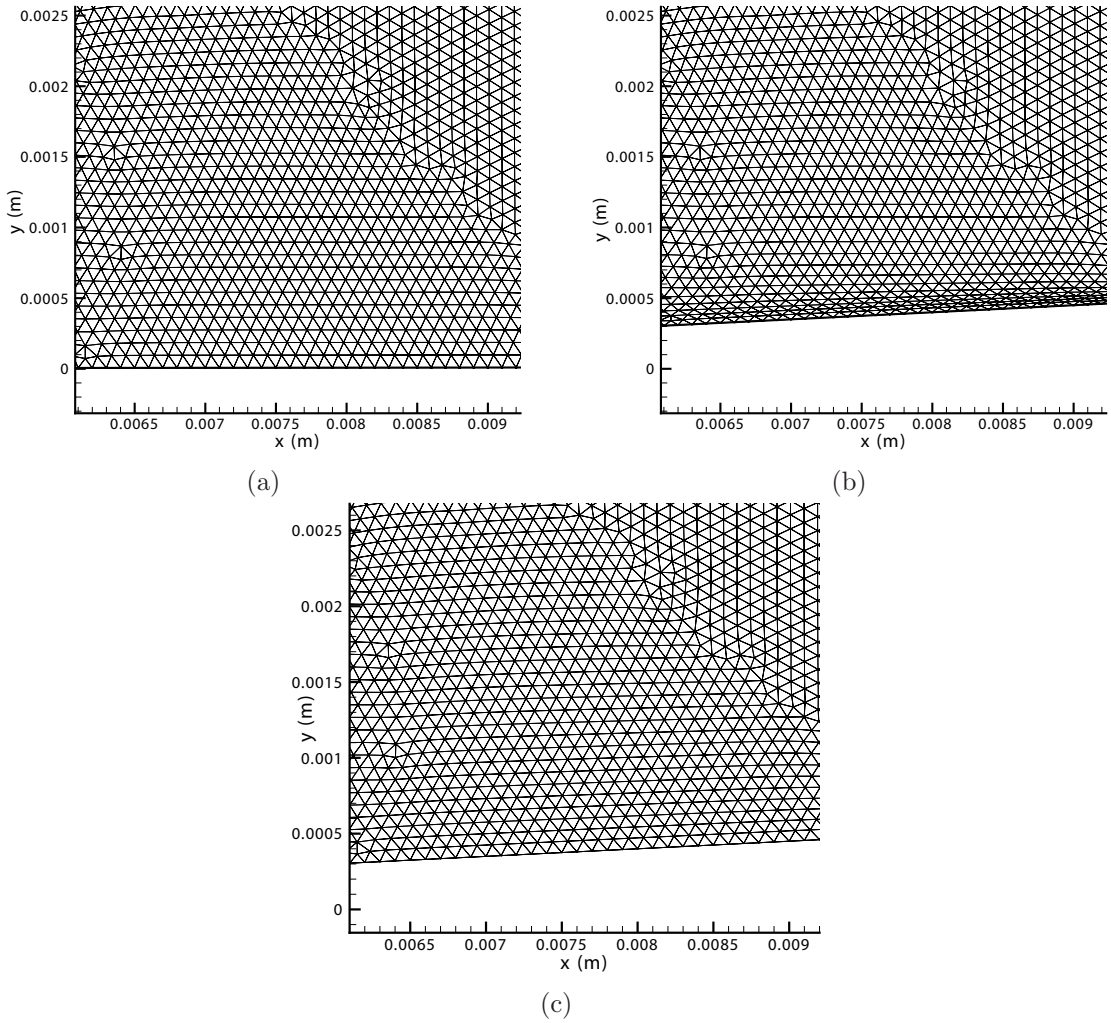

Figure 4.13: Plot of the (a) initial mesh, (b) mesh after successive boundary motions when $k_{spring} = 1$, and (c) mesh after successive boundary motions when $k_{spring} = 0$.

throughout.

Moreover, for triangular elements in regions in which the deterioration of the mesh quality and volume is unavoidable, an option to automatically remesh these elements is available. When remeshing is enabled, cells of poor quality are removed from the domain and new cells of acceptable quality are then incorporated, such that they connect to the remaining original mesh. Despite this, the method is not always able to remesh the cells and therefore, for the most robust approach, a combination of suitable spring constant parameters and remeshing should be implemented.

4.5 Coupled Fluid Flow Model - Crystallisation Model with Moving Boundary Techniques

Now that the individual components have been assessed and developed, this section considers the coupling of the models such that a complete framework for describing mass deposition from thin liquid films can be obtained. Whilst the techniques here can be used for a wide range of mass transfer problems, only deposition due to crystallisation will be considered in this case. The crystallisation mechanism considered will be due to heterogeneous nucleation, and therefore the crystallisation only occurs at the boundary (see Chapter 2). It is assumed that the nucleation timescales are small in relation to the timeframe considered and therefore the nucleation mechanism will not be modelled. Whilst the individual models have been discussed in depth, additional considerations often have to be made when coupling them, therefore this section highlights these considerations and tests the completed framework.

In this section, two methods are proposed. The first, whilst implementing finite volume models and solving the NVS, will only consider a single phase fluid. The position of the upper boundary in the domain is modified using moving boundary techniques, such that it represents the gas liquid interface. The height between the crystal surface and this upper boundary is given by the Nusselt approximation in (2.14). This approach will also aid in keeping computational cost to a minimum for the study when compared to the VOF, which is highly computationally expensive, and as the problem requires the modelling of crystallisation over large time-scales, the computational cost is already sig-

nificant. Furthermore, studies on moving boundaries and dynamic meshing have shown that quadrilateral meshes do not function well, whilst the VOF model has shown the need for highly refined quadrilateral mesh at the liquid-gas interface, suggesting that the two models are incompatible.

The second method proposed addresses the aforementioned challenges by coupling the VOF model with moving boundary techniques. Whilst the computational cost of using the VOF is more expensive than a single phase approach, it allows a wider range of model parameters to be considered. Furthermore, the VOF model allows greater flexibility in the final framework, such that there are less limitations when coupling additional physics in further work.

4.5.1 Coupled CFD - Crystallisation Model when using a Single Phase Fluid Model

4.5.1.1 Governing Equations

In the proposed framework developed here the fluid flow is described by the two-dimensional, steady state Navier Stokes equations, given by (4.1) and (4.2). After a solution to the fluid flow is obtained the solute transport equation in (4.14) is solved.

As this approach now models diffusion explicitly, the loss of solute in solution due to the crystallisation mechanism can be given by (4.16). The growth of crystalline mass is described by a moving boundary such that for a given timestep Δt the boundary displacement is given by,

$$\Delta \mathbf{S} = -(\Delta t) k_r \frac{M_s}{\rho_s} (c(\mathbf{x}, t) - c^*)^\eta \mathbf{n}, \quad \text{for } \mathbf{x} \in \Omega_{crystal}, \tag{4.18}$$

where $|\Delta \mathbf{S}|$ is the magnitude of the crystal growth at $\mathbf{x}$ in time Δt, $\mathbf{n}$ is the outward facing normal and $\Omega_{crystal}$ is the boundary describing the crystalline surface.

As the rate of crystallisation is slow relative to the fluid flow, it is assumed that over the time-frame, Δt, the fluid flow can assumed to be at a steady state.

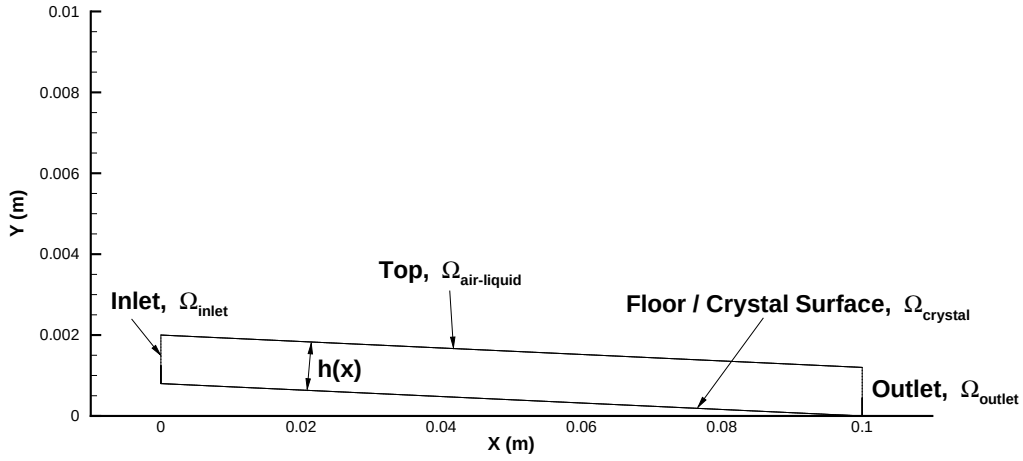

Figure 4.14: Plot of the initial domain used in the coupled CFD - crystallisation, single phase model.

4.5.1.2 Domain and Boundary Conditions

The initial domain used can be observed in Figure 4.14, where a mass flow boundary condition is placed on the inlet, given by,

$$\mathbf{u} \cdot \mathbf{n} = \frac{Q}{A}, \quad \text{on } \Omega_{inlet}, \tag{4.19}$$

where $\mathbf{u}$ is the fluid velocity, $\mathbf{n}$ is the inward normal to the surface, Q is the mass flow rate of liquid and A is the area of the inlet.

The crystal surface, $\Omega_{crystal}$, (or floor at the initial boundary condition) has a no-slip boundary condition implemented, where $\mathbf{u} = \mathbf{0}$.

The outlet, Ω_{outlet}, is classed as a pressure outlet where a gauge pressure, $p' = 0$ is specified.

A no-shear condition is in place on the liquid-air interface, $\Omega_{air-liquid}$ such that, $\frac{\partial u}{\partial n} = 0$. The height of the film is calculated by (2.14) and the nodes on $\Omega_{air-liquid}$ are displaced at each pseudo time-step such that the height of the domain satisfies this criteria.

Boundary	Boundary condition type
Liquid Inlet Ω_{inlet}	Mass Flow Inlet
Outlet, Ω_{outlet}	Zero Gradient Pressure Outlet
Floor / Crystal Liquid Interface, $\Omega_{crystal}$	No Slip Condition
Air-liquid interface $\Omega_{air-liquid}$	No Shear Condition

Table 4.3: Boundary condition types for the fluid model when using the coupled CFD - crystallisation, single phase model.

Boundary	Boundary condition type
Liquid Inlet Ω_{inlet}	Constant concentration
Outlet, Ω_{outlet}	Zero Flux
Floor / Crystal Liquid Interface, $\Omega_{crystal}$	Flux condition (4.16)
Air-liquid interface $\Omega_{air-liquid}$	Zero flux

Table 4.4: Boundary condition types for the solute transport model when using the coupled CFD - crystallisation, single phase model.

The boundary condition (4.15) is imposed at the inlet, Ω_{inlet}, and the flux condition (4.16) is implemented at $\Omega_{crystal}$. The boundary conditions for the fluid flow and solute transport are summarised in Tables 4.3 and 4.4.

4.5.1.3 Moving Boundary Specifications

In order for the moving boundary model to function correctly, the behaviour of each boundary has to be specified. The FLUENT CFD package allows various specifications for the moving boundary model, however the boundary conditions of interest in the work here, are the 'deforming boundary condition' and 'user defined boundary condition'. The deforming boundary condition states that if a boundary is moved somewhere in the domain, this propagation throughout the mesh due to this movement can also affect these boundary nodes. For example, in the case here, if the crystal surface $\Omega_{crystal}$ is moved, this motion is propagated throughout the mesh. If the propagation is not completely damped before it reaches the adjacent boundary, $\Omega_{air-liquid}$, the nodes of $\Omega_{air-liquid}$ would also experience some level of movement (provided deforming boundary is specified). In many cases, this boundary condition is preferable to stationary or user specified boundary placements, as these restrict the freedom in which the domain can adapt to the boundary motion, therefore reducing the robustness of the dynamic meshing. Moreover, a bounded deforming boundary condition can also be defined such that these boundary

Boundary	Boundary condition type
Inlet Ω_{inlet}	Deforming (bounded to the line $x = 0$)
Outlet, Ω_{outlet}	Deforming
Floor / Crystal Liquid Interface, $\Omega_{crystal}$	User defined condition
Air-liquid interface $\Omega_{air-liquid}$	User defined condition

Table 4.5: Boundary condition types for the moving boundary model when using the coupled CFD - crystallisation, single phase model.

nodes can move, however their movement is restricted to a given plane, or path.

The user defined boundary condition allows the implementation of a user defined function (UDF) on to the boundary. These functions are written in C programming language and either define the displacement of each boundary node relative to its current position, or an exact coordinate in which the node's new position should lie. It should be noted that for the moving boundary model to be successful, displacements of the boundary nodes should be kept small for any given pseudo timestep Δt.

A summary of the imposed boundary types for the model can be found in Table 4.5.

4.5.1.4 Computational Implementation

Various solvers were used in order to solve the different equations described in the previous section. Steady state, discretised versions of equations (4.1) and (4.2) were solved within FLUENT using the Pressure Implicit with Split Operator (PISO) algorithm [92] for the pressure-velocity coupling. The PRESTO scheme is used in order to calculate the pressures at the computational cell faces and a least-squares scheme is used to evaluate the gradient terms. A first-order upwind scheme is used to solve the momentum and solute transport equations (4.14). Higher order schemes were trialled, however it was found that increasing the order of the scheme had very little impact on the results for the problem here. Therefore in order to maximise the robustness, and minimise the computational cost, first order schemes were used throughout the work. A summary of the solvers is given in Table 4.6.

The solver process was fully automated using the scheme programming environment within FLUENT. This code allows the automatic iteration of the boundary displacement

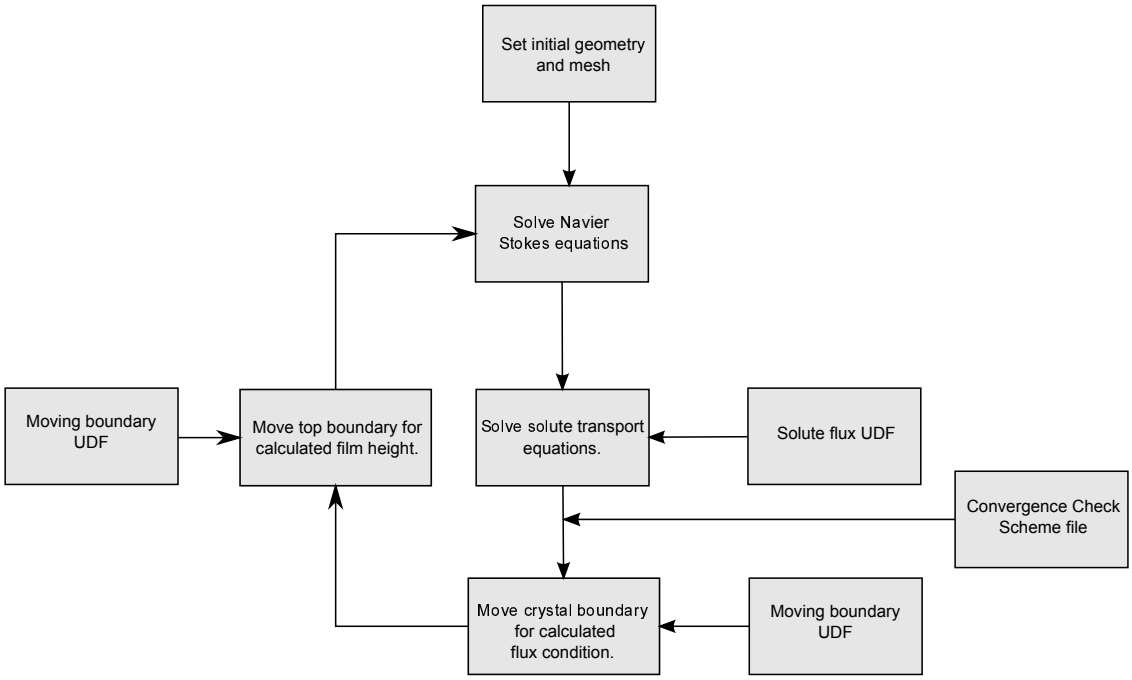

Figure 4.15: Flow diagram of the solution procedure for the single phase, coupled CFD - crystallisation model.

(4.18) and adjustment of the domain height $h(x)$ (2.14), for each steady-state solution of equations (4.1), (4.2) and (4.14), along with the boundary conditions described in this section. Using a combination of FLUENT scheme code and a UDF, a custom convergence criterion is set. As such, the convergence criterion can be changed such that it is based on surface monitors (such as mass flow rates and surface integrals). Convergence of these monitors identified that equations (4.1), (4.2) and (4.14) were solved, and the boundary displacement (4.18) could be carried out. The pseudo timestep was set to $\Delta t \leq 15$ minutes such that the boundary displacements at each timestep were small.

In addition to these procedures, remeshing is also enabled in an effort to improve the robustness of the moving mesh. Hence, a purely triangular mesh is used in this study. The full solver procedure can be seen within Figure 4.15.

4.5.1.5 Results

The work in this section considers the coupled implementation of the model to describe the growth of a two-dimensional crystal formation through time. The model is run with

Physics	**Solver**
Pressure Velocity Coupling	PISO
Gradient	Least-Squares
Pressure	PRESTO
Momentum	First-Order Upwind
Solute transport	First-Order Upwind

Table 4.6: Solvers used for the single phase, coupled CFD - crystallisation.

Mass flow rate, Q (kg s^{-1})	5×10^{-5}
Coefficient of surface integration, k_r (m s^{-1})	4.5×10^{-6}
Initial Concentration, c_{in} (Molar)	8
Saturation Concentration c^* (Molar)	7.75
Solution Density, ρ (kg m^{-3})	1000
Solution Viscosity, μ (kg m^{-3})	0.001
Pseudo-timestep, Δt (minutes)	15

Table 4.7: Parameters used in the single phase, moving boundary model.

parameters given in Table 4.7 and the initial geometry presented in Figure 4.14.

A plot of the domain after a simulated crystal growth time, $t = 2$ hours can be seen in Figure 4.16. From this figure it can be observed that the user defined moving boundary routines appear to be functioning correctly. It can be seen that the crystal surface begins to grow upwards close to the inlet. In response to this, the height of the domain begins to decrease in the regions in which the angle of inclination increases.

As the model was run for longer simulated growth times, it was noted that the internal meshing of the system starts to deteriorate. Whilst the remeshing facility implemented works to an extent, it appears to be unable to handle the high levels of deformation in the domain volume. Frequently the mesh quality deteriorates to a point where the numerical solver could no longer obtain a converged solution. Moreover, due to the sensitivity of the film height on the inclination angle of the surface, small changes in inclination would often lead to sharp changes in the film height. In extreme circumstances the dynamic meshing would produce an invalid mesh, such as cells with 'negative' volume, when the cell faces cross or overlap (Figure 4.17) or cases in which nodes or faces were placed out of the domain (Figure 4.18).

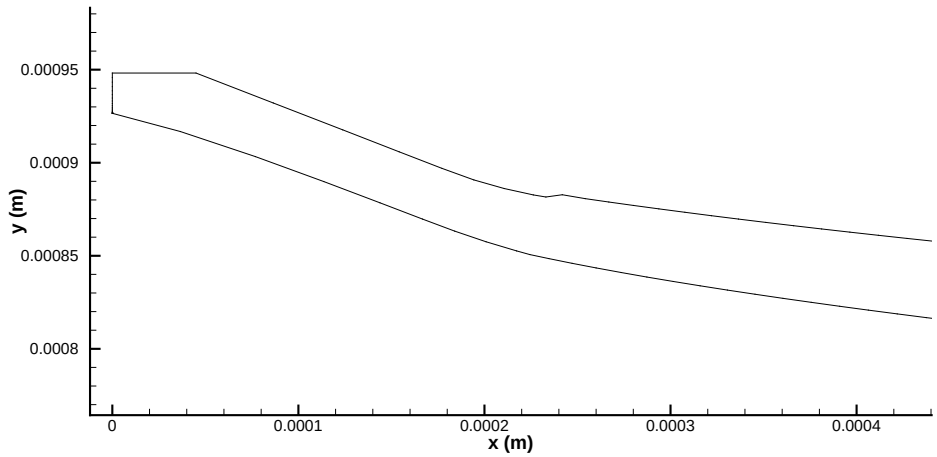

Figure 4.16: Plot of the displaced domain, after a simulated crystal growth time of $t = 2$ hours when using the single phase, coupled CFD - crystallisation model with parameters given in Table 4.7.

It is thought that these problems are experienced due to too many restrictions placed on the dynamic meshing. As the co-ordinates of the liquid-air surface were specified at each time-step, the mesh propagation through the domain due to motion of the crystal boundary did not propagate to the liquid-air boundary nodes, and over time the volume of the domain would decrease. As this is the case, the dynamic meshing facility begins to break down and eventually the solver fails. As the purpose here was to develop a robust moving boundary model, it was clear that this approach was not sufficient. Due to this an alternative approach was implemented, as described in the following subsection.

4.5.2 Coupled CFD - Crystallisation Model when using the VOF Model

While the concept of the first proposed model offered several advantages over the model in Chapter 3, whilst still keeping computational costs low, it is clear that limitations are present with regards to the robustness of the dynamic meshing. As the aim in the work is to produce a framework which can describe crystalline growths of a wide range of size and shapes, it is vital that the model continues to work for a large range of boundary deformations.

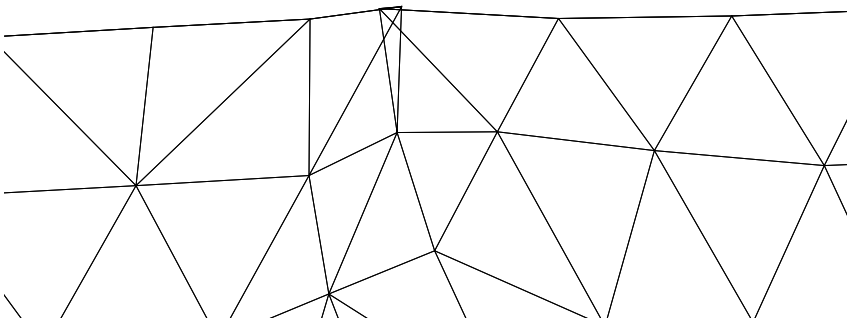

Figure 4.17: Example of a 'negative cell' volume experienced when using the single phase, using the single phase, coupled CFD - crystallisation model.

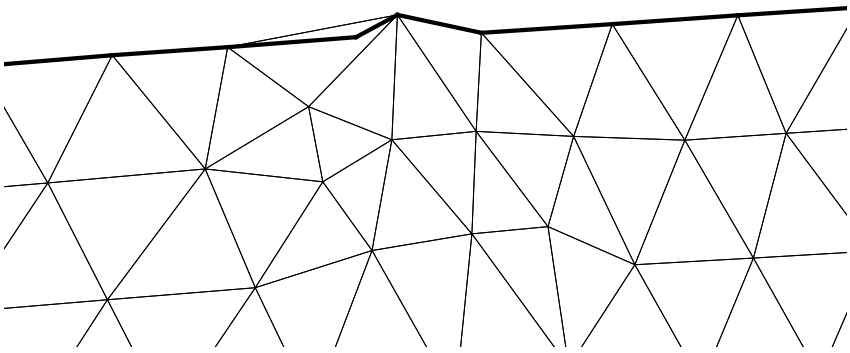

Figure 4.18: Example of a dynamic meshing failure when using the using the single phase, coupled CFD - crystallisation model, such that cell elements leave the domain.

4.5.2.1 Governing Equations

In this model, the steady state VOF equation is solved, such that time dependent terms in (4.8) can be ignored. In addition to this, the NVS equations (4.1) and (4.2), are solved such that a solution for the steady state fluid flow can be given.

Much like the model in Section 4.5.1, once a solution to the fluid flow has been obtained, the transportation of solute needs to be considered. The previous solute transport model considered the advection and diffusion of solute throughout the entire domain. As multiple fluids are now considered, the VOF model in (4.14) has to be modified such that solute is only considered in the liquid phase. Therefore (4.14) now becomes,

$$\mathbf{u} \cdot \nabla(\alpha_2 c) = \nabla \cdot (\alpha_2 D \nabla c), \tag{4.20}$$

where c is the concentration of sodium nitrate in solution and D is the diffusion coefficient. In this work, $q = 1$ corresponds to the gaseous phase and $q = 2$ corresponds to the liquid solution. Consequently, α_2 is the volume fraction of the liquid phase.

4.5.2.2 Domain and Boundary Conditions

The domain used can be seen in Figure 4.19 and is similar to that implemented in Section 4.5.1, however there are notable changes to the boundary conditions.

The previous boundary which represented the fluid inlet in the model in Section 4.5.1, is now split into two separate, but connected, boundaries. On these boundaries, $\Omega_{LiqInlet}$ and $\Omega_{AirInlet}$, mass flow boundary conditions are specified as,

$$\mathbf{u} \cdot \mathbf{n} = \frac{Q}{A_l}, \quad \text{on } \Omega_{LiqInlet}, \tag{4.21}$$

where $\mathbf{u}$ is the fluid velocity, $\mathbf{n}$ is the inward normal to the surface, Q is the mass flow rate of liquid and A_l is the area of the liquid inlet. A mass flow rate of,

$$\mathbf{u} \cdot \mathbf{n} = \frac{Q_a}{A_a}, \quad \text{on } \Omega_{AirInlet}, \tag{4.22}$$

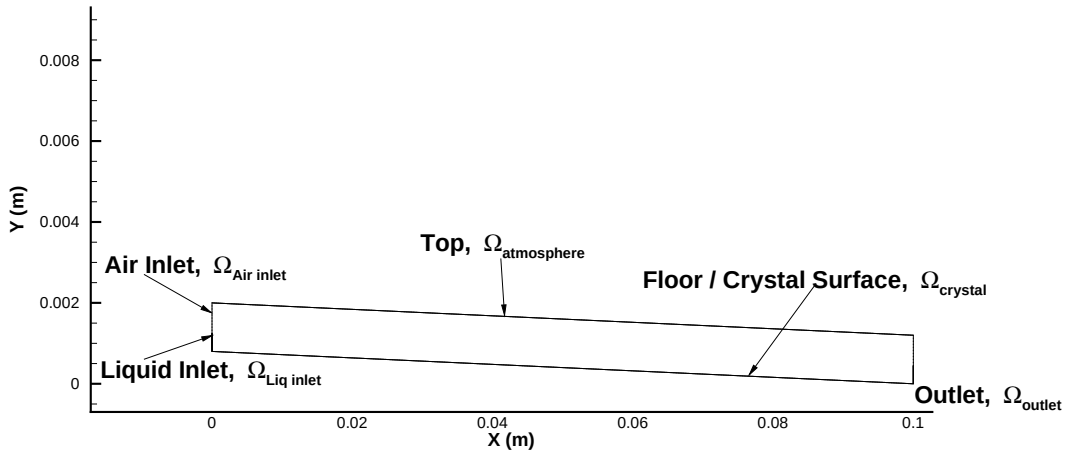

Figure 4.19: The initial domain and the boundary condition types used in the VOF, moving boundary model present in Chapter 4.5.2.

is imposed at the air inlet, where Q_a is the mass flow rate of the air phase and A_a is the area of the gaseous inlet.

The crystal surface, $\Omega_{crystal}$, has a no-slip boundary condition implemented, where $\mathbf{u} = \mathbf{0}$.

The outlet and atmosphere boundaries are defined as a pressure outlets, where a gauge pressure, $p' = p - p_{atm}$ specified (where p is the absolute pressure and p_{atm} is the atmospheric pressure). Within this work we specify $p' = 0$. This differs from the model in Section 4.5.1, where a no-shear condition was placed on the top boundary.

The concentration $c = \alpha_2 c_{in}$ is imposed at the inlets and the flux condition (4.16) is implemented at the floor / crystal-liquid interface using UDF's. A summary of the fluid and solute transport boundary conditions imposed in this model can be found in Tables 4.8 and 4.9, respectively.

4.5.2.3 Moving Boundary Specifications

Much like the previous implementation of the moving boundary model, the moving boundary conditions on each boundary of the domain need to be specified. The moving boundary conditions for the model here are the same as those presented in Section 4.5.1.3, with the

Boundary	Boundary condition type
Liquid Inlet $\Omega_{liqinlet}$	Mass Flow Inlet
Air Inlet $\Omega_{airinlet}$	Mass Flow Inlet
Outlet, Ω_{outlet}	Zero Gradient Pressure Outlet
Floor / Crystal Liquid Interface, $\Omega_{crystal}$	No Slip Boundary Condition
Top, $\Omega_{atmosphere}$	Zero Gradient Pressure Outlet

Table 4.8: Boundary condition types for the fluid model when using the VOF, coupled CFD - crystallisation model.

Boundary	Boundary condition type
Liquid Inlet Ω_{inlet}	Concentration
Air Inlet $\Omega_{airinlet}$	Concentration
Outlet, Ω_{outlet}	Zero flux
Floor / Crystal Liquid Interface, $\Omega_{crystal}$	Flux condition (4.16)
Top, $\Omega_{atmosphere}$	Zero flux

Table 4.9: Boundary condition types for the solute transport model when using the VOF, coupled CFD - crystallisation model.

exception that $\Omega_{air-liquid}$ is now defined as $\Omega_{atmosphere}$ and is specified as a 'deforming boundary'. A summary of the moving boundary conditions can be found in Table 4.10.

4.5.2.4 Computational Implementation

In order for the system of equations to be solved using the finite volume method, a numerical grid or mesh has to be mapped onto the domain. This domain can be seen in Figure 4.19. When constructing a mesh several things need to be considered. Firstly, it is desirable to keep the number of cells at a minimum whilst retaining an acceptable solution accuracy. This allows the computational costs to be kept low, such that increases in cell count have a negligible effect on the solution, known as mesh independence.

Boundary	Boundary condition type
Liquid Inlet, Ω_{inlet}	Deforming (bounded to the line $x = 0$)
Air Inlet, $\Omega_{airinlet}$	Deforming (bounded to the line $x = 0$)
Outlet, Ω_{outlet}	Deforming
Floor / Crystal Liquid Interface, $\Omega_{crystal}$	User defined condition
Top, $\Omega_{atmosphere}$	Zero flux

Table 4.10: Boundary condition types for the moving boundary model when using the VOF, coupled CFD - crystallisation model.

The multiphase VOF model being used to capture the fluid flow is a diffusive interface model and therefore there exists a numerical blending between the two regions. Due to this, a refined region of highly refined quadrilateral cells is required such that the interface lies within this region. This is in order to minimise the diffusive flux across the interface.

The last consideration needed when constructing the computational grid, which is specific to the moving boundary approach implemented here, is the robustness of the mesh when deformed using the dynamic meshing. The dynamic meshing facility has inbuilt remeshing, whereby if a given cell either exceeds a maximum volume or falls beneath a minimum volume, or if it becomes too distorted, the model attempts to remesh the region local to this cell. For this facility to work, the mesh must however consist of triangular elements (in two dimensions). This facility is required if the dynamic meshing is to be robust.

As the height of the liquid-gas interface is unknown prior to solving the steady state system of equations (4.1), (4.2), (4.8), an inefficient way of satisfying the first criterion would be to have a highly refined mesh throughout the entire domain. This however would violate the second criterion of keeping the mesh count to a minimum. Therefore, within this work a variable mesh size was used, with the height of the highly refined region being approximated by the Nusselt solution (2.14).

As the velocities of the gas phase are specified such that they are very small in comparison to the film flow, they have little impact on the solution and therefore a coarser mesh can be used throughout this region. In order to satisfy the last criterion when constructing the mesh, a coarse triangular mesh was placed in the region not covered by the refined region. The final mesh that was seen to satisfy all the required criteria is shown in Figure 4.20. Due to the previous study regarding the mesh independence of the VOF model, and that this model is considered to have the largest requirements with respect to the mesh size, an initial mesh of $40,000$ cells was used, such that the resultant formation shape was unchanged for increases in initial cell count.

The volume fraction equation (4.8) was solved using the HRIC scheme [136]. As previously mentioned, as a steady state solution to the model is considered for any given boundary position, the time dependant terms within the model can be neglected.

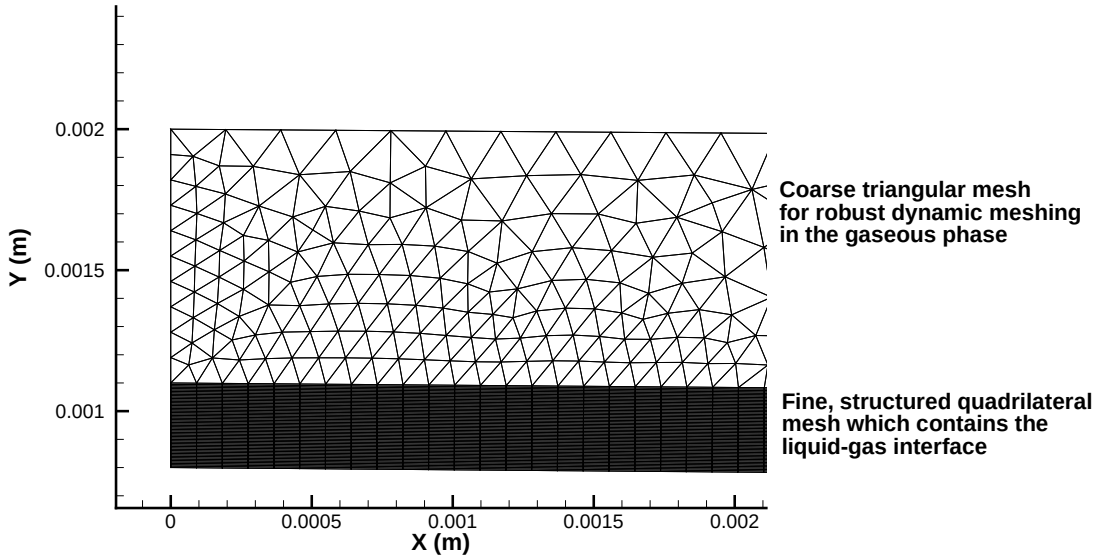

Figure 4.20: Example of the combined structured and unstructured mesh. Optimised for use with the VOF and moving boundary model.

Physics	**Solver**
Pressure Velocity Coupling	PISO
Gradient	Least-Squares
Pressure	PRESTO
Volume Fraction	HRIC
Momentum	First-Order Upwind
Solute transport	First-Order Upwind

Table 4.11: Solvers used for the VOF, coupled CFD - crystallisation model.

In a similar fashion to the previous implementation (Section 4.5.1.4), the governing system of equations (4.1), (4.2), (4.8) and (4.14) is solved to steady state. Once convergence is reached, the boundary denoting the crystal surface is then displaced by (4.18). The automation of the system is implemented by used of UDFs and FLUENT scheme code, as described in Section 4.5.1.4. A summary of the solver settings used can be found in 4.11. A full summary of the solver procedure can be seen in Figure 4.21.

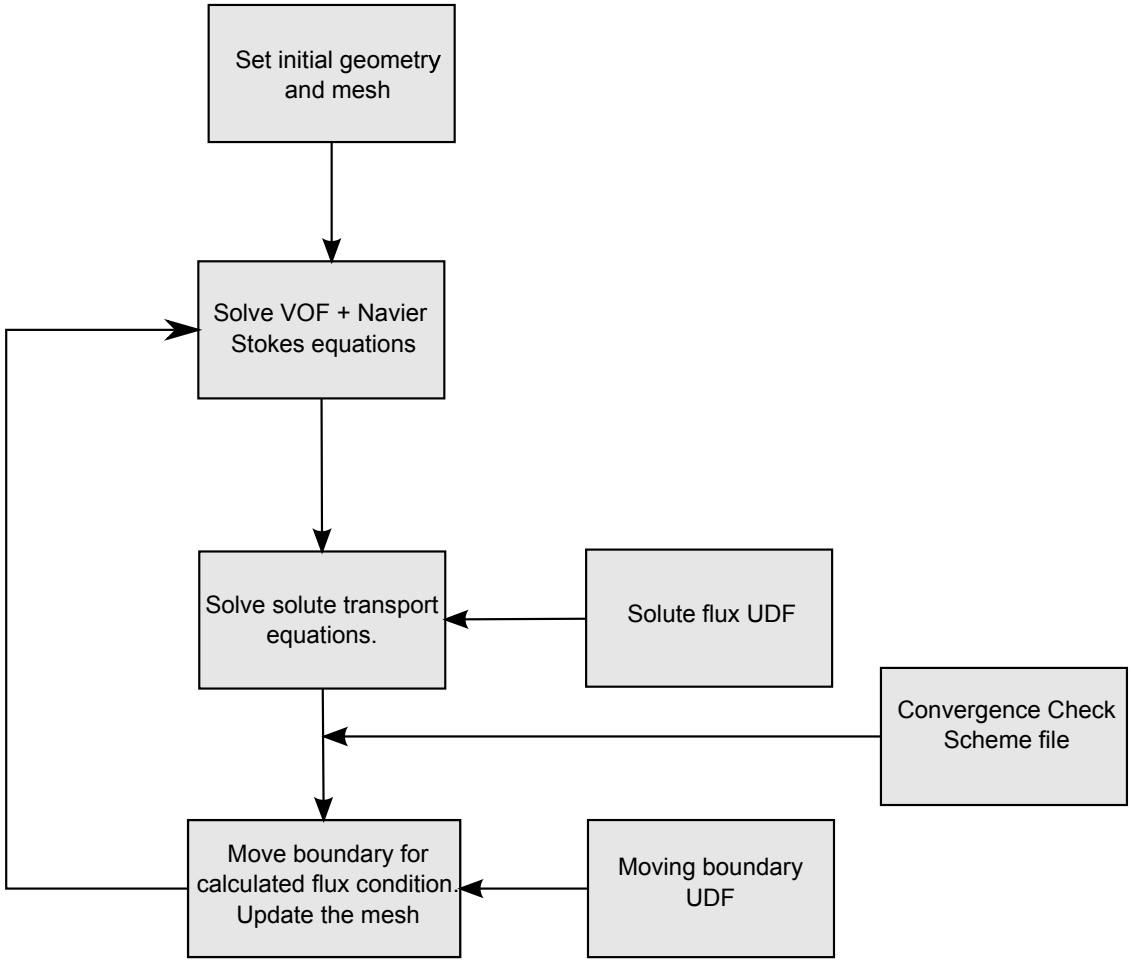

Figure 4.21: Plots of the initial domain used in the VOF, coupled CFD - crystallisation model.

Mass flow rate, Q (kg s^{-1})	5×10^{-5}
Coefficient of surface integration, k_r (m s^{-1})	4.5×10^{-6}
Initial Concentration, c_{in} (Molar)	8
Saturation Concentration c^* (Molar)	7.75
Solution Density, ρ (kg m^{-3})	1000
Solution Viscosity, μ (Pa s^{-1})	0.001
Pseudo-timestep, Δt (minutes)	15

Table 4.12: Parameters used in the VOF, coupled CFD - crystallisation model.

4.5.2.5 Results

In order to assess the framework outlined in this section, initial tests are carried out in order to test that the system of coupled models is functioning correctly. It is not the aim within this chapter to obtain physically meaningful results, but rather focus on the implementation and optimisation of the numerical framework. However, it is beneficial to compare the model here with the adapted stalagmite model in Chapter 3. This test case will provide confidence that the system is robust enough such that it can handle the size and shape of deformations typically found when considering the industrial salt solutions. It will also allow the model to be verified such that each component is functioning correctly, such that accurate and meaningful results are obtained.

Initial tests on the model were carried out on the domain and mesh described previously in this section. The parameters used are summarised in Table 4.12. Initial results from the model showed similar behaviour to the adapted stalagmite model developed in Chapter 3, such that nodes close to the inlet would diverge and eventually the solver would fail. This can be observed in Figure 4.22(a).

The adapted stalagmite model in Chapter 3 solved this problem by inserting additional nodes into the computational grid, such that if an element exceeded a given length a new node would bisect this element. However, as the quadrilateral elements of the grid cannot be remeshed, no additional nodes can be added during the solution process, therefore this approach cannot be taken. Due to this, a new mesh adaptive technique had to be developed. This scheme assumed that once a solution at a given timestep was obtained for the boundary position, if the spacing between successive nodes exceeded a given length or

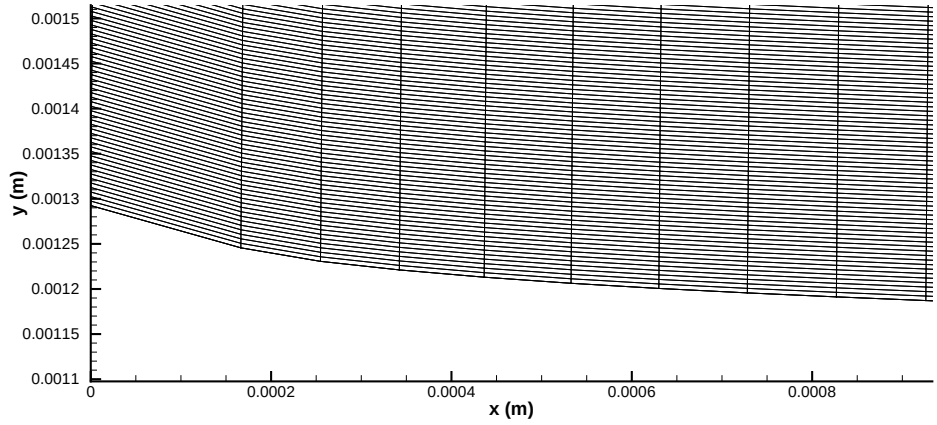

(a)

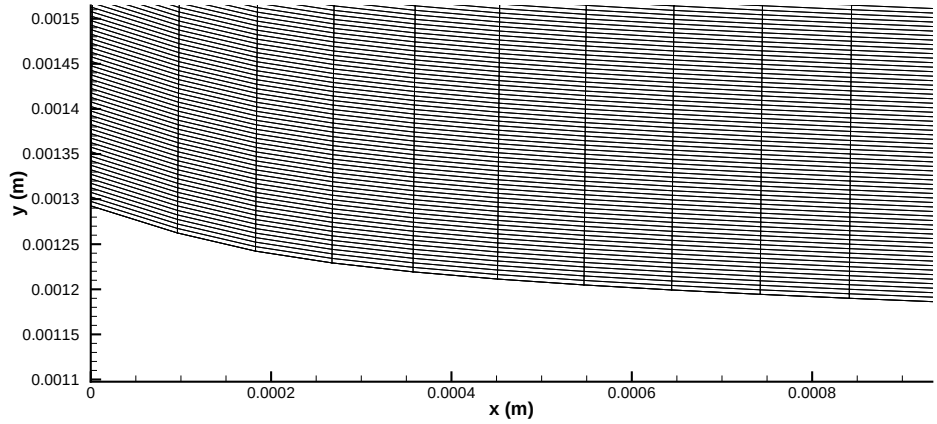

(b)

Figure 4.22: Plot of the nodes close to the inlet for the VOF, coupled CFD - crystallisation mode, after $t = 79$ minutes, with (a) no mesh adaption and (b) mesh adaption.

was smaller than a given length, the nodes could be repositioned on the current piecewise linear solution to the boundary. This method required that sufficient initial nodes were placed on the moving boundary, such that when large deformations were experienced, the resultant nodal spacing was still sufficiently small.

The model was run again using the same parameters as the previous study, however now the aforementioned adaptive meshing routine was implemented. The results from this run can be seen in Figure 4.22(b). These results only show a close up on a region of the domain, corresponding to the same position as the results in Figure 4.22(a). From comparing the results in Figures 4.22(a) and 4.22(b) it can be clearly observed that the results when using the mesh adaption no longer suffer from the divergence of the mesh points close to the inlet.

Following the framework being modified with the mesh adaption algorithms such that they functioned robustly, the model was run for a longer period of time such that the results obtained from this model can be compared to the results in Chapter 3. Whilst there are some key differences between the adapted stalagmite model and the model presented in this chapter, if the model here is seen to be functioning correctly the results obtained should be of a similar order of magnitude. Figure 4.23 shows the results for the model after 24 hours growth. From this figure it can be seen that whilst there are some differences between the results, as anticipated, they are similar enough to suggest that the model is functioning correctly.

A plot of the mesh close to the inlet boundary can be observed in Figure 4.24. From this figure it can be seen that the node spacing along the bottom boundary remains of an acceptable size, and the cells in the triangular region of the mesh remain a reasonable size and quality.

To offer further confidence, the models are compared again for a different parameter set, as shown in Table 4.13. The results from these trials can be found in Figure 4.25. From this figure it can be seen that again the results between the two models are comparable, therefore from these initial trials it can be assumed that the coupling between the individual models and and moving mesh is working correctly.

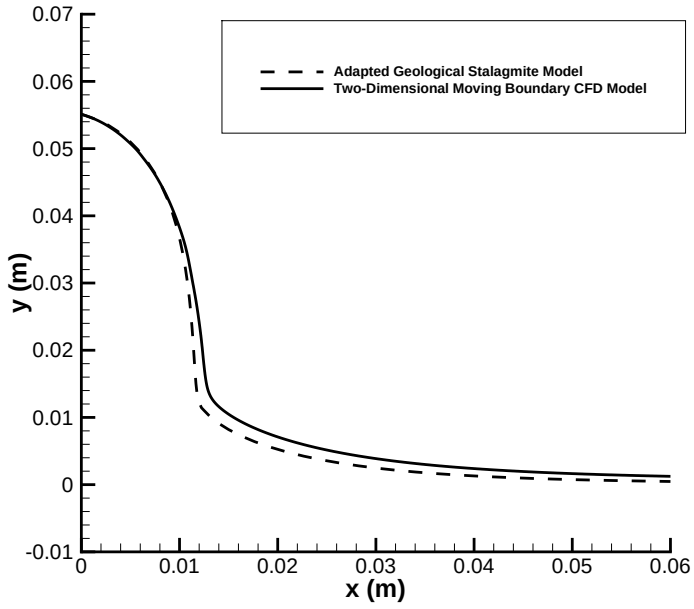

Figure 4.23: Plot of growths when comparing the adapted stalagmite model (Chapter 3) to the VOF, coupled CFD - crystallisation model, after $t = 24$ hours, using the parameters in Table 4.12.

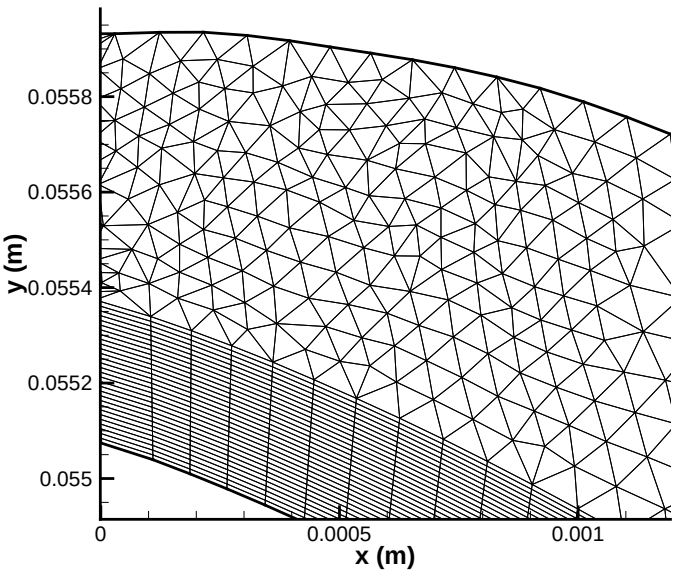

Figure 4.24: Plot of the mesh, close to the inlet, for the VOF, coupled CFD - crystallisation model after $t = 24$ hours, using the parameters in Table 4.12.

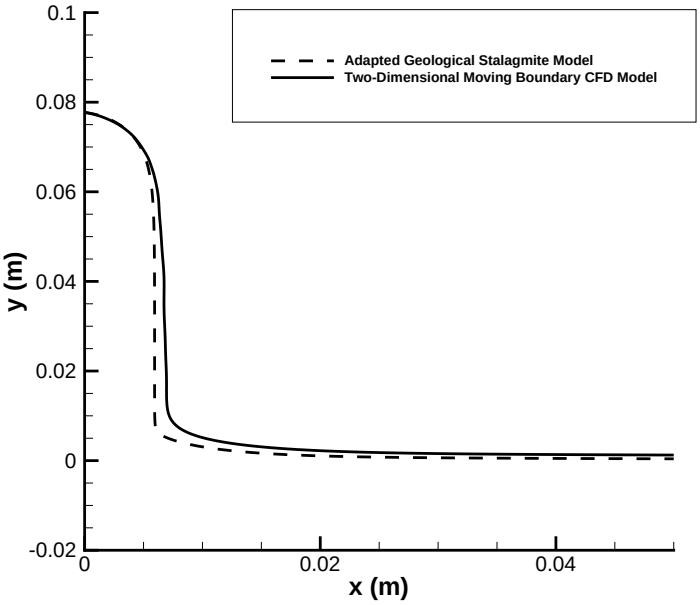

Figure 4.25: Plot of growths when comparing the adapted stalagmite model (Chapter 3) to the VOF, coupled CFD - crystallisation model, after $t = 36$ hours, using the parameters in Table 4.13.

Mass flow rate, Q (kg s^{-1})	2.89×10^{-5}
Coefficient of surface integration, k_r (m s^{-1})	4.5×10^{-6}
Initial Concentration, c_{in} (Molar)	8
Saturation Concentration c^* (Molar)	7.75
Solution Density, ρ (kg m^{-3})	1000
Solution Viscosity, μ (Pa s^{-1})	0.001
Pseudo-timestep, Δt (minutes)	15

Table 4.13: Parameters used in the VOF, coupled CFD - crystallisation model.

4.6 Summary and Conclusions

This chapter has developed a moving boundary method for use in modelling crystallisation problems from liquid films. The work assessed each individual model such that optimal numerical routines and mesh parameters are used. In addition to this, short parametric studies were carried out such that the models' behaviour with changing parameters could be observed. Once each model was assessed on an individual basis, a framework was developed which coupled these various models such that a complete moving boundary model describing the fundamental physics, i.e. fluid flow crystallisation and mass transfer, was obtained. The work assessed two possible approaches for the framework, however, it was found that the initial approach did not function in a robust manner when implemented computationally. The second approach used the VOF model such that a multiphase fluid system could be captured accurately. Initial investigations regarding each model suggested that the individual requirements of the models appeared to be in direct conflict. A proposed solution to this was developed such that a hybrid meshing approach was used. Once the framework was implemented it was tested against the previous model in Chapter 3, and the similarities in results offered confidence that the implementation was successful and working as intended. Moreover, the dynamic meshing facility remained robust throughout these calculations.

Simplified physics were considered in the adapted stalagmite model presented in Chapter 3. As such the model was restricted to thin fluid flows travelling at low velocities and also did not consider the explicit modelling of diffusion. Therefore, the fundamental framework developed here offers a new modelling approach such that these limitations are addressed. Despite this, there are further physical effects which should be considered in the problem meaning the model can be used in order to obtain meaningful results regarding the crystallisation of industrial salt solutions. The work here provides a numerical, FVM which currently captures the fundamental physics. Whilst this is useful in its current form, the main advantage of this approach is that the numerical framework provides a convenient and powerful tool for modelling coupled mass transfer - fluid flow systems, such that physics specific to the individual problem can be readily implemented. Using this framework as an initial starting point, the following chapter will develop a model which specifically describes the formations observed in the NNL drip trials.

Chapter 5

Simulating the Crystalline Formation Growth from a Thin Film of Surrogate Liquor

5.1 Introduction

The work in this chapter attempts to develop a model such that the growth of crystalline formations from liquid films can be considered. Parameters and physics considered in this model were chosen such that they related directly to those observed (or hypothesised) in the the NNL drip trials. Results from the model will be compared with the experimental data, such that the model can be validated. Validation of the data when using the simulant material, sodium nitrate, will offer confidence in the model such that it could be later used to predict potential heavy metal formations (provided that addition experiments are carried out in order to determine model parameters and input data).

In Chapter 4 a two-dimensional finite volume method (FVM) was developed such that a multiphase fluid flow system including a mass transfer or crystallisation process could be described by a moving boundary.

The following section highlights the various required physics and implements them into the existing framework such that a model can be developed for describing the crystalline formations. Following this, the accuracy and functionality of the additional models were

tested. Once the models were seen to function independently, the fully coupled model was used. The remainder of this chapter will assess the functionality of the new model against the previous adapted stalagmite model. Following this, the model is validated against experimental data. Once validated, we carry out a sensitivity study on the model parameters.

5.2 Methodology

5.2.1 Introduction

The framework developed in Chapter 4 is used here, such that a multiphase VOF model is used to describe the fluid flow and the concentration of solute within the solution is described by solving the solute transport equation. In addition to this, the deposited crystalline solid is described by a moving boundary, consequently, the fluid - solid interaction is captured. Whilst these three fundamental physics are considered, this framework was developed in two-dimensions, and as such, quantitative comparisons to the experimental data could not be made. Therefore, the first stage in the development of the model here was to advance this framework such that three-dimensional problems could be considered. In order to reduce the computational complexity and cost, an axisymmetric model was considered here, such that rotational symmetry can be considered about a given axis. It is expected that the transition to a three-dimensional model would be a simple matter, however the associated increase in computational cost and time required to perform a single computational experiment would likely restrict the thoroughness in which the model could be validated and tested.

It is know in the problem here that the driving force for crystallisation is governed by a change in temperature (i.e. changing the solubility) or a loss of solvent from the solution (i.e. driving the concentration up). The initial framework assumed that a temperature drop occurred during the falling liquid droplet, such that it was assumed that it had equilibrated to the current ambient temperature by the time the droplet entered the liquid film (and therefore was in a state of supersaturation - see Chapter 2). Whilst it is assumed that the temperature is the dominant mechanism for growth close to the point of impact (at the start of the film), it is hypothesised that growth away from this central feature is governed by an evaporative mechanism. Therefore, in addition to advancing

the dimensionality of the model, a evaporation model was also developed.

Finally, as it is known that the solubility is dependent on the temperature, a temperature model was implemented.

5.2.2 Advancement of the Framework for Axisymmetric Conditions

In Chapter 4, the robustness and capabilities of the moving boundary framework were tested by the capture of a crystallising thin liquid film as it flowed down an inclined surface. An initial geometry of 0.5m was assumed such that the floor surface and a small region above this were considered,see Figure 4.19. However, the solution will now be considered to have rotational symmetry about a given axis. As no rotation or swirl within the flow is considered, the two-dimensional equations outlined in Section 4.5.2 are still solved, however as the domain is assumed to be rotated 2π radians about the axis of symmetry, the cell volumes considered in the solver are also adjusted in relation to this change.

It should be noted that whilst only the cell volumes change, and no change is experienced in the governing equations, the computational implementation of the model when considering the axisymmetric model is not so trivial. When using the ANSYS Fluent CFD package, it is enforced that rotational system should occur about the x-axis (i.e. $y = 0$). As such, the initial domain has to be altered and the gravity vector changed such that the gravitational force acts in the x-direction. For ease of comparison, all subsequent results will be rotated such that they can be directly compared to the previous model and experimental data.

In addition to the rotation of the domain, the boundaries previously denoted as $\Omega_{liqinlet}$ and $\Omega_{airinlet}$ now have to be specified as axis of rotation. As these previous boundaries lie on the axis of rotation symmetry, they cannot be specified as inlet boundaries. This makes physical sense as rotation about this line would create a face of zero area. In cases such as this the boundary has to be specified as an axis condition. Due to this, new locations have to be imposed for the intake of liquid and air into the system. The most logical place to put these inlets, now the initial boundary is not possible, is in the boundary region adjacent to this new axis condition. The liquid inlet will replace a region of the floor boundary adjacent to the axis of rotational system, in order to keep the results as physical

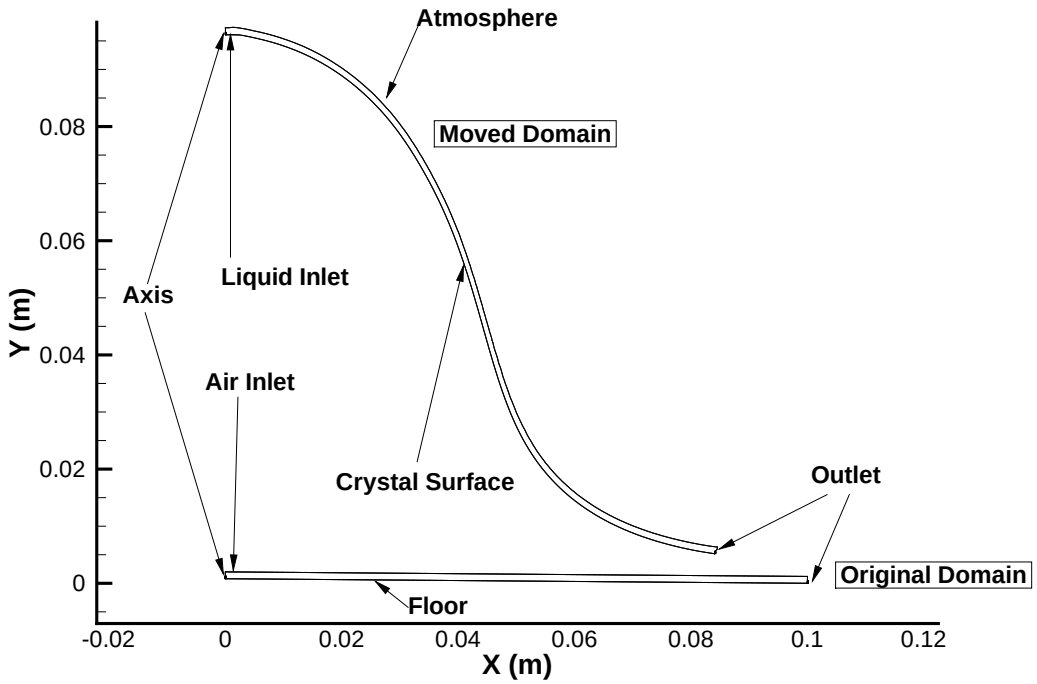

Figure 5.1: Plot of the domain before and after successive boundary motions.

as possible, the size of this boundary will be made such that it is roughly the same width as a droplet. The inlet for the gaseous phase will be placed in the corresponding position, now on the $\Omega_{atmosphere}$ boundary. The new boundaries can be observed in Figure 5.1.

When using these new boundary positions in the two-dimensional model, they can be directly compared to the flow when using the old boundary conditions. Here we used a simple test case of water flowing into a domain filled with air. Flow of air into the domain is negligible. Varying mass flow rates are trialled in order to see how the varying boundary conditions impacts on the interfacial location. From observing the results in Figure 5.2 it can be seen that at low mass flow rates the change in solution is minor.

It should be noted the FLUENT CFD package does not allow a mass flux of solute out of the domain at this point (i.e. Robin boundary condition) therefore here it is assumed that the previous boundary condition is maintained, such that the concentration at the inlet boundary is constant (Dirichlet condition). Due to this the minor differences in the

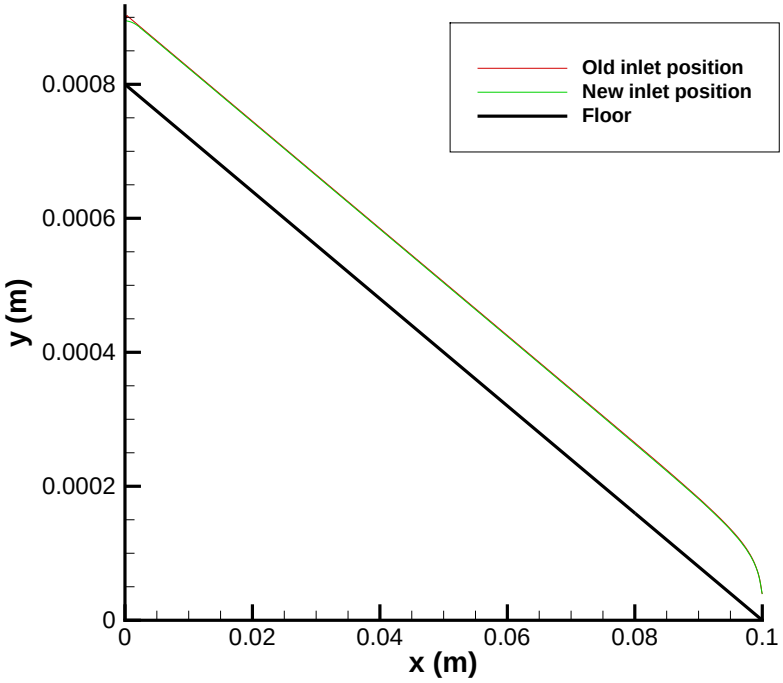

Figure 5.2: Plots of the liquid-air interface when considering the two-dimensional VOF model for varying inlet positions.

flow close to the inlet should have negligible impact on the overall result, additionally as the inlet boundary will be displaced at a constant rate, relative to the inlet concentration, the change in flow field in these regions will not influence the local solution. Due to the small size of the inlet it is assumed that these methodology will have negligible impact on the overall boundary position. Additional, the result after the inlet boundary could just be considered, such that the behaviour close to the inlet is not factored into the final solution.

5.2.3 The Development and Inclusion of Additional Physics; Evaporation and Heat Transfer

The framework in Chapter 3 implemented a solute transport and crystallisation model. However, it was noted that several of the key physics were not considered for application when modelling the NNL drip trial problem. Therefore, this section will focus on the addition of further physics such that solutions obtained should be more accurate.

From the experimental data it is clear that the formations found under certain situations cannot be solely attributed to a decline in temperature and therefore this suggests that there is a significant amount of evaporation occurring within the system. The NNL carried out some simple experiments as part of the drip trials in order to quantify the level of evaporation. It was found that the evaporative flux (evaporation rate per unit surface area) ranges between $E = 1.7 \times 10^{-6}$ kg m^{-2}s^{-1} and $E = 3 \times 10^{-5}$ kg m^{-2}s^{-1}, with an average value of $E = 1 \times 10^{-5}$ kg m^{-2}s^{-1}. Evaporation is an important process and can often have a major impact on many industrial process, e.g. liquid films, see [172, 10, 153], or sessile droplets, see [164].

In addition to the evaporation, changes in temperature are also the main driving force of crystallisation. The solubility of solution has a direct relation to its temperature. Therefore, a solubility - temperature relation is allowed. Whilst not completely necessary at this stage, this inclusion will make the model more versatile such that complex systems (i.e. temperature gradients, etc.) can be considered when the required temperature data is available.

5.2.4 Evaporation Model: Model Approach 1

Previous works on modelling evaporative effects when coupled to the VOF model often account for both the loss of mass from the liquid phase, and increase in mass into the gaseous phase. Here, a constant evaporative flux is considered, where flux values will be based on measurements from the NNL drip trial experiments. When considering evaporation in the VOF model, the mass loss due to evaporation is described by source/sink terms in (4.8). Only the loss of mass from the liquid phase is considered here, and therefore the increase in mass to the gaseous phase is ignored, that is, $S_{\alpha_1} = 0$ is not included in (4.8).

As the source/sink term in (4.8) is a volumetric flux (kg m^{-3} s), whilst evaporation is a surface reaction (kg m^{-2} s), this term must be given such that the amount of water extracted is not dependent on the volume of the cells located at the interface. When considering an evaporative flux, $E > 0$ over a surface area A_f, we can state that the rate

of mass leaving the volume containing that surface must equal,

$$S_{\alpha_2} V_{cell} = -E A_f, \tag{5.1}$$

where V_{cell} is the volume of the cell located at the interface. Clearly, this allows one to express the volumetric source, S_{α_2} in terms on the current cell volume and area, to ensure the correct mass of liquid is extracted from the system. From analysis in [30] it is known that

$$\int_{\Omega} |\nabla \alpha_2| d\Omega = \int_{A} dA, \tag{5.2}$$

where Ω is a volume containing the liquid-gas interface, $|\nabla \alpha_2|$ is the magnitude of the gradient vector of the volume fraction of water, and A is the interfacial surface area within the volume Ω. Therefore, for an individual cell, the following holds,

$$|\nabla \alpha_2| V_{cell} = A_f, \tag{5.3}$$

where V_{cell} is the volume of the cell located at the interface and A_f is the interfacial area of the free surface, within the cell.

The source term in (5.1) can then be written as

$$S_{\alpha_2} = -E |\nabla \alpha_2|. \tag{5.4}$$

This term is then included in (4.8), which accounts for the loss of mass due to evaporation.

In this work, E is assumed to take a constant value. Despite this, the model can be easily advanced such that E is dependent on water vapour concentrations, temperatures and velocities.

5.2.5 Evaporation Model: Model Approach 2

Hardt and Wondra [83] have previously reported that the evaporation model presented in Section 5.2.4 can show signs of being unstable due to the large amount of fluid being withdrawn from the system over a very small interface. Therefore, in their work they proposed a modification to this model such that these instabilities are damped.

This work assumes that the rate of evaporation, ϕ_0 can be written as

$$\phi_0 = -EA_f = N_{\phi_0} E \alpha_2 |\nabla \alpha_2|, \tag{5.5}$$

where the normalisation factor N_{ϕ_0} is given by,

$$N_{\phi_0} = \frac{\int_\Omega |\nabla \alpha_2| d\Omega}{\int_\Omega \alpha_2 |\nabla \alpha_2| d\Omega} \tag{5.6}$$

This model assumes that the evaporation rate can be written in terms of an additional scalar, ϕ such that it is described by the inhomogeneous modified Helmholtz equation

$$\nabla^2 \phi = \frac{1}{D_\phi}(\phi - \phi_0), \tag{5.7}$$

where D_ϕ is the Helmholtz diffusivity coefficient.

The final rate of evaporation in each computational cell can then be given by

$$S_{\alpha_2} V_{cell} = -\phi \alpha_2 N_\phi, \tag{5.8}$$

where

$$N_\phi = \frac{\int_\Omega \phi d\Omega}{\int_\Omega \alpha_2 \phi d\Omega} \tag{5.9}$$

5.2.6 Temperature-Solubility Modelling

Here the temperature is modelled by solution of the energy equation [8],

$$\frac{\partial \rho \tilde{E}}{\partial t} + \nabla(\mathbf{u}(\rho \tilde{E})) = \nabla \cdot (k_{eff} \nabla T) + S_h, \tag{5.10}$$

where k_{eff} is the conductivity due to both laminar and turbulent thermal conductivity, T is the temperature, S_h is a source/sink and $\tilde{E}$ is the energy given by,

$$\tilde{E} = h_E + \frac{|\mathbf{u}|^2}{2} \tag{5.11}$$

where h_E is the enthalpy defined as ,

$$h_E = \sum_j Y_j h_{Ej}, \tag{5.12}$$

such that Y_j is the mass fraction of phase j and h_{Ej} is enthalpy of phase j given by,

$$h_{Ej} = \int_{T_{ref}}^{T} (c_p)_j dt \tag{5.13}$$

where T_{ref} is the reference temperature which is set to $T_{ref} = 296.15K$ and c_p is the specific heat capacity.

For the coupling of the temperature to the solubility, the solubility is expressed as a function of temperature i.e. $c^* = c^*(T)$. For the work here, the temperature boundary conditions are set such that the system is an isothermal state of temperature T.

5.2.7 Solution Density and Viscosity Modelling

Here the rheological properties of the fluid such as the density and viscosity were coupled to the concentration and temperature. Generally, as solute is dissolved in the solution, the density also increases. The fluid rheology relations were defined such that $\rho_2 = \rho_2(c, T)$ and $\mu_2 = \mu_2(c, T)$.

5.3 Governing Equation and Boundary Conditions

The fluid field is described by the NVS equations given in (4.1) and (4.2). Also, the VOF model is solved in order to describe the interface between the liquid and gaseous phases, this is given by (4.8). The transport of solute is described by equation (4.14). The evaporation is described by either (5.4) or (5.8), depending on the choice of model. The temperature throughout the system can be obtained through solution of the energy equation (5.10).

The flux of solute out of the crystal boundary is given by (4.16), such that $c^* = c^*(T)$.

The boundary conditions for the fluid flow are outlined in Section 4.5.2.2.

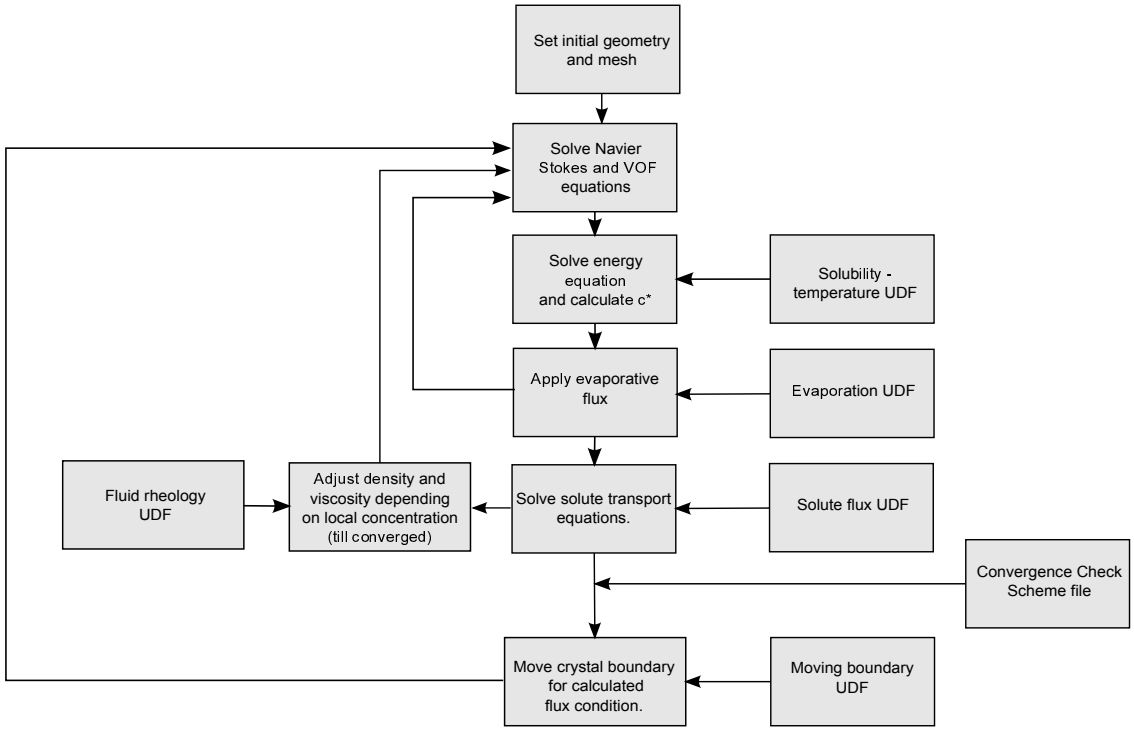

Figure 5.3: Flow diagram for the fully coupled model.

Once the aforementioned systems of equations are solved to steady state the boundary is then displaced by a pseudo timestep of Δt, given by (4.18).

5.4 Coupled Solver Process

The model here uses the framework outlined in Chapter 4, and therefore the solvers for the fluid flow, solute transport and moving boundary model are described in Section 4.5.2.4. The evaporative models are implemented through a UDF, and in the second evaporative model an additional scalar transport equation is solved (considering purely diffusion) such that the inhomogeneous modified Helmholtz equation in (5.7) is solved. The coupling between the temperature and solubility of solution is also implemented through a UDF, as is the coupling between the denisty and viscosity with the solution concentration. A diagram of the full solver process can be found in Figure 5.3.

5.5 Results

This section will implement the model to describe the growth of sodium nitrate formations, as seen in the NNL drip trials. Initial studies focused on testing the model with the newly included additional physics. Once the models were seen to be functioning both in an accurate and robust manner, the fully coupled CFD moving boundary model was validated against experimental data. Once validated, the remainder of the work carried out parametric studies.

5.5.1 Testing of the Additions to the Framework

5.5.1.1 Framework when Advanced to an Axisymmetric Model

In Chapter 4, results from the framework were tested against those of the adapted stalagmite model, developed in Chapter 3. In this chapter a similar approach is taken. The final boundary position or crystal surface obtained from the model when using parameters relating to run 1 in Table 5.1, and the results when using the corresponding parameters in the adapted stalagmite model, can be observed in Figure 5.4. From this figure it can be seen that close to the apex the coupled CFD moving boundary model predicted a lower formation height when comparing both models at the same width. When considering the results away from the apex of the formation, the coupled CFD moving boundary model predicted a thicker structure. The maximum heights of the formations were equal due to the constant concentration boundary condition imposed at the inlet. It is clear that both models, unlike the experimental results, predict no growth away from the central tower formation.

These initial tests highlighted the minor differences between the models. Due to the different modelling approaches, it was expected that some differences in results would be observed. Therefore, regardless of these minor differences these results offer assurance that the initial axisymmetric implementation of the model is working as intended.

In should be noted that in this chapter, unless explicitly stated otherwise, parameters $T_{in} = 30°\text{C}$, $T = 27°\text{C}$ and $c_{in} = 8$ Molar were imposed.

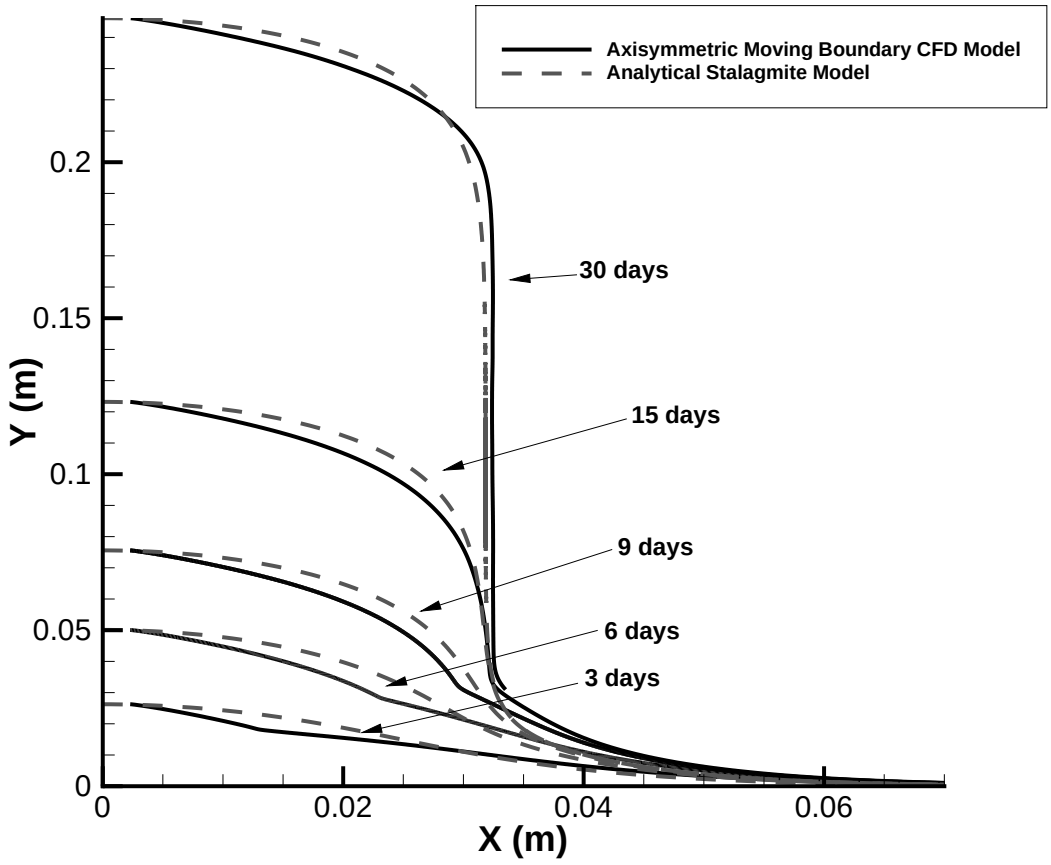

Figure 5.4: Axisymmetric formations through time comparing the axisymmetric coupled CFD - moving boundary model against the adapted stalagmite model, when $Q = 2.89 \times 10^{-5}$kg s^{-1}, $k_r = 8 \times 10^{-6}$ m s^{-1}, $K = 8 \times 10^{-6}$ m s^{-1}, $c_{in} = 8$ Molar, $E = 0$.

Run	ρ_2 (kg/m^3)	μ_2 (Pa s)	k_r (m/s)	Q (kg^3/s)	T (°C)	E (kg/(m^2 s))	D (m^2/s)
1	998.2	0.001	8×10^{-6}	2.89×10^{-5}	27	0	1.586×10^{-9}
2	eqn. (5.14)	eqn. (5.15)	8×10^{-6}	2.89×10^{-5}	27	10^{-5}	1.586×10^{-9}
3	eqn. (5.14)	eqn. (5.15)	8×10^{-6}	Varies	27	10^{-5}	1.586×10^{-9}
4	eqn. (5.14)	eqn. (5.15)	8×10^{-6}	2.89×10^{-5}	27	Varies	1.586×10^{-9}
5	eqn. (5.14)	eqn. (5.15)	8×10^{-6}	2.89×10^{-5}	27	10^{-5}	Varies

Table 5.1: Parameters for the computational crystal growth simulations carried out in this study. Parameters $c_{in} = 8$ Molar, $\rho_1 = 1.225$kg/m^3, $T_{in} = 30$°C, $\rho_s = 2260$kg/m^3 and $M_s = 0.084$kg/mol remain fixed for all simulations.

5.5.1.2 Evaporation Model: Model Approach 1

The next stage was the incorporation of an evaporation model into the coupled CFD moving boundary model. For evaluation, this was applied to a thin liquid film of water in two dimensions, such that no crystallisation or solute transport was considered. Varying constant evaporative fluxes, E were trialled and results can be observed in Figure 5.5.

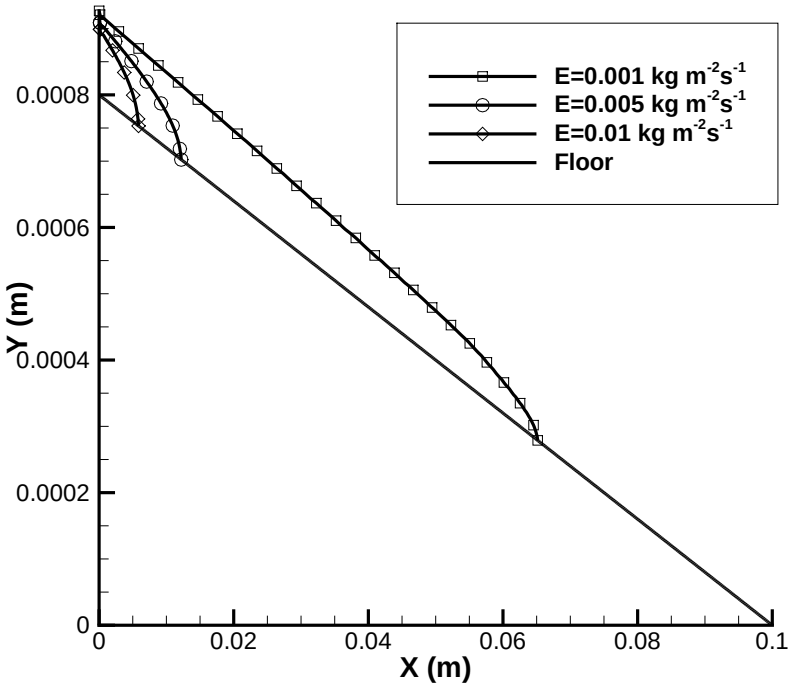

Figure 5.5: Two-dimensional plots of a water film for various evaporative fluxes, E.

From Figure 5.5 it can seen be that cessation of the liquid flow occurs at different points for different evaporative fluxes. As expected, for a larger evaporative flux, the film is completely evaporated quicker and therefore, a smaller interfacial area is observed. For known mass flow into the domain and a given evaporative flux, the expected interfacial area of the film can be calculated (at steady-state). The results for the expected and the calculated interfacial areas can be seen in Table 5.2. From this table it is clear that the evaporation model was working appropriately, however there were small discrepancies between the expected interfacial and computed areas. It is hypothesised that this is due to the inaccuracies involved in calculating the gradient of the volume fraction (from equa-

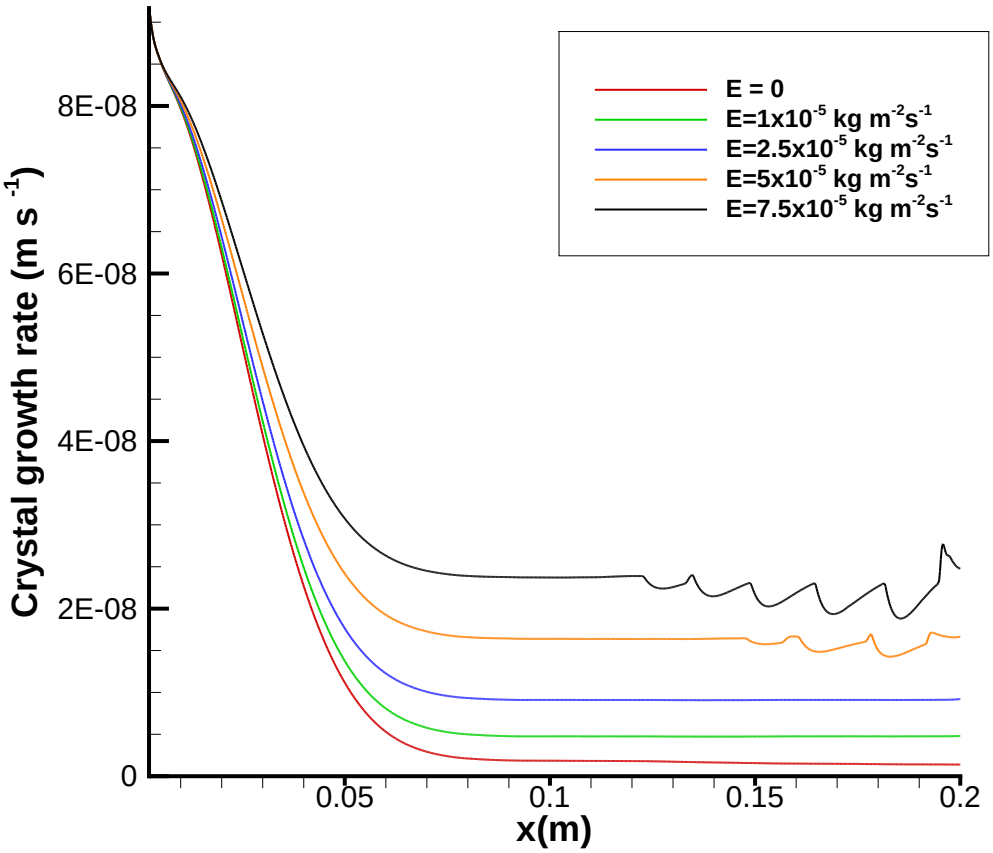

Figure 5.6: Plot of deposition rates at $t = 0$ for various evaporative fluxes, E, when $K = 8 \times 10^{-6}$ m s^{-1}, $c_{in} = 8$ Molar, $T_{in} = 30°$C, $T = 27°$C.

tion (5.4)). Similar inaccuracies are often found when coupling surface tension effects to the VOF model, as seen in [25].

The next stage in the modelling process was to check that the evaporation model functions correctly when coupled to the axisymmetric coupled CFD - moving boundary CFD model. Figure 5.8 shows the initial instantaneous rate of crystal growth for varying evaporative fluxes, E, given that the film had fully spread across the plate. From this figure it can be seen that as the rate of evaporation increased, the crystallisation rate also increased. This behaviour is expected as the volume of solvent decreases, the relative concentration of the solution is increased. This effect becomes more pronounced in regions away from

E (kg m^{-2} s^{-1})	Expected Interfacial Area (m^2)	Calculated Interfacial Area (m^2)
1×10^{-3}	0.05	0.063
5×10^{-3}	0.01	0.012
1×10^{-2}	0.005	0.0061

Table 5.2: Data for the evaporation of a water film for varying evaporative flux, E.

the apex of the formation. For large evaporative fluxes an unstable oscillatory solution is observed.

5.5.1.3 Evaporation Model: Model Approach 2

Hardt and Wondra [83] reported similar instabilities when using the model presented in Section 5.2.4. The work in this paper developed an alternative model, such the observed instabilities were damped. Therefore, the second suggested model here attempted to implement the model developed in [83]. The formulation of the model can be seen in Section 5.5.1.2.

Initial results from the model can be seen in Figure 5.7. From this figure it would suggest that the model had been implemented correctly, such that the solution of the inhomogeneous Helmholtz equation solved for the evaporation term, ϕ, can be seen in Figure 5.7(b) when considering the liquid film shown in Figure 5.7(a). Also, the diffusivity parameter D_ϕ was varied. As expected, Figure 5.8 shows that as D_ϕ increased, so did the magnitude of the interfacial smearing.

From the initial evaporation model it could be observed that at higher evaporative rates, instabilities were experienced. In order to assess the alternative model's behaviour and its ability to damp these oscillatory solutions, a series of number trials were carried out using a similar methodology to the previous model. Here a liquid film of mass flow $Q = 2.89 \times 10^{-5}$kg s^{-1} was considered, such that an evaporative flux of $E = 7.5 \times 10^{-5}$kg m^{-2} s^{-1} was imposed across the film. These values were used here as the oscillations of the deposition rates in the previous model were significant for these values. From assessing the results in Figure 5.9 it can be seen that for all values of D_ϕ the oscillations in the solution are damped. The results when using $D_\phi = 1 \times 10^{-4}$m^2 s^{-1} showed the closest solution to the previous evaporation model, such that for small x when

oscillations were not experienced, the solutions were identical. As D_ϕ increased, the high level of smearing introduced inaccuracies in the results, such that they diverged away from the results of the original evaporation model. It should also be noted that in all cases, a change in velocity was experienced close to the outlet. It is thought that this is due to the sharp change in the liquid-gas interface height at the outlet. This phenomenon was experienced due to the zero pressure condition imposed at the outlet. In reality the pressure across the outlet would vary depending on the interfacial height, however as no apriori knowledge of the film is assumed, these pressure conditions cannot be calculated.

It should be noted that due to the requirement that an additional equation is solved, the computational cost associated with the second model is larger than that of the first. Therefore, when considering a constant evaporative flux E, if this value is small it may be advantageous to use the first model. However, for maximum robustness in cases where E is unknown (i.e. determined from localised conditions), or in cases where E is sufficiently large such that instabilities are experienced, the second model should be implemented.

5.5.1.4 Solubility-Temperature Coupling

In order to test the solubility-temperature coupling, a film of sodium nitrate solution was considered. A temperature gradient was placed on the floor surface, such that the temperature of the film varied across the plate. The temperature solubility relationship used is given in (3.22). From observing the results in Figure 5.10 it can be seen that as the temperature changes, so does the solubility c^*. Temperature gradients will not be imposed in the remainder of the chapter, however this methodology allows the convenient change in isothermal temperature in later studies, and also allows scope for complex non-isothermal systems for further implementation in an industrial setting.

5.5.1.5 Density and Viscosity Coupling

In order to test the coupling between density and viscosity to the local liquid rheological properties, a thin solution flow was modelled over an axisymmetric domain of length 0.1m. For simplicity the temperature was assumed constant and only the density was assumed to change, such that $\rho_2 = \rho_2(c, T) = \rho_2(c)$. A concentration gradient was imposed in the flow, which can be observed in Figure 5.11. The functions governing the

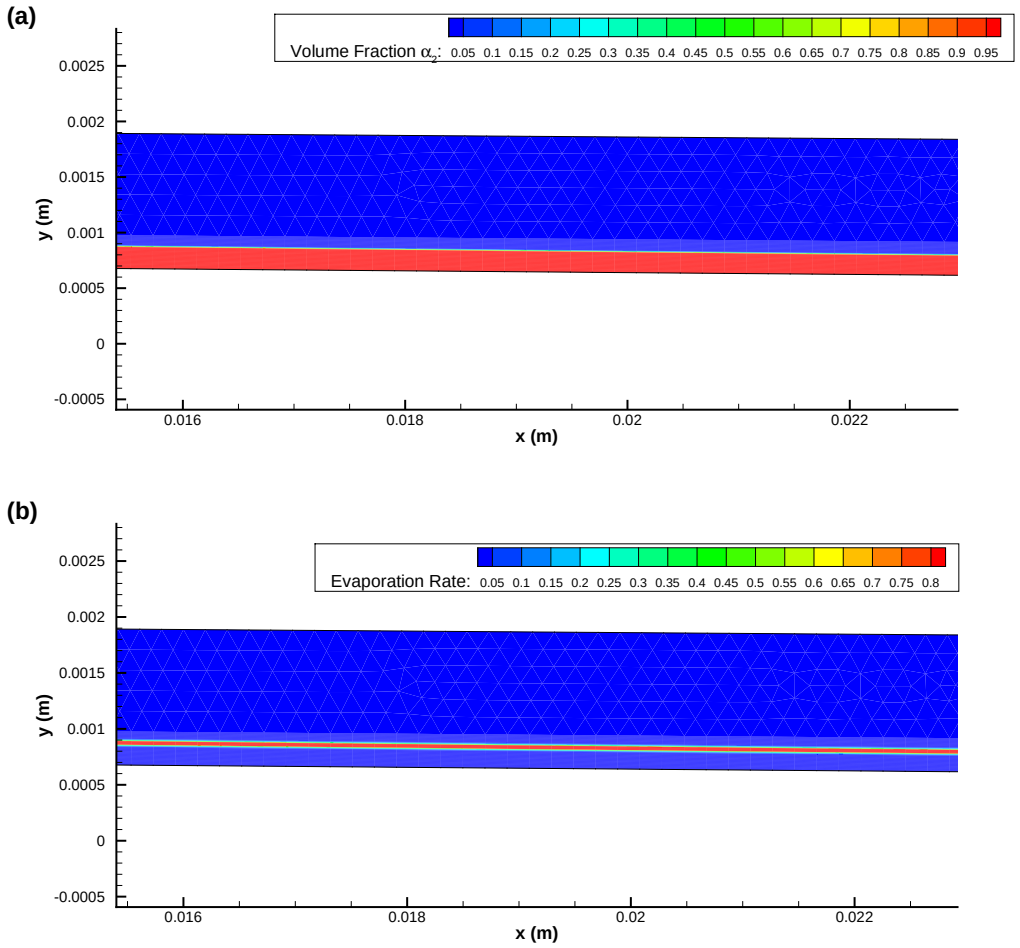

Figure 5.7: (a) The liquid-gas interface for a film of mass flow $Q = 2.89 \times 10^{-5}$kg s^{-1}. (b) The non-normalised evaporation rates, ϕ, from solution of (5.7), for $E = 7.5 \times 10^{-5}$kg m^{-2} s^{-1} and $D_\phi = 1 \times 10^{-4}$m^2 s^{-1}.

relationship, $\rho_2(c) = 400c - 1700$ was also imposed on the system. It should be noted that the functions here do not related to any specific material properties, but were used such that rate of density change was significant for small changes in concentration. This exaggerated change in density allows the testing of the robustness of the system, such that it is assured that the system would remain stable when considering the smaller (or more gradual) variations in the density of a real material.

It can be observed in Figure 5.11 that as the solution concentration decreases, the density decreases. The density declined approximately 100 kg m^{-3} over a 0.1m distance, from

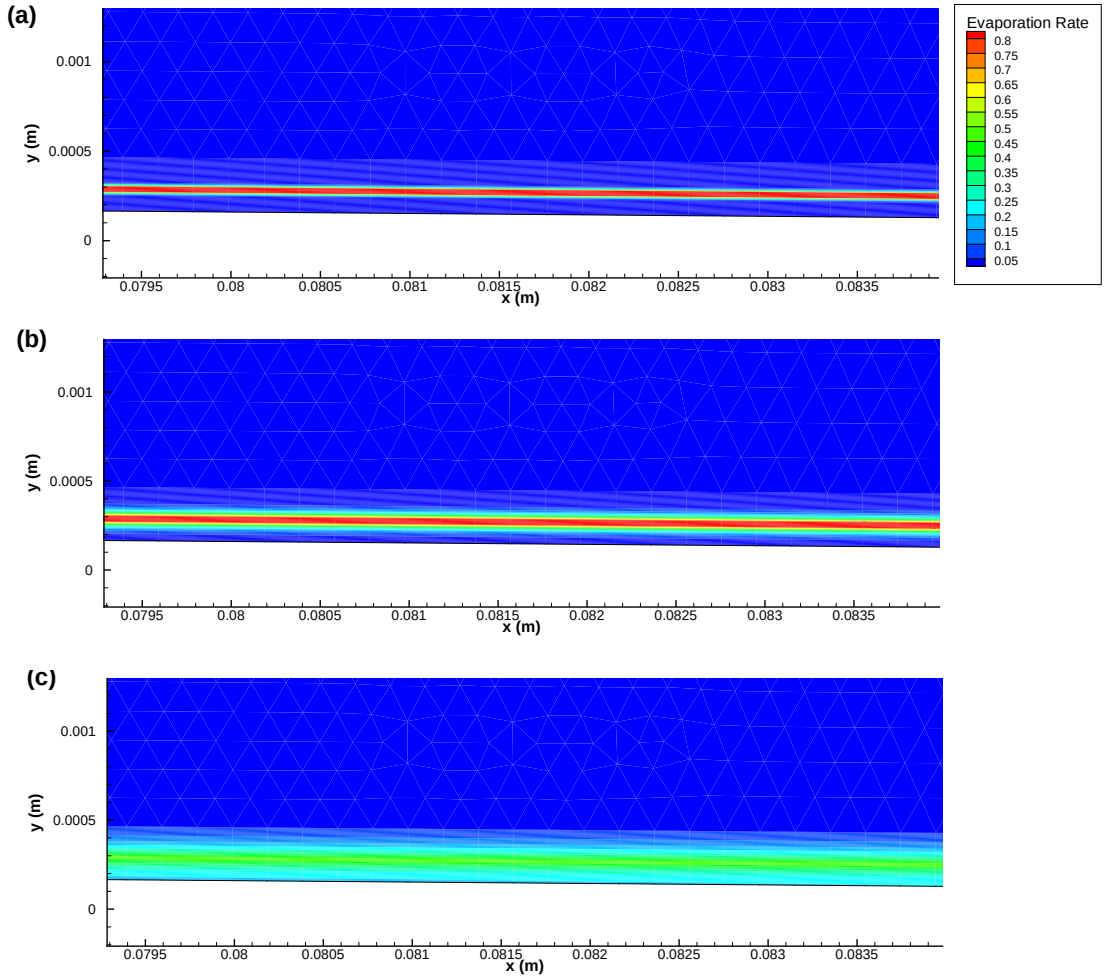

Figure 5.8: The non-normalised evaporation rates, ϕ, from solution of (5.7), for $Q = 2.89 \times 10^{-5}$kg s^{-1}, $E = 7.5 \times 10^{-5}$kg m^{-2} s^{-1}, (a) $D_\phi = 1 \times 10^{-4}$, (b) $D_\phi = 1 \times 10^{-3}$ and (c) $D_\phi = 1 \times 10^{-2}$

$\rho_2 = 1500$kg m^{-3} to $\rho_2 = 1400$kg m^{-3}.

As a preliminary investigation into the effects of the density on the crystal growth, the rate of crystal growth was calculated when considering $k_r = 8{\times}10^{-6}$m s^{-1} for $\rho_2 = 400c{-}1700$. These results were compared against a constant density solution of $\rho_2 = 1500$kg m^{-3}. Comparisons between the results showed that the change in crystal growth due to the density variation were negligible and are therefore not shown here. It should be noted that the difference in density between the two solutions reached a maximum value of 100 kg m^{-3}. For larger variations in density the effects may be more significant.

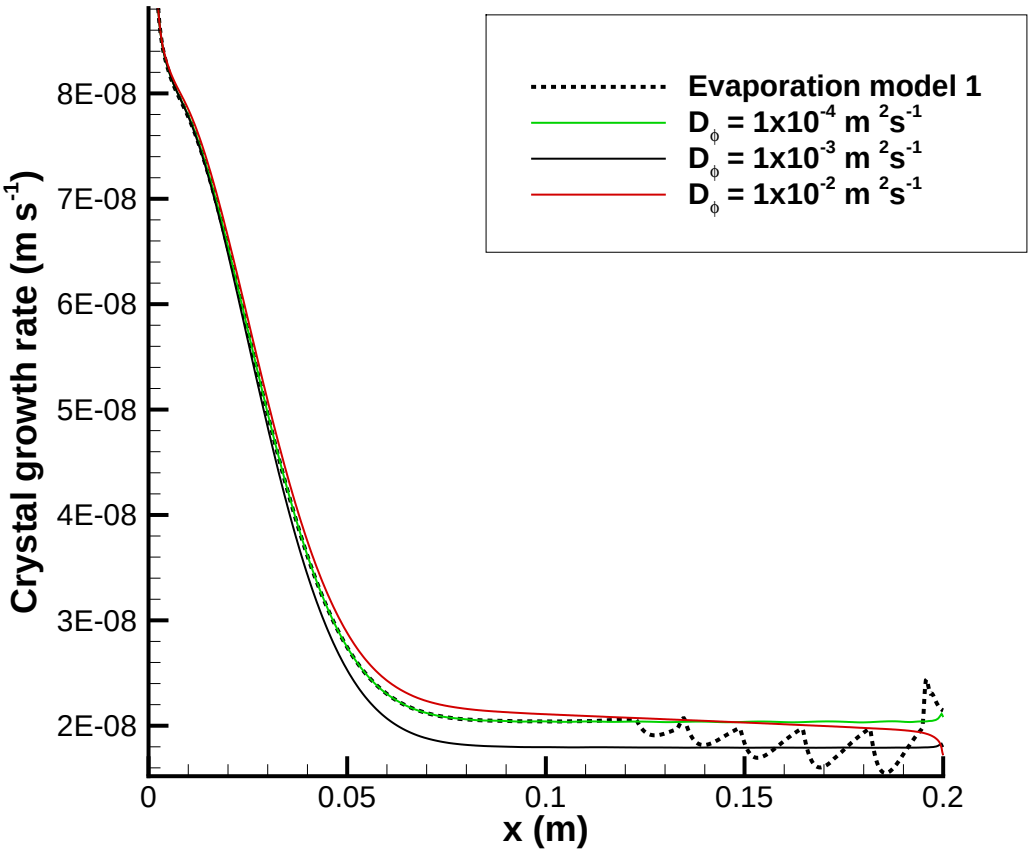

Figure 5.9: The crystal growth rates when considering $Q = 2.89 \times 10^{-5}$kg s^{-1}, $E = 7.5 \times 10^{-5}$kg m^{-2} s^{-1} and varying D_ϕ.

5.5.2 Validation of the Results with Experimental Data using a Surrogate Solution

5.5.2.1 Identification of Parameters

Following the verification that the advancements to the previous framework were functioning correctly, the newly coupled CFD - moving boundary model was next validated against the experimental data available from the NNL drip trials. The density - temperature and viscosity - temperature relations such that ρ_2 and μ_2 are defined by equation

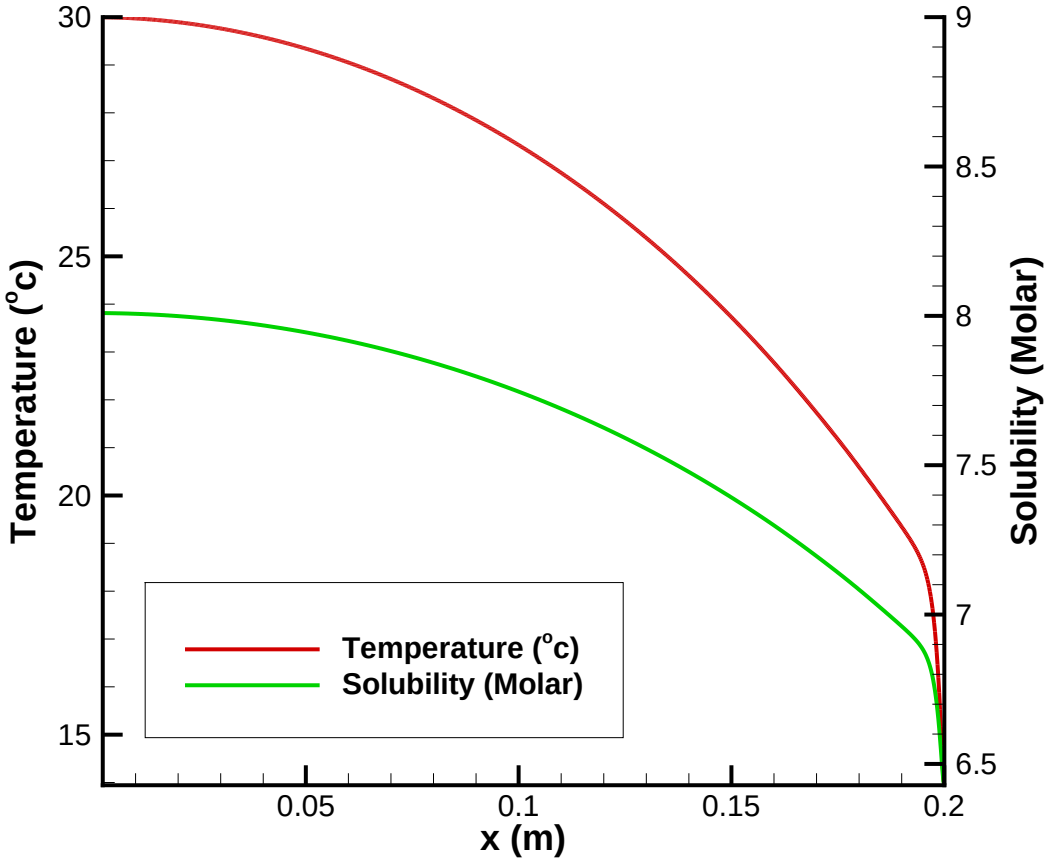

Figure 5.10: Example of the solubility-temperature coupling for an imposed temperature gradient. Values for c^* were calculated at the crystal surface.

in (4.8) for sodium nitrate are given by [190],

$$\rho_2 = \rho_2(c) = a - bT, \tag{5.14}$$

and,

$$\mu_2 = \mu_2(c) = 10^{-9} A\sqrt{T + 273.15} e^{\frac{B}{T+273.15-T_0}}, \tag{5.15}$$

where $a = 421.37X^2 + 629.7X + 1012.6$, $b = -168.16X^5 + 206.79X^4 - 89.845X^3 + 17.308X^2 - 0.6854X^+0.4789$, $X = \frac{cM_s}{cM_s+1}$ is the mass fraction, $A = 4219.6X^2 + 2995.2X + 991.72$, $B = 300834X^6 + 525458X^5 - 348368X^4 + 106051X^3 + 14531X^2 - 967.34X + 644.92$, $T_0 = 29.088X^2 + 15.881X + 134.68$ and T represents the temperature (in °C).

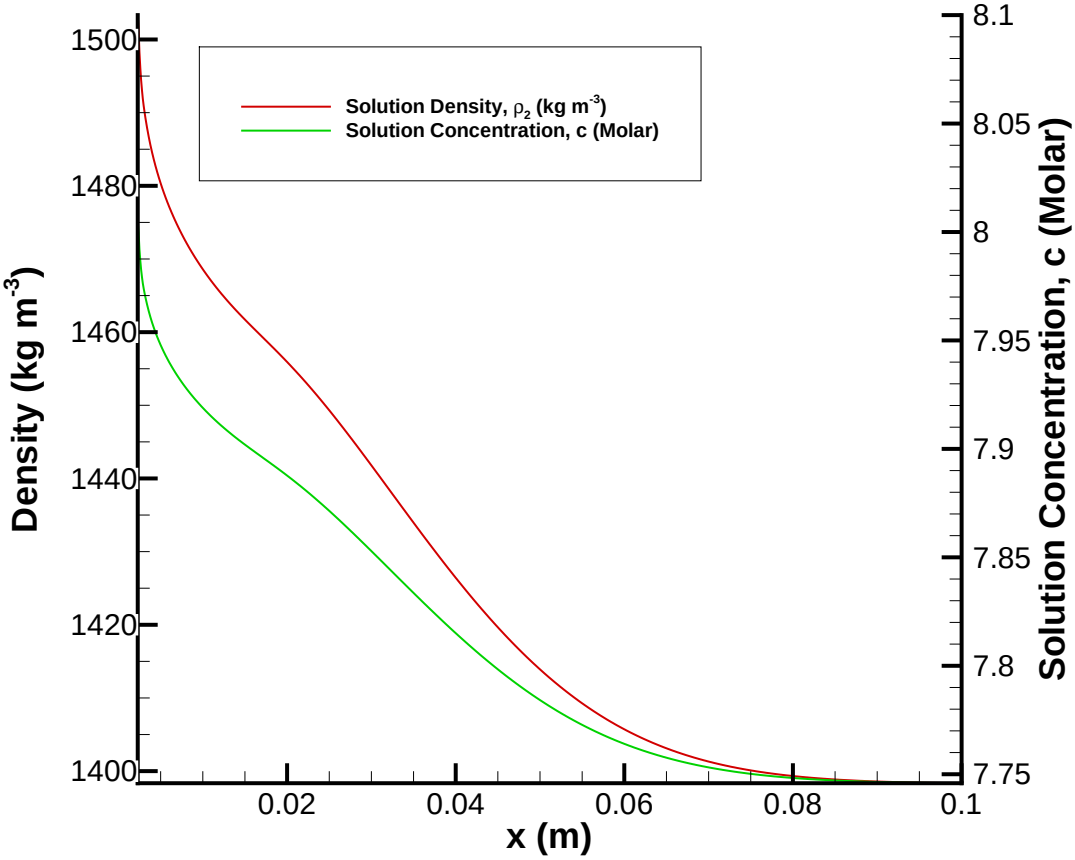

Figure 5.11: Example of the density-concentration coupling for an imposed concentration gradient.

For an initial $c = 8$ Molar solution of sodium nitrate at $T = 27°$C, expressions (5.14) and (5.15) obtained $\rho_2 = 1300$kg m^{-3} and $\mu_2 = 0.002$Pa s. The values $\rho_1 = 1.225$kg m^{-3} and $\mu_1 = 1.79 \times 10^{-5}$Pa s are imposed for the gaseous phase.

The diffusivity of sodium nitrate in solution was set at a constant value of $D = 1.586 \times 10^{-9}$m^2 s^{-1}, see [196]. This study showed the diffusivity to vary slightly with temperature and concentration, however these effects were considered negligible for the range of parameters considered here.

It should be noted that in the previous adapted stalagmite model, presented in Chapter 3, the full reaction-diffusion equations were solved such that an overall crystal growth coefficient was used. Here, only the reaction term from the model was considered, as diffusion was now modelled explicitly. The surface integration coefficient, k_r, was required. As the value of the coefficient of surface integration for sodium nitrate was not available, $k_r << k_d$ was considered. Hence, from (3.14), it was assumed that $k_r \approx K$. It is assumed that this assumption is physically valid, as for the liquid films considered here, the size of the mass transfer boundary layer was generally larger than that of the film height, therefore the diffusion pathway was small. Due to this, the surface integration step in (3.12) was considered to be the limiting step in the crystallisation process. As such, a value of $k_r = 8 \times 10^{-6}$m s^{-1} was used here. In addition to this, the air flow during the NNL experiments was intentionally restricted, as such the gas phase was considered to have negligible impact on the liquid film and therefore, $Q_a << Q$ was imposed.

The experimental temperatures varied through time, such that the mean temperature was $T = 27°$C with a standard deviation of 2.4°C. The solubility of the solution is defined in (3.22). The evaporative flux was assumed constant, with a value of $E = 10^{-5}$ kg m^{-2} s^{-1}, as observed in the experiments. The parameters for the validation case are summarised in Table 5.1 (run 2).

5.5.2.2 Results

The data obtained from the NNL drip trial experiments consisted of a number of photographs of the formations at various stages of growth. Furthermore, the height and width of the formations were measured quantitatively at various times in the experimental procedure. The model was run using the parameters outlined in Section 5.5.2.1. This was carried out three times with parameters relating to the mean temperature, and temperatures plus and minus one standard deviation from the mean. The formation heights at the apex are presented and compared against experimental results in Figure 5.12. From this figure it can be seen that the model closely resembles the experimental data, when using model parameters close to the mean temperature. The small deviations from the experimental are assumed to be due to the temporal fluctuations in the observed temperature.

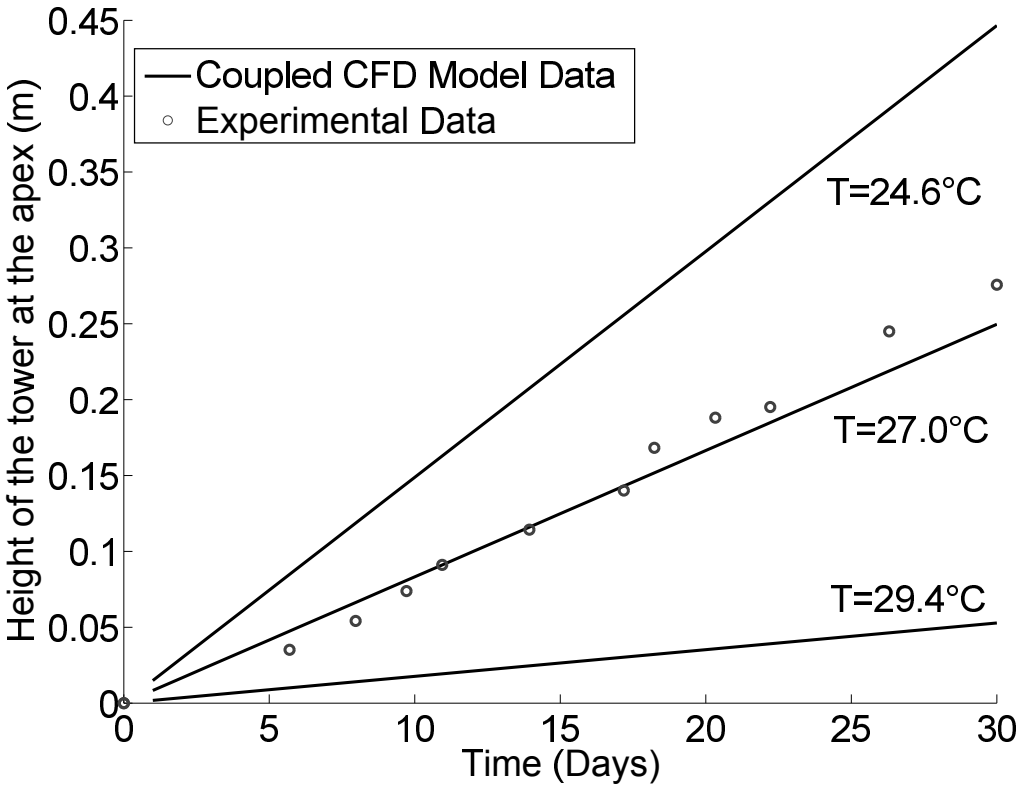

Figure 5.12: Height of the formation at its apex through time, when $E = 10^{-5}$kg m^{-2} s^{-1}, $Q = 2.89 \times 10^{-5}$kg s^{-1}, $k_r = 8 \times 10^{-6}$ m s^{-1}, $c_{in} = 8$ Molar, $T_{in} = 30$°C.

Following the comparison of the experimental heights with the model, the widths of the formations obtained were compared against the experimental data. It was noticed that both in the CFD moving boundary model and experimental results the width of the tower formation would change when considering its value at various heights. The geological stalagmite model in [162] obtained results which predicted constant width for the formation after the convex region at the base of the tower, referred to as an 'equilibrium radius'. It is unknown at which height the width of the formations were measured in the experiments. Due to the uncertainty in the experimental data, both the 'equilibrium radius' and the width close to the base of the formation were compared. In order to visually clarify the position of these two measurements, they have been highlighted in Figure 5.13. The figure shows a crystalline growth after 3 days, when $E = 0$ and $T = 27°\text{C}$. From looking at Figure 5.13, the expansion of the formation close to the surface can be observed.

Figure 5.14 (run 2) shows the experimental widths when compared against the equilibrium radius and formation width at height $H = 0.01\text{m}$, obtained by the axisymmetric moving boundary CFD model. From this figure it can be seen that the experimental widths measured by the NNL are between the equilibrium radius and formation width obtained from the model when run with $E = 10^{-5}\text{kg m}^{-2}\text{ s}^{-1}$. It was noted that unlike the adapted stalagmite model, the equilibrium radius does not remain fixed in time, but rather continued to grow in magnitude. It is hypothesised that this behaviour was due to the now considered evaporative effect. In order to test this hypothesis, the model was run again for $E = 0$. The results from this were plotted on the same figure and from these it is clear to see that much like the earlier adapted stalagmite model the formation widths approach a constant limiting value.

As mentioned, in addition to the measurements of the height and width, the set of experimental data contained several photographs of the formations through time. Due to lack of data regarding the orientation and position of the camera in respect to the experiment equipment, it was difficult to make direct quantitative comparisons with any degree of certainty between the experimental and model results. Despite this, attempts were made to digitise the photographs, such that a preliminary assessment the formation shape could be compared to the model results.

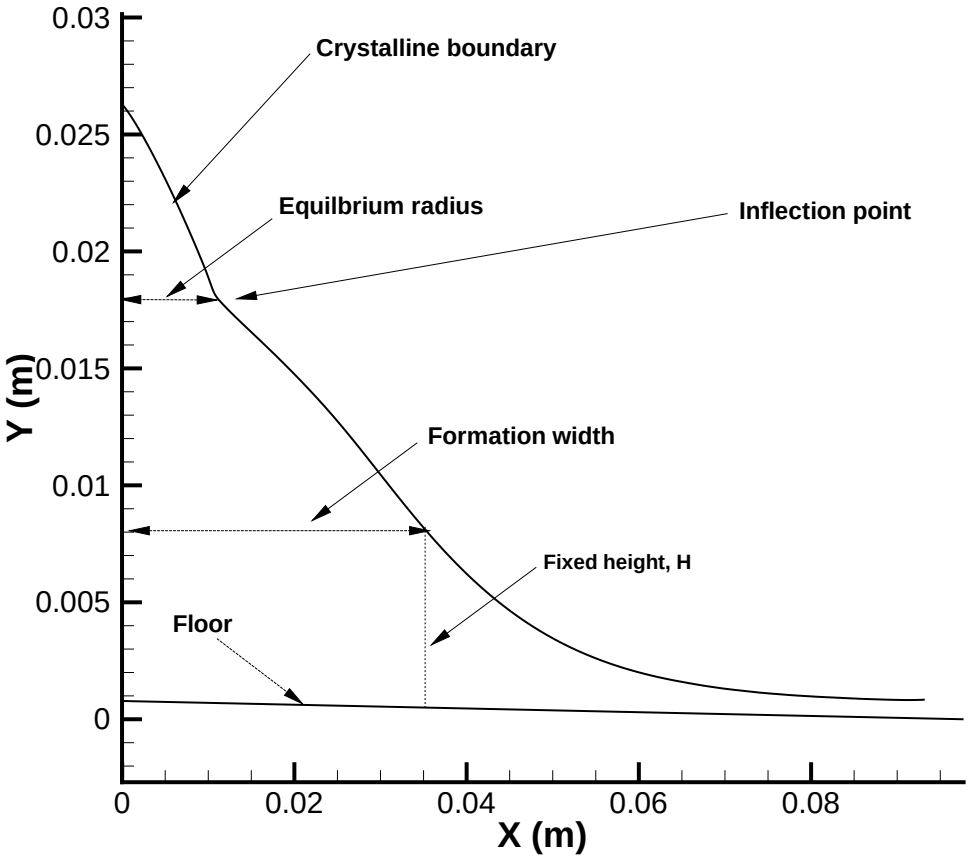

Figure 5.13: Plot of tower width measurement locations.

Firstly, the model was compared against the formation after 17 days. The results can be observed in Figure 5.15 (run 2) where it can be seen that the the width of the formation is under predicted by the model at the top of the formation, whilst slightly over predicted when considering lower heights. It can also be seen that the height of the formation was slightly over predicted by the model.

The model results were then compared against the experimental data relating to 30 days growth. The results for this can be seen in Figure 5.16 (run 2), where it can be observed that the computational model overpredicted the height at the apex of the formation. Much like the result for 17 days, the width of the formation was under predicted close to the center of the formation, however results further away from the apex were moderately

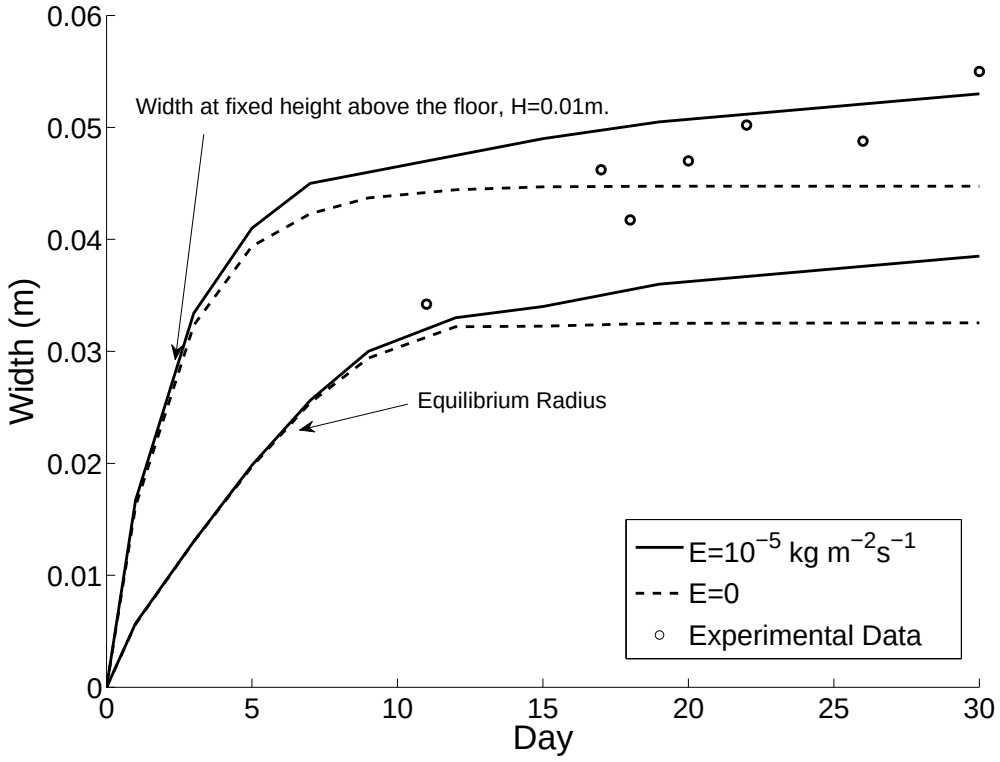

Figure 5.14: Plot of the experimental widths through time compared with the axisymmetric coupled CFD - moving boundary model, when $Q = 2.89 \times 10^{-5}$kg s^{-1}, $K = 8 \times 10^{-6}$ m s^{-1}, $c_{in} = 8$ Molar, $T_{in} = 30°$C, $T = 27°$C.

overpredicted.

When considering the aforementioned uncertainty in the quantification of the photographic results, and that no *a priori* knowledge on the formations size and shape was assumed, it can be concluded that the model provides a good estimate for the size and shape of these formations. It should also be noted that the temperature varied both spatially and temporally during the experimental procedures, however in the work here an isothermal system was considered. Due to this, slight variations between the model and experimental results were expected. Further experiments could be conducted such that additional temperature data is recorded, allowing the aforementioned hypothesis to be investigated further.

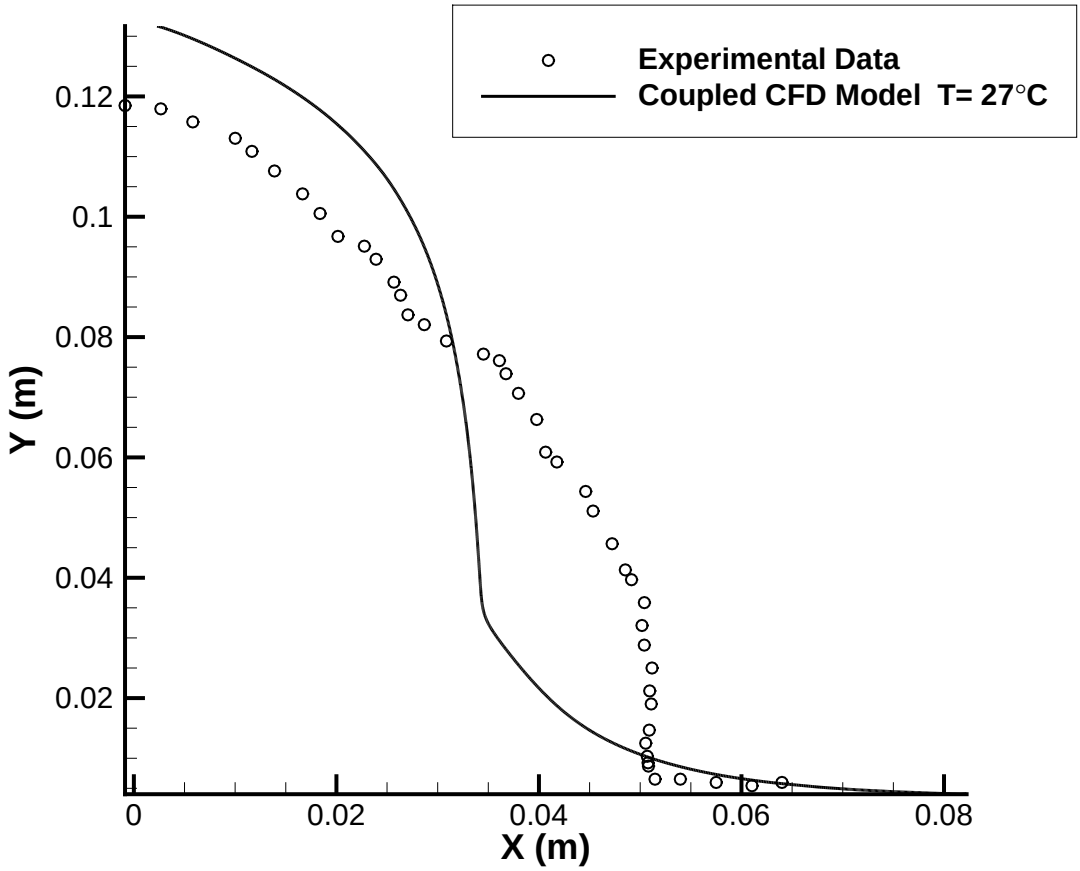

Figure 5.15: Comparison of the experimental data and the axisymmetric moving boundary CFD model for the profile of the crystal formation after 17 days growth when $Q = 2.89 \times 10^{-5}$kg s^{-1}, $K = 8 \times 10^{-6}$ m s^{-1}, $c_{in} = 8$ Molar, $T_{in} = 30°$C, $T = 27°$C, $E = 10^{-5}$kg m^{-2} s^{-1}.

5.5.3 Effects of Varying the Process and Environmental Parameters

Once the model was shown to give reasonable predictions for the crystalline formations experienced in the experimental work, the model was used to assess how varying parameters affect the build up of material through time. In this section, the parameters denoting the process and environmental conditions, namely the mass flow and evaporation rates, will be considered. The temperature of the system were considered to remain at a constant temperature of $T = 27°$C.

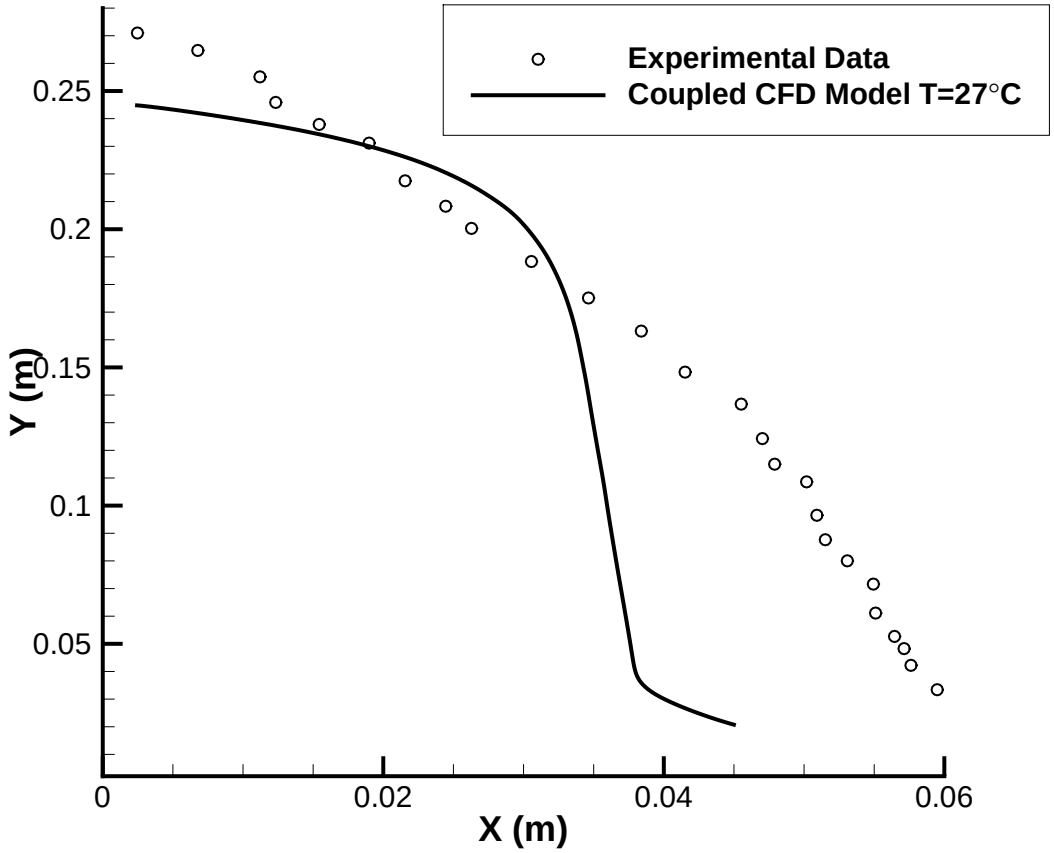

Figure 5.16: Comparison of the experimental data and the axisymmetric moving boundary CFD model for the profile of the crystal formation after 30 days growth when $Q = 2.89 \times 10^{-5}$kg s^{-1}, $K = 8 \times 10^{-6}$ m s^{-1}, $c_{in} = 8$ Molar, $T_{in} = 30$°C, $T = 27$°C, $E = 10^{-5}$kg m^{-2} s^{-1}.

5.5.3.1 Mass Flow Rate

In order to assess the effects of altering the mass flow rate, the axisymmetric, moving boundary CFD model was run for varying mass flow rates, Q. Figure 5.17 shows these results for parameters given in Table 5.1 (run 3). From this figure it can be seen that as the mass flow rate increases, so does the width of the formation.

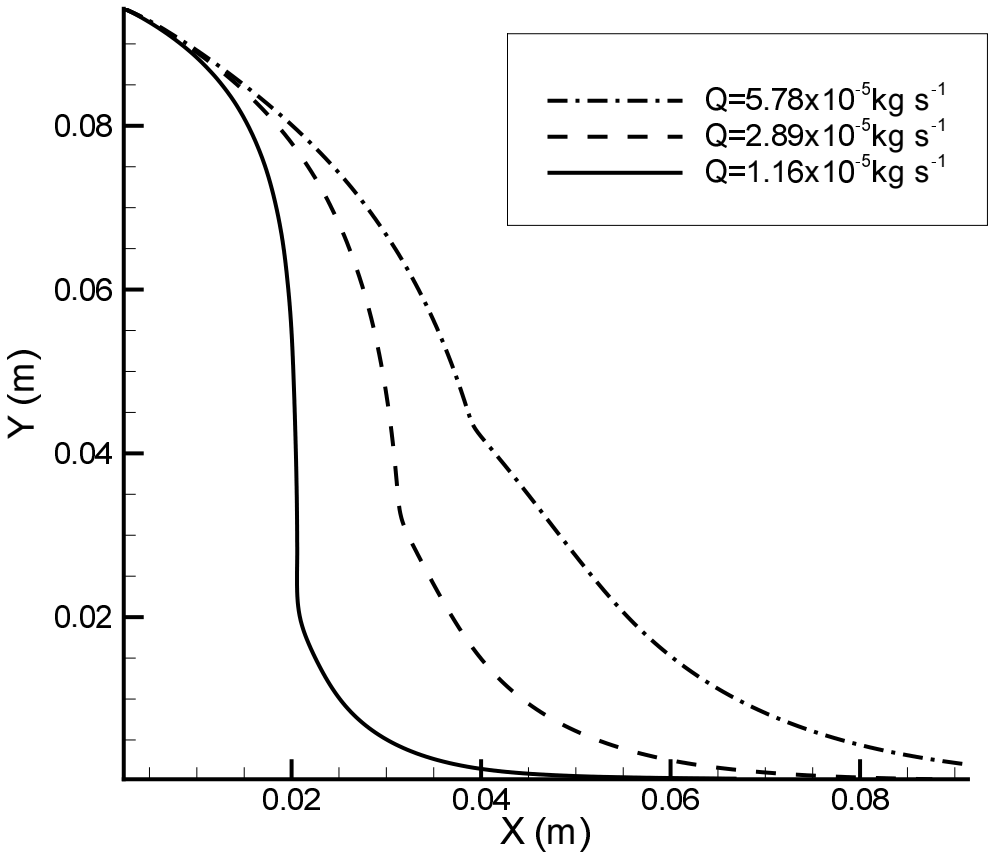

Figure 5.17: Axisymmetric plots of the stalagmite through time after 11 days for varying mass flow rates, Q, when $K = 8 \times 10^{-6}$ m s^{-1}, $c_{in} = 8$ Molar, $T_{in} = 30°$C, $T = 27°$C, $E = 0$.

5.5.3.2 Evaporative Rates

In order to assess how the formation shape would vary if the overall rate of evaporation changed (i.e. due to a change in humidity or temperature) the model was run using a range of evaporative fluxes. Results for 9 days growth when simulated with parameters in Table 5.1 (run 4), can be seen in Figure 5.18. From this figure it can be seen that increasing the evaporative flux causes a thickening of the formation away from the apex. These results suggest that in conditions that favour evaporation, the centralised tower formation will not experience much change in overall shape, however there will be a noticeable thickening of the surrounding crystalline bed. This behaviour agrees with

the previous hypothesis which suggests that growth away from the central formation is dominated by an evaporative mechanism. Furthermore, for higher room temperatures or lower solution concentrations, the solution is not found to be supersaturated at the point of entry into the system, thus growth in these regions may not be experienced. However, due to the evaporation, growth may still be seen to occur away from this point. It is hypothesised that this behaviour is the reason for the annular formations experienced in the NNL experiments when considering undersaturate solutions (see 5 Molar results in Chapter 1). Clearly, both the evaporation and temperature changes experienced within the system influence the spatial deposition pattern, and therefore the overall characteristic shape of the formation.

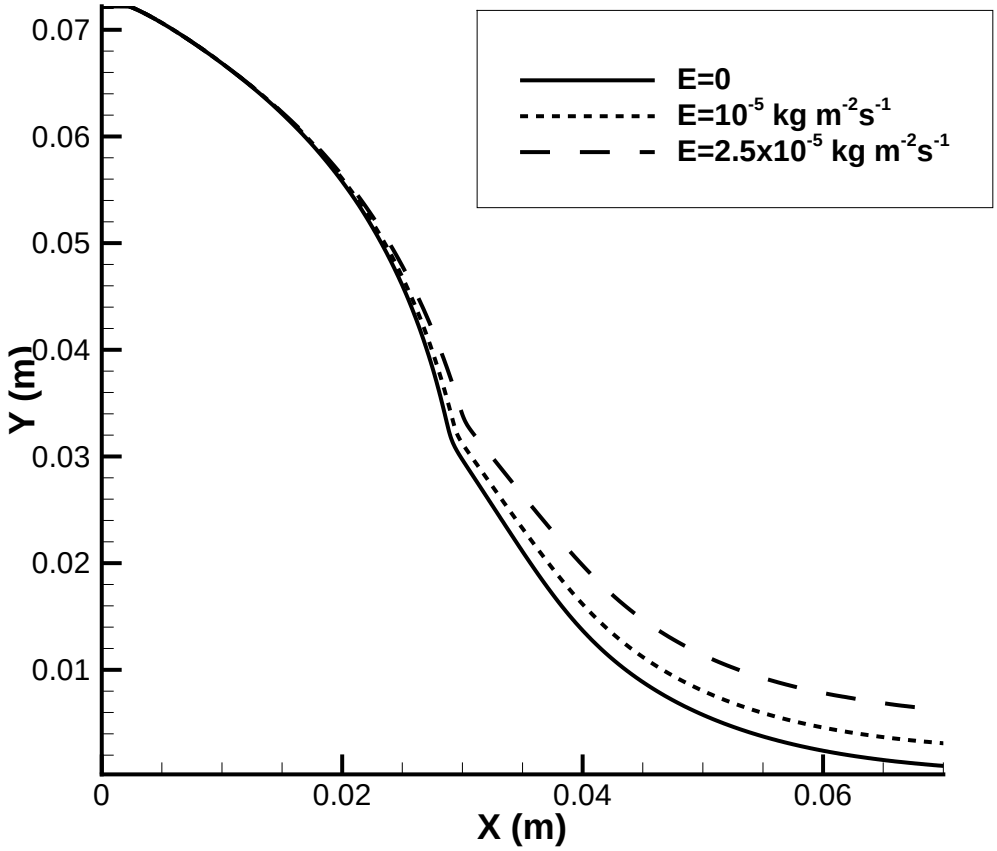

Figure 5.18: Axisymmetric plots of the stalagmite through time after 9 days growth for varying evaporative fluxes, E, when $Q = 2.89 \times 10^{-5}$kg s^{-1}, $T = 27°$C, $K = 8 \times 10^{-6}$ m s^{-1}, $c_{in} = 8$ Molar, $T_{in} = 30°$C.

5.5.4 Implications of the Model when Considering Alternate Materials

5.5.4.1 Diffusivity Effects

In order for the model to be used when predicting the crystallisation of different materials, it should be run over a range of parameters relating to the material properties, such that the robustness of the model can be tested. Moreover, varying the diffusivity parameter, D, will give insight into how the diffusion of solute within the solution affects the size and shape of the crystalline formations. The results, when simulated with parameters given in Table 5.1 (run 5), can be observed in Figure 5.19 where it can be seen that as the diffusivity decreases, the amount of solute deposited close to the apex is reduced. This is due to the solute's ability to flow from the bulk of the solution to the crystal growth site. Due to this, more solute remains within the solution further away from the apex, and as such decreasing D leads to thicker formations being formed away from the apex. For purposes of comparison, the crystal growth from the previous adapted stalagmite model is also plotted on the Figure 5.19. This comparison shows that our result has the thickest formation close to the apex, and also the narrowest formation further away from the apex.

5.6 Summary and Conclusions

Results presented in this chapter directly addressed the fourth objective of the thesis (see Chapter 1), by developing a multi-physics CFD model from the coupled CFD moving boundary framework developed in Chapter 4, such that it now considers the physics required in order to describe the growth of crystalline formations from salt solutions. The coupled model allows essential physical behaviour associated with the problem to be reliably accounted for (i.e. liquid film flow, evaporation, diffusion, temperature dependent solubility and concentration dependent fluid rheology).

Prior to coupling the individual models such that the complete system was considered, each individual model was assessed independently. This modelling methodology gave confidence that when considered as a whole, this coupled system would be robust over a wide range of parameters.

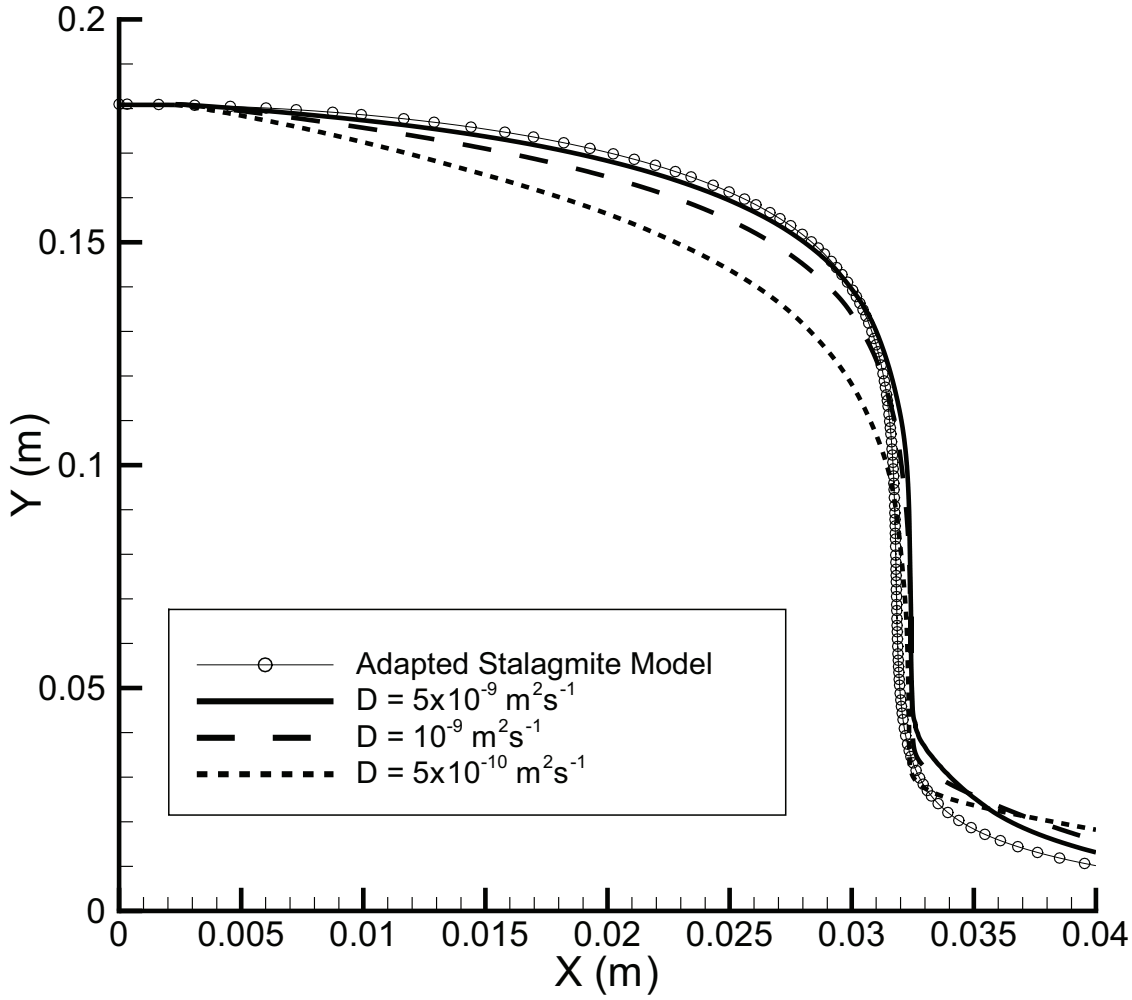

Figure 5.19: Axisymmetric plots of the crystalline growth after 22.2 days for varying material diffusivities, D, when $Q = 2.89 \times 10^{-5}$kg s^{-1}, $K = 8 \times 10^{-6}$ m s^{-1}, $c_{in} = 8$ Molar, $T_{in} = 30°$C, $T = 27°$C, $E = 10^{-5}$kg m^{-2} s^{-1}.

Once the individual models were shown to be robust, the fully coupled model was validated using the experimental dataset provided by the NNL, which monitored developing crystalline growths from a sodium nitrate solution. The results from the model were shown to be in good agreement for both the width and height of the crystalline formations through time. Having demonstrated that the model can simulate some of the key morphological aspects of the experimentally observed formations, when considering the 8 Molar sodium nitrate solution, the model was then used to assess the morphology of formations likely to occur under different process and environment conditions. Furthermore, the effects on varying material properties have been observed.

Results presented in this chapter suggest that both severity of the leakage (mass flow rate) and environmental parameters, such as room temperature and evaporative rates (temperature, humidity and air velocity), significantly influence the final formation shape. Additionally, results have also shown that the solution has relatively little impact for significant changes in the diffusivity. This suggests that the rate of crystal growth here is not limited by the diffusion of solute, implying the limiting factor in this crystallisation problem is the surface reaction step. This agrees with the previous assumption that $k_r << k_d$ and therefore suggests that the modelling assumption used here, $k_r \approx K$, is reasonable. Additionally, the work in Chapter 3 concluded that the final formation was highly sensitive to the material specific crystal growth kinetics. Based on this, the diffusivity trials in this chapter imply that the system is in fact highly sensitive to the surface reaction step k_r.

When considering the simulation of crystalline deposition of heavy metal salts the work here highlights several key areas which need to be considered. Therefore, it is recommended that input data for temperatures, liquor flow rates and environmental factors affecting the rate of evaporation should be given close consideration if using the model for criticality safety assessments. It should also be noted that systems dependence on both the diffusion and surface reaction step depends on the specific system in question, therefore diffusion could play a more significant role when considering alternate materials or flow regimes. It is therefore proposed that further studies are needed to reduce uncertainty in crystalline growth parameters for particular heavy metal solutions.

Chapter 6

Inverse Problem Methods for the Detection and Monitoring of Growing Crystalline Formations

6.1 Background and Introduction

Previous chapters in this thesis have developed models which highlight key behaviour for crystallisation behaviour experienced for a surrogate solution used in the problem described by the NNL drip trials. This previous work focused on the direct, forward modelling of the problem, such that a coupled, governing system of equations was established in order to describe the physical problem. Through implementation of varying solution methodologies, these models could be solved such that for a given set of input parameters the growing crystalline formations could be described. Results from the models determined the possible range of physical formations when considering this surrogate solution. Using this preliminary analysis and additional results when considering experimentally determined model parameters, it is expected that this work will be of use when developing an industrial safety case, such that a risk assessment factoring these potential formations can be formulated prior to the implementation of an industrial process. As discussed in Chapter 1, due to the nature of the materials in question (i.e. heavy metals), industrial process equipment is generally isolated in large concrete cells, such that in the event of a malfunction plant personnel are protected. Due to this, combined with the fact that it is not possible to implement standard monitoring equipment (due to radiation

levels), it is often difficult to obtain the required (transient) set of input data, such that the forward modelling approach can be used to accurately map the internal contents of a cell. Therefore, whilst offering information regarding the potential behaviour of a system, it may not be appropriate for non-invasively determining the size and shape of formations in an ongoing leakage. Thus, this chapter will focus on developing the mathematical groundwork for an non-invasive method such that the crystalline structures within a contained unit can be mapped through time, using assessable input data. The work in this chapter therefore addresses the fifth objective of this thesis.

6.1.1 Inverse problems

For an observable system it is often possible to formulation a model in which for a given parameter set, some physical or observable result can be determined. This is often called the forward or direct problem. Therefore, in this case an operator O can be defined such that for set of model parameters $\tilde{P}$ there exists a mapping such that $O : \tilde{P} \mapsto M$ where M is the set of measurable outputs. The form of this operator varies, however generally speaking, this is the physical or mathematical theory which links $\tilde{P}$ and M.

The inverse problem is then defined such that using the measurable data, the model parameters can be determined, such that $O^{-1} : M \mapsto \tilde{P}$. It should be noted that the exact form of O and $\tilde{P}$ can change depending on the availability of the measurable data, and the model parameters of interest. These problems can often be difficult to solve due to a number of factors. One problem experienced in inverse problems is that often the problem is underdetermined. For problems in which non-invasive or non-destructive methods are used, it is often the case that the required set of measurable parameters may not be available. This lack of observed data can often lead to non-uniqueness, such that for given set of observed data, differing sets of model parameters can be obtained. Problems of this nature are often considered to be 'ill-posed'. Hadamard stated that for a problem to be well-posed three conditions must hold, namely,

1. The solution exists
2. The solution must be unique
3. The solution's behaviour changes continuously with the initial conditions

Inverse problems have a wide range of application in many industries. Example of which include medical imaging techniques, e.g. x-ray and CT scanning, computational imagining for the reconstruction of photographic data, locating oil and gas deposits in the Earth's interior, industrial process monitoring, computational finance and shape optimising the aerodynamic configuration in the aerospace industry, etc. It is therefore no surprise that a great deal of research has been carried out in this area. Research in the field of inverse problems can usually be classified into one of the following areas:

Geometric inverse problems or shape determination: These problems involve the determination of an unknown geometric shape and can be used to consider a variety of different phenomena, such as internal cavities or inclusions, unobservable boundaries, as in corrosion engineering.

Initial or boundary value inverse problems: These problems are concerned with the identification of boundary or initial conditions. Applications of which could include the determination of temperatures, or pressures on an inaccessible boundary. Also, initial values of a system can be determined such as the initial chemical composition in a reactive system.

Source determination problems: The determination of sources in the governing equations can relate to a number of physical phenomena, such as sources of heat or radiation. In structural dynamics, the force or stresses acting on a system could also be considered.

Material properties identification: Here observed data from the system is used to calculate model parameters relating to the materials in question. Examples of which could include the determination of the thermal conductivity in heat transfer, the fluid density in fluid flow, or the electric conductivity in electrostatics.

6.1.2 A Geometric Inverse Problem and the Method of Fundamental Solutions

The problem here can be considered as a geometric inverse problem such that the crystalline contents of an isolated cell can be described by a geometric shape or boundary.

Using measurable data these boundaries or shapes can be determined through solution of the inverse problem. Due to the nature of inverse geometric problems, considerations have to be made regarding the implication of the numerical discretisation when factoring the dynamic moving boundary. Clearly, from Chapters 4 and 5 there are several challenges involved in the discretisation (meshing) of domains when considering moving boundaries. In addition to the boundaries movement through time, iterative solvers generally attempt several perturbations of the boundary position for any given timestep, such that criteria imposed by the system are satisfied. This behaviour is non trivial to solve numerically when using traditional mesh based numerical methods, e.g. FVM, due to the difficulty of remeshing the numerical grid for each attempted solver iteration. Due to this, the work in this chapter considers a meshless numerical method, namely, the Method of Fundamental Solutions (MFS). The MFS is a relatively new, powerful meshless numerical method which can be used to obtain accurate solutions to linear partial differential equations. It has many advantages over other conventional discretisation methods, e.g. the finite element method (FEM), the finite-difference method (FDM), and the boundary element method (BEM), one of the primary reasons being that unlike the aforementioned methods the MFS requires neither domain nor boundary meshing (An example of a traditional method compared with a meshless method can be seen in Figure 6.1). Hence, it is able to solve problems involving both irregular domains and moving boundaries when governed by equations such as the Laplace and Helmholtz equation, see [26, 100, 101]. It should be noted that the MFS also presents advantages over methods such as the BEM as the formulation of complicated integral expressions is not necessary. A thorough review of the MFS and its application to inverse problems can be found in [102].

The measurable data in the nuclear case is likely to be limited due to the hostile environment present. When considering the measurable data that may be available when non-invasively monitoring from outside the cell, it is thought that the heat flux would be obtainable. In addition to this, it is expected that the solid crystalline body will obey the physical laws for the diffusion of heat, such that it can be described by the transient (two-dimensional) heat equation. Due to the aforementioned advantages of using meshless methods for boundary determination problems, the work in this chapter develops a model for the two-dimensional heat equation such that the inverse geometric problem of locating a boundary describing the crystal formation can be solved through time. Previous studies

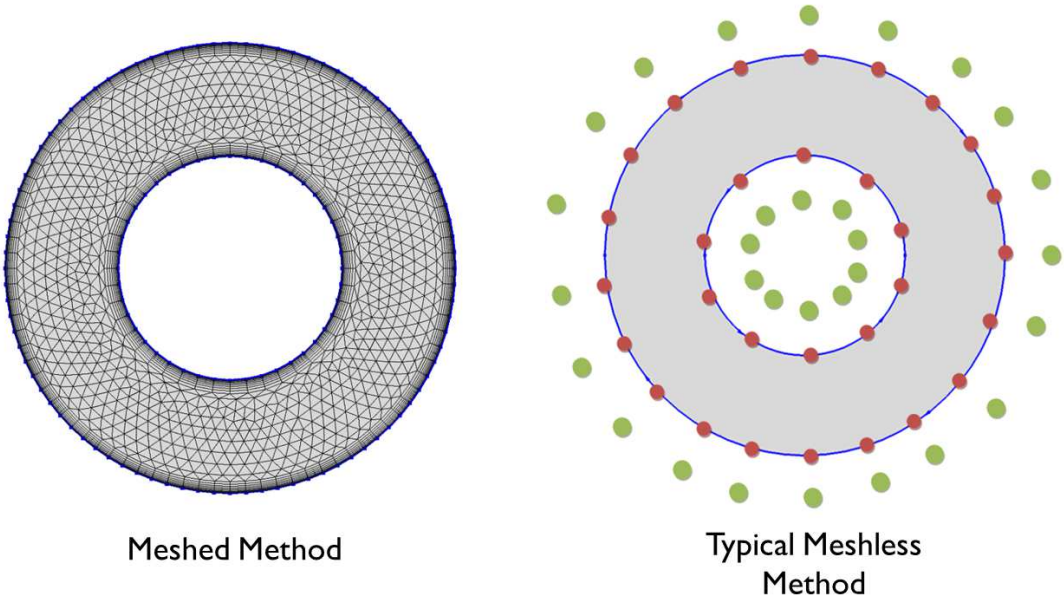

Figure 6.1: Comparison of an arbitrary domain when discretised with a meshless method and a traditional meshed method.

generally focused on a steady state problem, such that the boundary of interest remained stationary, therefore the work presented in this chapter presents a novel approach for solving an inverse geometric moving boundary problem governed by the transient heat equation.

6.2 Mathematical Model

The mathematical formulation of the inverse geometric problem under investigation requires finding the temperature, now denoted by $\tilde{u}$, and a moving internal defect $\Gamma(t)$ satisfying the heat equation,

$$\frac{\partial \tilde{u}}{\partial t}(\mathbf{x}, t) - \Delta \tilde{u}(\mathbf{x}, t) = 0, \quad (\mathbf{x}, t) \in (\Omega \setminus \overline{\Gamma(t)}) \times (0, \tilde{T}], \tag{6.1}$$

subject to the initial condition,

$$\tilde{u}(\mathbf{x}, 0) = \tilde{u}_0(\mathbf{x}), \quad \mathbf{x} \in \overline{\Omega} \setminus \Gamma(0), \tag{6.2}$$

the Cauchy (Dirichlet + Neumann) boundary conditions on the fixed outer boundary $\partial\Omega$,

$$\tilde{u}(\mathbf{x},t) = \tilde{f}(\mathbf{x},t), \quad (\mathbf{x},t) \in \partial\Omega \times [0,\tilde{T}], \tag{6.3}$$

$$\frac{\partial \tilde{u}}{\partial n}(\mathbf{x},t) = \tilde{g}(\mathbf{x},t), \quad (\mathbf{x},t) \in \partial\Omega \times [0,\tilde{T}], \tag{6.4}$$

and the Dirichlet or Neumann boundary condition on $\partial\Gamma(t)$, namely,

$$\tilde{u}(\mathbf{x},t) = \tilde{h}(\mathbf{x},t), \quad (\mathbf{x},t) \in \partial\Gamma(t) \times [0,\tilde{T}], \tag{6.5}$$

or,

$$\frac{\partial \tilde{u}}{\partial n}(\mathbf{x},t) = \tilde{h}(\mathbf{x},t), \quad (\mathbf{x},t) \in \partial\Gamma(t) \times [0,\tilde{T}]. \tag{6.6}$$

Here Ω and $\Gamma(t)$ are simply connected bounded smooth domains such that $\overline{\Gamma(t)} \subset \Omega$ and $\Omega \setminus \Gamma(t)$ is connected, $\tilde{T} > 0$ is an arbitrary time of interest and $\mathbf{n}$ is the outward unit normal to the boundary. It is assumed that the functions $\tilde{u}_0(\mathbf{x}), \tilde{f}(\mathbf{x},t), \tilde{g}(\mathbf{x},t)$ and $\tilde{h}(\mathbf{x},t)$ are known. In (6.5) or (6.6) the function $\tilde{h}$ is usually taken to be uniform, e.g. zero, such that $\Gamma(t)$ represents a rigid inclusion for the homogeneous Dirichlet boundary condition (6.5) and a cavity for the homogeneous Neumann boundary condition (6.6). These type of inverse problems are common in studies relating to various industries, for example, the related inverse boundary determination problem which arises in corrosion engineering and in which $\partial\Gamma(t)$ consists of an unknown portion of $\partial\Omega$ has been investigated with the MFS in [88].

Also the Neumann boundary condition (6.4) may be partially limited to a portion $\Sigma \times [T_0, T_1]$ of $\partial\Omega \times (0,\tilde{T}]$. When the domain Γ is independent of time t, the solution of the inverse problem (6.1)-(6.5), or (6.1)-(6.4), (6.6) is unique, see [43, 44], respectively, and for numerical reconstructions, see [41, 42]. However, these problems are still ill-posed since small errors in the input data (6.2)-(6.4) cause large deviations in the solution. For more comprehensive investigations on the determination of unknown steady-state or time-varying boundaries for the heat equation, see [36, 106, 179, 91]. It should be noted that these studies are not restricted to use of the MFS.

The MFS assumes that the solution of the heat equation (6.1) can be approximated by a

linear combination of fundamental solutions of the form, see [94],

$$U_{M,N}(\mathbf{x},t)=\sum_{m=1}^{2M}\sum_{j=1}^{2N}c_j^m\tilde{F}(\mathbf{x},t;\mathbf{y}_j^m,\tau_m),\quad (\mathbf{x},t)\in(\overline{\Omega}\setminus\Gamma(t))\times[0,\tilde{T}], \tag{6.7}$$

where $(\mathbf{y}_j^m)_{j=\overline{1,2N}}^{m=\overline{1,2M}}$ are space 'singularities' (sources) located outside the space domain $\overline{\Omega}\setminus\Gamma(t)$, τ_m are times located in the interval $(-\tilde{T},\tilde{T})$ and $\tilde{F}$ is the fundamental solution for the two-dimensional heat equation given by,

$$\tilde{F}(\mathbf{x},t;\mathbf{y},\tau)=\frac{H(t-\tau)}{4\pi(t-\tau)}\exp\left(-\frac{|\mathbf{x}-\mathbf{y}|^2}{4(t-\tau)}\right), \tag{6.8}$$

where H is the Heaviside function which is included in order to emphasize that the fundamental solution is zero for $t\leq\tau$.

Without loss of generality, based on the conformal mapping theorem, it can be assumed that the smooth, bounded and simply-connected domain Ω is the unit disk. Furthermore, for simplicity, it is assumed that the smooth, simply-connected domain $\overline{\Gamma}(t)\subset\Omega$ is star-shaped with respect to the origin, hence its boundary, $\partial\Gamma(t)$ can be represented in parametric polar form by a 2π - periodic smooth function $r:[0,2\pi)\times[0,\tilde{T}]\to(0,1)$ as,

$$\partial\Gamma(t)=\left\{\big(r(\theta,t)\cos(\theta),r(\theta,t)\sin(\theta)\big)\mid\theta\in[0,2\pi)\right\},\quad t\in[0,\tilde{T}]. \tag{6.9}$$

In three-dimensions one can use spherical coordinates. Whilst the geometry considered in this problem relates to a quadrilateral surface, the primary work here is to address the numerical stability and accuracy of the model. The domain here allows for simple parameterisation of the boundaries and provides the simplest possible framework in which the model can be evaulated.

In the direct problem, when the domain $\Gamma(t)$ is known, the unknown coefficients $(c_j^m)_{j=\overline{1,2N}}^{m=\overline{1,2M}}$ in the MFS expansion (6.7) are determined by collocating the initial condition (6.2) and either of the boundary conditions (6.3) or (6.4), and (6.5) or (6.6). In the inverse problem, the unknown coefficients $(c_j^m)_{j=\overline{1,2N}}^{m=\overline{1,2M}}$ and also some time-dependent radii $(\mathbf{r}_j^m)_{j=\overline{1,N}}^{m=\overline{0,M}}$ are to be determined by collocating equations (6.2)-(6.4), and (6.5) or (6.6).

6.2.1 Distribution of Source and Collocation Points

In this section, we describe how the source and boundary collocation points are distributed for problems in which the outer boundary $\partial\Omega$ is a circle of radius 1 and the inner boundary $\partial\Gamma(t)$ is that of a star-shaped domain.

The outer source points are located outside $\Omega = B(\mathbf{0}, 1)$ on a circle $\partial B(\mathbf{0}, R)$ of radius $R > 1$, namely

$$\mathbf{y}_j^m = (R\cos(\theta_j), R\sin(\theta_j)), \quad \theta_j = \frac{2\pi j}{N}, \quad j = \overline{1, N}, \quad m = \overline{1, 2M}. \tag{6.10}$$

We also take

$$\tau_m = \begin{cases} \frac{(2m-1)\tilde{T}}{2M}, & m = \overline{1, M} \\ \\ -\frac{[2(m-M)-1]\tilde{T}}{2M}, & m = \overline{M+1, 2M} \end{cases} \tag{6.11}$$

The inner source points are located inside $\Gamma(t)$, namely,

$$\mathbf{y}_{j+N}^m = \frac{1}{2}(r_j^m \cos(\theta_j), r_j^m \sin(\theta_j)), \quad j = \overline{1, N}, \quad m = \overline{1, 2M}, \tag{6.12}$$

where the radii $r(\theta_j, \tau_m) =: r_j^m \in (0, 1)$ constitute a radial parameterisation of the star shaped domain $\Gamma(t)$ whose boundary at time t is approximated by, (see (6.9)),

$$\partial\Gamma(t) = \left\{ \left(r(\theta_j, t)\cos(\theta_j), r(\theta_j, t)\sin(\theta_j) \right) \mid j = \overline{1, N} \right\}, \quad t \in (-\tilde{T}, \tilde{T}), \tag{6.13}$$

and the symmetry condition $\partial\Gamma(-t) = \partial\Gamma(t)$ for $t \in (0, \tilde{T})$ is imposed. From (6.10) and (6.12) one can see that a total of $4MN$ source points have been specified. The collocation points on the boundaries and initial domain are now collocated.

On the outer boundary $\partial\Omega$ the boundary collocation points are given by,

$$(\mathbf{x}_i, \tau_j) = (\cos(\theta_i), \sin(\theta_i), \tau_j), \quad i = \overline{1, N}, \quad j = \overline{0, M}, \tag{6.14}$$

where $\tau_0 = 0$. On the inner boundary $\partial\Gamma(t)$ the boundary collocation points are given by,

$$(\mathbf{x}_i^j, \tau_j) = (r_i^j \cos(\theta_i), r_i^j \sin(\theta_i), \tau_j), \quad i = \overline{1, N}, \quad j = \overline{0, M}. \tag{6.15}$$

Collocating the boundary conditions (6.3), (6.4) and (6.6) results in $3(M+1)N$ equations. Another $(\tilde{K}-1)N$ equations are obtained by imposing the initial condition (6.2). We collocate the initial condition (6.2) in the domain $\Omega \setminus \overline{\Gamma(0)}$ at time $t = 0$ at the points

$$\mathbf{x}_{i,j} = \left(\left(r_j^0 + \frac{(1-r_j^0)i}{\tilde{K}} \right) \cos(\theta_j), \left(r_j^0 + \frac{(1-r_j^0)i}{\tilde{K}} \right) \sin(\theta_j) \right), \quad i = \overline{1, (\tilde{K}-1)}, \quad j = \overline{1, N}, \tag{6.16}$$

where $r_j^0 = r(\theta_j, 0)$ for $j = \overline{1, N}$.

The full time-dependent inverse geometric problem amounts to $4MN + N(M+1) = N(5M+1)$ unknowns represented by the $4MN$ coefficients $\mathbf{c} = (c_j^m)_{j=\overline{1,2N}}^{m=\overline{1,2M}}$ in the MFS expression (6.7), and the $N(M+1)$ radii $\mathbf{r} = (r_j^m)_{j=\overline{1,N}}^{m=\overline{0,M}}$, for the parametrisation of the boundary, $\Gamma(t)$. On the other hand, the collocation of the conditions (6.2)-(6.4) and (6.6) amounts to $N(3M + \tilde{K} + 2)$ equations, namely, $(\tilde{K}-1)N$ equations for the initial condition (6.2) imposed at the points (6.16), $2(M+1)N$ equations for the Cauchy boundary condition (6.3) and (6.4) imposed at the points (6.14), and $(M+1)N$ equations for the boundary condition (6.5) or (6.6) imposed at the points (6.15). From summing the above, it follows that a necessary solution for a non underdetermined system, and hence a unique solution, is $\tilde{K} \geq 2M - 1$.

6.2.2 Least-Squares Minimisation Problem

When considering the Dirichlet boundary condition on the inclusion, since boundary conditions (6.3)-(6.5) and the initial condition (6.2) are known, we can fit the approximated data of the MFS to these values using a non-linear least-squares formulation to find the unknown values of $\mathbf{c}$ and $\mathbf{r}$. Then, the following functional is minimised,

$$S(\mathbf{c}, \mathbf{r}) = ||U_{M,N} - \tilde{f}||^2 + ||U_{M,N} - \tilde{h}||^2 + \left|\left| \frac{\partial U_{M,N}}{\partial n} - \tilde{g} \right|\right|^2 + ||U_{M,N} - \tilde{u}_0||^2. \tag{6.17}$$

In discretised form, expression (6.17) to be minimized can be written as:

$$\begin{aligned} S(\mathbf{c},\mathbf{r}) = \sum_{i=1}^{N}\sum_{j=0}^{M}\left[(U_{M,N}(\mathbf{x}_i,\tau_j)-\tilde{f}(\mathbf{x}_i,\tau_j))^2+\left(\tfrac{\partial U_{M,N}}{\partial n}(\mathbf{x}_i,\tau_j)-\tilde{g}(\mathbf{x}_i,\tau_j)\right)^2\right] \\ +\sum_{i=1}^{N}\sum_{j=1}^{M}\left(U_{M,N}(\mathbf{x}_i^j,\tau_j)-\tilde{h}(\mathbf{x}_i^j,\tau_j)\right)^2 \\ +\sum_{i=1}^{\tilde{K}-1}\sum_{l=1}^{N}\left(U_{M,N}(\mathbf{x}_{i,l},0)-\tilde{u}_0(\mathbf{x}_{i,l})\right)^2. \end{aligned} \tag{6.18}$$

For the case where the Neumann condition is imposed, boundary conditions (6.3),(6.4), (6.6) and the initial condition (6.2) are known, and therefore the following objective functional is minimised,

$$S(\mathbf{c},\mathbf{r}) = ||U_{M,N}-\tilde{f}||^2+\left|\left|\frac{\partial U_{M,N}}{\partial n}-\tilde{h}\right|\right|^2+\left|\left|\frac{\partial U_{M,N}}{\partial n}-\tilde{g}\right|\right|^2+||U_{M,N}-\tilde{u}_0||^2. \tag{6.19}$$

In discretised form, expression (6.19) to be minimized can be written as:

$$\begin{aligned} S(\mathbf{c},\mathbf{r}) = \sum_{i=1}^{N}\sum_{j=0}^{M}\left[(U_{M,N}(\mathbf{x}_i,\tau_j)-\tilde{f}(\mathbf{x}_i,\tau_j))^2+\left(\tfrac{\partial U_{M,N}}{\partial n}(\mathbf{x}_i,\tau_j)-\tilde{g}(\mathbf{x}_i,\tau_j)\right)^2\right] \\ +\sum_{i=1}^{N}\sum_{j=0}^{M}\left(\tfrac{\partial U_{M,N}}{\partial n}(\mathbf{x}_i,\tau_j)-\tilde{h}(\mathbf{x}_i^j,\tau_j)\right)^2 \\ +\sum_{i=1}^{\tilde{K}-1}\sum_{l=1}^{N}\left(U_{M,N}(\mathbf{x}_{i,l},0)-\tilde{u}_0(\mathbf{x}_{i,l})\right)^2. \end{aligned} \tag{6.20}$$

In expressing the third term in (6.17) or the second and third term in (6.19), the normal derivative of the fundamental solution (6.7) is needed, namely

$$\frac{\partial\tilde{F}}{\partial n}(\mathbf{x},t;\mathbf{y},\tau) = -\frac{(\mathbf{x}-\mathbf{y})\cdot\mathbf{n}}{8\pi(t-\tau)^2}\ \exp\left(-\frac{|\mathbf{x}-\mathbf{y}|^2}{4(t-\tau)}\right)H(t-\tau), \tag{6.21}$$

where,

$$\mathbf{n} = \begin{cases} cos\theta\mathbf{i}+sin\theta\mathbf{j}, & \text{if } (\mathbf{x},t)\in\partial\Omega\times[0,\tilde{T}] \\ \frac{1}{\sqrt{r^2(\theta)+r'^2(\theta)}}\Big[(-r'(\theta)\sin\theta+r(\theta)\cos\theta)\mathbf{i} & \\ +(r'(\theta)\cos\theta-r(\theta)\sin\theta)\mathbf{j}\Big] & \text{if } (\mathbf{x},t)\in\partial\Gamma(t)\times[0,\tilde{T}] \end{cases} \tag{6.22}$$

When calculating this value within the minimisation of (6.19) such that the normal derivative is required on $\partial\Gamma(t)$ a central finite difference approximation is taken for the value of $\mathbf{r}'$, given by,

$$r_i'^j = \frac{\partial r_i^j}{\partial \theta} = N\left(\frac{r_{i+1}^j - r_{i-1}^j}{4\pi}\right) \tag{6.23}$$

where $r_0^j = r_N^j$ and $r_{N+1}^j = r_1^j$,

6.2.3 Regularisation Method

The geometric problem under investigation is ill-posed, and therefore some form of regularisation is often required when solving it. Here the Tikhonov regularisation technique is used. This technique often employed when solving inverse and ill-posed problems in order to obtain a stable solution. This technique is imposed by the addition of an extra term to (6.17) and (6.19), namely,

$$S_\lambda(\mathbf{c}, \mathbf{r}) = S(\mathbf{c}, \mathbf{r}) + \lambda||\mathbf{c}||^2, \tag{6.24}$$

where $\lambda > 0$ is a regularisation parameter.

The Tikonhov regularisation technique also states that regularisation can be placed on the other unknown sets of variables. In this problem the terms $\lambda||\mathbf{r}||$ and $\lambda||\mathbf{r}'||$ could be included. However, preliminary numerical trials have shown this deemed unnecessary for the problem here. Therefore only regularisation on the $||\mathbf{c}||^2$ term, is imposed.

It should also be noted that when solving for the direct problem, which is linear, the above technique can yield an explicit solution of the form,

$$\mathbf{c} = (\mathbf{A}^{tr}\mathbf{A} + \lambda\mathbf{I})^{-1}\mathbf{A}^{tr}\mathbf{b}, \tag{6.25}$$

for the original ill-conditioned MFS system of linear equations, generically written as $\mathbf{Ac} = \mathbf{b}$.

6.2.4 Introduction of Noise to the Boundary Flux Data

In industrial practice, the heat flux values (6.4) on the outer boundary $\partial\Omega$ would be measured using experimental techniques and equipment. Generally, no measurement device is completely accurate and there is a level of uncertainty in the data is expected. Due to this, a numerical noise factor is numerically simulated to mimic the inherent errors in the experimental data that would be used. Noisy data was achieved by using the MATLAB function *normrand*$(0, \sigma)$, which generates a random number from a given normal distribution space, namely,

$$\tilde{g}^{\eta}(\mathbf{x}_i^j, t_j) = \tilde{g}(\mathbf{x}_i^j, t_j) + \epsilon_{i,j}, \quad i = \overline{1, N}, \quad j = \overline{0, M}, \tag{6.26}$$

where $\epsilon_{i,j}$ are normal random variables with mean zero and standard deviation σ=max$|\tilde{g}(\mathbf{x}_i^j, t_j)|p$, where p represents the percentage of noise.

6.3 Computational Implementation

There are several choices of routines which can solve the non-linear optimisation problems as defined in (6.17) and (6.19), each method has its own inherent advantages and disadvantages and as such the choice of solver is often non-trivial. In this study, the minimisation of (6.17) or (6.19) is performed using the optimisation toolbox function 'FMINCON' in MATLAB. The FMINCON function employs an 'interior point' algorithm, which is suited to solving non-linear convex optimisation problems, [40]. This algorithm was used for several reasons. Firstly, it allows bound constraints to be imposed on resultant solution, this allowed the minimisation of (6.18) and (6.20) subject to the physical constraints $\mathbf{0} < \mathbf{r} < \mathbf{1}$ such that the defect $\overline{\Gamma(t)}$ in contained within the fixed domain Ω. Restricting the solution domain can often increase the likelihood of obtaining a unique solution in many non-linear problem, additionally, restricting the possible choices for the unknowns can speed up the solution process.

The second reason for choosing the FMINCON routine was that many algorithms require the user to input an analytical expression for the gradient vector. These can often be complicated and time consuming to code, however, the routine used here calculates this

gradient vector by use of an internal finite differencing procedure, removing the need for these challenging expressions.

Lastly, one of the main advantages when using the FMINCON routine is its ability to operate in parallel over multiple CPU cores. The number of unknowns within the optimisation problem here is of size, $5N(M+1)$, this therefore amounts to a much larger optimisation problem than solved in previous steady state inverse geometric problems using the MFS [26, 100, 101]. Due to the large size of the time-dependent optimisation problem, the ability to run in parallel using multiple cores is almost a necessity in order to obtain a solution within a feasible time. This facility was utilised on the University of Leeds 'ARC1' high performance computer, running the process in parallel over 8 cores. To demonstrate the computational benefits of the parallel approach, the times required to solve the problem outlined in Case 1 (see results), have been compared for a range of discretisation sizes (MFS parameters). Figure 6.2 presents the computational times for $N(5M+1)$ points when $\tilde{K} = 2M-1$ for increasing values of M and N. It can be clearly seen from this figure that the parallel toolbox speeds up the solver process significantly.

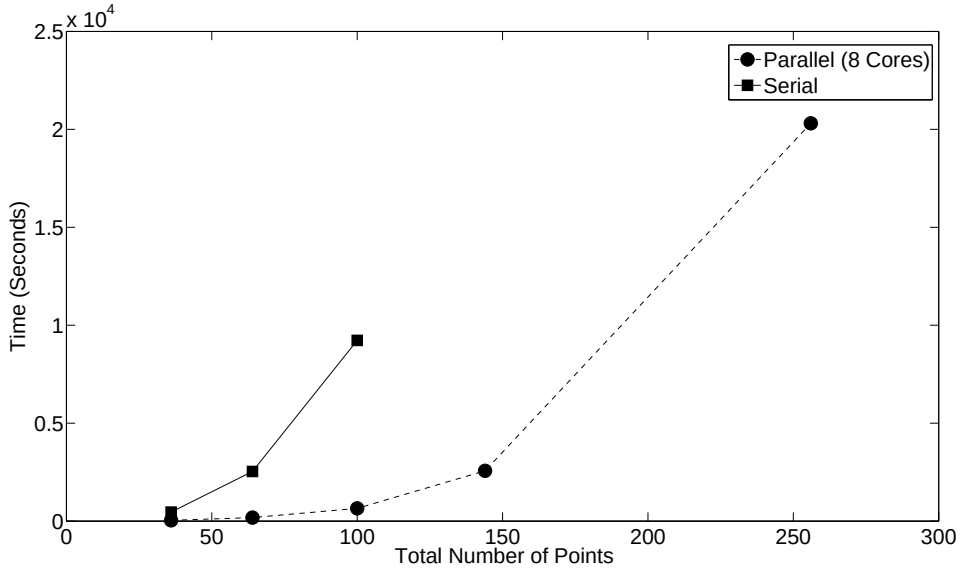

Figure 6.2: Comparison of computational times for runs in parallel and serial for Case 1.

6.4 Results

In order to test the stability and accuracy of the method, several examples were evaluated. These example both varied the shape of the defect $\Gamma(t)$, and the boundary condition imposed upon it.

6.4.1 Case 1: Circular Inclusion with Imposed Dirichlet Boundary Condition (6.5)

Here a stationary star-shaped inclusion given by the circle, $B(\mathbf{0}, 0.5)$ centred at the origin with radius 0.5 within the unit circle domain $\Omega = B(\mathbf{0}, 1)$ was located. This case considered the Dirichlet condition imposed on the boundary $\partial\Gamma(t)$. The initial and boundary conditions (6.2), (6.3) and (6.5) were given by

$$\tilde{u}(\mathbf{x}, 0) = \tilde{u}_0(\mathbf{x}) = |\mathbf{x}|^2, \quad \mathbf{x} \in \overline{\Omega} \setminus \Gamma(0), \tag{6.27}$$

$$\tilde{u}(\mathbf{x}, t) = \tilde{f}(\mathbf{x}, t) = 4t + 1, \quad (\mathbf{x}, t) \in \partial\Omega \times [0, \tilde{T}], \tag{6.28}$$

$$\tilde{u}(\mathbf{x}, t) = \tilde{h}(\mathbf{x}, t) = 4t + 0.25, \quad (\mathbf{x}, t) \in \partial\Gamma(t) \times [0, \tilde{T}]. \tag{6.29}$$

As described previously, the inverse problem here is non-linear and ill-posed where the internal boundary $\partial\Gamma(t)$ is unknown, therefore it is necessary that extra information is supplied in order to determine the additional unknowns relating to the discrete radial parametrisation of the internal boundary, such that the system is not underdetermined. This then allows the reconstruction of the moving boundary, $\partial\Gamma(t)$, within the domain Ω. This additional information is in the form of the heat flux on $\partial\Omega$, as described by equation (6.4), namely

$$\frac{\partial \tilde{u}}{\partial n}(\mathbf{x}, t) = \tilde{g}(\mathbf{x}, t) = 2, \quad (\mathbf{x}, t) \in \partial\Omega \times [0, \tilde{T}]. \tag{6.30}$$

The accuracy of the solution was analysed using the RMS value of the error between the analytical and estimated internal boundary defined as,

$$\text{RMS} = \sqrt{\frac{\sum_{j=1}^{N} \sum_{m=0}^{M} \left(r_j^m - 0.5\right)^2}{N(M+1)}}. \tag{6.31}$$

As such, if the boundary is located exactly the RMS value would be zero.

6.4.1.1 Results: Inverse Problem

The results for Case 1 are presented for a range of discretisation parameters (MFS parameters M and N). In each of these cases it was found that no regularisation was necessary (i.e. in (6.24), $\lambda = 0$). The minimisation process was stopped when a suitable level of convergence was obtained.

Firstly in the case of no noise, i.e. $p = 0$, Figures 6.3(a) and 6.3(b) display the objective function (6.18) and the RMS (6.31), for each iteration. Results shown were obtained taking MFS parameters $M = N = 6$ and 12, with $\tilde{K} = 2M - 1 = 11$ and 23, respectively. In these cases, the objective functional (6.18) contained $N(5M + 1) = 186$ and 732 conditions, respectively. Results are summarised in Table 6.1.

From Figure 6.3, when considering the case $M = N = 6$, it can be seen that even though the objective function continued to decrease though out the solver process, the RMS value was seen to diverge at a given iteration (iteration 30). In an attempt to increase the stability, larger values for the MFS parameters were trialled. Analysis of the problem with parameters $M = N = 12$, $\tilde{K} = 2M - 1 = 23$ was carried out. Results for these parameters show that the RMS value no longer increased as the objective function is minimised. In Figure 6.3(a), when considering MFS parameters $M = N = 12$, after 118 iterations the objective function (6.18) appeared to reach a stationary value. This suggested that the method remained stable for larger parameter sizes, additionally the accuracy of the solution was improved, which can be shown from the RMS values in Figure 6.3(b).

In order to visually demonstrate the minimisation process, the radial parametrisation of the internal boundary is shown for various iterations. These results consider MFS parameters $M = N = 12$ and are presented in Figure 6.4. From this figure it can be seen that a convergent and stable reconstruction of the moving inclusion is realised after 118 iterations. This corresponds to the objective function reaching a stable value.

The parameter set of $M = N = 12$, $\tilde{K} = 23$ was deemed sufficiently large for the purposes of achieving an accurate result when balanced with the high computational time required for larger MFS parameter sizes. It can be clearly seen from the results presented in Table

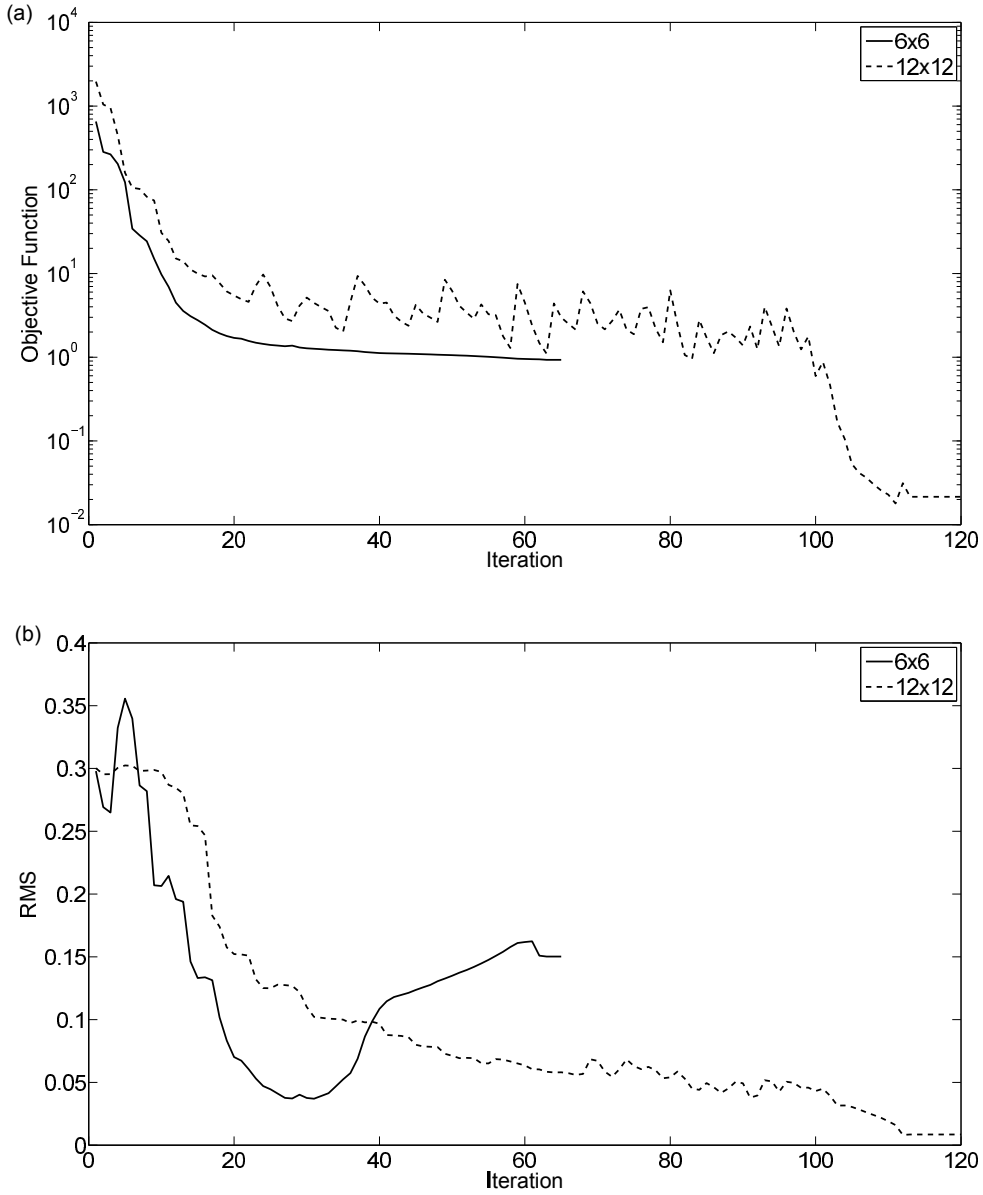

Figure 6.3: (a) The objective function (6.18) and (b) the RMS values (6.31) for MFS parameters $M = N = 6$ and 12, $\tilde{K} = 11$ and 23, respectively. For Case 1, $p = 0$.

6.1 that as the parameter size increases, the overall accuracy of the estimated solution also increases. One can also deduce from Table 6.1 that larger parameter sets require more iterations in order to reach a stable solution. Additionally, the time for each iteration also increases with increasing parameter size.

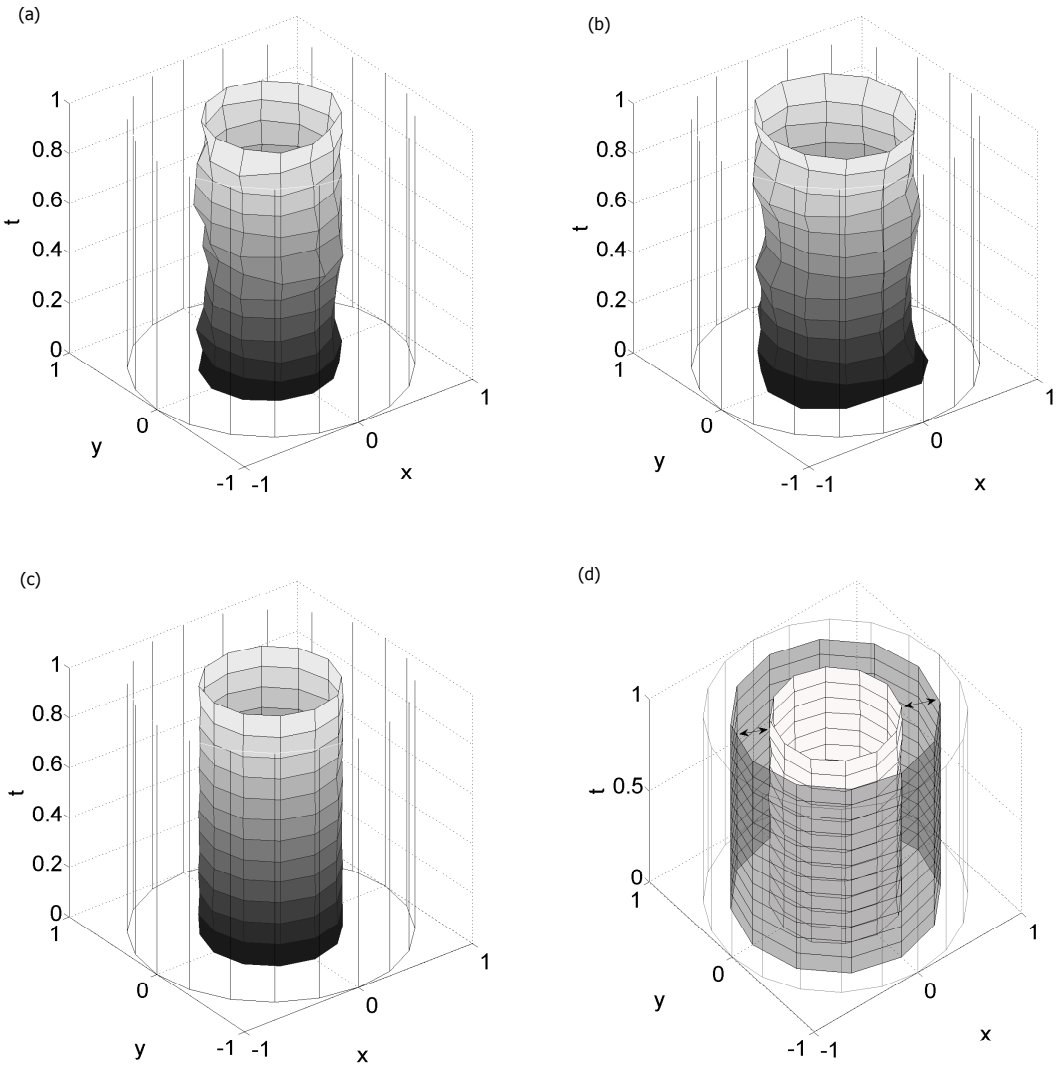

Figure 6.4: Plots of the inclusion at iterations: (a) 42, (b) 90, and (c) 118 (final), when trying to locate a circular inclusion of radius 0.5. d) Shows the initial guess (grey) and the final solution (white). For Case 1, $p = 0$.

Next, the measured flux (6.26) on the outer boundary was contaminated with numerical noise. Figures 6.5(a) and 6.5(b) display the minimisation of the objective function (6.18), and the corresponding RMS (6.31) when both $p = 10\%$ and 25% noise was added to the flux data (6.30), where the noise was given by (6.26). From these figures it can be observed that introducing noise decreased the accuracy and stability of the solution. In order to further confirm this statement, a graphical representation of the solution is given

Size	Obj. Func.	RMS	CPU Time (s)	Iterations
$M = N = 6$, $\tilde{K} = 11$	0.92969	0.15021	16.587	65
$M = N = 8$, $\tilde{K} = 15$	0.08784	0.03370	72.736	68
$M = N = 10$, $\tilde{K} = 19$	0.04311	0.01897	336.55	105
$M = N = 12$, $\tilde{K} = 23$	0.02151	0.00852	1116.8	118

Table 6.1: Numerical results in Case 1 for the objective function (6.18), the RMS (6.31), the CPU time and the number of iterations required for convergence, obtained with various MFS parameter sizes.

in Figure 6.6. Results are summarised in Table 6.2.

From Figure 6.5 it can be observed that the numerical results become less accurate and stable as the amount of noise increases from for $p = 10\%$ to 25% noise. However, the numerical solution for $p = 25\%$ noise is still in reasonable agreement with the exact solution when considering the magnitude of the noise in which the input flux data was contaminated. The relatively high robustness with these large amounts of noise is potentially related to the simple geometry of the inclusion being reconstructed. It is not anticipated that this would be the case with more challenging geometries, as investigated in later examples.

By taking a plot of the final solution at the final time, $t = \tilde{T} = 1$, the effects of increasing the noise can be seen from Figure 6.7 and Table 6.2. It can be observed that as the amount of noise decreases, the numerical solution becomes closer to the exact boundary location.

Overall, the numerical results obtained for Case 1 demonstrate that the MFS provides a powerful method for solving inverse geometric problems concerned with the reconstruction of simple smooth internal boundaries, such as a circle. It has been shown that high levels of accuracy and resolution can be obtained and in this case, the method was shown to be particularly resilient to large amounts of noise in the input data.

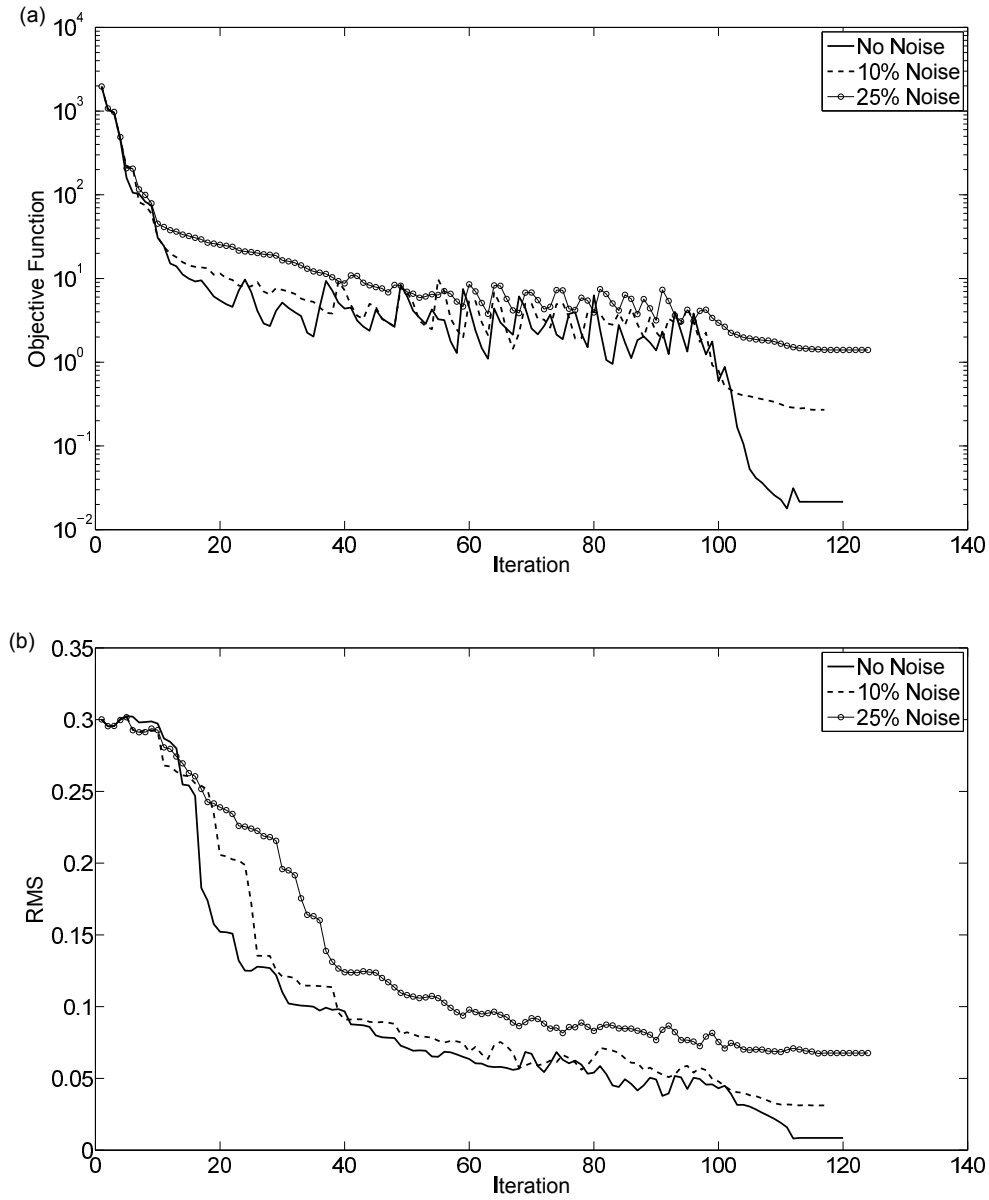

Figure 6.5: (a) The objective function in Case 1 (6.18), and (b) the RMS values (6.31) for MFS parameters $M = N = 12, \tilde{K} = 23$, for $p = 0$, 10% and 25% noise.

6.4.2 Case 2: Stationary, Bean Shaped Rigid Inclusion

In this case a bean shaped stationary star-shaped inclusion that is parametrised by,

$$r(\theta) = \frac{0.55 + 0.4\cos(\theta) + 0.15\sin(2\theta)}{1 + 0.7\cos(\theta)}, \tag{6.32}$$

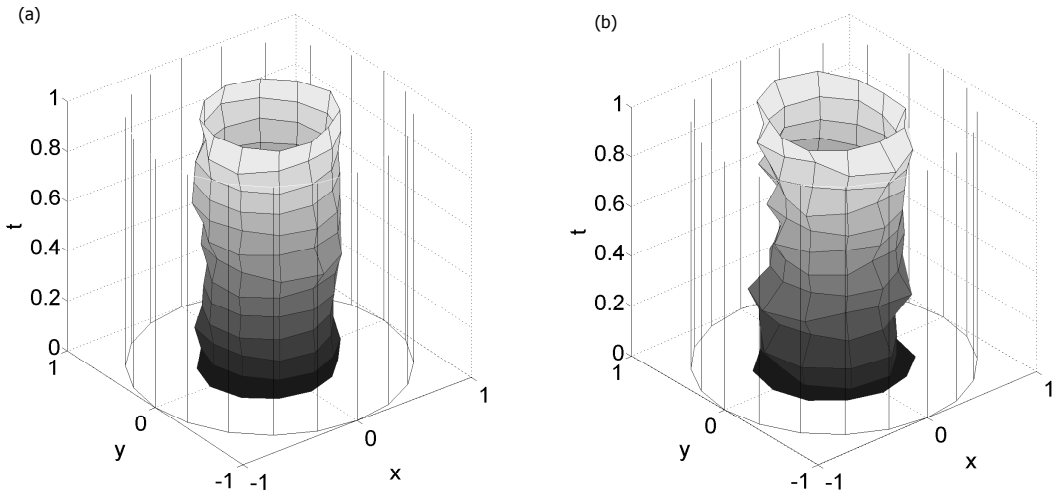

Figure 6.6: Final plot of the inclusion for Case 1 after the final 107 iterations. $M = N = 12$, $\tilde{K} = 23$, for (a) $p = 10\%$, and (b) $p = 25\%$ noise.

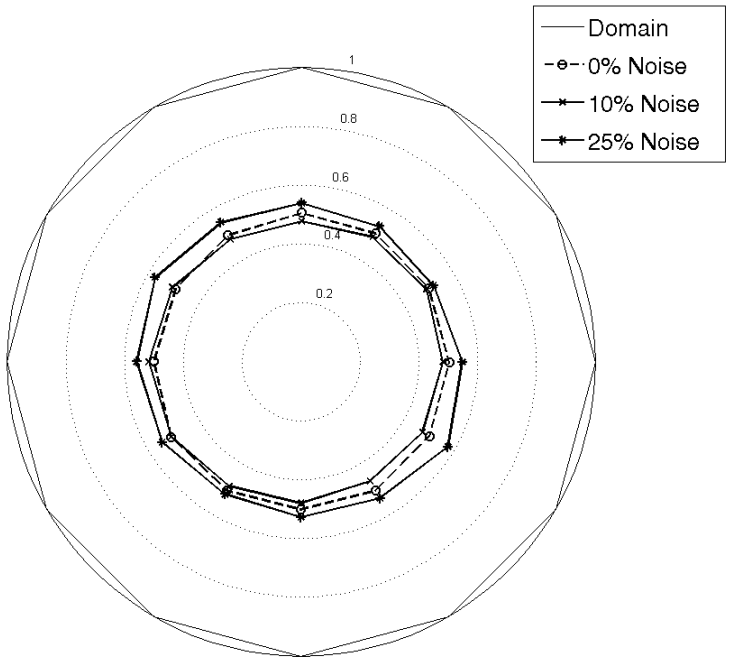

Figure 6.7: Reconstructed inclusion for Case 1 at $t = T = 1$, with $M = N = 12$, $\tilde{K} = 23$, for various levels of noise.

Noise (%)	Obj. Func.	RMS	Iterations
0	0.02151	0.00852	118
5	0.10689	0.02030	109
10	0.27019	0.03119	118
25	1.40198	0.06796	122

Table 6.2: Numerical results for the objective function in Case 1 (6.18), the RMS (6.31) and the number of iterations required for convergence, obtained with $M = N = 12$, $\tilde{K} = 23$ and various levels of noise.

within the domain $\Omega = B(\mathbf{0}, 1)$, is attempted to be located. This is a typical validation shape when considering geometric inverse problems. The initial and boundary conditions (6.2), (6.3) and (6.5) are given by,

$$\tilde{u}(\mathbf{x}, 0) = \tilde{u}_0(\mathbf{x}) = 0, \quad \mathbf{x} \in \overline{\Omega} \setminus \Gamma(0), \tag{6.33}$$

$$\tilde{u}(\mathbf{x}, t) = \tilde{f}(\mathbf{x}, t) = xt, \quad (\mathbf{x}, t) \in \partial\Omega \times [0, \tilde{T}], \tag{6.34}$$

$$\tilde{u}(\mathbf{x}, t) = \tilde{h}(\mathbf{x}, t) = 0, \quad (\mathbf{x}, t) \in \partial\Gamma(t) \times [0, \tilde{T}], \tag{6.35}$$

where $\mathbf{x} = (x, y)$.

In an initial study, it was assumed that the inclusion does not move in time, and that this is known *a priori*. Note that in the previous example the source and collocation points were placed in relation to the current location of the inclusion $\Gamma(t)$, namely the polar radius $r(\theta, t)$ was dependent on both space and time, however the inclusion is now fixed throughout time, and therefore the parametrisation of $\Gamma(t)$, as a stationary defect Γ, can be simplified. Due to this simplification, the locations of source and collocation points need to be modified, as described below.

Equation (6.12) can now be expressed as,

$$\mathbf{y}_{j+N}^{m} = \frac{1}{2}(r_j \cos(\theta_j), r_j \sin(\theta_j)), \quad j = \overline{1, N}, \quad m = \overline{1, 2M}, \tag{6.36}$$

where the radii $r(\theta_j) =: r_j \in (0, 1)$ constitute a radial parameterisation of the stationary

star-shaped domain Γ whose boundary at any time $t \in (-\tilde{T}, \tilde{T})$ is approximated by,

$$\partial\Gamma = \left\{ \left(r(\theta_j)\cos(\theta_j), r(\theta_j)\sin(\theta_j) \right) \mid j = \overline{1,N} \right\}. \tag{6.37}$$

By comparing this with equations (6.9) and (6.13), one can now observe that the radial parametrisation is no longer dependent on time, but only on its position in space. Modifications to the position of the inclusion dependent collocation points will now be stated.

Equations (6.15) and (6.16) now become

$$(\mathbf{x}_i^j, \tau_j) = (r_i\cos(\theta_i), r_i\sin(\theta_i), \tau_j), \quad i = \overline{1,N}, \quad j = \overline{0,M}, \tag{6.38}$$

$$\mathbf{x}_{i,j} = \left(\left(r_j + \frac{(1-r_j)i}{\tilde{K}} \right)\cos(\theta_j), \left(r_j + \frac{(1-r_j)i}{\tilde{K}} \right)\sin(\theta_j) \right), \quad i = \overline{1,(\tilde{K}-1)}, \quad j = \overline{1,N}, \tag{6.39}$$

The final problem entails to $4MN + N = N(4M+1)$ unknowns represented by the $4MN$ coefficients $\mathbf{c} = (c_j^m)_{j=\overline{1,2N}}^{m=\overline{1,2M}}$ in the MFS expression (6.7), and the N radii $\mathbf{r} = (r_j)_{j=\overline{1,N}}$.

6.4.2.1 Results: Direct Problem

Since for the irregular bean shape (6.32) an analytical solution for the direct problem (6.1), (6.33)-(6.35) is not available, the direct problem is solved numerically using the MFS and the resultant MFS constants, $\mathbf{c}$, are obtained. These are then used to calculate the heat fluxes, (6.4) on the fixed outer boundary, $\partial\Gamma$. These heat flux values input into the inverse problem, assuming $\partial\Gamma(t)$ is unknown. Figure 6.8 shows the heat flux values (6.4) at times $t \in \{\frac{1}{18}, 1\}$, obtained by solving the direct problem (6.1), (6.33)-(6.35), with various MFS parameter sizes $M = N \in \{30, 45, 60\}$ and the regularisation parameter $\lambda = 10^{-7}$. It can be deduced from Figure 6.8 that the numerical solutions did not change significantly when the MFS parameter sizes were in excess of $M = N = 60$.

Next, the heat flux values (6.4) at times $t \in \{\frac{1}{18}, 1\}$, obtained by solving the forward problem with the MFS parameter size $M = N = 60$ are plotted in Figure 6.9, for various regularisation parameters. The fluxes are output at 18 points across the boundary $\partial\Omega$ which was used as input data for the inverse problem of Case 2 (for $M = 18, N = 18$).

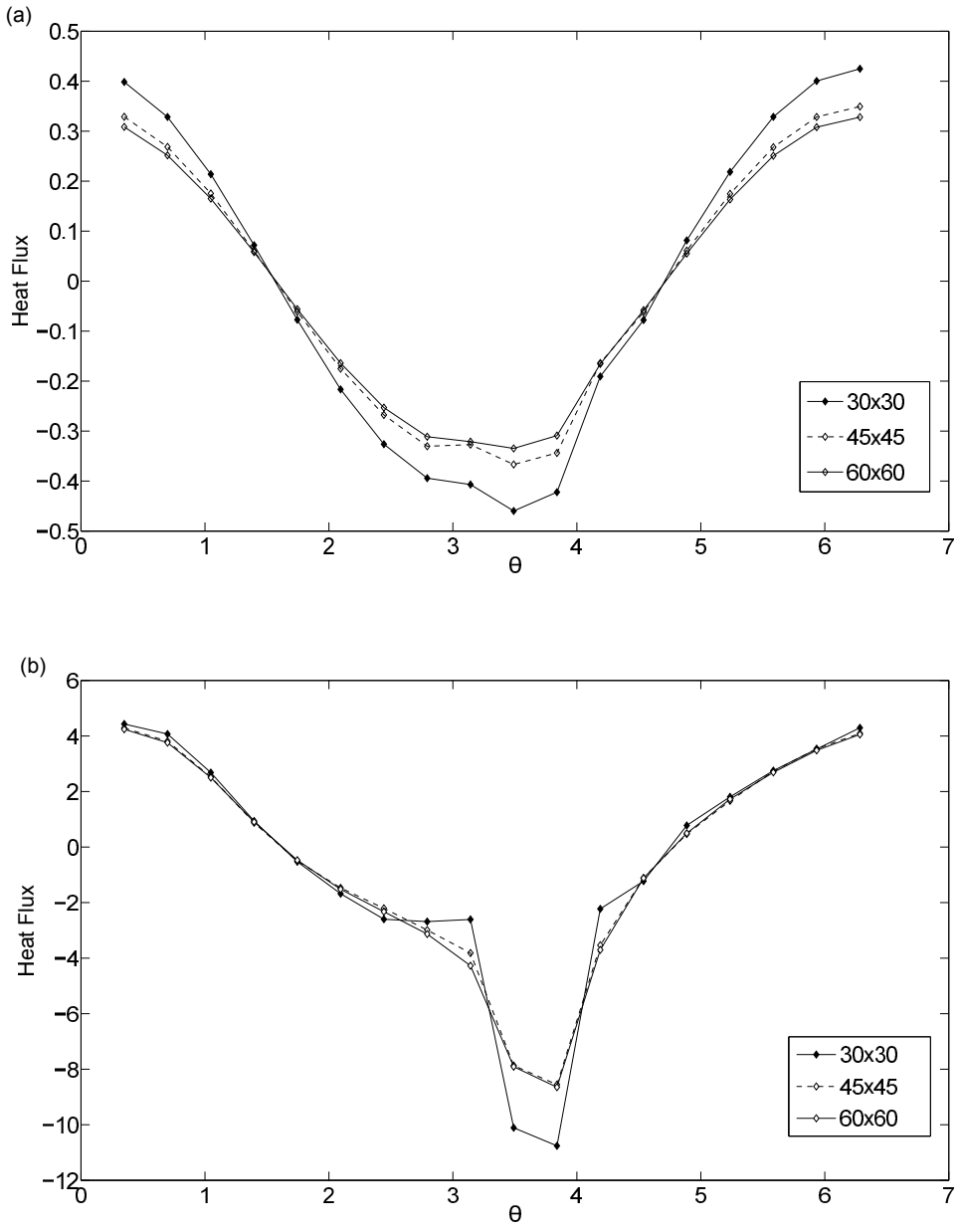

Figure 6.8: The heat flux values (6.4) across $\partial\Omega$ at times (a) $t = \frac{1}{18}$, and (b) $t = 1$, for various MFS parameters sizes.

This way, the inverse problem will be run with the MFS parameter size $M = N = 18$. This also avoids committing an inverse crime as the direct and inverse solvers have different MFS parameter sizes.

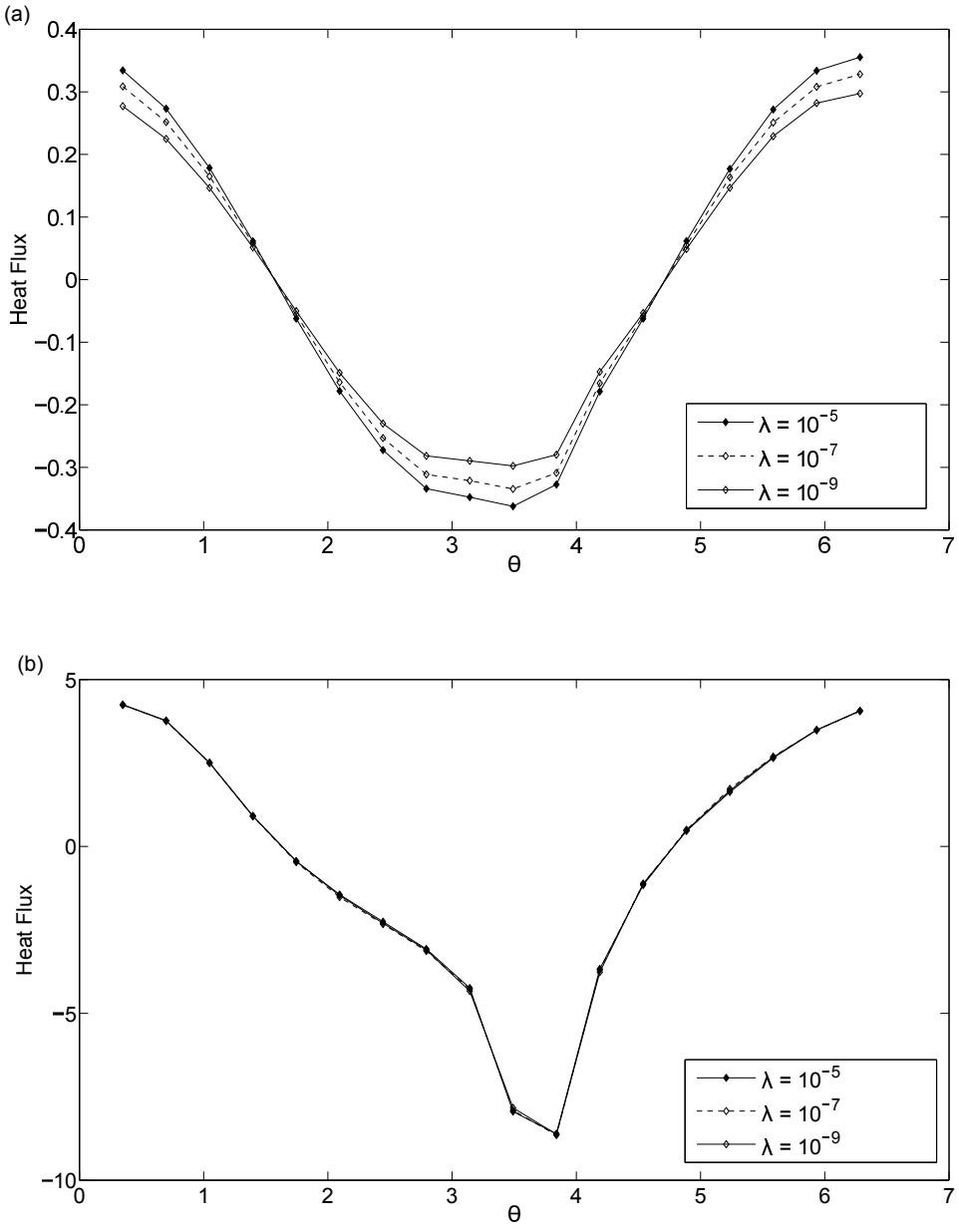

Figure 6.9: The flux values (6.4) across $\partial\Omega$ at times (a) $t = \frac{1}{18}$, and (b) $t = 1$, for various regularisation parameters, in Case 2.

When selecting a suitable regularisation parameter in equation (6.25) for solving the forward problem, a compromise value is taken, which should be large enough to remove the effects of ill-conditioning of the MFS system of equations, and small enough to have minimal effect on the accuracy of the solution. From Figure 6.9(a), when $\lambda = 10^{-9}$ the

ill-conditioning of the system is still visible, however the solution appears to to be stable for $\lambda = 10^{-7}$. As such this value shall be used when solving the forward problem for the MFS parameter size $M = N = 60$.

6.4.2.2 Results: Inverse Problem

Analysis of the results for Case 2 follow a similar format to that of Example 1. Results for both the objective function (6.18) and the RMS value,

$$\text{RMS} = \sqrt{\frac{\sum_{j=1}^{N} \left(r_j - r_j^*\right)^2}{N}}, \tag{6.40}$$

where

$$r_j^* = r^*(\theta_j) = \frac{0.55 + 0.4\cos(\theta_j) + 0.15\sin(2\theta_j)}{1 + 0.7\cos(\theta_j)}, \quad \theta_j = \frac{2\pi j}{N}, \quad j = \overline{1, N}. \tag{6.41}$$

for various parameter sizes $M = N$ are shown in Figure 6.10. From this figure it can be seen that as the MFS parameter size increases, the accuracy of the solution also increases. To evaluate the optimisation process, an 'inverse crime' was also committed (i.e. the heat flux data is generated using the same forward mesh size in the inverse problem). From these results it can be observed that the error is very small in relation to the other parameter sizes, hence providing further confirmation that the solver is functioning correctly.

Unlike the majority of previous works where the MFS is used to solve steady state inverse problems, the time-dependent case produces a much larger system of unknowns and as such, the objective function is more costly to evaluate. Consequently, parameter sizes typically have to be smaller than those used in aforementioned works otherwise, the computational time required to solve becomes infeasibly large. A parameter size of $M = 26$, $N = 16$ has been found to be the largest parameter size when drawing a compromise between accuracy and computational expense. A two-dimensional plot of the results obtained is displayed in Figure 6.11. As the solution remains stationary in time, it is unnecessary to provide a full space-time plot of the inclusion.

As one can observe from Figures 6.10(b) and 6.11, as the parameter size increases, the

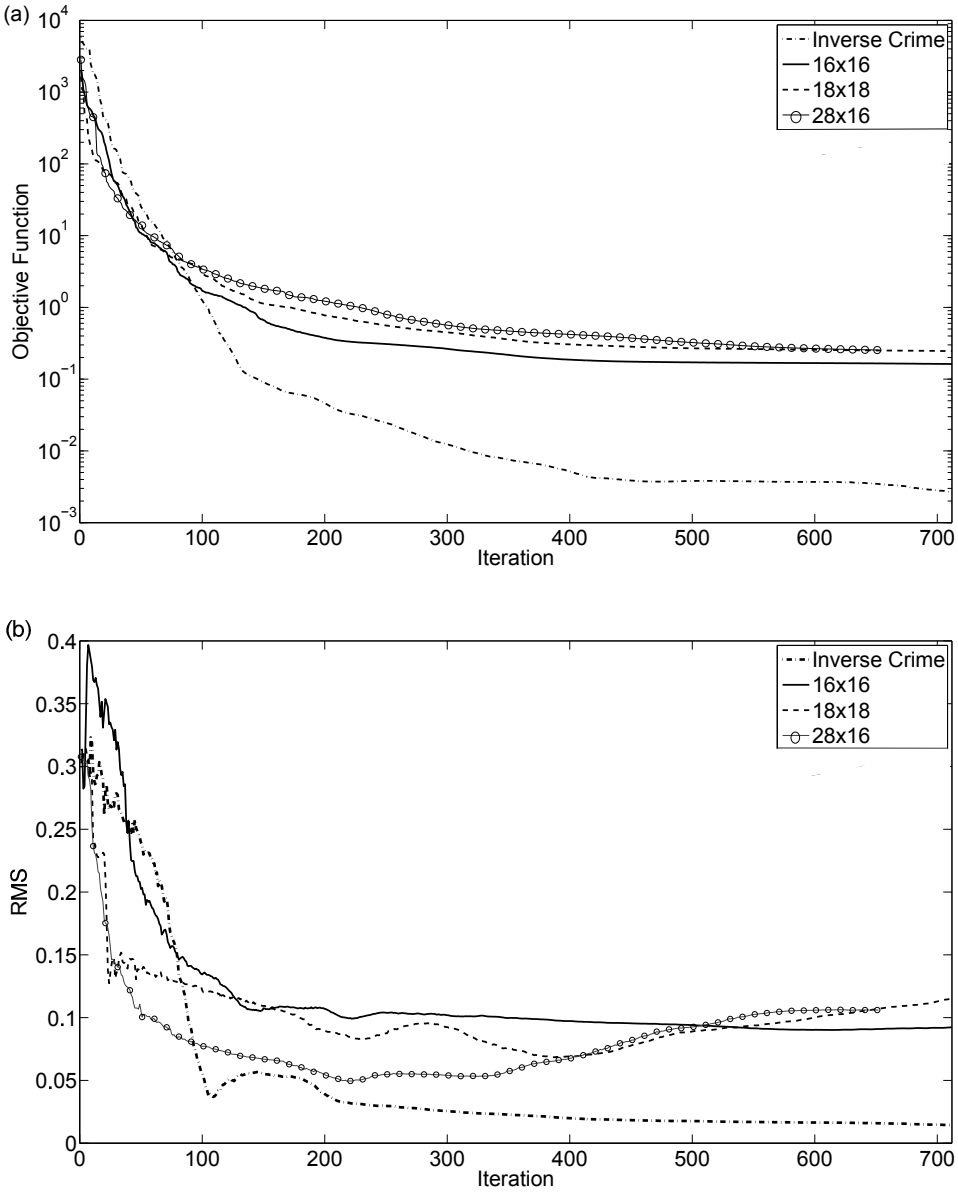

Figure 6.10: The objective function (6.18) and the RMS value (6.40) for various MFS parameters, in Case 2.

accuracy of the numerical solution also increases. In order to further highlight this, a plot of the absolute errors squared versus the polar angle θ, is given in Figure 6.11. From observing this figure it can be seen that as the mesh size increases the accuracy generally increases. One can also observe that the level of error from performing the inverse crime is very small, providing reassurance that the computational implementation

and methodology are correct.

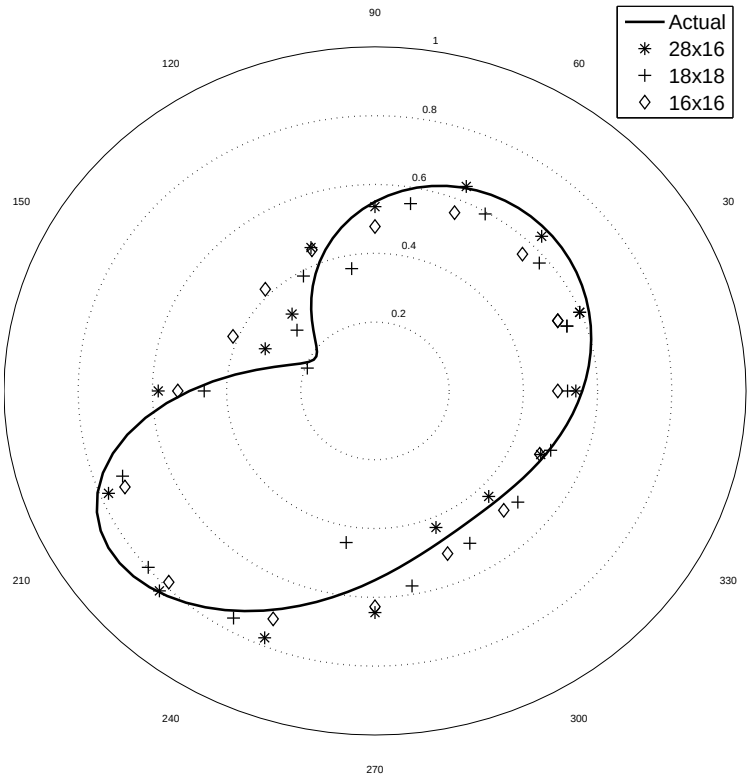

Figure 6.11: Plot of the inclusion in Case 2 for various MFS parameter sizes.

Following the successful implementation of the method when considering $p = 0$, trials were then carried out using noisy data for a variety of regularisation parameters λ. The residual (6.18) and RMS values (6.40) for these trials are presented in Figure 6.13. It should be noted that the residual in Figure 6.13 takes the form of (6.18), however (6.24) is the regularised objective function being minimised. The residual (6.18) was plotted in Figure 6.13(a), as this is necessary in order to use a discrepancy principle. As the solution is unknown *a prior* criteria must be set such that the regularisation parameter and stopping criteria can be determined. In addition to this, in physical applications where the input data is likely to be contaminated with noise, it is necessary to have a stopping criterion to prevent the solution becoming unstable.

For trials where no regularisation is imposed, i.e. the objective function (6.18) is min-

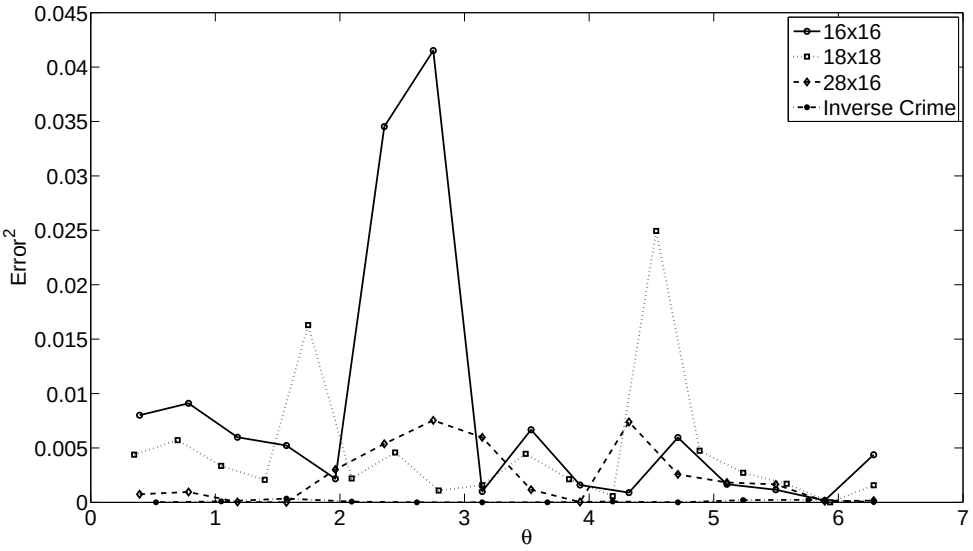

Figure 6.12: The absolute error squared versus θ for various MFS parameter sizes, in Case 2.

imised, the discrepancy principle can be used in order to select the stopping criteria. In this case the solver was stopped at the iteration number for which the residual (6.18) attains approximately the noise level,

$$\epsilon^2 = \sum_{i=1}^{N}\sum_{j=0}^{M}(\tilde{g}^{\eta}(\mathbf{x}_i^j, t_j) - \tilde{g}(\mathbf{x}_i^j, t_j))^2. \tag{6.42}$$

This is graphically illustrated in Figure 6.13(a) where the value of ϵ^2 is shown as the horizontal line.

In cases where regularisation is imposed, the discrepancy principle can also be used in order to select the regularisation parameter. In this case, various regularisation parameters were initially trialled such that the solution process is stopped after a fixed number of iterations (300 in Case 2), and the residuals after 300 iterations are presented in Figure 6.14. The choice of λ was then made based on which residual was closest to ϵ^2 ($= 3.9$ for 1% noise in Case 2), this technique is also termed as the discrepancy principle. Figure 6.14 shows that this value is between $\lambda = 10^{-3}$ and 10^{-2}.

RMS values for trials with 1% noise and Tikhonov regularisation in conjunction with the

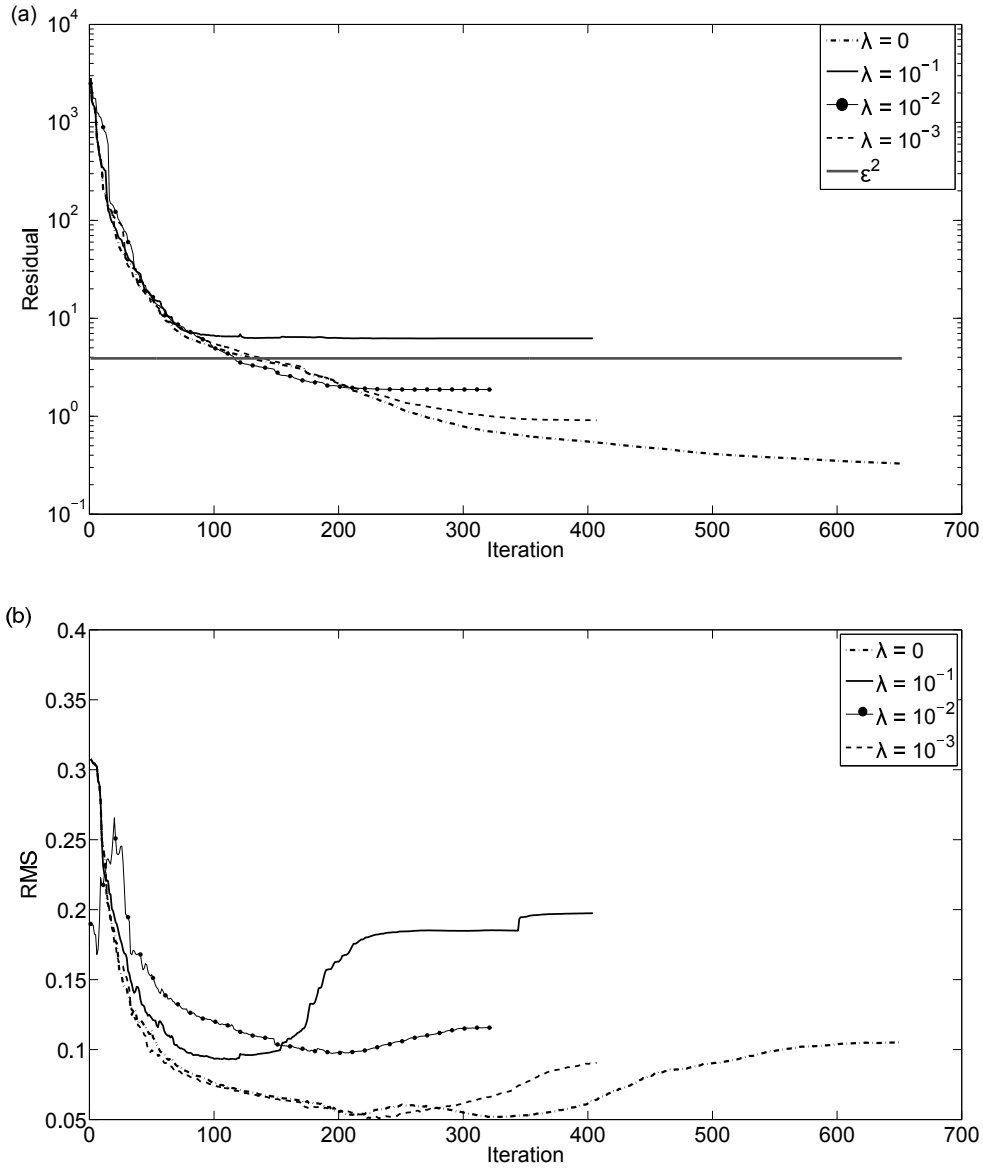

Figure 6.13: (a) The residual (6.18), and (b) the RMS values (6.40) in Case 2 for various regularisation parameters when the heat flux data (6.4) is contaminated with 1% noise.

two discrepancy principles described above are shown in Table 6.3. The corresponding numerical reconstructions of the inclusion are shown in Figure 6.15. It can be seen in Figure 6.15(a) that the method proposed is stable when small amounts of noise are included in the input data. Results presented in this figure show that when exact data is considered, the optimal solution (assuming *a prior* knowledge of the boundary as a stopping criteria) obtainable by the method is close to the prescribed boundary. By

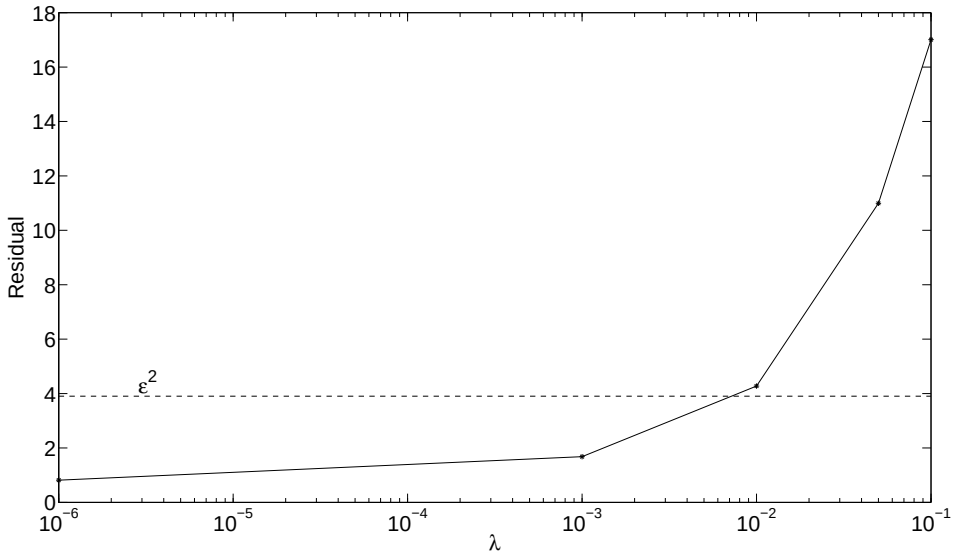

Figure 6.14: Residuals (6.18) after 300 iterations for various values of λ. For Case 2.

Noise (%)	RMS	Regularisation (λ)	Iteration (Final Result)
0	0.043	0	220
1	0.069	0	131
1	0.0616	0.001	300
1	0.1151	0.01	300

Table 6.3: Numerical results in Case 2 for the RMS (6.40) obtained with $M = 28$, $N = 16$ and $\tilde{K} = 55$.

employing the first discrepancy principle, such that the optimal solution would not be known (as in a real life case), with no regularisation, the formation shape was also shown to predict the prescribed boundary. Both when using the $p = 0$ and $p = 0.1$ input data generated a good likeness to the target solution, with the largest error occurring near the cusp region. The numerical results presented in Figure 6.15(b), obtained using the regularisation parameter λ chosen according to the second discrepancy principle (based on Figure 6.14), do not show much improvement over the results presented in Figure 6.15(a).

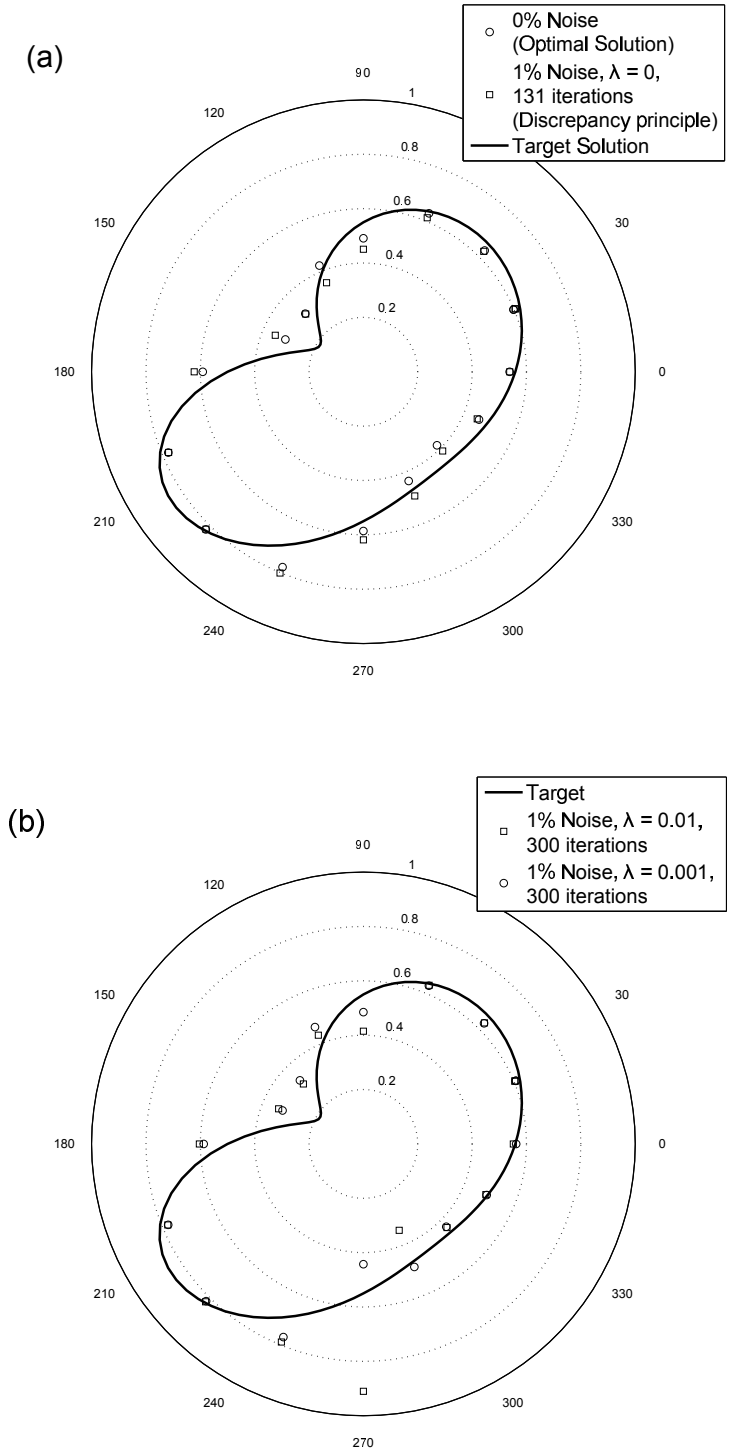

Figure 6.15: (a) Plot of the inclusion for 0 and 1% noise in Case 2. The iteration process is stopped according to the first discrepancy principle. (b) Plot of the inclusion for 1% noise in Case 2. The regularisation parameter is chosen according to the second discrepancy principle.

6.4.3 Case 3: Bean Shaped Rigid Inclusion

Similarly to Case 2, a stationary star-shaped inclusion is parametrised by (6.32) is attempted to be located. However, this time there is no assumption that the boundary $\partial\Gamma(t)$ is stationary throughout time $t \in (0, \tilde{T} = 1)$. The initial and boundary conditions are given by equations (6.33)-(6.35). In order to ensure a unique solution it is imposed that $\Gamma(0)$ is known, see [107], and therefore a non-linear system of $5MN$ unknowns is solved.

6.4.3.1 Results: Inverse Problem

Analysis of the results for Case 3 follow a similar format to that of the previous examples. The RMS now takes the form,

$$\text{RMS} = \sqrt{\frac{\sum_{j=1}^{N}\sum_{m=0}^{M}\left(r_j^m - r_j^*\right)^2}{N(M+1)}}, \tag{6.43}$$

where r_j^* are given by equation (6.32). Initial results presented correspond to MFS parameters of varying sizes. The minimisation of the objective function can be observed in Figure 6.16(a). From this figure it can be seen that there only appears to be a small correlation between increasing the MFS parameters size and RMS values. It was shown that minimum achievable RMS value, appears to be approximately 0.1, as presented in Figure 6.16(b). In order to further understand the reasoning for these relatively low accuracies, Figure 6.17 plots the errors in both time and space. From Figure 6.17 it can be observed that the errors were large close to the initial time ($t = 0$) and also close to the concave region of the cusp. Accuracy in other regions was found to be of a good standard. In order to evaluate whether this behaviour is apparent for other MFS parameter sizes, Figure 6.18 shows the absolute errors, averaged over θ, as a function of time. From this figure it can be seen that for all MFS parameters attempted in Case 3, the error was largest at times close to $t = 0$, and slowly decreased through time.

Finally a full plot of the inclusion, as a function of $\mathbf{x}$ and t can be found in Figure 6.19. From this figure it can be seen that the accuracy of the solution increases away from the initial time $t = 0$.

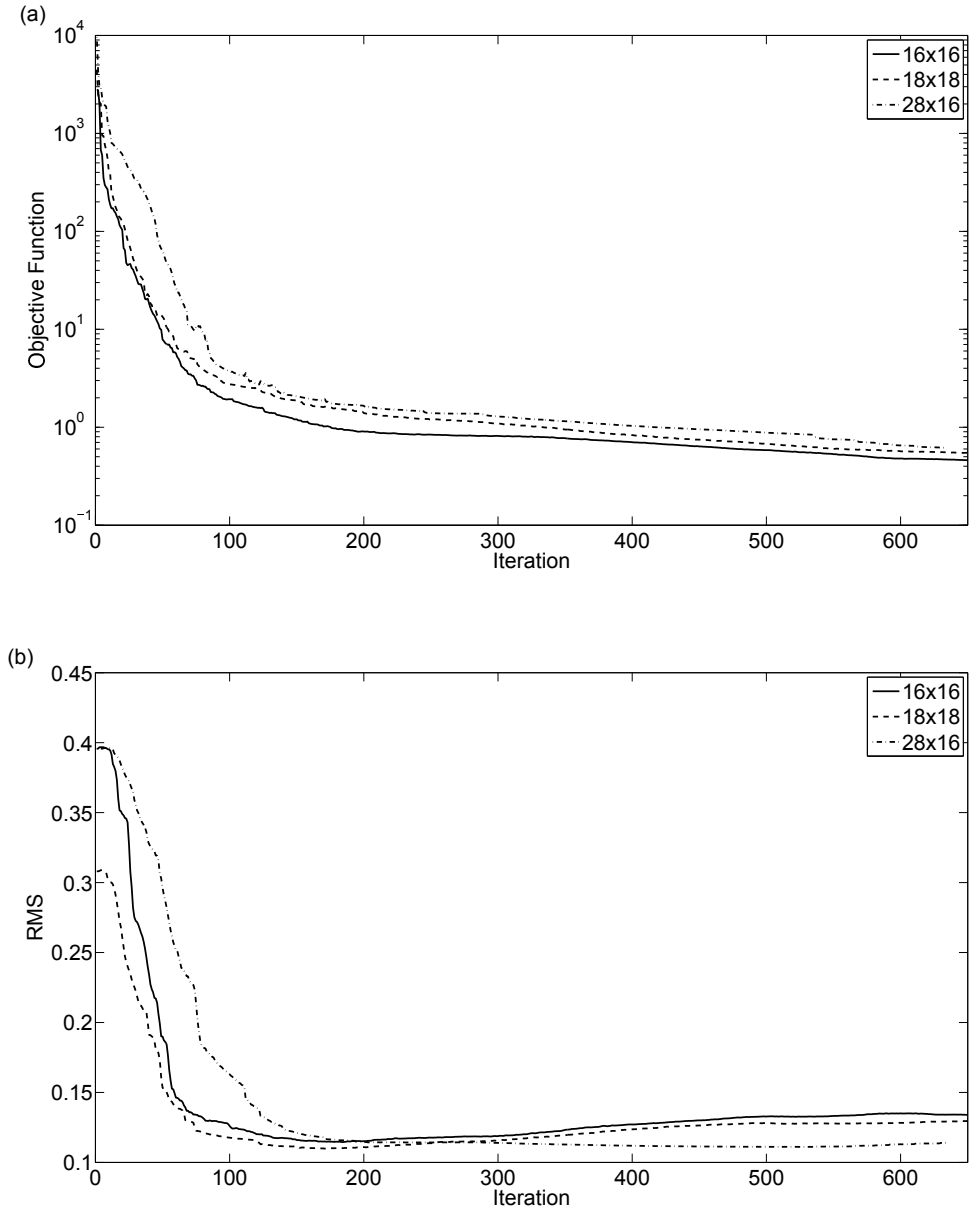

Figure 6.16: (a) The objective function (6.18), and (b) the RMS values (6.43) for various MFS parameter sizes.

Summarising, when applying the method for Case 3, there were noticeable errors observed close to the initial solution time. However, when considering the solution away from the initial time, the solver's ability to reconstruct the internal structure appeared to function well. An example the solution at the final time $t = T = 1$ is shown in Figure 6.20.

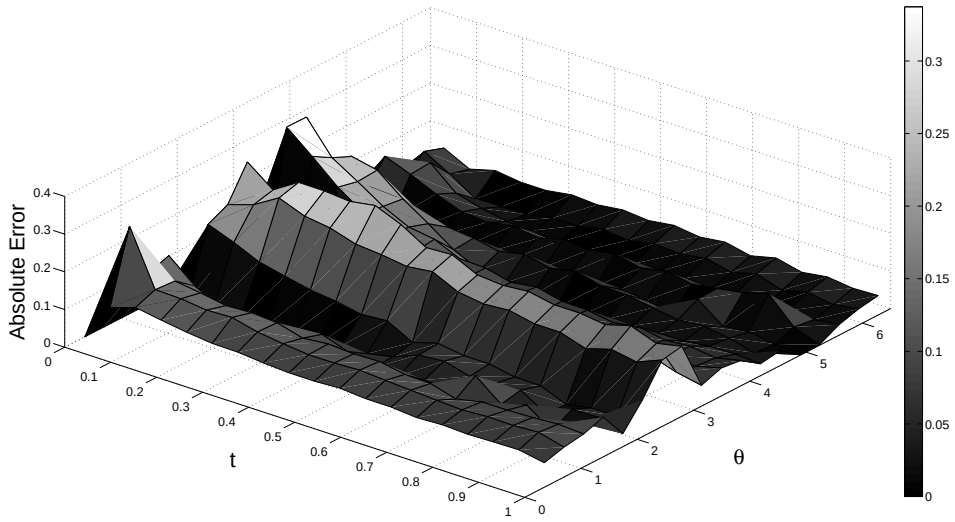

Figure 6.17: The absolute error between the target and obtained solution for $M = N = 18$ at iteration 171.

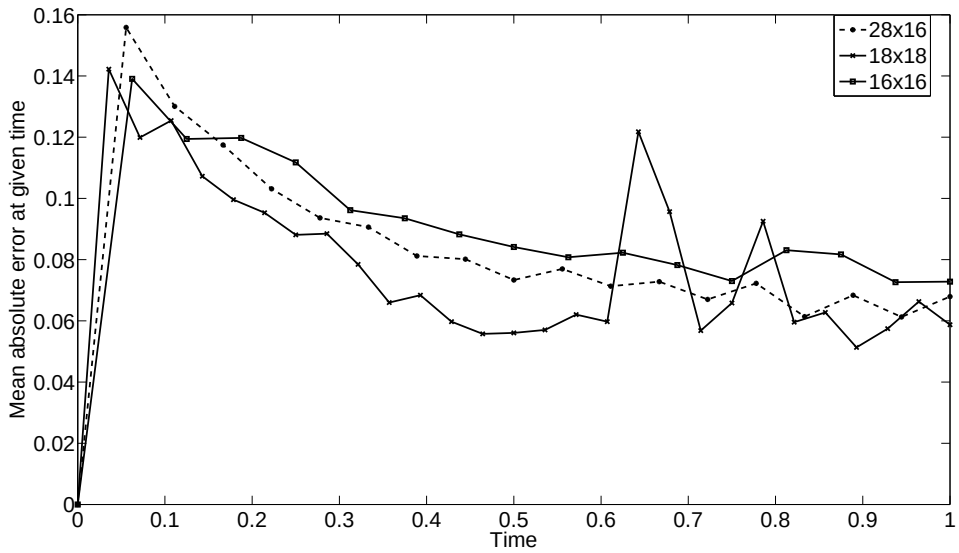

Figure 6.18: The mean absolute error between the target and obtained solution over time for a variety of MFS parameters at optimal stopping iterations.

6.4.4 Case 4: Transient Rigid Inclusion

In this example, an internal moving boundary star-shaped rigid inclusion $\Gamma(t)$ parametrised by

$$r(t) = 0.9 - \frac{t}{2}, \quad t \in [0, \tilde{T}], \tag{6.44}$$

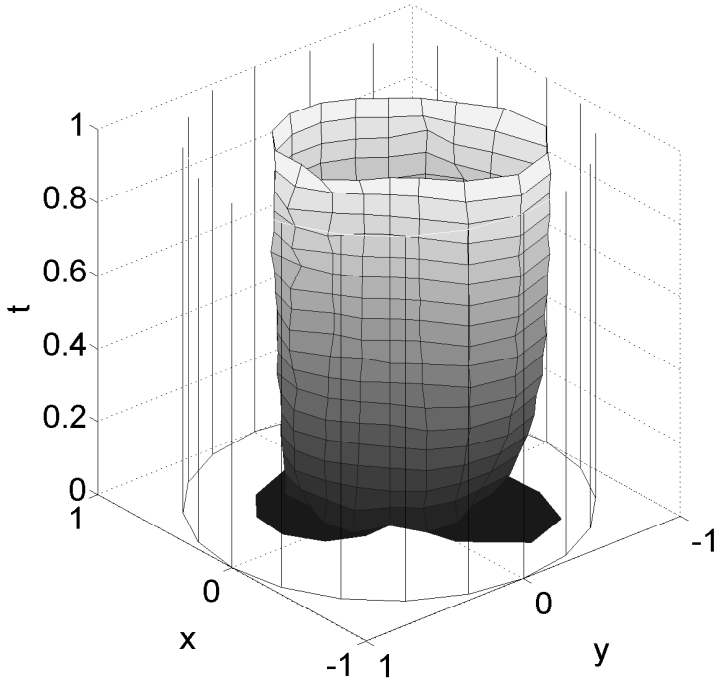

Figure 6.19: Plot of the inclusion in Case 3 for $M = N = 18$ after 171 iterations.

within the domain $\Omega = B(\mathbf{0}, 1)$, is attempted to be reconstructed. The initial and boundary conditions (6.2) and (6.5) are given by (6.33) and (6.35), and the Dirichlet boundary condition (6.3) is taken as,

$$\tilde{u}(\mathbf{x}, t) = \tilde{f}(\mathbf{x}, t) = t, \quad (\mathbf{x}, t) \in \partial\Omega \times [0, \tilde{T}]. \tag{6.45}$$

In order to ensure a unique solution to the inverse problem, it is assumed the circular shape $r(0) = 0.9$ of the inclusion $\Gamma(0)$ at the initial time $t = 0$ is known.

In this example the added complexity of the bean shaped formation was removed to see if the method has the ability to reconstruct a simple moving circular formation, as parametrised by equation (6.44). Due to the simplicity of the shape, MFS parameter sizes similar to those in Case 1 were used. Input flux data was obtained by solving the forward problem, as described in Case 2.

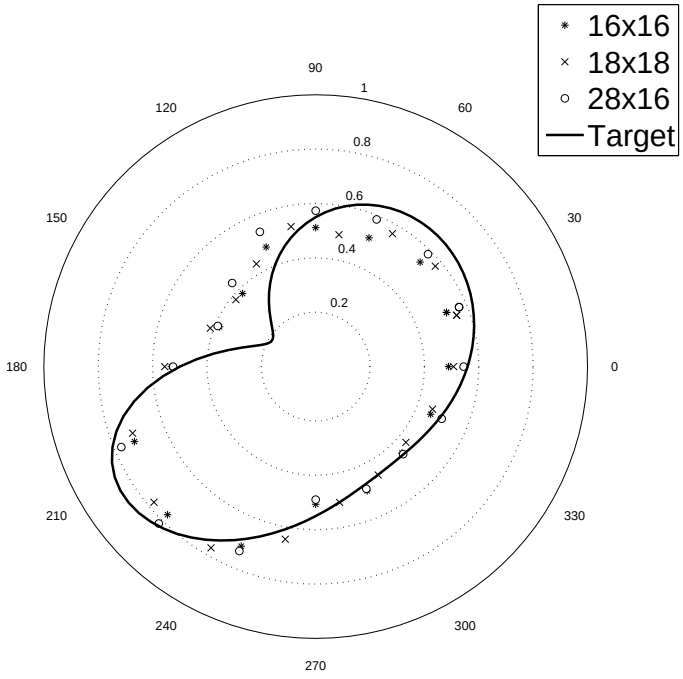

Figure 6.20: Plot of the inclusion for Case 3, at the final time $t = T = 1$, for various MFS parameter sizes.

6.4.4.1 Inverse Problem: Results

The minimisation of the objective function (6.18) is presented in Figure 6.21. Furthermore, the RMS values are presented and take given by equation (6.43). From Figure 6.21, it can be shown that the numerical results with lower MFS parameter sizes appear to obtain the most accurate, stable solutions. This behaviour is contradictory to of that observed in the previous cases. In order to further evaluate the source of the inaccuracies Figure 6.22 presents the absolute error across the interior reconstruction for the MFS parameter sizes $M = N = 8$ and 12. From this figure it can be seen that as the MFS parameter size increases, the effects of the ill-conditioning start to become apparent. These effects appear to be dominant close to $t = 0$, similarly to results in Case 3. The small MFS parameter sizes appear to reduce this error, however the errors remain large at times away from $t = 0$. In order to illustrate more clearly this point, Figure 6.23 shows the mean absolute errors, between the target and obtained solution at the various times. From this figure it can be observed that for low MFS parameter sizes the solution is more

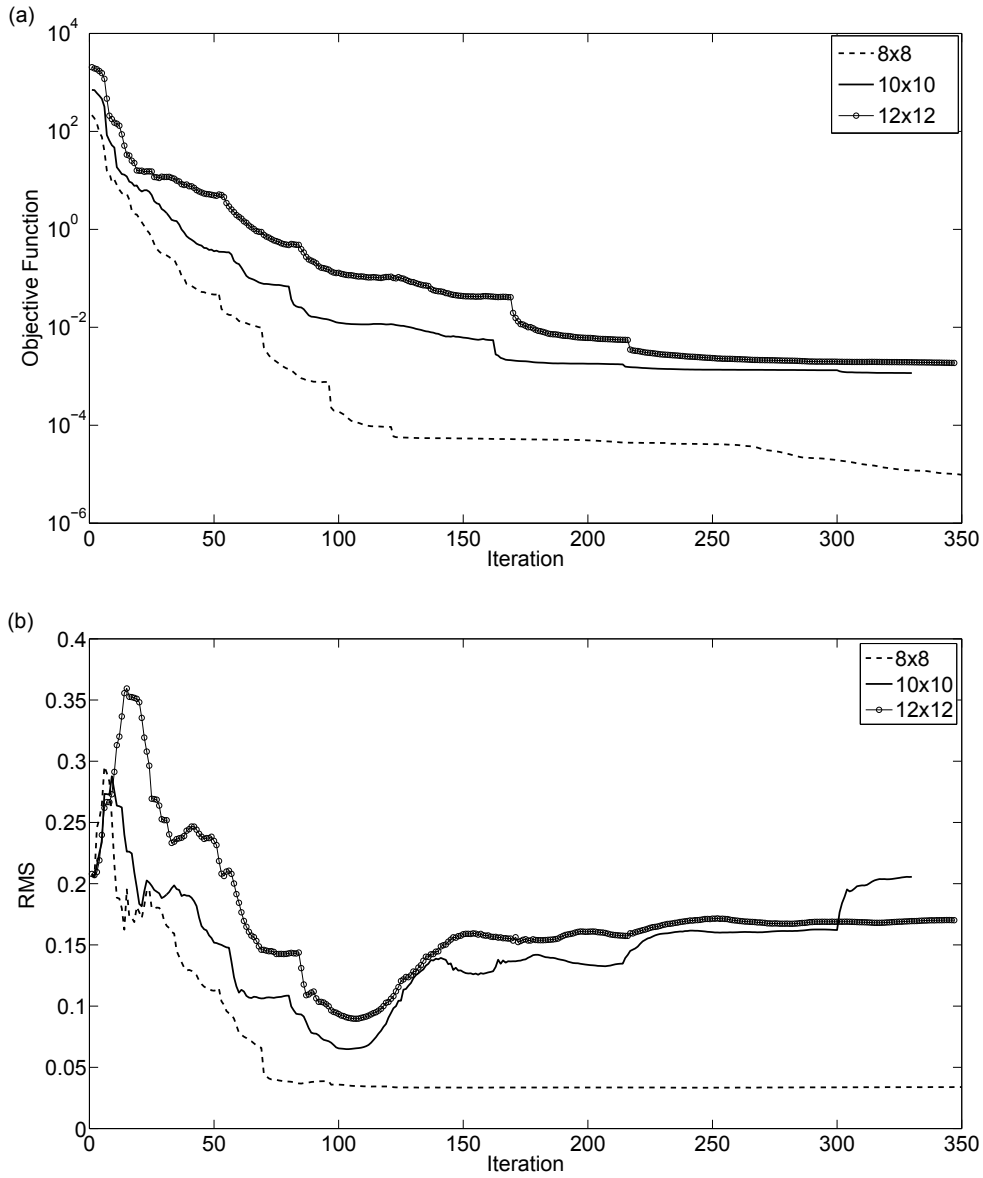

Figure 6.21: (a) The objective function (6.17), and (b) the RMS values (6.31) for various MFS parameters. For Case 4

accurate close to $t = 0$, however at later times the larger MFS parameters are closer to the target solution.

Finally, Figure 6.24 shows the full space-time solution for parameters $M = N = 8$ and 12. From this figure, the previously determined behaviour is clearly visible.

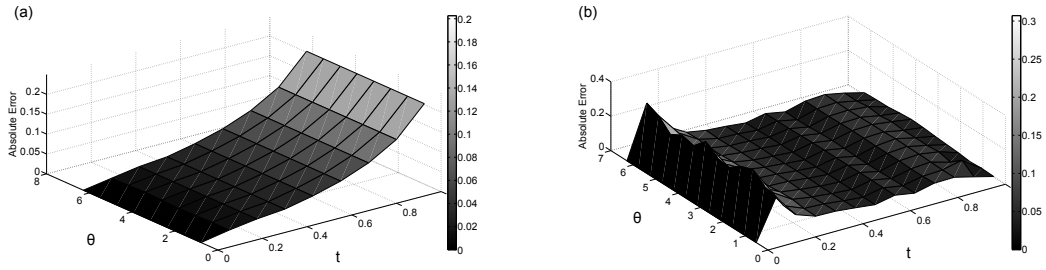

Figure 6.22: The absolute error between the target and obtained solution in Case 4 for (a) $M = N = 8$, and (b) $M = N = 12$ at optimal stopping iterations.

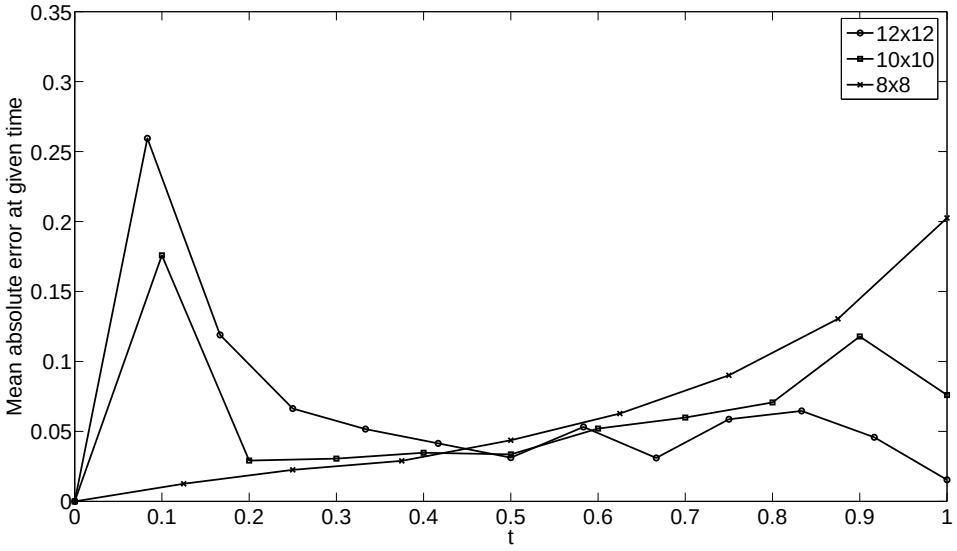

Figure 6.23: The mean absolute error between the target and obtained solutions in Case 4, over time for a variety of MFS parameters at optimal stopping iterations.

6.4.5 Case 5: Circular Cavity

Here a stationary star-shaped cavity given by the circle, $B(\mathbf{0}, 0.4)$ centred at the origin with radius 0.4 within the unit circle domain $\Omega = B(\mathbf{0}, 1)$ is attempted to be located. This case now considers the problem of finding an internal cavity, such that a zero flux Neumann condition is imposed on $\partial\Gamma$. The initial and boundary conditions (6.2), (6.3)

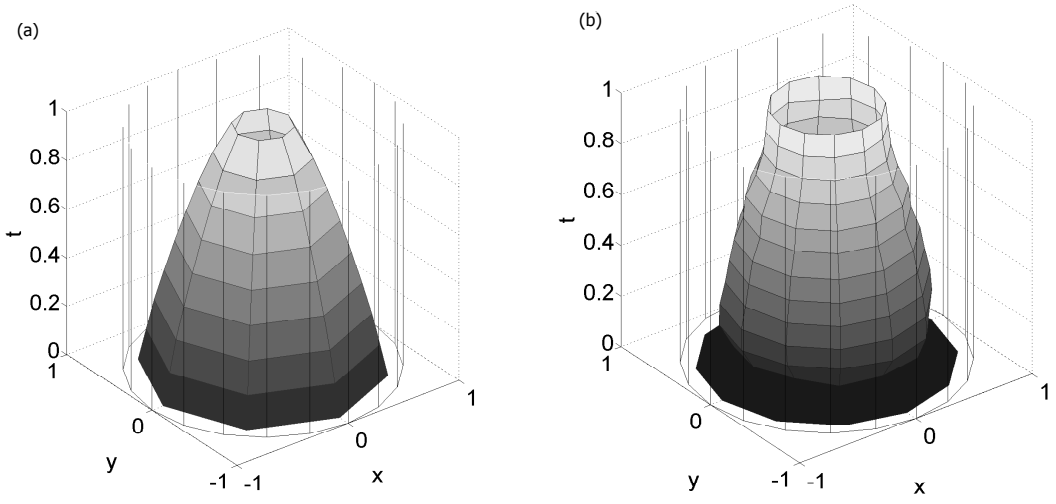

Figure 6.24: The moving inclusion for: (a) $M = N = 8$, and (b) $M = N = 12$ at the optimal stopping iterations.

and (6.6) are given by ,

$$\tilde{u}(\mathbf{x}, 0) = \tilde{u}_0(\mathbf{x}) = 0, \quad \mathbf{x} \in \overline{\Omega} \setminus \Gamma(0), \tag{6.46}$$

$$\tilde{u}(\mathbf{x}, t) = \tilde{f}(\mathbf{x}, t) = 4t, \quad (\mathbf{x}, t) \in \partial\Gamma \times [0, \tilde{T}], \tag{6.47}$$

$$\frac{\partial \tilde{u}}{\partial n} = \tilde{h}(\mathbf{x}, t) = 0, \quad (\mathbf{x}, t) \in \partial\Gamma(t) \times [0, \tilde{T}]. \tag{6.48}$$

As no analytic solutions are available, the direct problem was solved in order to generate input data (6.4) on $\partial\Omega$.

6.4.5.1 Results: Direct Problem

The direct problem given by (6.1), (6.46)-(6.48) was solved in order to generate input data for the heat flux on $\partial\Omega$. Figure 6.25 shows the relative heat flux on $\partial\Omega$ for 18 uniform points for various MFS parameters, M and N at $t = \frac{13}{18}$.

From solving the direct problem, it was determined that increasing the spatial MFS parameter, N, had little effect on the solution if $N \geq 20$. The resultant system of equations, of size $4MN \times 4MN$, could solved within reasonable computational time for $MN \leq 4900$,

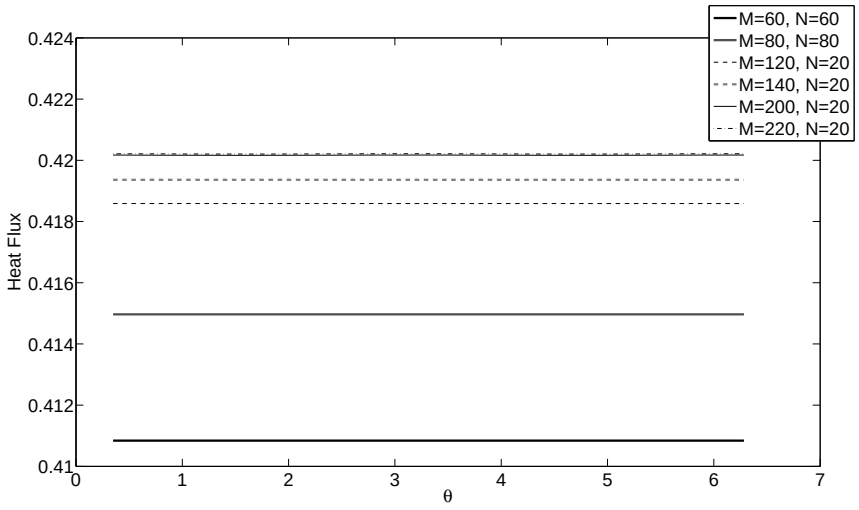

Figure 6.25: The heat fluxes at 18 uniform points across $\partial\Omega$ for various MFS parameters, M and N, at time $t = \frac{13}{18}$, for Case 5.

once this value was exceeded, solution times increased rapidly. Due to this, the spatial resolution was fixed to $N = 20$, this allowed for increased temporal resolution, without excessive computational expense. Figure 6.25 shows a constant increase in magnitude for the heat fluxes, with increasing parameter M, until a temporal parameter of $M = 200$ is given. Increasing the parameter further has little effect on the solution, therefore, when obtaining heat flux data for the inverse problem in Case 5, MFS parameters of $M = 200$, $N = 20$ were used.

Once a suitable MFS parameter size was selected. An appropriate regularisation parameter was chosen. Figure 6.26 shows the heat fluxes across the outer boundary, at time $\frac{8}{18}$. It should be noted that a different time was used here from that in Figure 6.25, as it was found that the effects of changing the regularisation parameter were more promienent here than when $t = \frac{13}{18}$. From this figure it can be seen for values of $\lambda = 10^{-5}, 10^{-7}, 10^{-9}$ there was very little variation in the solution. However, it can be observed that for small values of λ the solution starts to becoming unstable, and oscillate. Hence for the remainder of Case 5, $\lambda = 10^{-7}$ was used when solving the forward problem.

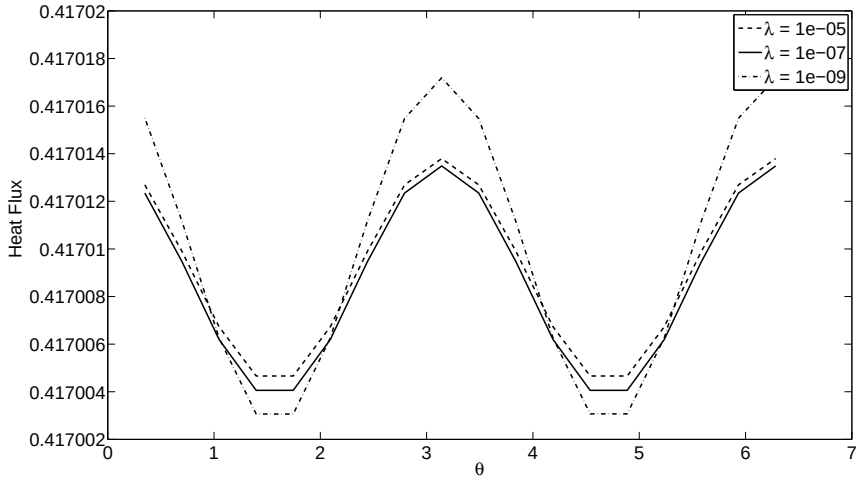

Figure 6.26: The heat fluxes at 18 uniform points across $\partial\Omega$ for various regularisation parameters, λ, at time $t = \frac{8}{18}$, for Case 5.

6.4.5.2 Results: Inverse Problem

The initial guess for the cavity was the circle $B(\mathbf{0}, 0.8)$ with MFS coefficients $\mathbf{c} = (c_j^m)_{j=\overline{1,2N}}^{m=\overline{1,2M}} = 0.1$.

The accuracy of the solution was analysed using the RMS value of the error between the analytical and estimated internal boundary defined as,

$$\text{RMS} = \sqrt{\frac{\sum_{j=1}^{N}\sum_{m=0}^{M}\left(r_j^m - 0.5\right)^2}{N(M+1)}}. \tag{6.49}$$

Figures 6.27 and 6.28 show the objective function and corresponding RMS value during the minimisation process for various regularisation parameters, λ. From these figures it can be seen that as the objective function decreases, so does the RMS value, suggesting that the solution steadily moves towards the target solution , $B(\mathbf{0}, 0.4)$. Figure 6.29 shows the resultant cavity for $\lambda = 1 \times 10^{-8}$ at various times. The solution was taken at the final iteration, 953. From observing this figure it can be seen that whilst the overall accuracy of the solution does vary at different times, the resultant solution gives a good approximation to the target cavity.

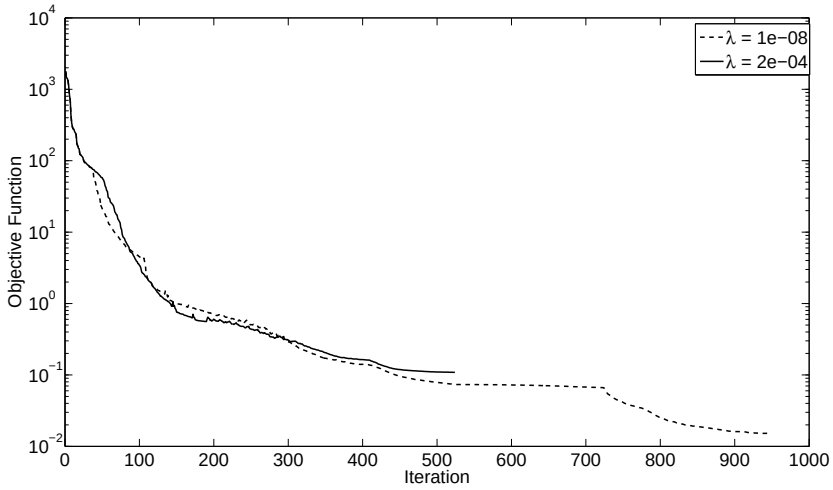

Figure 6.27: The objective function (6.20) for different regularisation parameters, λ. MFS parameters $M = N = 18$, $\tilde{K} = 35$.

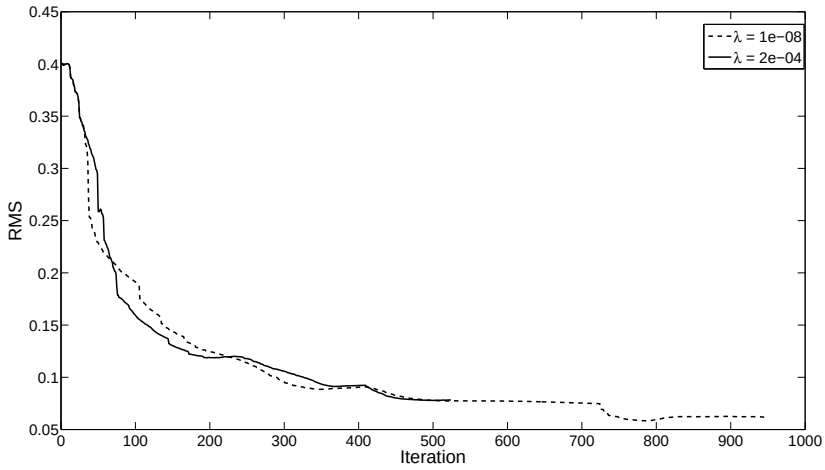

Figure 6.28: The RMS (6.49) for different regularisation parameters λ. MFS parameters $M = N = 18$, $\tilde{K} = 35$.

In order to investigate the effects of contaminating the input heat flux, 5% noise was added to the outer boundary flux.

Figures 6.30 and 6.31 show the minimisation of the objective function and corresponding RMS values for 5% noisy data. From this figure it can be observed that the RMS decreases

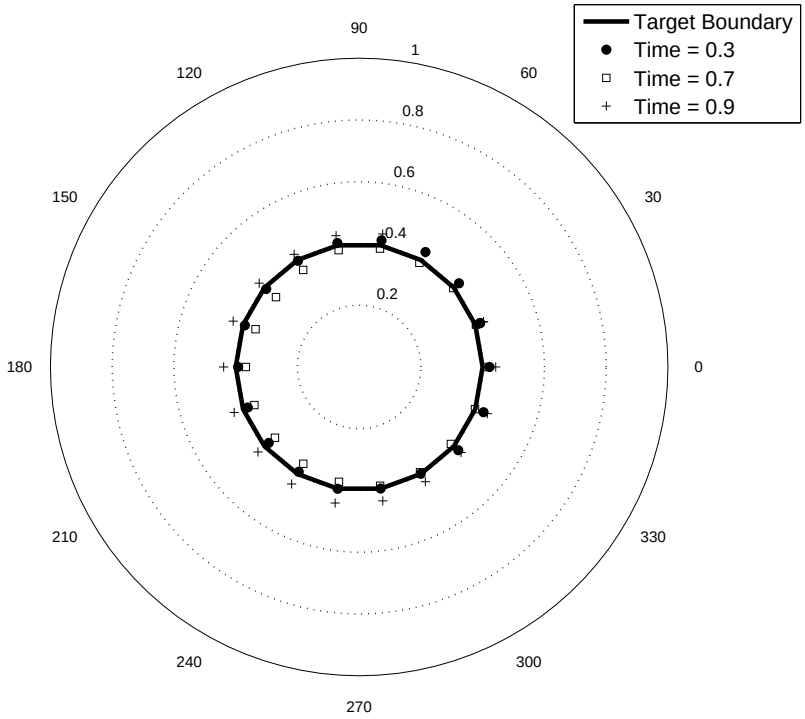

Figure 6.29: Plot of the resultant cavity at various time for MFS parameters, $M = N = 18$, $\tilde{K} = 35$.

much slower than that of the noiseless case. The final RMS value is also much higher than the noiseless case, suggesting that the noise has impacted on the solution accuracy. In order to visualise this, Figure 6.32 shows the resultant cavity at various times when using 5% noise. It can be seen from this figure that the solution accuracy has deteriorated when compared to the noiseless case, but the retrieval remains stable.

6.5 Conclusions

The work in this chapter has used a variety of examples to test both the accuracy and stability of the MFS for solving a geometric inverse problem, governed by the two-dimensional time-dependent heat equation in order to locate an unknown internal boundary. The initial work focused on locating an internal rigid inclusion, such that the boundary condition

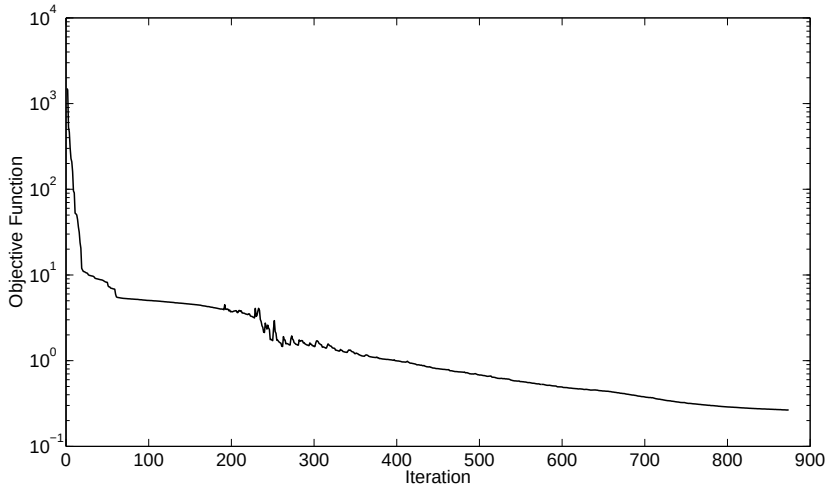

Figure 6.30: The objective function (6.20) in Case 5 at various time for MFS parameters, $M = N = 18$, $\tilde{K} = 35$, $p = 5\%$ noise

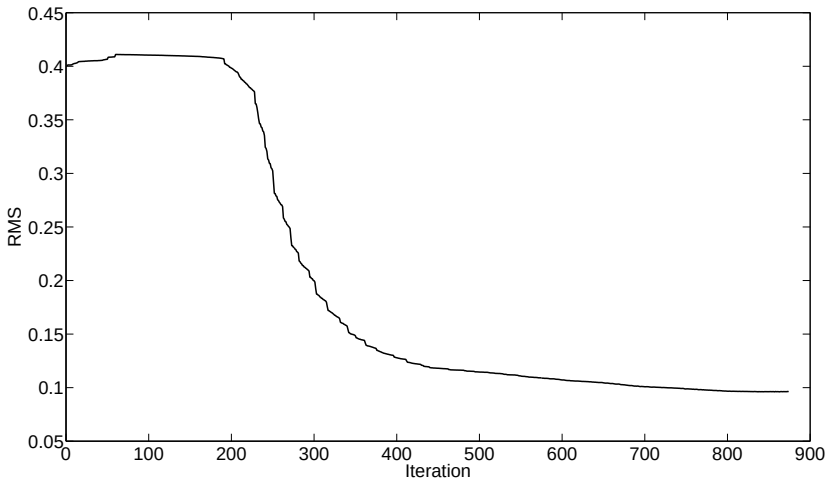

Figure 6.31: The RMS (6.49) in Case 5 at various time for MFS parameters, $M = N = 18$, $\tilde{K} = 35$, $p = 5\%$ noise

on this could be described by a constant or zero temperature (Dirichlet problem). It was demonstrated that the method can reconstruct simple circular boundaries to a high degree of accuracy. The solution remained stable, even when considering large amounts of noise. Additionally, for more complex stationary geometries such as the considered bean-shape, the model also obtains stable solutions to a high level of accuracy. For complex shapes

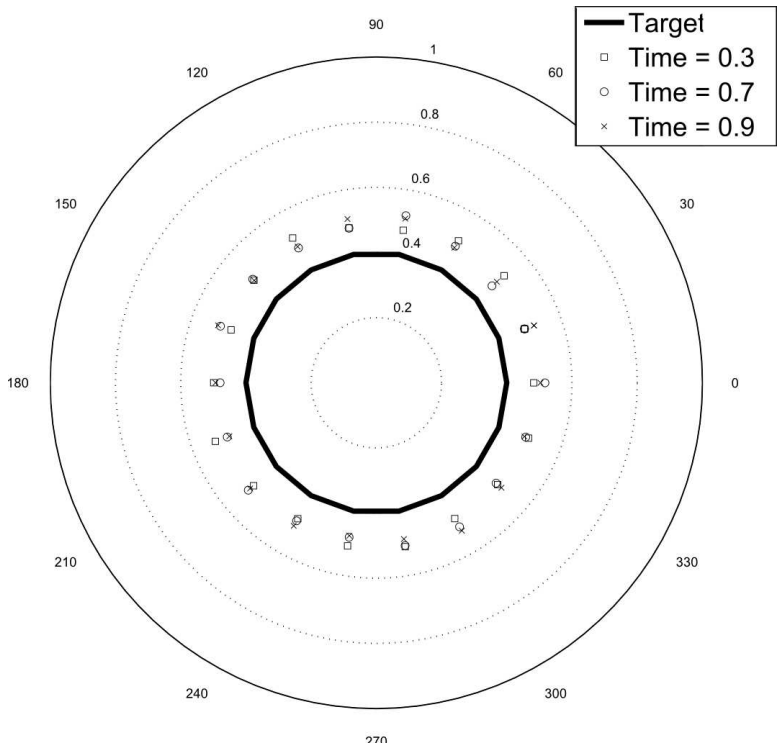

Figure 6.32: The resultant cavity in Case 5 at various time for MFS parameters, $M = N = 18$, $\tilde{K} = 35$, $p = 5\%$ noise

which were not fixed in time, it was shown that the difficulties in obtaining an accurate solution at early times. However, results further in time were of a reasonable accuracy. Finally, when considering the Dirichlet problem, the work has shown that the method presented here can successfully locate simple moving boundaries.

Later work in this chapter focused on the location of an internal cavity, such that a zero flux condition was placed on its boundary. A simple circular case was tested. The results showed that the solution was both accurate and stable when the input data is noise free. In cases where 5% noise was applied to the measured boundary flux, the resultant cavity gives a less accurate estimation to the true solution, but the numerical solution remains stable.

Chapter 7

Conclusions, Implications of the Research and Further Work

The work in this thesis focused on several problems relating to the growth and fouling of crystal mass in industrial environments, due to leakage of salt solutions or process liquor. The main part of the thesis focused on the development and implementation of models such that the growth behaviour of crystalline formations could be evaluated and quantified for varying physical parameters. This was accomplished through the both the adaptation of previous geological models, and the development of a coupled multi-physics model such that fluid flow, heat transfer and crystallisation mechanisms could be considered. The second part of the thesis focused on the development of a model such that a geometric inverse problem was solved, and a potential non-invasive method was evaluated for the monitoring and detection of growing crystalline formations. This allowed the internal mapping of a moving boundary system through external heat flux data. The four main elements of the research and their key findings are summarised in the following section. Following this several areas are suggested for future research. Finally, the implications of the research presented in this thesis are summarised.

7.1 Key Findings from the Research

In this section the key findings of each Chapter are summarised.

7.1.1 Adaptation of a Geological Stalagmite Model for Use in Industry

Due to the differences in time scales between fluid flow and crystallisation phenomena, models which related to the long term crystallisation behaviour of industrial materials were limited. Industrial crystal growth systems tended to focus on the growth of crystals from highly controlled or simple fluid flows. In addition to this they generally described either the early onset of growth of a singular crystal or the evolution behaviour of populations of crystalline system. Despite this, crystals were generally only described by a scalar function and therefore had no effect on the localised topography. When exploring alternate areas of research, removed from the traditional process background, it was found that a particular area of interest in which these problems were commonly experienced was in geological modelling. Due to the long time-scales in which geological formations are grown, it is often found that the differences between the timescales for fluid flow and crystallisation are large, and as such specifically developed models consider this. The work in Chapter 3 adapted a previous geological model [162] for describing the growth of stalagmite formations.

The numerical implementation of the model in [162] was modified such that it was robust for the modelling of formations over smaller time and length scales. Following a simple qualitative verification study to show that the results were agreeable with the experimental data, a set of numerical studies was carried out such that the effects of the model parameters on the final formation could be found. The key findings of this study were:

- From comparing model results to the experimentally observed formation heights and widths, it was clear that the model was capable of predicting the formations obtained in the experiments. The model highlighted that if accurate solutions were to be obtained, due to the sensitivity to changes in temperature and crystal growth coefficient, regular, accurate temperature data and detailed knowledge of the material properties are required.

- The width of the formation was sensitive to changes in the mass flow rate. In the case of a non-constant mass flow rate, the formation widths varied through time, such that in the case of the 8 Molar solution, the widths of the material deposited in the central tower formation over a given timeframe were governed by the solution's

flow rate at that particular point in time. Due to this, clear changes in formation width could be seen when considering different points in the formation height.

- The final crystalline formation's height was shown to be particularly sensitive to variations in the liquid solution's temperature. Studies involved the generation of varying sets of input temperatures, interpolated from a small dataset of experimental temperatures provided by the NNL.
- The results suggest that the width and height of the final formation is highly dependent on the empirically calculated, material specific crystal growth coefficient, K.

For all parameter sets it was noted that limited growth occurred away from the centralised tower formation. This study therefore concluded that in order for the full system to be considered, the final formation across the plate was dependent on physical effects currently not considered in the model. In addition to this the model was based on simplified physics for the fluid flow, such that a limited range of parameters could be considered.

7.1.2 Development of a Moving Boundary Framework for Crystallisation Problems

The work in Chapter 4 developed a generalised two-dimensional numerical framework which could potentially form the modelling basis for many crystallisation or other mass transfer problems. The work in this chapter considered various models, such as a multiphase fluid model, solute transport model and moving boundary model for capturing the fundamental governing physics in crystallisation problems. The work here was not applied to any particular physical problem, but rather was concerned with the numerical and computational implementation of the framework. The key findings of this Chapter were:

- Through validation of the work using a test case from the adapted stalagmite model in Chapter 3, the framework developed in Chapter 4 was shown to be capable of modelling crystalline formations, when assuming similar physics to the previous model.
- The VOF for capturing the multiphase fluid flow model is highly dependent on the computational mesh. It was found that a refined quadrilateral mesh performed

best, and that the model performed poorly over triangular mesh types. Different discretisation methods and solver parameters were considered and assessed for the robustness of the model. It was determined that the HRIC scheme was most appropriate when using the VOF model. Finally, the model was shown to be accurate and appropriate for describing steady state liquid films.

- The solute transport model was shown to capture the mass transfer boundary layers experienced in crystallisation. Additionally, the model demonstrated the correct boundary layer behaviour when considering different flow parameters. This agreed with the crystallisation literature [134], suggesting that the solute transport model was appropriate in this case.

- User defined functions could be implemented in order to describe the required physics and boundary conditions for crystallisation processes.

- A moving boundary method was developed in order to describe the growth of crystalline mass. The model was shown to function well when using a triangular mesh, however this criteria was not ideal when considering the the VOF. Through the development of hybrid meshing techniques, the VOF method was successfully coupled to a moving boundary, dynamic meshing model in a robust manner.

- The moving boundary model could be optimised in order to improve the robustness when considering quadrilateral meshes, through the use of user defined code or functions.

Simplified physics were considered in the adapted stalagmite model presented in Chapter 3. As such the model was restricted to thin fluid flows travelling at low velocities. In addition to this the model also did not consider the explicit modelling of diffusion. Therefore, the fundamental framework developed in Chapter 5 offers a new modelling approach such that these limitations are addressed. In addition to this the numerical framework provides a convenient and powerful tool for modelling coupled mass transfer - fluid flow systems, such that any additional physics specific to the individual problem can be readily implemented.

7.1.3 Modelling the Growth of Sodium Nitrate from Thin Liquid Films

The work in Chapter 5 developed a multi-physics CFD model from the coupled CFD moving boundary framework developed in Chapter 4. Additional physics were coupled to the model such that the growth of crystalline formations from salt solutions could be considered. In addition to this, the model here extends the previous framework such that an axisymmetric solution is obtained. This allowed the direct comparison of the model's results to experimental data. Summarising, the main conclusions of the work were:

- Through validating the model against the experimental dataset provided by the NNL, the developed model was shown to be able to successfully model the growth of crystalline formations of a surrogate liquor.
- User defined codes could be included such that additional physics could be incorporated into the CFD framework model, i.e. evaporation and variable material properties. The implementation of these was shown to function correctly.
- The solute diffusivity has a small impact on the shape of the tower formation and the solution density has negligible impact for the considered range of parameters investigated.
- The severity of the leakage (mass flow rate) heavily influences the final formation width, confirming the results from Chapter 3,
- Environmental parameters significantly influence the final formation shape away from the centralised tower.

The coupled model allows essential physical behaviour associated with the problem to be reliably accounted for, i.e. liquid film flow, evaporation, diffusion, temperature dependent solubility and concentration dependent fluid rheology. Through validation studies the model was shown successful when considering the case for supersaturated solutions, however it should be noted that due to the implementation of the addition physics, a full parameter set can be considered such that the torus formations observed when using under-saturate solution (5 Molar case in NNL trials) could be described.

7.1.4 Inverse Problem Methods for the Detection and Monitoring of Growing Crystalline Formations

The work in Chapter 6 solved an inverse geometric problem for the two-dimensional heat equation in order to locate an internal moving defect, described by a smooth connected boundary. This work was carried out in order to test both the accuracy and stability of the MFS, and hence its feasibility to be applied in an industrial environment. The key findings of the research were:

- In these cases the work has shown that the modelling approach is capable for reconstructing simple circular boundaries to a high degree of accuracy (when assumed a Diriclet condition on the internal boundary). Results remained accurate and stable even when large amounts of noise were imposed on the input data.

- For stationary complex shapes the method obtained stable solutions to a high level of accuracy (when assumed a Diriclet condition on the internal boundary).

- For dynamically changing complex shapes which were not fixed in time, the model had difficulty in obtaining accurate solutions for times close to the initial configuration. Results away from $t = 0$ were of a reasonable accuracy (when assumed a Dirichlet condition on the internal boundary).

- When considering the Neumann problem on the internal boundary, it was shown that for simple circular shapes the method was accurate and stable when the input data remained uncontaminated. Solutions close to $t = 0$ were shown to be inaccurate, unless large MFS parameters sizes were chosen. For noisy input data the accuracy of the model decreased rapidly.

  The work here showed that the MFS method has potential for being applied in an industrial setting, such that information regarding the internal structure of an enclosed unit could be obtained. For an accurate and robust model to be implemented it was shown that careful consideration is needed when selecting the regularisation parameters in the model.

7.2 Future Research

The work presented in this thesis is novel and up-to-date with current research and as such it was published in several peer review journals. However, certain work may benefit from additional studies. Furthermore, whilst this work is appropriate for the problem here, the applicability of alternative approaches could be explored.

Expanding the parameter set to consider varying solution concentrations It should also be noted that work here generally focused on the simulation of the tower formations, as experienced in the 8 Molar sodium nitrate drip trials. For lower concentration solutions, different characteristic shapes were found. Due to the robustness of the model here and the inclusion of the relevant physics, there is no reason why it could not also capture these formations. In order to future understand the system such that the knowledge can be applied to the modelling of heavy metal solution, studies relating to this parameter set could be carried out

Experimental determination of model parameters The work presented in Chapters 3 and 5 implemented crystallisation models which depend on experimentally determined coefficients. Whilst the crystal growth coefficient K (used in Chapter 3) has been determined in several studies, it is known to vary depending on the system conditions. In addition to this, the parameter k_r was estimated in this work due to lack of empirical data. As there is no way to deterministically or mechanistically obtain these parameters, it is thought that additional experimental would be beneficial. Further studies regarding sodium nitrate could be carried out in order to obtain a temperature related expression for k_r. Furthermore, the experimental dataset provided by the NNL was limited when considering the measured spatial and temporal temperatures. Due to this, work relied on techniques to interpolate the data in order to generate several possible datasets. With these additional factors the model could be validated further to increase confidence.

Expanding the model to capture the crystallisation of heavy metal solutions Experiments in order to determine the model parameters for sodium nitrate would be relatively trivial. Obtaining the parameters for heavy metal solutions would be more difficult due to the cost implications and the safety aspects. If experimental determination

of parameters is deemed infeasible it is thought that experiments could be carried out on a range of simulant materials, such that a wider parameter set is available. Through this, and by comparing the chemical composition of the materials, it is thought that a closer approximation to heavy metal behaviour could be obtained.

Fully three dimensional modelling The model in chapter 5 was implemented and tested such that two-dimensional axisymmetric results were obtained. Whilst this initial modelling work was a good approximation to the formations found, the formations were not perfectly axisymmetric. Also, due to the incline of the plate, this axisymmetric assumption only held strictly true in the path directly to the outlet. As such, in order to obtain further accuracy in describing the size and shape of the formation, and to fully account for the incline of the plate, a three-dimensional modelling approach could be taken. It should be noted that the user defined routines developed in this work here could be easily adapted such that they can be applied to a three-dimensional model. It is thought that the implementation of three-dimensional model would be relatively trivial, however due to the computational cost of running the model, a full parametric study would be time consuming.

Furthermore, the initial stalagmite model also assumes an axisymmetric result. Further work has been found in geological literature such that terrace formations have been modelled. These models employ a fully three-dimensional, cellular model such that for a given cell, a region on the terrace is described. Following this, the elevation of the cell relative to its neighbours determines the distribution of flow from this cell into its neighbouring cells. Simplified flow models are assumed within this work, which hold similar limitations to those of the adapted stalagmite model. Despite this, it is thought that a similar technique could be applied to the work in Chapter 3, such that quick approximations to the three-dimensional configuration of the formations could be found.

Development and further testing of the inverse problem model for implementation in an industrial setting. The work in Chapter 6 carried out a study such that a novel approach for solving an geometric inverse problem for the transient two-dimensional heat equation could be solved. It is thought that through additional testing of the regularisation parameters the accuracy and robustness of the models could be im-

proved. In addition to this further optimisation methods could be explored, such that parallel computing could be developed further. At the time of writing this thesis, modern GPU technology was beginning to receive a great deal of interest from researchers. It is thought with the development of a non-linear optimisation which harnesses this emerging technology, it would be possible to consider much larger MFS parameter sets.

Application of the framework for alternative applications The framework developed in Chapter 4 was developed such that it could be applied to other crystallisation problems of interest. A key example of this would be in the fouling of industrial heat exchangers. Current studies regarding this problem often do not allow the calculation of the local deposition rate, but rather an overall rate of fouling such that localised effects are ignored. In addition to this, the few studies that do observe local deposition rates do not then account for the changes on the flow and temperature fields due to the deposited mass.

7.3 Implications of the Research and Conclusions

The work here has focused on the problem regarding the deposition of crystallisation mass in nuclear processing environments. This problem has not received much attention in the past, despite it being a major concern for industries involved in the nuclear process cycle. As such, several key issues and gaps in the knowledge were previously highlighted. This proved problematic for the nuclear industry where it is a governmental requirement that safety standards remain at a high level, and all elements of the process cycle must be shown to satisfy given safety criteria. As such, potential problems need to be understood fully, such that informed safety and risk assessments can be made regarding the potential impact of possible incidents.

The first key issue addressed by the thesis was that for known process parameters, industrial specialists currently possess no methods for predicting the size or morphology of a resultant crystalline formation. These properties are of key important when considering the potential criticality risk. Therefore the work here has addressed this problem through the development and implementation of several mathematical models. The implications of these models is that now industry researchers have a potential method such that safety

and risk assessments can be made in order to assess the impact of a potential leakage of process liquor. In addition to this, results from the research have shown the formation's sensitivity to various process and environmental parameters. This will allow physical parameters to be controlled and optimised such that in an event of a leakage, the criticality of formations can be minimised.

The second key issue regarding the problem here was that due to the safety protocols in place, plant operators have no means in which they can externally assess the build up of material when a leakage is known to have occurred within a contained vessel. As such, the work in this thesis has also attempted a preliminary study, such that a mathematical geometric inverse problem is solved, and internal mappings of the geometric configuration can be made, based on available external data. The implications of the work here suggest that whilst the availability of observational data is low in a typical nuclear process environment, there is scope to find useful information using measured heat flux values. The implications of this are of particular importance as these values are readily obtainable, even when considering the current infrastructure of safety measures implemented in a nuclear process facility.

Bibliography

[1] C. Albert, H. Marschall, and D. Bothe. Direct numerical simulation of interfacial mass transfer into falling films. *International Journal of Heat and Mass Transfer*, 69:343 – 357, 2014.

[2] C. Albert, H. Raach, and D. Bothe. Influence of surface tension models on the hydrodynamics of wavy laminar falling films in volume of fluid-simulations. *International Journal of Multiphase Flow*, 43:66 – 71, 2012.

[3] M. Amaouche, A. Djema, and H. A. Abderrahmane. Film flow for power-law fluids: Modeling and linear stability. *European Journal of Mechanics - B/Fluids*, 34:70 – 84, 2012.

[4] W. Ambrosini, N. Forgione, and F. Oriolo. Statistical characteristics of a water film falling down a flat plate at different inclinations and temperatures. *International Journal of Multiphase Flow*, 28(9):1521 – 1540, 2002.

[5] H. A. Amiri and A. Hamouda. Evaluation of level set and phase field methods in modeling two phase flow with viscosity contrast through dual-permeability porous medium. *International Journal of Multiphase Flow*, 52:22 – 34, 2013.

[6] J. D. Anderson. *Computational Fluid Dynamics*. McGraw-Hill, New York, 1995.

[7] A. Andrews. Nuclear fuel reprocessing: U.S. policy development. Technical report, Congressional Research Service, 2008.

[8] ANSYS Inc. Fluent v14.0 user guide.

[9] M. Arellano, H. Benkhelifa, G. Alvarez, and D. Flick. Coupling population balance and residence time distribution for the ice crystallization modeling in a scraped surface heat exchanger. *Chemical Engineering Science*, 102:502 – 513, 2013.

[10] A. Avci, M. Can, and A. B. Etemoğlu. A theoretical approach to the drying process of thin film layers. *Applied Thermal Engineering*, 21(4):465 – 479, 2001.

[11] M. M. Awad. Fouling of heat transfer surfaces. In A. Belmiloudi, editor, *Heat Transfer - Theoretical Analysis, Experimental Investigations and Industrial Systems*. InTech, 2011.

[12] G. Azimi, V. Papangelakis, and J. Dutrizac. Modelling of calcium sulphate solubility in concentrated multi-component sulphate solutions. *Fluid Phase Equilibria*, 260(2):300 – 315, 2007.

[13] S. D. Aziz and S. Chandra. Impact, recoil and splashing of molten metal droplets. *International Journal of Heat and Mass Transfer*, 43(16):2841 – 2857, 2000.

[14] V. Badalassi, H. Ceniceros, and S. Banerjee. Computation of multiphase systems with phase field models. *Journal of Computational Physics*, 190(2):371 – 397, 2003.

[15] A. Baker and C. Bradley. Modern stalagmite δ^{18}: Instrumental calibration and forward modelling. *Global and Planetary Change*, 71(3-4):201–206, 2010.

[16] M. Baltussen, J. Kuipers, and N. Deen. A critical comparison of surface tension models for the volume of fluid method. *Chemical Engineering Science*, 109:65 – 74, 2014.

[17] B. Bansal, H. Muller-Steinhagen, and X. D. Chen. Performance of plate heat exchangers during calcium sulphate fouling - investigation with an in-line filter. *Chemical Engineering and Processing: Process Intensification*, 39(6):507 – 519, 2000.

[18] E. Bard, F. Antonioli, and S. Silenzi. Sea-level during the penultimate interglacial period based on a submerged stalagmite from Argentarola cave (Italy). *Earth and Planetary Science Letters*, 196(34):135 – 146, 2002.

[19] K. G. Barraclough. Manufacture of bulk crystals in western europe. Technical report, KGB Consulting Ltd, 2006.

[20] T. Barth and D. Jespersen. The design and application of upwind schemes on unstructured meshes. *27th Aerospace Sciences Meeting, Nevada*, 1989.

[21] M. Bayat, J. Aminian, M. Bazmi, S. Shahhosseini, and K. Sharifi. CFD modeling of fouling in crude oil pre-heaters. *Energy Conversion and Management*, 64:344 – 350, 2012.

[22] A. Bejan and D. Gobin. Constructal theory of droplet impact geometry. *International Journal of Heat and Mass Transfer*, 49(15-16):2412 – 2419, 2006.

[23] A. Bekker, T. Li, and I. Livk. 2-D population balance modelling of nucleation and growth of needle-shape crystals. In I. A. Karimi and R. Srinivasan, editors, *11th International Symposium on Process Systems Engineering*, volume 31 of *Computer Aided Chemical Engineering*, pages 175 – 179. Elsevier, 2012.

[24] R. Bird, W. Stewart, and E. Lightfoot. *Transport Phenomena*. Wiley International Edition. Wiley, 1960.

[25] J. Bohacek. Surface tension model for high viscosity ratios implemented in VOF model. *ILASS, 23rd Annual Conference on Liquid Atomization and Spray Systems, Brno, Czech Republic*, 2010.

[26] D. J. Borman, D. B. Ingham, B. T. Johansson, and D. Lesnic. The method of fundamental solutions for detection of cavities in EIT. *Journal of Integral Equations and Applications*, 21:383–406, 2009.

[27] G. Botsaris. Secondary nucleation a review. In J. Mullin, editor, *Industrial Crystallization*, pages 3–22. Springer US, 1976.

[28] C. H. Bovington and A. L. Jones. Tracer study of the kinetics of dissolution of barium sulphate. *Trans. Faraday Soc.*, 66:764–768, 1970.

[29] C. Boxler, W. Augustin, and S. Scholl. Composition of milk fouling deposits in a plate heat exchanger under pulsed flow conditions. *Journal of Food Engineering*, 121:1 – 8, 2014.

[30] J. Brackbill, D. Kothe, and C. Zemach. A continuum method for modeling surface tension. *Journal of Computational Physics*, 100(2):335 – 354, 1992.

[31] F. Brahim, W. Augustin, and M. Bohnet. Crystallisation fouling of CaCO3 effect of bulk precipitation on mass deposition on the heat transfer surface. *Heat Exchanger*

Fouling and Cleaning: Fundamentals and Applications, Santa Fe, New Mexico, USA, 2003.

[32] F. Brahim, W. Augustin, and M. Bohnet. Numerical simulation of the fouling process. *International Journal of Thermal Sciences*, 42(3):323 – 334, 2003.

[33] A. Bravais and A. Etudes. *Crystallographiques*. Gauthier Villers, Paris, 1866.

[34] J. C. Brice. *Crystal Growth Processes*. Blackie Academic & Professional, 1986.

[35] F. Brown. A review of best practices for Monte Carlo criticality calculations. Technical report, Los Alamos National Laboratory, 2009.

[36] K. Bryan and L. F. Caudill, Jr. Stability and reconstruction for an inverse problem for the heat equation. *Inverse Problems*, 14:1429–1453, 1998.

[37] D. Buhmann and W. Dreybrodt. The kinetics of calcite dissolution and precipitation in geologically relevant situations of karst areas: 1. Open system. *Chemical Geology*, 48(14):189 – 211, 1985.

[38] C. Burrows, C. Phillips, and A. Milliken. The Thermal Oxide Reprocessing Plant at Sellafield - Lessons Learned from 10 Years of Hot Operations and their Applicability to the DOE Environmental Management Program. In *Wm'06 Conference,February 26 - March 2, Tucson, Az*, 2006.

[39] W. K. Burton, N. Cabrera, and F. C. Frank. The growth of crystals and the equilibrium structure of their surfaces. *Philosophical Transactions of the Royal Society of London. Series A, Mathematical and Physical Sciences*, 243(866):299–358, 1951.

[40] R. H. Byrd, J. C. Gilbert, and J. Nocedal. A trust region method based on interior point techniques for nonlinear programming. *Mathematical Programming*, 89:149–185, 2000.

[41] K. Chaji and M. E. Bagdouri. Identification of an internal material boundary. *Inverse Problems in Science and Engineering*, 16:511–522, 2008.

[42] K. Chaji, M. E. Bagdouri, and R. Channa. A 2D domain boundary estimation. *Journal of Physics: Conference Series*, 135:012029, 2008.

[43] R. Chapko, R. Kress, and J. Yoon. On the numerical solution of an inverse boundary value problem for the heat equation. *Inverse Problems*, 14:853, 1998.

[44] R. Chapko, R. Kress, and J. Yoon. An inverse boundary value problem for the heat equation: the neumann condition. *Inverse Problems*, 15:1033, 1999.

[45] C. Chen, Y. Tsai, and C. Lan. Adaptive phase field simulation of dendritic crystal growth in a forced flow: 2D vs 3D morphologies. *International Journal of Heat and Mass Transfer*, 52(5-6):1158–1166, 2009.

[46] C. H. Chen, J. C. Chen, C. W. Lu, and C. M. Liu. Numerical simulation of heat and fluid flows for sapphire single crystal growth by the Kyropoulos method. *Journal of Crystal Growth*, 318(1):162 – 167, 2011.

[47] S. Chen and G. D. Doolen. Lattice boltzmann method for fluid flows. *Annual Review of Fluid Mechanics*, 30(1):329–364, 1998.

[48] J. Cheng, C. Yang, and Z. S. Mao. CFD-PBE simulation of premixed continuous precipitation incorporating nucleation, growth and aggregation in a stirred tank with multi-class method. *Chemical Engineering Science*, 68(1):469 – 480, 2012.

[49] J. M. Chenoweth. Final report of the HTRI/TEMA joint committee to review the fouling section of the TEMA standards. *Heat Transfer Engineering*, 11(1):73–107, 1990.

[50] A. Chernov. Present-day understanding of crystal growth from aqueous solutions. *Progress in Crystal Growth and Characterization of Materials*, 26:121 – 151, 1993.

[51] A. A. Chernov. The spiral growth of crystals. *Soviet Physics Uspekhi*, 4(1):116, 1961.

[52] W. Choi, S. Jun, L. Nguyen, N. Rungraeng, H. Yi, S. Balasubramanian, V. Puri, and J. Lee. 3D milk fouling modeling of plate heat exchanges with different surface finishes using computational fluid dynamics codes. *Journal of Food Process Engineering*, 36(4):439–449, 2012.

[53] H. K. Clark. Subcritical limits for plutonium systems. *Nuclear Science and Engineering*, 79:65–84, 1981.

[54] F. Coletti and S. Macchietto. A dynamic, distributed model of shell-and-tube heat exchangers undergoing crude oil fouling. *Industrial & Engineering Chemistry Research*, 50(8):4515–4533, 2011.

[55] J. Cooke, L. Armstrong, K. Luo, and S. Gu. Adaptive mesh refinement of gas-liquid flow on an inclined plane. *Computers & Chemical Engineering*, 60:297 – 306, 2014.

[56] P. Cubillas and M. W. Anderson. *Synthesis Mechanism: Crystal Growth and Nucleation*, pages 1–55. Wiley-VCH Verlag GmbH & Co. KGaA, 2010.

[57] X. Cui, X. Li, H. Sui, and H. Li. Computational fluid dynamics simulations of direct contact heat and mass transfer of a multicomponent two-phase film flow in an inclined channel at sub-atmospheric pressure. *International Journal of Heat and Mass Transfer*, 55(21-22):5808–5818, 2012.

[58] M. M. J. Decré and J. C. Baret. Gravity-driven flows of viscous liquids over two-dimensional topographies. *Journal of Fluid Mechanics*, 487:147–166, 6 2003.

[59] Y. Deng, J. B. Harsh, M. Flury, J. S. Young, and J. S. Boyle. Mineral formation during simulated leaks of hanford waste tanks. *Applied Geochemistry*, 21(8):1392 – 1409, 2006.

[60] J. J. Derby, J. R. Chelikowsky, T. Sinno, B. Dai, and Y. I. Kwon. Large-scale numerical modeling of melt and solution crystal growth. in perspectives on inorganic, organic, and biological crystal growth:from fundamentals to applications. *13th International Summer School on Crystal Growth, (Eds. M. Skowronski, J. J. DeYoreo and C. A. Wang).*, 2007.

[61] W. J. Deutsch, K. J. Cantrell, K. M. Krupka, M. L. Lindberg, and R. J. Serne. Hanford tank residual waste: Contaminant source terms and release models. *Applied Geochemistry*, 26(910):1681 – 1693, 2011.

[62] J. A. Diez, A. G. Gonzlez, and L. Kondic. On the breakup of fluid rivulets. *Physics of Fluids (1994-present)*, 21(8):082105, 2009.

[63] J. Ding, X. Wang, X. F. Zhou, N. Q. Ren, and W. Q. Guo. CFD optimization of continuous stirred-tank (CSTR) reactor for biohydrogen production. *Bioresource Technology*, 101(18):7005 – 7013, 2010.

[64] J. Doelman. Preventing scale buildup. http://www.pollutionengineering.com/, 2013. Accessed June 23, 2014.

[65] N. Epstein. Thinking about heat transfer fouling: A 5x5 matrix. *Heat Transfer Engineering*, 4(1):43–56, 1983.

[66] R. Eymard, T. Gallout, and R. Herbin. Finite volume methods. In P. Ciarlet and J. Lions, editors, *Solution of Equation in* $\mathbb{R}^n$ *(Part 3), Techniques of Scientific Computing (Part 3)*, volume 7 of *Handbook of Numerical Analysis*, pages 713–1018. Elsevier, 2000.

[67] A. Falola and A. Borissova. Crystsim: A software environment for modelling industrial batch cooling crystallization. *Computers and Chemical Engineering*, 38:35–43, 2012.

[68] H. Foste, F. Stehmann, W. Augustin, and S. Scholl. Pulsed flow and surface coatings to mitigate fouling. *International Conference of Heat Exchanger Fouling and Cleaning, Hungary*, 2013.

[69] S. Frisia, A. Borsato, A. Mangini, C. Sptl, G. Madonia, and U. Sauro. Holocene climate variability in sicily from a discontinuous stalagmite record and the mesolithic to neolithic transition. *Quaternary Research*, 66(3):388 – 400, 2006.

[70] M. Gao and X. P. Wang. An efficient scheme for a phase field model for the moving contact line problem with variable density and viscosity. *Journal of Computational Physics*, 272:704 – 718, 2014.

[71] J. Garside. The concept of effectiveness factors in crystal growth. *Chemical Engineering Science*, 26(9):1425 – 1431, 1971.

[72] J. Garside and R. J. Davey. Invited review secondary contact nucleation: Kinetics, growth and scale-up. *Chemical Engineering Communications*, 4(4-5):393–424, 1980.

[73] P. H. Gaskell, P. K. Jimack, M. Sellier, and H. M. Thompson. Flow of evaporating, gravity-driven thin liquid films over topography. *Physics of Fluids*, 18(1), 2006.

[74] P. H. Gaskell, P. K. Jimack, M. Sellier, H. M. Thompson, and M. C. T. Wilson. Gravity-driven flow of continuous thin liquid films on non-porous substrates with topography. *Journal of Fluid Mechanics*, 509:253–280, 2004.

[75] J. W. Gibbs. *The Collected Works of J. Willard Gibbs, Volume 1.* Yale University Press, 1957.

[76] G. Gilmer, R. Ghez, and N. Cabrera. An analysis of combined surface and volume diffusion processes in crystal growth. *Journal of Crystal Growth*, 8(1):79 – 93, 1971.

[77] J. E. Gittens, T. J. Smith, R. Suleiman, and R. Akid. Current and emerging environmentally-friendly systems for fouling control in the marine environment. *Biotechnology Advances*, 31(8):1738 – 1753, 2013.

[78] T. A. Graber, M. E. Taboada, M. N. Alvarez, and E. H. Schmidt. Determination of mass transfer coefficients for crystal growth of nitrate salts. *Crystal Research and Technology*, 34(10):1269–1277, 1999.

[79] Y. Guo, L. Wei, G. Liang, and S. Shen. Simulation of droplet impact on liquid film with CLSVOF. *International Communications in Heat and Mass Transfer*, 53:26 – 33, 2014.

[80] S. Haeri and S. Hashemabadi. Three dimensional CFD simulation and experimental study of power law fluid spreading on inclined plates. *International Communications in Heat and Mass Transfer*, 35(8):1041 – 1047, 2008.

[81] L. Hageman and D. Young. *Applied Iterative Methods.* New York: Academic Press, 1981.

[82] O. Hammer, D. Dysthe, B. Lelu, H. Lund, P. Meakin, and B. Jamtveit. Calcite precipitation instability under laminar, open-channel flow. *Geochimica et Cosmochimica Acta*, 72(20):5009 – 5021, 2008.

[83] S. Hardt and F. Wondra. Evaporation model for interfacial flows based on a continuum-field representation of the source terms. *Journal of Computational Physics*, 227(11):5871–5895, 2008.

[84] Y. Haroun, D. Legendre, and L. Raynal. Volume of fluid method for interfacial reactive mass transfer: Application to stable liquid film. *Chemical Engineering Science*, 65(10):2896–2909, 2010.

[85] Health and Safety Executive. Report of the investigation into the leak of dissolver product liquor at the thermal oxide reprocessing plant (THORP), Sellafield, notified to HSE on 20 April 2005, February 2007.

[86] A. Heath and I. Livk. Coupled population balance and CFD model for a continuous gibbsite crystalliser. *Fifth International Conference on CFD in the Process Industries, CSIRO, Melbourne, Australia*, 2006.

[87] C. Hirt and B. Nichols. Volume of fluid (VOF) method for the dynamics of free boundaries. *Journal of Computational Physics*, 39(1):201–225, 1981.

[88] Y. Hon and M. Li. A computational method for inverse free boundary determination problem. *International Journal for Numerical Methods in Engineering*, 73:1291–1309, 2008.

[89] B. Hu and S. L. Kieweg. The effect of surface tension on the gravity-driven thin film flow of Newtonian and power-law fluids. *Computers & Fluids*, 64:83 – 90, 2012.

[90] B. R. Hutchinson and G. D. Raithby. A multigrid method based on the additive correction strategy. *Numerical Heat Transfer*, 9(5):511–537, 1986.

[91] M. Ikehata and M. Kawashita. On the reconstruction of inclusions in a heat conductive body from dynamical boundary data over a finite time interval. *Inverse Problems*, 26:095004, 2010.

[92] R. I. Issa. Solution of the implicitly discretised fluid flow equations by operator-splitting. *Journal of Computational Physics*, 62:40–65, 1986.

[93] M. Jabbari, R. Bulatova, J. Hattel, and C. Bahl. An evaluation of interface capturing methods in a VOF based model for multiphase flow of a non-Newtonian ceramic in tape casting. *Applied Mathematical Modelling*, 38(13):3222 – 3232, 2014.

[94] B. Johansson, D. Lesnic, and T. Reeve. A method of fundamental solutions for two-dimensional heat conduction. *International Journal of Computer Mathematics*, 88:1697–1713, 2008.

[95] A. G. Jones. *Crystallization Process Systems*. Butterworth-Heinemann, 2002.

[96] W. Jones and B. Launder. The prediction of laminarization with a two-equation model of turbulence. *International Journal of Heat and Mass Transfer*, 15(2):301 – 314, 1972.

[97] C. Joseph. Growth and characterization of mixed rare earth oxalate crystals. *PhD Thesis, Mahatma Gandhi University*, 1995.

[98] S. Jun and V. M. Puri. 3D milk-fouling model of plate heat exchangers using computational fluid dynamics. *International Journal of Dairy Technology*, 58(4):214–224, 2005.

[99] P. Kapitza. Wave flow of thin layers of a viscous fluid. In D. T. Haar, editor, *Collected Papers of P.L. Kapitza*, pages 662 – 709. Pergamon, 1965.

[100] A. Karageorghis and D. Lesnic. Dectection of cavities using the method of fundamental solutions. *Inverse Problems in Science and Engineering*, 17:803–820, 2008.

[101] A. Karageorghis and D. Lesnic. Application of the MFS to inverse scattering problems. *Engineering Analysis with Boundary Elements*, 35:631–638, 2011.

[102] A. Karageorghis, D. Lesnic, and L. Marin. A survey of applications of the MFS to inverse problems. *Inverse Problems in Science and Engineering*, 19(3):309–336, 2011.

[103] M. N. Kashani, J. Aminian, S. Shahhosseini, and M. Farrokhi. Dynamic crude oil fouling prediction in industrial preheaters using optimized ANN based moving window technique. *Chemical Engineering Research and Design*, 90(7):938 – 949, 2012.

[104] G. Kaufmann. Stalagmite growth and palaeo-climate: the numerical perspective. *Earth and Planetary Science Letters*, 214:251–266, 2003.

[105] G. Kaufmann and W. Dreybrodt. Stalagmite growth and palaeo-climate: an inverse approach. *Earth and Planetary Science Letters*, 224:529–545, 2004.

[106] H. Kawakami, Y. Moriyama, and M. Tsuchiya. An estimation problem for the shape of a domain varying with time via parabolic equations. *Inverse Problems*, 23:755–783, 2007.

[107] H. Kawakami and M. Tsuchiya. Uniqueness in shape identification of a time-varying domain and related parabolic equations on non-cylindrical domains. *Inverse Problems*, 26:125007, 2010.

[108] Y. S. Khor and Q. Xiao. CFD simulations of the effects of fouling and antifouling. *Ocean Engineering*, 38(10):1065 – 1079, 2011.

[109] E. Kim and J. Baek. Numerical study of the parameters governing the impact dynamics of yield-stress fluid droplets on a solid surface. *Journal of Non-Newtonian Fluid Mechanics*, 173-174:62 – 71, 2012.

[110] K. V. Kumar. Regression analysis for the two-step growth kinetics of crystals in pure solutions. *Industrial & Engineering Chemistry Research*, 48(16):7852–7859, 2009.

[111] H. Lan, M. Friedrich, B. Armaly, and J. Drallmeier. Simulation and measurement of 3D shear-driven thin liquid film flow in a duct. *International Journal of Heat and Fluid Flow*, 29(2):449 – 459, 2008.

[112] M. Lappa. An attachment kinetics-based volume of fraction method for organic crystallization: a fluid-dynamic approach to macromolecular-crystal engineering. *Journal of Computational Physics*, 191(1):97 – 129, 2003.

[113] C. Lavarenne, D. Mennerdahl, and C. Dean. Evaluation of nuclear criticality safety data and limits for actinides in transport. Technical report, French Institute for Radiological Protection and Nuclear Safety, 2001.

[114] B. Leonard. A stable and accurate convective modelling procedure based on quadratic upstream interpolation. *Computer Methods in Applied Mechanics and Engineering*, 19(1):59 – 98, 1979.

[115] R. J. LeVeque. *Finite Volume Methods for Hyperbolic Problems*. Cambridge University Press., 2002.

[116] B. Lewis. The growth of crystals at low supersaturation: II. comparison with experiment. *Journal of Crystal Growth*, 21(1):40 – 50, 1974.

[117] W. Li, X. Y. Wu, Z. Luo, S. C. Yao, and J. L. Xu. Heat transfer characteristics of falling film evaporation on horizontal tube arrays. *International Journal of Heat and Mass Transfer*, 54(9-10):1986 – 1993, 2011.

[118] X. Li, J. Glimm, X. Jiao, C. Peyser, and Y. Zhao. Study of crystal growth and solute precipitation through front tracking method. *Acta Mathematica Scientia*, 30(2):377–390, 2010.

[119] M. Liiri, Y. Enqvist, J. Kallas, and J. Aittamaa. CFD modelling of single crystal growth of potassium dihydrogen phosphate (KDP) from binary water solution at 30°c. *Journal of Crystal Growth*, 286(2):413 – 423, 2006.

[120] J. López, J. Hernández, P. Gómez, and F. Faura. A volume of fluid method based on multidimensional advection and spline interface reconstruction. *Journal of Computational Physics*, 195(2):718 – 742, 2004.

[121] Los Alamos National Laboratory. Nuclear criticality safety guide, July 2005.

[122] M. Losurdo, H. Spliethoff, and J. Kiel. Ash deposition modeling using a visco-elastic approach. *Fuel*, 102:145 – 155, 2012.

[123] P. Martin, N. Chin, and G. Campbell. Aeration during bread dough mixing: II. a population balance model of aeration. *Food and Bioproducts Processing*, 82(4):268 – 281, 2004.

[124] Matlab. http://www.mathworks.co.uk/products/matlab/. Accessed August 28th, 2014.

[125] M. Mayer, J. Bucko, W. Benzinger, R. Dittmeyer, W. Augustin, and S. Scholl. The impact of crystallization fouling on a microscale heat exchanger. *Experimental Thermal and Fluid Science*, 40:126 – 131, 2012.

[126] M. Mayer, J. Bucko, W. Benzinger, R. Dittmeyer, W. Augustin, and S. Scholl. Crystallization fouling in experimental micro heat exchangersoptical and thermal investigations. *Experimental Heat Transfer*, 26(5):487–502, 2013.

[127] P. Meakin and B. Jamtveit. Geological pattern formation by growth and dissolution in aqueous systems. *Proceedings of the Royal Society A: Mathematical, Physical and Engineering Science*, 466(2115):659–694, 2010.

[128] A. M. Meirmanov. *The Stefan Problem*. De Gruyter expositions in mathematics. Walter de Gruyter, 1992.

[129] M. Mittermaier, P. Schulze, and F. Ziegler. A numerical model for combined heat and mass transfer in a laminar liquid falling film with simplified hydrodynamics. *International Journal of Heat and Mass Transfer*, 70:990 – 1002, 2014.

[130] N. Moelans, B. Blanpain, and P. Wollants. An introduction to phase-field modeling of microstructure evolution. *Calphad*, 32(2):268 – 294, 2008.

[131] MONK - a Monte Carlo program for nuclear criticality safety and reactor physics analyses. http://www.answerssoftwareservice.com/monk/. Accessed June 11, 2014.

[132] K. Moran, J. Inumaru, and M. Kawaji. Instantaneous hydrodynamics of a laminar wavy liquid film. *International Journal of Multiphase Flow*, 28(5):731 – 755, 2002.

[133] H. Muller-Steinhagen, M. R. Malayeri, and A. P. Watkinson. Fouling of heat exchangers-new approaches to solve an old problem. *Heat Transfer Engineering*, 26(1):1–4, 2005.

[134] J. W. Mullin. *Crystallization*. Chemical, Petrochemical & Process. Elsevier Science, 2001.

[135] J. W. Mullin and J. Garside. The crystallization of aluminium potassium sulphate: Study in the assessment of crystallizer design data. part i: Single crystal growth rates single crystal growth rates, part ii - growth in a fluidised bed. *Transactions of the institution of chemical engineers and the chemical engineer*, 45:285–295, 1967.

[136] S. Muzaferija, M. Peric, P. Sames, and T. Schellin. A two-fluid Navier-Stokes solver to simulate water entry. *Twenty-Second Symposium on Naval Hydrodynamics*, pages 277–289, 1999.

[137] Nast2d. http://wissrech.ins.uni-bonn.de/research/projects/NaSt2D/index.html. Accessed August 19th, 2014.

[138] W. Noh and P. Woodward. SLIC (simple line interface calculation). In A. van de Vooren and P. Zandbergen, editors, *Proceedings of the Fifth International Conference on Numerical Methods in Fluid Dynamics June 28 - July 2, 1976, Twente Uni-*

versity, Enschede, volume 59 of *Lecture Notes in Physics*, pages 330–340. Springer, Berlin, 1976.

[139] A. Noyes and W. Whitney. Über die auflösungsgeschwindigkeitvon festen stoffen in ihren eigenen lsungen. *Zeitschrift fr Physikalische Chemie*, 23:689 – 692, 1897.

[140] W. Nusselt. Die Oberflachenkondensation des Wasserdampfes. *VDI-Zeitschrift*, 60:541546, 1916.

[141] Oak Ridge National Laboratory. Minimum critical values study, September 1996.

[142] M. Ohara and R. C. Reid. *Modeling Crystal Growth Rates from Solution*. Prentice-Hall, 1973.

[143] H. Oosterhof, R. Geertman, G. Witkamp, and G. Rosmalen. The growth of sodium nitrate from mixtures of water and isopropoxyethanol. *Journal of Crystal Growth*, 198:754–759, 1999.

[144] Openfoam: The open source cfd toolbox. http://www.openfoam.com/. Accessed August 19th, 2014.

[145] A. Oron, S. H. Davis, and S. G. Bankoff. Long-scale evolution of thin liquid films. *Rev. Mod. Phys.*, 69:931–980, 1997.

[146] S. Osher and J. A. Sethian. Fronts propagating with curvature-dependent speed: Algorithms based on Hamilton-Jacobi formulations. *Journal of Computational Physics*, 79(1):12 – 49, 1988.

[147] J. G. Otakar Söhnel. *Precipitation: Basic Principles and Industrial Applications*. Butterworth-Heinemann, 1992.

[148] T. Paakkonen, M. Riihmaki, E. Puhakka, E. Muurinen, C. Simonson, and R. Keisi. Numerical simulation of the fouling on structured heat transfer surfaces (fouling). *International Conference of Heat Exchanger Fouling and Cleaning, Austria*, 2014.

[149] S. V. Patankar. *Numerical Heat Transfer and Fluid Flow*. New York, McGraw-Hill., 1980.

[150] A. Pritchard. The economics of fouling. In L. Melo, T. Bott, and C. Bernardo, editors, *Fouling Science and Technology*, volume 145 of *NATO ASI Series*, pages 31–45. Springer Netherlands, 1988.

[151] P. Queutey and M. Visonneau. An interface capturing method for free-surface hydrodynamic flows. *Computers & Fluids*, 36(9):1481 – 1510, 2007.

[152] A. Radu, L. Bergwerff, M. Loosdrecht, and C. Picioreanu. A two-dimensional mechanistic model for scaling in spiral wound membrane systems. *Chemical Engineering Journal*, 241:77 – 91, 2014.

[153] R. Ranjan, J. Y. Murthy, and S. V. Garimella. A microscale model for thin-film evaporation in capillary wick structures. *International Journal of Heat and Mass Transfer*, 54(1-3):169–179, 2011.

[154] B. Rapko, S. Sinkov, and T. Levitskaia. Removal of 137cs from dissolved hanford tank saltcake by treatment with ie-911. Technical report, Pacific Northwest National Laboratory, 2003.

[155] J. Reddy. *An Introduction to the Finite Element Method*. McGraw-Hill, New York, 2005.

[156] C. M. Rhie and W. L. Chow. Numerical study of the turbulent flow past an airfoil with trailing edge separation. *AIAA Journal*, 21:1525–1532, 1983.

[157] M. Rieber. Numerische modellierung der dynamik freier grenzflchen in zweiphasenstrmungen. *Ph.D. thesis, University of Stuttgart*, 2004.

[158] M. Rieber and A. Frohn. A numerical study on the mechanism of splashing. *International Journal of Heat and Fluid Flow*, 20(5):455 – 461, 1999.

[159] H. F. Robey. Numerical simulation of the hydrodynamics and mass transfer in the large scale, rapid growth of KDP crystals. Part 2: Computation of the mass transfer. *Journal of Crystal Growth*, 259:388–403, 2003.

[160] H. F. Robey and D. Maynes. Numerical simulation of the hydrodynamics and mass transfer in the large scale, rapid growth of KDP crystals. Part 1: Computation of the transient, three-dimensional flow field. *Journal of Crystal Growth*, 222:263–278, 2001.

[161] I. V. Roisman and C. Tropea. Impact of a drop onto a wetted wall: description of crown formation and propagation. *Journal of Fluid Mechanics*, 472:373–397, 2002.

[162] D. Romanov, G. Kaufmann, and W. Dreybrodt. Modeling stalagmite growth by first principles of chemistry and physics of calcite precipitation. *Geochimica et Cosmochimica Acta*, 72(2):423–437, 2008.

[163] J. Rosam. A fully implicit, fully adaptive multigrid method for multiscale phase-field modelling. *PhD Thesis, The University of Leeds*, 2007.

[164] S. S. Sazhin. Advanced models of fuel droplet heating and evaporation. *Progress in Energy and Combustion Science*, 32(2):162–214, 2006.

[165] H. J. Scheel. Historical aspects of crystal growth technology. *Journal of Crystal Growth*, 211(1-4):1 – 12, 2000.

[166] Sellafield Ltd. Key to Britain's energy future: The Strategy for Sellafield, November 2013.

[167] Y. Shikhmurzaev. The moving contact line on a smooth solid surface. *International Journal of Multiphase Flow*, 19(4):589 – 610, 1993.

[168] M. B. Short, J. C. Baygents, J. W. Beck, D. A. Stone, R. S. Toomey, and R. E. Goldstein. Stalactite growth as a free-boundary problem: A geometric law and its platonic ideal. *Physics Review Letters*, 94:018501, 2005.

[169] M. B. Short, J. C. Baygents, and R. E. Goldstein. Stalactite growth as a free-boundary problem. *Physics of Fluids*, 17(8):083101, 2005.

[170] S. Sinkov. Candidate reagents for dissolution of Hanford site tank sludgesscoping studies with simulants using single reagents and their mixtures. Technical report, Pacific Northwest National Laboratory, 2003.

[171] A. Soare, S. A. P. Escobar, A. I. Stankiewicz, M. R. Pascual, and H. J. M. Kramer. 2D flow and temperature measurements in a multiphase airlift crystallizer. *Industrial & Engineering Chemistry Research*, 52(34):12212–12222, 2013.

[172] E. Sultan, A. Boundaoud, and M. B. Amar. Evaporation of a thin film: diffusion of the vapour and Marangoni instabilities. *Journal of Fluid Mechanics*, 543:183–202, 2005.

[173] A. Z. Szeri. *Fluid Film Lubrication*. Cambridge University Press, 2010.

[174] L. G. Tao, S. S. Qiang, G. Y. Li, C. J. Xian, Y. Huan, and L. Y. Qiao. Special phenomena of droplet impact on an inclined wetted surface with experimental observation. *Acta Physica Sinica*, 62(8):84707, 2013.

[175] A. A. Thorburn. THORP simulated crystal accumulation trials: Nexia Solutions report (07) 8380 (issue 3). Technical report, Nexia Solutions (National Nuclear Laboratory), 2007.

[176] Y. Y. Tsui, S. W. Lin, T. T. Cheng, and T. C. Wu. Flux-blending schemes for interface capture in two-fluid flows. *International Journal of Heat and Mass Transfer*, 52(2324):5547 – 5556, 2009.

[177] O. Ubbink and R. Issa. A method for capturing sharp fluid interfaces on arbitrary meshes. *Journal of Computational Physics*, 153(1):26 – 50, 1999.

[178] J. P. Van Doormaal and G. D. Raithby. Enhancements of the simple method for predicting incompressible fluid flows. *Numerical Heat Transfer*, 7(2):147–163, 1984.

[179] S. Vessella. Quantitative estimates of unique continuation for parabolic equations, determination of unknown time-varying boundaires and optimal stability estimates. *Inverse Problems*, 24:023001, 2008.

[180] M. Volmer and W. Schultze. Condensation on crystals. *Zeitschrift fur Physikalische Chemie*, 156:1–22, 1931.

[181] I. Šutalo, A. Bui, and M. Rudman. The flow of non-newtonian fluids down inclines. *Journal of Non-Newtonian Fluid Mechanics*, 136(1):64 – 75, 2006.

[182] T. Waclawczyk and T. Koronowicz. Comparison of cicsam and hric high-resolution schemes for interface capturing. *Journal of Theoretical and Applied Mechanics*, 46(2), 2008.

[183] P. G. Walker and R. Sheikholeslami. Development and validation of an unsteady state numerical model of fouling within a crystalline system. *Developments in Chemical Engineering and Mineral Processing*, 14(1-2):287–302, 2006.

[184] G. Wang and W. Um. Mineral dissolution and secondary precipitation on quartz sand in simulated hanford tank solutions affecting subsurface porosity. *Journal of Hydrology*, 472-473:159 – 168, 2012.

[185] X. Wang, M. Li, Y. Cao, M. Cheng, and J. Song. Computational analysis of three-dimensional flow and mass transfer in a non-standard configuration for growth of a KDP crystal. *Journal of Crystal Growth*, 312(20):2952 – 2961, 2010.

[186] X. Wang, M. Li, Y. Cao, J. Song, and Z. Hu. 3D numerical simulation for single crystal growth of potassium dihydrogen phosphate in a new solution growth system. *Journal of Crystal Growth*, 327(1):102 – 109, 2011.

[187] F. K. Wasden and A. E. Dukler. A numerical study of mass transfer in free falling wavy films. *AIChE Journal*, 36(9):1379–1390, 1990.

[188] H. Wei and J. Garside. Application of CFD modelling to precipitation systems. *Chemical Engineering Research and Design*, 75(2):219 – 227, 1997.

[189] Wikimedia Commons Public Domain. Socotra cave. http://upload.wikimedia.org/wikipedia/commons/9/9a/Socotra_Cave_06.JPG, 2009. Accessed September 1, 2014.

[190] T. Xu and K. Pruess. Solubility and crystal growth of sodium nitrate from mixed alcohol water solvents. Technical Report, Curtin University of Technology. 2009.

[191] Z. Xu and P. Meakin. Phase-field modeling of solute precipitation and dissolution. *Journal of Chemical Physics*, 129(1):014705, 2008.

[192] Z. Xu and P. Meakin. Phase-field modeling of two-dimensional solute precipitation/dissolution: Solid fingers and diffusion-limited precipitation. *Journal of Chemical Physics*, 134(4):044137, 2011.

[193] A. Yarin. Drop impact dynamics: Splashing, spreading, receding, bouncing. *Annual Review of Fluid Mechanics*, 38(1):159–192, 2006.

[194] A. L. Yarin and D. A. Weiss. Impact of drops on solid surfaces: self-similar capillary waves, and splashing as a new type of kinematic discontinuity. *Journal of Fluid Mechanics*, 283:141–173, 1995.

[195] A. Yeckel and J. J. Derby. *Computer Modelling of Bulk Crystal Growth*, pages 73–119. John Wiley & Sons, Ltd, 2010.

[196] H. S. Yeh and G. B. Wills. Diffusion coefficient of sodium nitrate in aqueous solution at 25.deg. as a function of concentration from 0.1 to 1.0m. *Journal of Chemical & Engineering Data*, 15(1):187–189, 1970.

[197] W. Ying, L. Qunhui, Z. Yangyan, Y. Biao, and T. Hanzhong. A CFD-based analysis on trends of heat exchanger fouling. *Power and Energy Engineering Conference (APPEEC), Asia-Pacific*, pages 1–4, 2012.

[198] Y. Yu and X. Cheng. Experimental study of water film flow on large vertical and inclined flat plate. *Progress in Nuclear Energy*, 77:176 – 186, 2014.

[199] P. J. Zwart, A. D. Burns, and P. F. Galpin. Coupled algebraic multigrid for free surface flow simulations. *26th International Conference on Offshore Mechanics and Arctic Engineering*, pages 655 – 664, 2007.